Charge Selective Contacts and Interfaces for Perovskite Solar Cells with Improved Stability and Efficiency



Kelly Schutt

Oriel College

A thesis submitted for the degree of

Doctor of Philosophy

at the University of Oxford

Trinity Term 2019

Acknowledgements

I would like to thank the Marshall Aid Commemoration Commission for providing the funding that made my DPhil possible. I'd also like to thank Mary Denyer and the many other people at the Commission for organizing the events that make the Marshall Scholarship an outstanding cultural and intellectual experience.

I also express my deep gratitude to Henry Snaith, FRS, for his endless ideas, encouragement, and support. Your enthusiasm for research and for life is infectious and inspiring.

The many members of the Snaith research group, new and old, have my appreciation and respect. In particular, Nakita Noel and Severin Habisreutinger were tremendously helpful early in my program as they passed on the foundational knowledge required to make great perovskite solar cells. I am truly grateful to have been part of such a friendly and fun group. Special thanks to my collaborators including Pabitra Nayak, Michiel Petrus, Daniel Ramirez, and Marie-Hélène Tremblay among many others.

I would also like to thank my family for their love and guidance. I'm beginning to understand the complexity, joy, and frustration that come with parenting, and I realize that a few words can't adequately express my sincere gratitude for the many sacrifices you made for me over all these years. However, I will say that the pinnacle of great parenting is generational progress. For a child from a modest, working-class background to complete a PhD at one of the best universities in the world is clear evidence that you are both awesome. Thank you for giving me the time, freedom of thought, and unconditional support to find my own path in life. To my friends: thank you for keeping in touch, for taking the time to visit, and for all the great memories we've co-created.

Finally, I would like to thank my wife, Shiela. It hasn't always been easy over the past three years, managing two tiny children and graduate school, but we've had incredible experiences along the way that I will always cherish. We have come a very long way in such a short time, and I am excited to see where the future takes us. To my son Kepler and daughter Vera, I hope that I can inspire you to become the best possible versions of yourselves.

An Address to the Graduating Class of the California Institute of Technology.



"Why does this magnificent applied science which saves work and makes life easier bring us so little happiness? The simple answer runs: Because we have not yet learned to make sensible use of it. In war it serves that we may poison and mutilate each other. In peace it has made our lives hurried and uncertain. Instead of freeing us in great measure from spiritually exhausting labor, it has made men into slaves of machinery, who for the most part complete their monotonous long day's work with disgust and must continually tremble for their poor rations.

You will be thinking that the old man sings an ugly song. I do it, however, with a good purpose, in order to point out a consequence. It is not enough that you should understand about applied science in order that your work may increase man's blessings. Concern for the man himself and his fate must always form the chief interest of all technical endeavors; concern for the great unsolved problems of the organization of labor and the distribution of goods in order that the creations of our mind shall be a blessing and not a curse to mankind.

Never forget this in the midst of your diagrams and equations."
-Albert Einstein, 1931

"Albert Einstein Sees Lack in Applying Science", *The New York Times*. February 17, 1931.
Photo from the George Grantham Bain Collection, Library of Congress. Library of Congress Call Number 2014712247.

Contents

Acknowledgements **ii**

Contents **v**

List of Figures **ix**

List of Tables **xii**

List of Publications **xiii**

List of Abbreviations **xv**

1 Introduction **1**
- 1.1 Tragedy and Hope in the Anthropocene . . . 1
- 1.2 A Brief History of Energy and Civilization . . . 4
  - 1.2.1 Energy, Agriculture, and Population Growth . . . 5
  - 1.2.2 Energy and Human Development . . . 6
- 1.3 Paths Towards Sustainability . . . 8
  - 1.3.1 Population Stabilization . . . 8
  - 1.3.2 Biodiversity and Agriculture . . . 10
  - 1.3.3 Sustainability Oriented Economics and Policy . . . 12
  - 1.3.4 Climate Change and Stabilization . . . 15
- 1.4 Renewable Energy . . . 17
- 1.5 Considerations for Terawatt-scale Photovoltaics . . . 18
- 1.6 Commercial Viability of Perovskite Solar Cells . . . 22
- 1.7 Sustainability Outlook . . . 25

1.8 Aims of This Thesis . . . 26
References . . . 29

2 Theory and Background **37**
2.1 Semiconductor Theory . . . 37
2.1.1 Doping and Defects . . . 41
2.1.2 Semiconductor Junctions . . . 45
2.2 Fundamentals of Photovoltaic Devices . . . 48
2.2.1 Absorption and Charge Extraction . . . 48
2.2.2 J-V Characterization of Solar Cells . . . 54
2.2.3 Limits to Power Conversion Efficiency . . . 57
2.3 Perovskites . . . 59
2.3.1 Organic-Inorganic Metal Halide Perovskites for Photovoltaics 62
2.4 Perovskite Solar Cell Stability . . . 65
2.4.1 Degradation Mechanisms for Perovskite Absorbers . . . 66
2.4.2 Degradation Mechanisms for Hole Transport Materials . . . 68
2.4.3 Degradation Mechanisms for Electron Transport Layers . . . 70
2.4.4 Degradation Mechanisms for Electrodes . . . 71
References . . . 73

3 Experimental Methods **78**
3.1 Device Fabrication . . . 78
3.1.1 n-i-p devices . . . 78
3.1.2 p-i-n devices . . . 81
3.2 Characterization . . . 82
3.2.1 Optical and Spectroscopic Characterization . . . 82
3.2.2 Material Characterization . . . 86
3.2.3 Photovoltaic Device Characterization . . . 89
3.3 Hole Transport Material Synthesis . . . 90
3.3.1 EDOT-Amide-TPA Synthesis . . . 90
3.3.2 CL1-2 Synthesis . . . 90
References . . . 91

4 Meso-Superstructured Perovskite Solar Cells: Revealing the Role of the Mesoporous Layer **93**
4.1 Introduction . . . 94
4.2 Electronic Effects of Mesoporous Layer . . . 97
4.3 Photoluminescence and Photoconductivity . . . 99
4.4 Comparing Mesoporous and Planar Device Architectures . . . 103
4.5 Champion Devices and External Quantum Efficiency . . . 105
4.6 Mechanism of Mesoporous Doping Effect . . . 108
4.7 Conclusion . . . 109
References . . . 111

5 Overcoming Zinc Oxide Interface Instability with a Methylammonium-free Perovskite for High Performance Solar Cells **114**
5.1 Introduction . . . 115
5.2 Chemical Reactions at the ZnO-Perovskite Interface . . . 118
5.3 The Effect of Cation Acidity on Interface Degradation . . . 122
5.4 Device Stability . . . 125
5.5 Device Performance . . . 126
5.6 Interface Quality . . . 129
5.7 Conclusion . . . 131
References . . . 133

6 Cesium Salt Passivation of SnO_2 for Perovskite Solar Cells with Improved Stability and Performance **137**
6.1 Introduction . . . 138
6.2 Device Data . . . 140
6.3 Interface Characterization . . . 142
6.4 Stability of Cs Salt Passivated Interfaces and Devices . . . 145
6.5 Future Work . . . 146
6.6 Conclusion . . . 148
References . . . 149

7 New Generation Hole Transporting Materials for Perovskite Solar Cells: Amide-Based Small-Molecules with Nonconjugated Backbones **153**
7.1 Introduction . . . 154
7.2 Synthesis . . . 156
7.3 Molecular Geometry Simulations . . . 158
7.4 EDOT-Amide-TPA Characterization . . . 159
7.5 Device Characterization . . . 162
7.6 Charge Transfer Characterization . . . 164
7.7 Conclusion . . . 167
References . . . 169

8 A Photo-Crosslinkable Bis-Triarylamine Side-Chain Polymer as a Hole-Transport Material for Stable Perovskite Solar Cells **174**
8.1 Introduction . . . 175
8.2 Characterization of the HTM . . . 177
8.3 Characterization of HTM Films and Perovskite Growth . . . 179
8.4 Device Fabrication and Characterization . . . 183
8.5 HTM Wettability and Tandem Proof of Concept . . . 186
8.6 Device Stability Studies . . . 188
8.7 Conclusion . . . 191
References . . . 192

9 Conclusion **197**
9.1 Summary 197
9.2 Future Work 199
References 202

List of Figures

1.1 Global Human Ecological Footprint Time Series 3
1.2 Energy Use and Human Development Index of Selected Countries . . 7
1.3 Fertility Rate Over Time, By Geographic Region 9
1.4 CO_2 and Land Use per kg Protein, by Food Source 12
1.5 Spatial Distribution of Temperature Increases Under RCP8.5 Emissions Scenario 16
1.6 Global Energy Production by Source 18
1.7 Renewable Energy Cost Trends. 19
1.8 Elemental Scarcity 21
1.9 LCOE as a Function of Module Efficiency and Lifetime. 23

2.1 Origin of the Band Gap. 39
2.2 Band Structure Schematic of Metals, Semiconductors, and Insulators 40
2.3 p- and n-type Doping of a Semiconductor 42
2.4 p-type Doping of an Organic Semiconductor 44
2.5 Types of Defects in Crystalline Materials. 46
2.6 p-n Junction Bias 47
2.7 Absorption of Photons by Semiconductor 49
2.8 Recombination Mechanisms 51
2.9 Band Diagram for p-n Junction and p-i-n Solar Cells 53
2.10 Photovoltaic J-V Curves and Equivalent Circuit 56
2.11 Shockley-Queisser Efficiency Limit. 60
2.12 $Pm\bar{3}m$ Perovskite Crystal Structure 61
2.13 Triple Cation Ternary Tolerance Diagram. 62
2.14 Hysteresis in Perovskite Solar Cells. 65

3.1 Time-Resolved Photoluminescence Spectroscopy Schematic 83
3.2 Kelvin Probe and Surface Photovoltage 87

4.1 Surface Electronic Properties of Perovskite on Mesoporous Layer . . 97
4.2 Time-Resolved Photoluminescence and Photoconductivity of Perovskite Films on Mesoporous Al_2O_3 100
4.3 Steady State Photoluminescence and Reflectivity of Mesoporous Samples 101
4.4 Comparing Device Architectures With and Without a Mesoporous Layer 104
4.5 Comparison of JV and EQE Data for Mesoporous Architecture 107
4.6 SEM Cross-Section of Mesoporous and Planar Devices 107
4.7 Mesoporous Layer and Trapping Mechanism 109

5.1 Probing the Degradation Mechanism of $MAPbI_3$-ZnO. 119
5.2 XPS Spectra of O, Zn, I, and ZnO for MA cation films annealed on ZnO 121
5.3 ZnI_2 XRD Pattern 121
5.4 Absorbance of DNT Solutions After Treatment with Gas Evolved from ZnO and FACs Perovskite 123
5.5 Thermal Stability of Perovskites on Zinc Oxide. 124
5.6 Time-dependent XRD of FACs and FAMACs films annealed on SnO_2. 125
5.7 UV and Thermal Stability of FACs PSC on Metal Oxides. 127
5.8 Photovoltaic Performance of Formamidinium-Cesium Perovskite Solar Cells Utilizing ZnO and SnO_2 Electron Transport Layers. 128
5.9 Transmittance of ZnO and SnO_2 Films on Quartz Glass. 128
5.10 Morphology of Zno Spin Coated on Quartz Glass. 129
5.11 ZnO and SnO_2 Interfacial Data. 132

6.1 Scanning Electron Microscopy Images of Top Secret on FTO 141
6.2 Top Secret Device Statistics 142
6.3 Champion Devices 143
6.4 Interface and TFT Characteristics 145
6.5 Thermal Stability of Films and Devices 147

7.1 Structure of EDOT-Amide-TPA 158
7.2 Optoelectronic properties of EDOT-Amide-TPA 161
7.3 Photovoltaic performance of perovskite solar cells with EDOT and Spiro-OMeTAD HTM's. 165
7.4 Photovoltaic performance and stability of $FA_{0.83}Cs_{0.17}Pb(I_{0.83}Br_{0.17})_3$ perovskite solar cells comprising EDOT-Amide-TPA or Spiro-OMeTAD as HTM. 166
7.5 Stability of Perovskite Solar Cells with EDOT and Spiro-OMeTAD HTM's. 167
7.6 Time resolved microwave conductivity traces. 168

8.1 Synthesis, Doping, and Absorption of P1-2 and PolyTPD 179
8.2 AFM and SEM of Hole Transport Materials and Perovskite Films Grown on HTM's. 180

8.3 XRD patterns of perovskite films grown on PolyTPD and doped and pristine CL1-2. 181
8.4 4-point probe conductivity measurement of PolyTPD and P1-2/CL1-2 182
8.5 Steady State and Time-Resolved Photoluminescence of Perovskites Grown on HTM's. 183
8.6 Device Data for CL1-2 and PolyTPD. 184
8.7 Wettability of CL1-2 and PolyTPD on ITO Substrates. 187
8.8 Solution Processed Tandem Proof of Concept. 188
8.9 Device Stability Data for CL1-2 and PolyTPD. 190

List of Tables

1.1 Temperature Rises Associated with RCP Scenarios 16

4.1 Solar Cell Performance Parameters for Devices with and without Mesoporous Al_2O_3 105

5.1 Solar Cell Performance Parameters for Devices with ZnO and SnO_2 Transport Layers 129

7.1 Optoelectronic properties of EDOT-Amide-TPA and Spiro-OMeTAD 162
7.2 Solar Cell Performance Parameters for Devices with Spiro-OMeTAD and EDOT-Amide-TPA. 164

8.1 Optoelectronic Properties of PolyTPD and P1-2. 180
8.2 Solar Cell Performance Parameters for Devices with CL1-2 and PolyTPD 185

List of Publications

1. M. L. Petrus, K. Schutt, M. T. Sirtl, E. M. Hutter, A. C. Closs, J. M. Ball, J. C. Bijleveld, A. Petrozza, T. Bein, T. J. Dingemans, T. J. Savenije, H. Snaith, and P. Docampo, "New Generation Hole Transporting Materials for Perovskite Solar Cells: Amide-Based Small-Molecules with Nonconjugated Backbone", *Advanced Energy Materials*, 2018, 8, (32), 1801605

2. D. Ramirez, K. Schutt, Z. Wang, A. J. Pearson, E. Ruggeri, H. J. Snaith, S. D. Stranks, and F. Jaramillo, "Layered mixed tin-lead hybrid perovskite solar cells with high stability", ACS Energy Letters, 3 (9), 2246-2251

3. D Ramirez, K. Schutt, J. Montoya, S. Mesa, J. Lim, H. J. Snaith, F. Jaramillo, "Meso-Superstructured Perovskite Solar Cells: Revealing the Role of the Mesoporous Layer", *The Journal of Physical Chemistry C*, 122, (37), 21239-21247

4. K. Schutt, P. K. Nayak, A. J. Ramadan, B. Wenger, Y. Lin, H. J. Snaith, "Overcoming Zinc Oxide Interface Instability with a Methylammonium-Free Perovskite for High-Performance Solar Cells", *Advanced Functional Materials*, recently accepted (28th June, 2019)

5. J. Godding, A. Ramadan, Y. Lin, K. Schutt, H. J. Snaith, B. Wenger, "Oxidative Passivation of Metal Halide Perovskites", *Joule*, recently accepted (22nd July, 2019)

6. M. Tremblay, K. Schutt, Y. Zhang, J. Lim, Y. Lin, J. Warby, S. Barlow, H. J. Snaith, S. Marder, "A Photo-Crosslinkable Bis-Triarylamine Side-Chain Polymer as a Hole-Transport Material for Stable Perovskite Solar Cells", *Sustainable Energy and Fuels*, recently accepted (6th September, 2019)

7. S. Shahriar, V. Castaneda, M. Martinez, A. Mishra, T. Akter, K. Schutt, J. Boscoboinik, D. Hodges, "Oxidation states in perovskite layers formed using various deposition techniques", *Renewable and Sustainable Energy*, recently accepted (September, 2019)

List of Abbreviations

AFM atomic force microscopy

EDX energy dispersive x-ray spectroscopy

EQE external quantum efficiency

F4-TCNQ 2,3,5,6-tetrafluoro-7,7,8,8-tetracyanoquinodimethane

FA formamidinium

FF fill factor

FTIR Fourier-transform infrared spectroscopy

FTO fluorine-doped tin oxide

HTM hole transport material

ITO indium-doped tin oxide

J$_{SC}$ short-circuit current

Li-TFSI lithium bis(trifluoromethanesulfonyl)imide

MA methylammonium

MAPbI3 methylammonium lead triiodide perovskite

MPP maximum power point

P3HT poly(3-hexylthiophene-2,5-diyl)

$PC_{60}BM$ phenyl-C_{61}-butyric acid methyl ester

PCE power conversion efficiency

PL photoluminescence

PMMA poly(methyl methacrylate)

PolyTPD poly(4-butyl-triphenylamine-4',4''-diyl)

PSC perovskite solar cells

SEM scanning electron microscopy

Spiro-OMeTAD 2,2',7,7'-tetrakis-(N,N-di-4-methoxyphenylamino)-9,'-spirobifluorene

SPO steady-state power output

tBP 4-tert-Butylpyridine

TFT thin film transistor

TRMC time-resolved microwave conductivity

TRPL time-resolved photoluminescence

V_{OC} open circuit voltage

XRD x-ray diffraction

CHAPTER 1

Introduction

1.1 Tragedy and Hope in the Anthropocene

Scientific progress and technology have greatly increased humanity's extraction and processing of natural resources and expanded access to energy supplies. Expanded energy supplies have, in turn, enabled the human population to grow from one to 7.7 billion people over the past 200 years while greatly improving living standards. Today, the global middle class has a quality of life that in many ways exceeds that of nobility from the recent past: fresh produce from distant corners of the world is available year-round, global communication is nearly instantaneous at minimal cost, medical advances have increased lifespans and eliminated diseases, indoor climate control assures continual comfort, and rapid transportation is ubiquitous. The improvement in the material standard of living has also been accompanied by moral progress. As a percentage of deaths, violent conflicts claim fewer lives than ever before,[1] and as a percentage of the population, fewer people are desperately poor than ever.[2] Slavery was prevalent throughout human history,[3,4] and at the turn of the 19th century up

to three-quarters of humanity endured bonded labor.[5,6] While not eliminated, slavery is about a hundred times less prevalent today than 200 years ago.[7] Throughout much of the developed world, human rights and democratic participation have also been extended to every person regardless of their race, gender, religion, and other characteristics.

While social values and incomes have achieved commendable progress, population growth and a rising standard of living have come at a substantial cost to the natural world that provides the physical basis for material prosperity, and for life itself. Since the early 1970s, humanity's total take from the Earth has exceeded regenerative capacity, with total human demands now requiring 1.7 Earths to satisfy sustainably, as shown in Figure 1.1. A new mass extinction is beginning, driven by the fragmentation and replacement of ecosystems by roads, farmland, housing, and other human developments. The global human footprint on the environment is immense: in the next 30 years, the mass of plastic in the oceans has been predicted to outweigh all the fish they contain.[8] On land, equally drastic changes are taking place. Climate change and population growth are predicted to stress the majority of aquifers in the United States within the next century.[9] By the end of the 21st century, heatwaves in some of the most densely populated regions of the world could become unsurvivable without access to air conditioning. The extent of human-induced changes will even be recognizable to geologists looking back at this era from the vantage point of millions of years in the future. The rapid rise of atmospheric CO_2 will be locked into the ice core record, the proliferation of plastics is likely to leave a fossil record, and sediment deposition is widely disturbed since the volume of sediments processed for mineral extraction is about three times greater than the volume of sediments transported by the all world's rivers.[10]

The alternative to the present condition is sustainability, an idea that has transformed from a niche concern raised by scarce visionaries to a global movement that captures the public imagination. While sustainability is a broad concept with numerous definitions, a foundational minimum goal is restraining humanity's ecological footprint

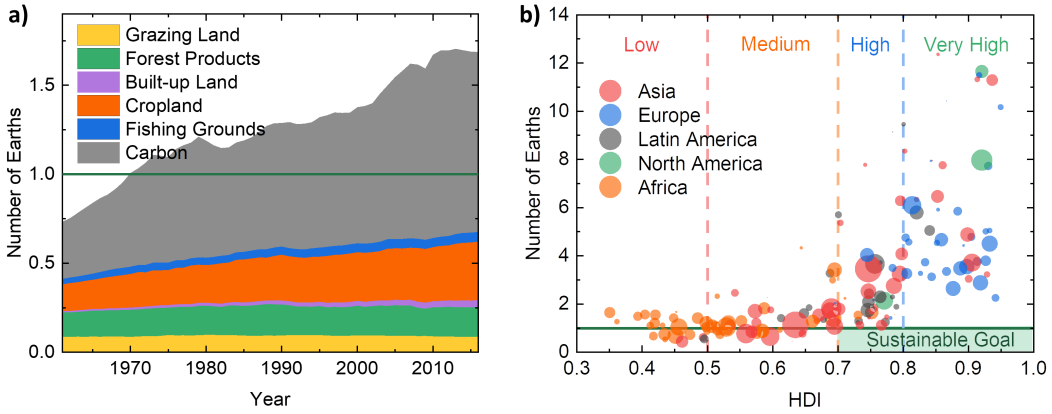

Figure 1.1: a) Human ecological footprint over time shows the carrying capacity of the Earth has been exceeded since the early 1970s. The increase has been driven by a growing population and increasing income per capita. b) Ecological footprint segmented by region, with each data point representing one country. The radius of each data point is determined by the $\log_{10}$ of its population. The bottom right sector is highlighted as the global sustainable development target. Data from the Global Footprint Network.[11] Further details on methodology available.[12]

to the regenerative biocapacity of the planet,[13] thus ensuring that humanity remains viable and prosperous into the future. Achieving sustainability is a critical challenge facing humanity in the 21st century.

Perspectives on the environmental challenges humanity faces can be bounded by the cornucopian and catastrophist perspectives.[14] Cornucopians hold that there is no fundamental resource scarcity, population, or pollution problems that cannot be overcome through human ingenuity and technological innovation, and this viewpoint is often associated with economics and social sciences. In this view, rising consumption, environmental transformations, and the burgeoning human population are seen as positive developments, and evidence of increasing human mastery of the environment. The catastrophist position is more frequently held by those with a natural science background, and it maintains that the finite limits of planetary resources cannot withstand the demands of human population growth and rising incomes; from this perspective, the future will bear declining or collapsing resources, population, or income. Rather than settling this 200-year-old debate, this introduction seeks only to outline environmental challenges, examine the consequences that lie ahead, and review routes to achieving sustainability.

1.2 A Brief History of Energy and Civilization

Throughout most of human history and pre-history, there was little to no economic growth; when there were annual increases in population or agricultural output, they were often at growth rates well below 1%.[15,16] Millenia passed without an increase in human lifespans or improved nutrition.[17,18] One way to understand this long period of stagnation, sometimes referred to as a Malthusian Trap, is by quantifying the glacially slow progress in the exploitation of energy sources.

At the dawn of the human species, energy resources were limited to food and heat absorbed through the environment. The power an individual received from food in a foraging or hunting society may have averaged 125 W,[19] an amount of power equivalent to that used by two conventional (incandescent) household light bulbs. The use of fire for heating and cooking began about 400,000 years ago, but the average heating power for a single Neanderthal was only about 135 W.[20] The development of agriculture and the use of animal muscle power from around 10,000 years ago resulted in per capita energy growth of 100 - 200 W.[19] Despite these advances, the energy used by a typical person only doubled from 125,000 BC to 900 AD.[21]

The industrial revolution and the use of fossil fuels rapidly increased humanity's energy use, with average power per capita in affluent societies such as the United States now reaching about 10,000 W.[22] The rapid transition into a high growth era has been extensively studied and attributed to a wide variety of causes, and is sometimes referred to as the Great Divergence. In contrast to the growth in energy use, human power output is restricted by muscle power and is limited to about 100 W per person over sustained periods.[19] The transition away from muscle power to external energy sources and fossil fuels transformed society and living standards. Today, the average American's lifestyle is supported by energy flows equivalent to the continuous muscle power of 100 human beings working 24 hours a day, 365 days per year.[19] A single barrel of oil (42 gallons or 191 liters) contains the energy equivalent of nearly 6 years of human labor, assuming 100 W output over 8 hours each day.

1.2.1 Energy, Agriculture, and Population Growth

Commensurate with the increase in living standards enabled by the transition away from muscle power is the improvement in energy produced by prime movers, such as water wheels and turbines. The power produced by the best mechanical source in the middle ages, a water wheel, peaked at a few thousand watts. The power of a modern steam turbine is a million times greater.[23] In 1900, a farmer plowing fields with six large horses had at most 5,000 W of power available. Just a century later, that farmer's great-grandson could enjoy the air-conditioned cabin of tractor powered by a 250,000 W diesel engine. The productivity gains resulting from the transition to non-animal power sources were the primary driver in a dramatic reduction of agricultural employment, as fewer farmers could produce vastly increased amounts of food.[24] In the United States, agricultural employment as a percentage of the population fell by 93% from 1900 to the year 2000. Fossil fuels increased agricultural productivity by providing the energy to smelt metals used for machinery, power irrigation pumps, dry grain, run tractors and harvesters, and crucially, enable the Haber-Bosch nitrogen-fixing process utilized for fertilizer synthesis.[24,25]

While improvements in sanitation and medicine reduced mortality, the food energy provided by increased agricultural output permitted greater human populations. A fundamental principle in population ecology is that a population will grow exponentially when free from external constraints such as predators, disease, or food scarcity.[26] When environmental resources are limited, growth rates slow and the population reaches equilibrium near the asymptote of environmental limits.[27] While food security concerns are often raised with respect to the future needs of a growing population, an alternative view holds that food availability itself is the driver of population growth. In support of this view are a variety of studies showing food supply is the primary cause of population growth in many animal species.[28] Human population can also be accurately modeled using the Food and Agriculture Organization's food production index.[27]

Population growth, fossil fuel use, and the consequent atmospheric CO_2 concentration, and economic productivity over the past 2,000 years have an interdependent relationship and are plotted in Figure 1.2a.

1.2.2 Energy and Human Development

While the growth of energy resources is a crucial factor in the improvement of living standards, its importance should not be overstated. Political and economic systems, technological innovation, and social values all promote or constrain progress even in energy abundant nations. Coal has been used in China for about 3,500 years, and while it was used from around 200 BC for metalworking this did not lead directly to industrialization.[29] More recently, the Soviet Union was the world's leading producer of oil and gas, yet living standards lagged far behind many Western nations with comparatively limited domestic energy resources.[23] More contemporary instances of energy-rich nations with constrained development include Venezuela and Libya. Despite the limitations illustrated by these examples, energy use remains an important predictor of human progress, as measured by the human development index (HDI).

The HDI is a metric developed by the United Nations Development Program that incorporates life expectancy, education, and per capita income. As shown in Figure 1.2b, across more than 120 nations there are no instances of high HDI when energy use is below 1 kW per capita. Therefore, while a society's level of energy use cannot guarantee prosperity, the lack of energy resources appears to set an upper bound for development.

Also notable from the data in Figure 1.2b are the rapidly diminishing returns in HDI for nations with greater than 3 kW of power per capita. The data can be fitted reasonably well with a non-linear model that accounts for this saturation effect.[35] The steep initial rise in HDI as a function of energy use suggests that living standards could be greatly improved in much of the world with modest increases in energy supplies. In

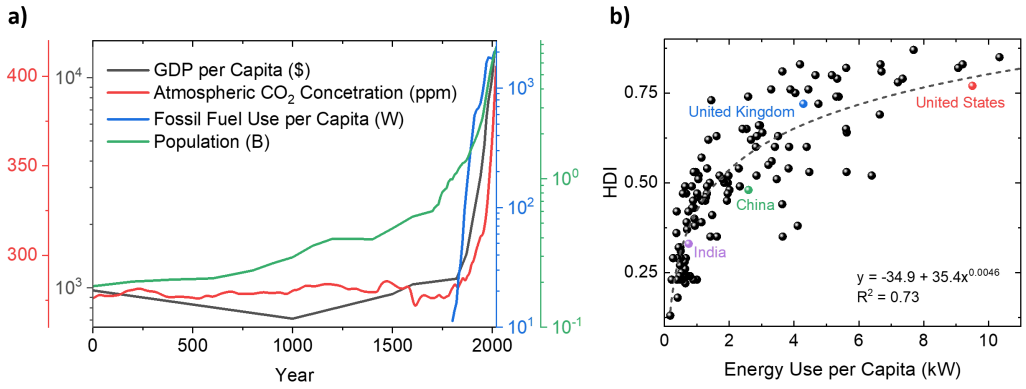

Figure 1.2: a) The development of human civilization as reflected in the growth of population, fossil fuel use, GDP, and atmospheric CO_2 concentrations. Population data from the History Database of the Global Environment,[30], fossil fuel data from Smil[31] and BP[22], GDP data from the Maddison Project Database.[15], and CO_2 data from the Scripps Institute of Oceanography CO_2 Program.[32,33]. b) Energy use per capita and human development index. HDI from the United Nations,[34] energy data from the World Bank.[2]

the years ahead, emerging, affordable and distributed technologies such as thin film solar could make this possibility a reality.

At the other end of the spectrum, affluent countries demonstrate that increased energy consumption results in only negligible HDI gains. The United States and the United Kingdom have virtual parity in human development, but a British citizen consumes less than half the energy the average American does. While it could be argued that the HDI neglects to account for potential psychological benefits of increased energy consumption, other metrics such as the United Nations World Happiness Report also find parity between the United States and United Kingdom.[36] In developed nations, changes in lifestyle choices and public policy may reduce energy use with few negative effects and potentially widespread benefits, ranging from improved air quality to diminished geopolitical risks associated with dependence on foreign oil producers.

Whatever good may come from moderating energy use, the trend is towards increasing demand; the International Energy Agency (IEA) forecasts global energy demand will increase by 25% over the next two decades.[37] India will be the largest single driver of this growth, with India's energy demand doubling over this period. While North America and Europe account for over 40% of global energy demand and developing economies in Asia account for 20% today, the IEA predicts this pattern

will be reversed in just 20 years.[37] Since 2005, China and India have relied heavily on coal to meet rising demand, and together account for 85% of new coal generating capacity since 2005.[38] One of the great global challenges of this century is meeting humanity's growing energy demand with energy sources that do not emit greenhouse gases and further exacerbate climate change.

1.3 Paths Towards Sustainability

1.3.1 Population Stabilization

Despite the failed forecasts of population overwhelming food supplies, made by Thomas Malthus in 1798 and more recently by Paul Ehrlich in 1968, population growth has remained a sustainability concern as larger populations demand greater natural resources.[39] Population growth and projections are a function of the total fertility rate. Two children per couple are adequate to replace their parents, but since not all children reproduce or live to adulthood, a fertility rate of 2.1 is required to ensure a stable population. In many industrialized nations, fertility sharply declined over the past century, resulting in sub-replacement level fertility rates. The strong inverse correlations between fertility rates and female education, affluence, and contraceptive availability have bolstered hopes of stabilizing global population by addressing these factors.[40] The UN forecasts that global fertility rates will converge below the replacement rate in the second half of the 21st century, as illustrated in Figure 1.3.[41] The convergence to low fertility rates as incomes and technology increase has been explained through multiple approaches. This trend is one of the most well established and accepted findings in the social sciences, and is referred to as the demographic transition.[42] The demographic transition is also explained in economic models through Unified Growth Theory and understood through population ecology as K-selection, a reproductive strategy that prioritizes the quality of offspring over the quantity.

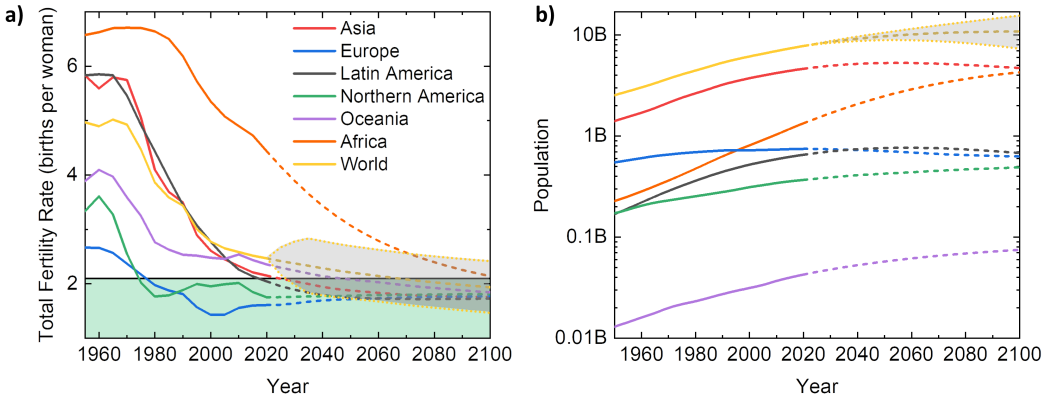

Figure 1.3: a) Fertility rates in every region of the world are converging to sub-replacement rates. The fertility rate for no population growth is 2.1 births per woman, with a fertility rate below this number resulting in a declining population (green shaded region). Future projections are shown as dashed lines. The high and low variant projections for the global population are bounded by the gray, shaded region. It should also be noted that rapid population growth in developing countries can have a relatively small emissions footprint in the near term, as the United States has 50 times the per capita CO_2 emissions of Africa.[43] b) Population by region. Data and forecasts are from the United Nations Population Division.[44]

There are a few objections to these forecasts. One concern is based on fertility variation between cultures. Even if 99.9% of Earth's population adheres to a fertility rate of 2, a high fertility culture of just 0.1% of the population would grow to over 7 billion people in 250 years if their fertility rate were 4. Mormons in the United States are an example of a culture with an emphasis on high fertility despite residing within a country with high education and income, and access to contraception.[45] Other research finds that religious preference is a better predictor of fertility rate than all other major social variables, bolstering this concern.[46] However, the global population would only be substantially affected by high fertility cultures if their emphasis on high fertility could be maintained for many generations into the future. Another concern has been raised over immigration from poor to wealthier countries, which can result in first-generation immigrants having a higher fertility rate than they would in their native country.[45] Yet other findings may make these concerns irrelevant, as the birth rate for second-generation immigrants rapidly converges to that of the native population in the wealthier country.[47] Demographers also raise concerns over "demographic traps" that arise when countries advance far enough to reduce mortality rates, but slow economic

progress results in sustained high fertility rates as parents use children as insurance against the loss of income in old age.[48] Time will tell whether these concerns upend UN projections, but thus far declining fertility rates bode well for future sustainability.

1.3.2 Biodiversity and Agriculture

During the 3.5 billion years that life has existed on Earth, there have been 5 mass extinction events, spaced at roughly 100 million year intervals, with species diversity taking an average of 10 million years to recover from each event.[49] It now appears that a sixth mass extinction event is beginning, and it is driven by human activity. The current extinction rate is about 1,000 times higher than Earth's historical background extinction rate,[50] and future extinction rates could increase to 10,000 times the background rate.[51] Conservative estimates find that 11,000 - 58,000 species are going extinct each year[52] and that mammal biodiversity will take millions of years to recover from the damage already done by the growth of civilization.[53]

The largest single driver of this biodiversity loss is food production because native ecosystems are converted to land for crops and animal grazing.[54] As just one of many examples, the transformation of the American plains for agricultural uses destroyed 99% of the grasslands biome.[55] The largest driver of agricultural land conversion, in turn, is the production of meat for human consumption, as there are large energy losses involved as one "moves up" the food chain (increases the trophic level). For every 100 calories of food consumed by cattle, only 3 calories are transferred to a human consuming beef. Poultry is more than four times as energy-efficient, and in the United States, transitioning land from cattle feed to poultry feed would meet the caloric and protein demands of about 130 million more Americans. Converting agricultural land for cattle feed to cropland for a plant-based diet would be more energy-efficient still, and provide for the caloric and protein needs of an additional 190 million people.[56] Adoption of a plant-based diet would also greatly reduce greenhouse gas emissions, as animal agriculture accounts for greater methane release than the

natural gas and oil industries combined; the carbon footprints of pulses (beans, peas, soy) are 10 to 100 times lower than for beef.[57,58] The environmental impacts of dietary choices are summarized in Figure 1.4.

Despite the high impact of meat-based diets, the clear trend is for increasing meat consumption, with some countries expected to increase land use for meat production by up to 50% over the next 30 years.[59] Meat consumption is also linearly correlated with GDP per capita,[60] and thus as the world's population becomes increasingly wealthy it is likely that in the future meat production will only increasingly compromise climate stability and biodiversity unless substitutes such as cultured meat ("lab meats") become affordable, appetizing, and widely available.[61]

Regenerative agriculture practices may also offer a simple alternative to meat substitutes, which require further technological innovation. A very recent life cycle assessment found that beef production is actually carbon negative when regenerative grazing occurs on degenerated cropland. When carefully managed, moderate grazing promotes denser root structures in grass, sequestering carbon in the process. Encouragingly, an early assessment finds that the land footprint required for rearing cattle on regeneratively grazed land may be comparable to that of conventional confined animal feeding operations, but more work is needed to further assess and then scale regenerative agriculture. Soil carbon content may also saturate as regenerative practices are sustained, which could make beef production on restored soil carbon positive over longer time periods.[62]

Even if the carbon emissions associated with animal agriculture can be substantially reduced, the large land footprint needed for raising meat has considerable impacts on biodiversity loss. The biodiversity crisis could be largely addressed by reserving half of all land for conservation, a strategy that proponents have termed Nature Needs Half.[49,66] Mapping land usage in the United States, as in Figure 1.4b, reveals that substantial progress could be made towards this goal in high beef consumption countries simply by changing dietary preferences through individual choice or tax policy.

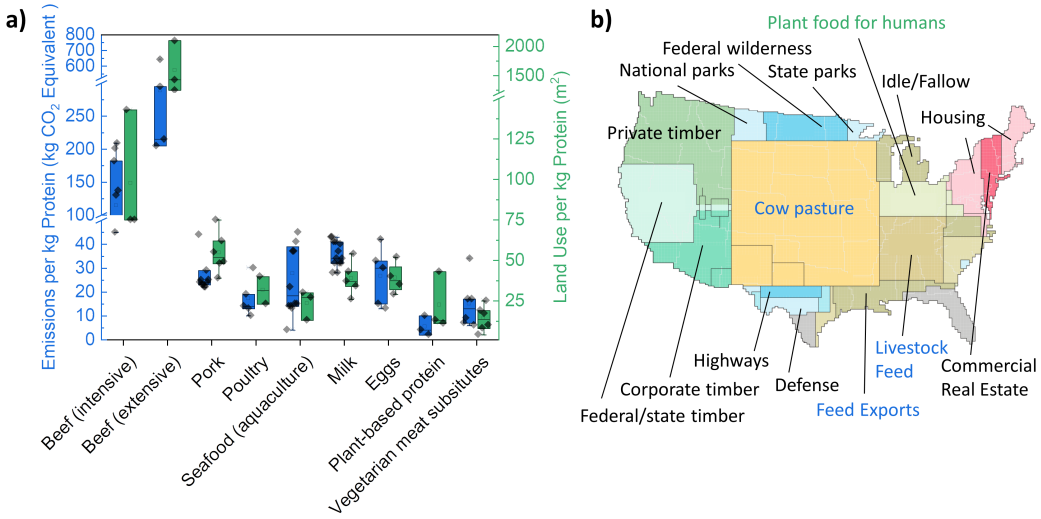

Figure 1.4: a) CO_2 and Land Use per kg Protein, by Food Source. Note the use of axis breaks. Each data point represents data from a peer-reviewed study. Data sources.[58] b) Land use in the United States. Figure originally appeared in Bloomberg[63] and was developed with data from the United States Department of Agriculture.[64] Figure adapted with permission from Oxford University Press.[65] Notably, cattle may graze on land that has no other economic uses or may graze on land with shared uses; further criticism of this figure along these lines is available elsewhere.[65]

1.3.3 Sustainability Oriented Economics and Policy

Economic decoupling proposes limiting the environmental impacts of economic growth by divorcing economic production from natural resource scarcity as much as possible. Decoupling can occur as relative decoupling, where resource use per unit of economic output falls but aggregate demand for resources increases, and also as absolute decoupling, which allows for economic growth despite an overall reduction in raw materials and energy inputs. Absolute decoupling has been observed at the national level; in Germany from 1994 to 2007, GDP grew 22% despite raw material inputs decreasing by nearly 10%.[67] Unfortunately, absolute decoupling is unlikely to occur at a global level in the foreseeable future. The gap between the global middle class and the poor is so wide that if four-fifths of humanity reaches just a third of the living standard in affluent countries, aggregate demand for raw materials will continue to grow for generations to come.[68] Demand for natural resources is projected to double by 2050.[69]

Another method for managing the increasing demand for raw materials while minimizing the associated environmental impact is by transitioning to a circular economy. To address resource scarcity, waste, and emissions, circular economy models seek to maximize the reuse and recycling of materials, the sharing of durable goods, and the longevity and repair of products. There is substantial room for improvement on each of these fronts as globally only 6% of materials are recycled,[70] 91% of users of ride-sharing services in the U.S. have not reduced their ownership of personal vehicles,[71] and the lifespan of some consumer goods is falling due to cost-saving measures or planned obsolescence.[72] A significant hurdle to the adoption of a circular economy is that economists and policymakers conventionally prioritize GDP growth when conservation strategies may hinder growth.[73]

Therefore, another strategy to address sustainability issues is through innovation in economics. A greater understanding of the relationship between affluence and subjective well-being can illustrate why the conventional emphasis on growth at all costs may be misguided. For instance, one study found that the happiness of Americans no longer improves after household income surpasses $75,000,[74] and that beyond this point personal well-being was constrained by life circumstances and temperament. This phenomenon is not uniquely American, either. Despite having Europe's wealthiest large economy, Germans are less satisfied with their lives than people surveyed in Colombia and Rwanda.[68] The link between material prosperity and happiness is equally problematic over longer periods, as both North Americans and Europeans have reported stagnant well-being since World War II despite substantial increases in incomes and material possessions.[75] A variety of research connects materialistic values with problematic interpersonal relationships, reduced personal well-being, and even depression.[76] The evidence suggests that like energy consumption, affluence also has a saturation point when it comes to happiness and satisfaction. Once this saturation point is reached, personal well-being is not strongly influenced by the acquisition of additional goods but rather by our ability to live consistently with our values, achieve our goals, and find belonging and acceptance within our social groups.[76] Another

explanation is offered by the concept of a hedonic treadmill, which posits that humans quickly return to a baseline level of happiness after a temporary perturbation from life events. Landmark studies supporting this concept have found that lottery winners were not happier than non-winners and that paraplegics were no happier than those who could walk.[77]

Despite the tenuous connection between materialism and subjective well-being, there is great social inertia for materialistic values. Freud's nephew, Edward Bernays, revolutionized public relations in the 1930s by conflating personal identity and well-being with materialistic consumption.[78,79] The public has been inundated with advertisements for generations now, which continually reinforce the perceived link between consumption and well-being.[80] Since consumer spending accounts for nearly 70% of U.S. GDP,[81] large scale moderation of consumption could precipitate a recession or depression; the Great Depression was accompanied by negative annual growth rates of about 10%. Therefore, while the moderation of materialistic values could reduce demands on ecosystems it is challenging to address these values without invoking new economic paradigms.

Finally, government policies can have a much larger impact on sustainability goals than collective individual actions. For brevity, only one policy case will be summarized here. A crucial factor for implementing successful policy is to align incentives with public support, and recent policy proposals in France and Canada illustrate how a particular implementation of a sustainability policy can elicit a wide disparity in public reaction.[82] In 2018, both Canada and France planned to increase petrol taxes to meet emissions goals. Canada implemented a carbon tax at a national level under a fee and dividend model, such that all the taxes collected would be redistributed equally to citizens. In the Canadian model, citizens with emissions below the average receive a rebate greater than the taxes paid in. Through this mechanism, citizens have a financial incentive to reduce their emissions, creating market incentives for producers to make fuel-efficient products, and at the same time, people with low incomes are not excessively burdened. The French tax was simply a flat tax increase on petrol and

ignited yellow vest protests that caused the plan to be abandoned. The Canadian plan passed amidst milder resistance.[83]

1.3.4 Climate Change and Stabilization

Climate change already has costly and dangerous effects throughout the world. In the Western United States, for example, wildfires burn twice the area they did in 1984, and from 1995 - 2005 the portion of the US Forest Service budget dedicated to wildland fire rose from 16% to 52%.[84,85] A further 1 °C increase is expected to increase the area burned each year across the Western United States by 200-400% of present levels.[86] In the Eastern United States, hurricanes cause significant damage, and the global frequency and intensity of hurricanes is predicted to increase with a warming climate.[87] The National Oceanographic and Atmospheric Administration reports that the cost for natural disasters in the United States over the past 5 years is more than double the historical average, with annual costs now approaching $100 billion.[88] Given that current climate change effects are already a cause for concern, understanding likely future impacts is vital to guiding a response of the appropriate magnitude.

The Intergovernmental Panel on Climate Change forecasts future greenhouse gas emissions under four scenarios known as representative concentration pathways (RCP). Together, these four pathways represent a range of emissions mitigation scenarios ranging from low to aggressive. Each pathway is named by the radiative forcing in the year 2100 resulting due to greenhouse gas emissions, where radiative forcing is the difference between sunlight absorbed by the Earth and energy radiated back to space. As an example, RCP 2.6 results in the Earth absorbing power equal to an additional 2.6 W/m^2 in the year 2100. The RCP scenarios and associated temperature rises are listed in Table 1.1, while emissions over time for each scenario are shown in Figure 1.5a.

The high emissions scenario RCP 8.5 is built around a world where income growth remains slow in developing nations, which inhibits the demographic transition to low

Scenario	ΔT 2100 (°C)	ΔT 2300 (°C)	Model assumptions
RCP 2.6	+1.0 (0.3 - 1.7)	<1	Aggressive emissions mitigation beginning now
RCP 4.5	+1.8 (1.1 - 2.6)	∼3	Moderate to high emissions mitigation
RCP 6.0	+2.2 (1.4 - 3.1)	∼4	Moderate emissions mitigation
RCP 8.5	+3.7 (2.6 - 4.8)	∼6	Population growth, low tech., poor policy

Table 1.1: Temperature Rises Associated with RCP Scenarios. Data from the IPCC[89] and Center for Climate Systems Research at Columbia University.[90] Further descriptive details on modeling assumptions are available.[91]

fertility rates and also implies slow advances in energy efficiency. In this scenario, the population reaches 12 billion people by 2100, and low technological development results in humanity's continued reliance on fossil fuels through the end of this century. Energy demand triples by 2100, tar sands and oil shale replace dwindling conventional fuel reserves, and the use of coal increases nearly 10-fold.[92] Under this scenario, some of the most densely populated regions of the world may become uninhabitable at the end of the century because extreme heatwaves are predicted to become unsurvivable without air conditioning. A map of regional temperature increases is shown in Figure 1.5b.

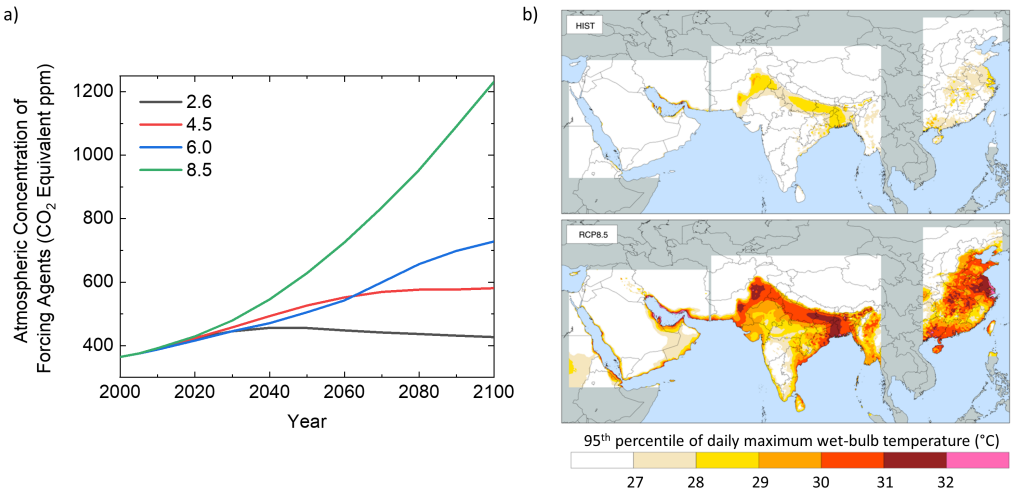

Figure 1.5: a) Emissions through 2100 under each RCP scenario. b) Historical temperatures during heatwaves (1975-2005) (top). Modeled temperatures under RCP8.5 high emissions scenario (2070-2100). Figure originally appeared in Nature Communications,[93] and adopted under Creative Commons Attribution 4.0 International License. License details available at http://creativecommons.org/licenses/by/4.0/

At the other end of the spectrum, keeping climate change to a safely manageable

1.5 °C will require a CO_2 emissions decline 45% over the next decade (relative to 2010 emissions) while limiting warming to 2 °C requires a reduction of 25% over the same period. Limiting warming to 1.5 °C will require transitions that are unprecedented in scale across society, with major changes needed in energy, infrastructure, and industry. If these transitions do not occur over the next decade, restricting warming to 2 °C will be the next option. 2 °C is described as dangerous,[94,95] as the increases in temperature means and extremes can be 2-3 times greater in some regions relative to 1.5 °C warming.[95]

Major benefits of limiting warming to 1.5 °C rather than 2.0 °C are listed below[95]:

1. Frequently exposing 420 million fewer people to extreme heatwaves.
2. Limiting ice-free summers in the arctic to once per century, rather than once per decade.
3. Reducing sea level rise by 10 centimeters at the end of this century.

1.4 Renewable Energy

The historic shift towards renewable energy is already underway, with wind and solar energy conversion growing rapidly, as shown in Figure 1.6a. Fossil fuels still provide about 85 times more energy than wind and solar combined, yet the supply of solar is vast. The amount of sunlight reaching Earth is about 5,000 times greater than humanity's energy demand. Finite energy reserves, including coal, petroleum, natural gas, and uranium for nuclear fission, will also be substantially depleted over the next century even with flat energy demand, as shown in Figure 1.6b.

One of the key factors that have inhibited the growth of solar energy is its historically high cost relative to fossil fuels, as shown in Figure 1.7. Solar energy costs have decreased more rapidly than any other energy source over the past decade due to improvements in efficiency, economies of scale, improved production yields, and a variety of serendipitous events.[97] Wind and hydroelectric provide a slightly

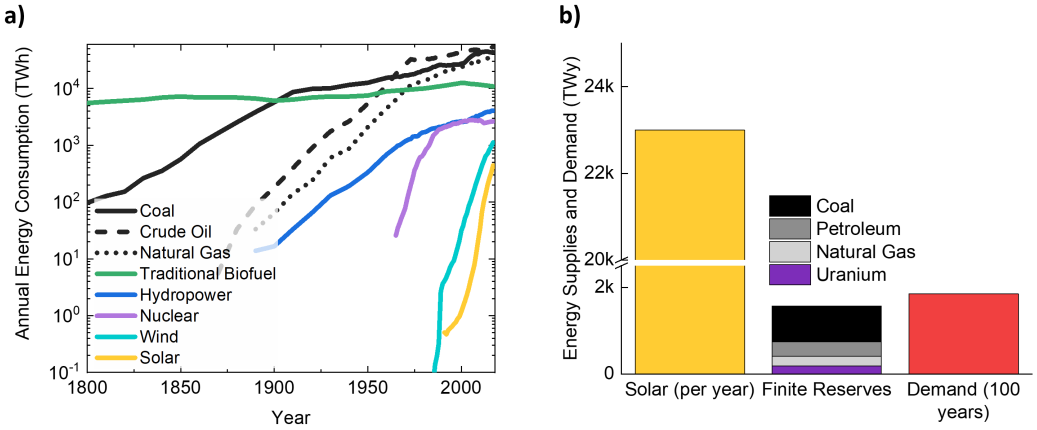

Figure 1.6: Global Energy Production by Source a) Historical energy production. b) Annual incident solar energy, total fossil fuel, uranium reserves, and energy demand. Note that energy demand over the next 100 years assumes the current 18.5 TWy demand is flat. This assumption is unrealistic due to population growth and growth in energy demand per capita, but still useful in developing a broad perspective. Data from Smil[31], BP[22], and the International Energy Agency.[96] Reserves of fossil fuels may also greatly expand with discoveries of new deposits or as technology develops to economically extract lower-grade deposits.

lower cost of energy than solar photovoltaic (PV), but this advantage will soon be eliminated if cost reduction trends in PV continue. Further PV cost reductions can also be achieved by researching emerging, efficient, thin-film materials that utilize Earth-abundant materials.[98] For these thin-film technologies to contribute meaningfully to climate stabilization, they must be commercially successful and ubiquitously adopted. Commercial success, in turn, requires low cost, high power conversion efficiency, and long module lifetimes.[99] One of the most promising thin-film technologies that could meet these requirements is metal halide perovskite solar cells (perovskite solar cellss (PSCs)), which are the focus of this thesis.

1.5 Considerations for Terawatt-scale Photovoltaics

One important consideration for solar energy is that, despite its abundance relative to fossil fuels, it is a much lower density energy source. Therefore, the ability for solar energy to meet humanity's energy demands may be restricted by the availability of the materials required to cover a sufficient area of the earth with solar panels. Fossil fuels also serve as an on-demand energy source, while solar energy is highly variable and

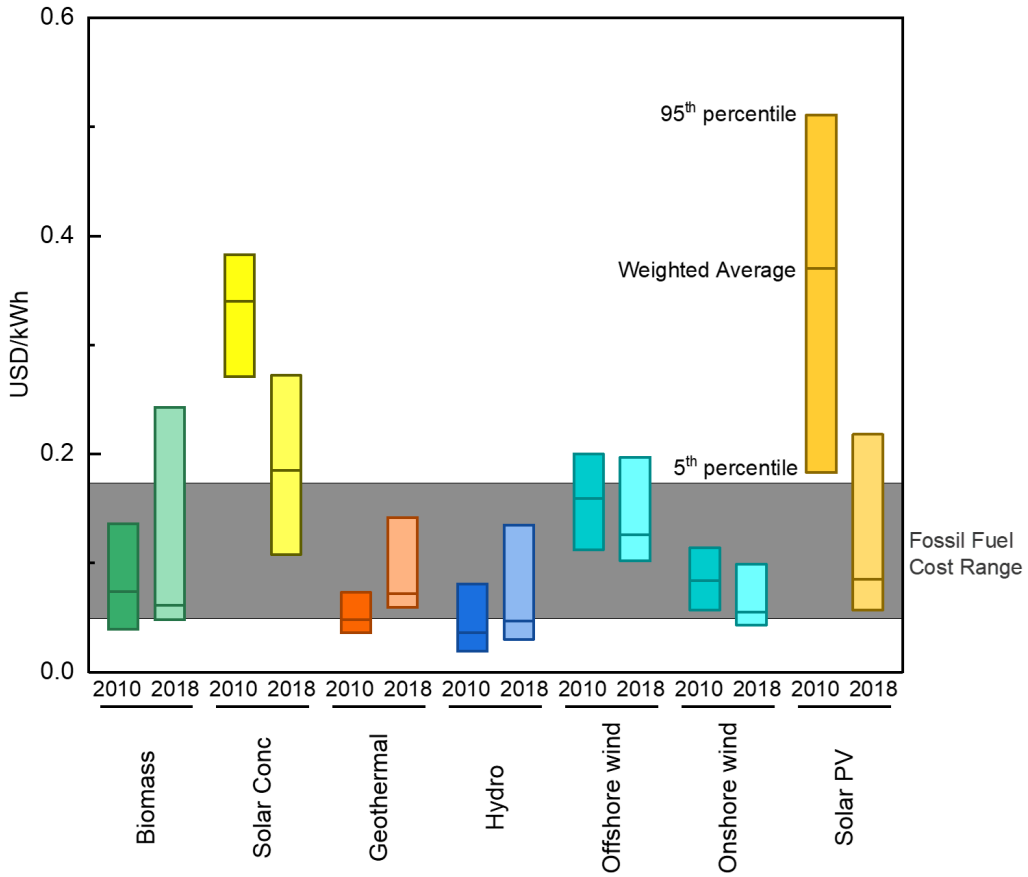

Figure 1.7: Renewable Energy Cost Trends. Levelized cost of energy for utility-scale renewable sources from the International Renewable Energy Agency.[100] While most renewable costs were essentially flat over the past decade, the cost of energy from solar photovoltaic decreased by 77%, making it cost-competitive with fossil fuels in many parts of the world.

thus material scarcity must also be considered for batteries and other storage systems. The surface area required for 20% efficient solar panels to provide all of humanity's energy needs is roughly equivalent to the area of Spain or California, assuming solar irradiance of 6 kWh/m^2/day, which is equal to the solar power throughout most of the Southwestern United States.[101] Sunnier regions could also distribute power to remote locales, with high voltage electrical transmission losses amounting to only 3% per 1,000 km.

Turning to mineral scarcity, conventional Si solar cells would be limited to a few TW of power by the Ag content of electrodes, but other metals might be substituted before this became an issue. Commercially available thin film solar cells, including

CIGS and CdTe, are limited to providing about 0.02 TW and $<$ 0.1 TW of power based on current reserves of In and Te.[102] Perovskite solar cells are much less restricted by materials limitations than these commercial thin film technologies. While analyses for PSC resource scarcity are not published, an approximation can be made with the following data:

- A unit cell volume of 2.51 x 10^{-28} m^3 for the organic-inorganic $MAPbI_3$ and 9.47 x 10^{-28} m^3 for the inorganic $CsPbI_3$.
- Panels are 20% efficient at a perovskite absorber thickness of 600 nm.
- The area required to power humanity's energy demand in 2030 is 453,900 km^2, based on the International Energy Agency's energy demand forecast[103] and 6 $kWh/m^2/day$ irradiance.
- United States Geological Survey for mineral production and reserves.

With this data, the $MAPbI_3$ perovskite would require 372 x 10^6 kg of Pb to provide the estimated power the world will demand in 2030, which is just over 9% of annual Pb production. Elements for the organic cation (methylammonium) are abundant. The iodide required (685 x 10^6 kg) would take about 11% of known reserves but would consume all of the elemental iodine production for 24 years at current production levels. However, this constraint could ease with increased demand; lithium production increased nearly 3-fold over a decade in part due to consumer demand for batteries.[104] Inorganic perovskite absorbers, such as $CsPbI_3$, offer improved thermal stability relative to organic counterparts but the quantity of Cs required (63.5 x 10^6 kg) would consume a large fraction of world reserves (85 x 10^6 kg). The high cost of Cs, combined with the fact that global Cs production currently isn't tracked makes scaling this particular perovskite questionable.[105] The abundance, cost, production, and reserves of elements utilized for perovskite solar cells are shown in Figure 1.9 It should be noted that the absolute depletion of economically extractable minerals is a contentious issue. Annual production sometimes exceeds past reserves due to discoveries of new deposits,

technological innovation allows lower grade ores to be processed, and substitution of alternative materials may alleviate scarcity.[106] Proponents of mineral scarcity report that even when accounting for UNEP's finding that the global extractable mineral supply is 35 times greater than USGS reserves, several key elements will be exhausted in the decades to centuries ahead.[107]

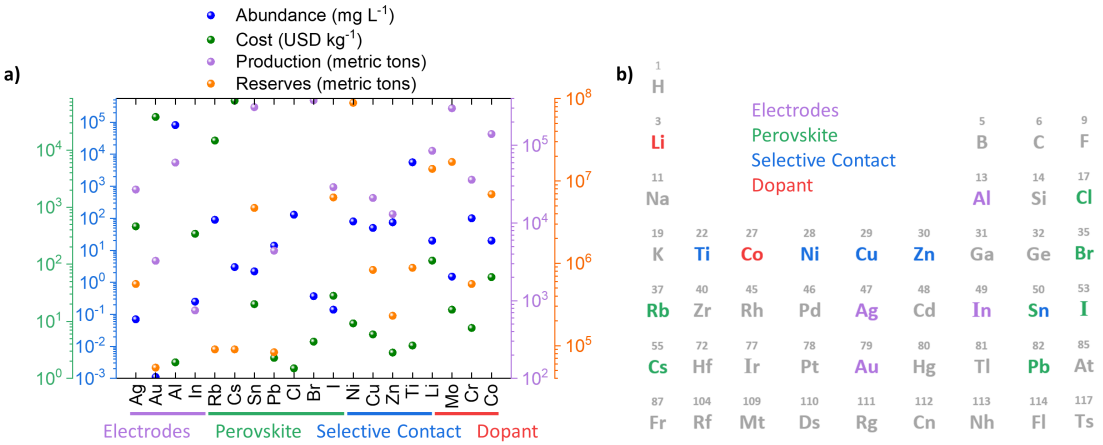

Figure 1.8: a) Abundance, cost, production, and reserves for commonly used elements in perovskite solar cells. b) Condensed periodic table showing commonly used elements in perovskite solar cells. Data for production and reserves from the United States Geological Survey[105], Abundance data from the CRC Handbook of Chemistry and Physics.[108], and cost data aggregated from London and Shanghai Metals Markets and other sources.[109]

Moving beyond raw materials constraints, some argue that a transition to an electric grid fed by 100% renewable energy is infeasible without the inclusion of nuclear power generation,[110] yet others find that the barriers to a 100% renewable energy grid are more social and political than purely technical or economic.[111] Limited uranium reserves and the uncertainty of unconventional nuclear reactors pose challenges to scaling nuclear energy. Current uranium reserves would be depleted in 5 years at 15 TW scale, and fast breeder reactors that can generate additional fissile material have largely been abandoned due to cost and safety concerns.[112] With or without nuclear energy, as renewables provide a greater fraction of electric power innovation will be required to maintain grid stability, and several strategies have already been outlined to achieve this.[113] All things considered, the transition to a renewable energy future could occur rapidly. The solar industry is on target to reach 3 TW of cumulative

generation capacity in about a decade, and combined solar generation and storage costs may reach 8 cents/kWh by 2030, a cost that is similar to conventional energy generation.[114]

1.6 Commercial Viability of Perovskite Solar Cells

Commercially available photovoltaic technologies can be evaluated in part on their minimum sustainable price, which is the minimum selling price a manufacturer must set to cover their manufacturing costs, overhead, and cost of capital. On this basis, a study from 2016 found perovskite solar cells could be sold at about $0.41 per watt of peak power (Wp) at a module power conversion efficiency of 16%, while crystalline silicon required a price of $0.64-$0.76 per watt peak. Further reductions of minimum selling price for perovskite solar cells could be achieved with higher module efficiencies (∼$0.32 Wp at 20% power conversion efficiency). Uniquely, PSC could scale rapidly to meet climate targets if capital expenditure could be reduced by an order of magnitude relative to silicon solar cells, which may be feasible through roll to roll processing routes that have achieved 16.8% power conversion efficiency.[115] In 2019, perovskite on silicon tandem cells were found to be economically viable if the loss in power conversion efficiency for the perovskite cell could be reduced to about 1% per year.[116] However, despite reaching high power conversion efficiency (PCE), PSC lifetimes have required dramatic improvements to compete with Si photovoltaics, as will be discussed further in Chapter 2.

In addition to being economically viable, photovoltaic technologies can also be evaluated on their ecotoxicity and energy payback times. Energy payback time is the operating time for a photovoltaic device to produce the same quantity of energy that was required to manufacture it. By this measure, solution processed-perovskite solar cells are expected to reach energy payback after about 0.2 years, while c-Si requires nearly 2.5 years.[117] Long lifetime requirements may also be somewhat relaxed if degraded panels can be effectively recycled. Lab-scale recycling efforts have shown

PSC materials can effectively be dismantled and redeployed in new solar cells, with solar cells made from recycled materials retaining about 90% of their initial performance even after being completely recycled twice.[118,119]

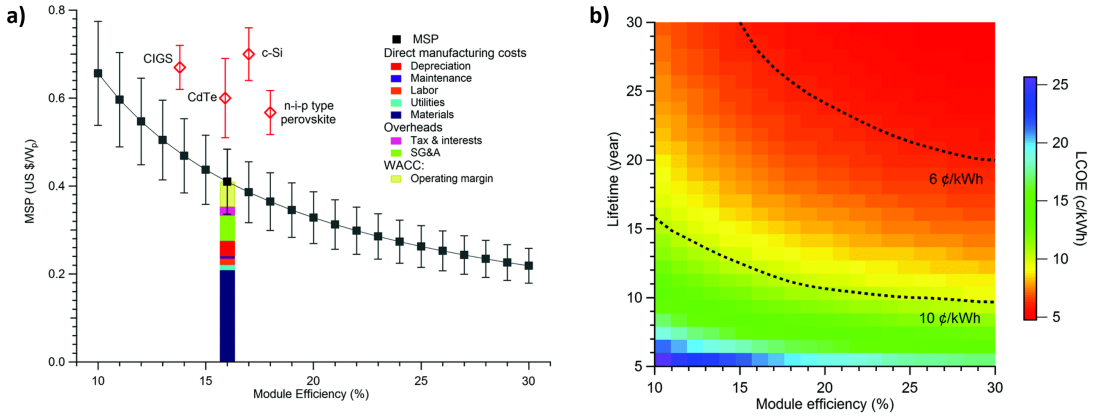

Figure 1.9: a) Minimum selling price of competing solar technologies. b) To be cost-competitive with other electricity generation sources, perovskite solar cell lifetimes must be extended dramatically from their current lifetimes, which are hundreds to a few thousands of hours. The 10 c/kWh line is the average cost of electricity in the United States, while the 6 c/kWh line is the Department of Energy Sunshot Initiative goal. Figure adopted with permission from Energy & Environmental Science.[120]

Aside from stability issues, the Pb content of perovskite solar cells has been raised as an environmental concern that could inhibit commercial deployment. Proponents of PSC often argue that the relatively low mass of Pb in thin films makes the risks of scale up negligible or manageable. In fact, existing c-Si manufacturing also relies on Pb for Pb-Sn solder and glass bonding.[121–124] The Pb content of a 1 m^2 PSC is comparable to the naturally occurring Pb content of a 1 cm thick slab of 1 m^2 soil, and only about 2% of the Pb content of a typical Si solar cell.[125] Pb is still used industrially for lead acid batteries and other applications, but there is no safe level of Pb exposure.[126] In a different perspective, the Pb released to the environment by a coal burning power plant could be comparable to that from PSC if module failure rates (failures that release all Pb in the perovskite absorber to the environment) are from ~0.3% to ~3% over a 20 year period.[127]

Skeptics of Pb-based PSC scale up argue that unlike the Pb in Si solar cells, Pb in perovskite solar cells is water soluble, which could create environmental and health

risks if modules or their encapsulation are compromised. While the relatively low mass of Pb used for PSC could meet current environmental regulations even if all the Pb content were released to underlying soil, a very recent study found these regulations may be inadequate since they do not account for the greatly increased bioavailability of Pb salts relative to metallic Pb. Increasing soil Pb concentration by just 10% through perovskite contamination resulted in an increase of Pb of more than 100% for plants grown in the contaminated soil.[128] An argument can be made that Pb must be replaced for PSC to reach ubiqutous adoption.[129] Certainly, a strong case can be made for rigorous environmental testing before wide Pb-PSC deployment since the few tests done to date are limited in scope and there appears to be much to discover with respect to environmental safety.

Unfortunately, the best PCE acheived by a Pb-free $MASnI_3$ is just 6.4%, and the environmental stability of this material is dramatically diminished due to the oxidation kinetics of Sn^{2+}. Sn itself may also be problematic as studies of a model organism (a zebrafish) showed that SnI_2 was lethal at about one third of the concentration of PbI_2 and also resulted in embryonic defects.[130] The search for safer Pb replacements is a formidable challenge, and while several alternatives have been reported, many of them offer PCE below 1% and rely on scarce, expensive, and potentially unscalable elements such as Bi and Ag.[131] Without a suitable Pb replacement, the ability of PSC to meet climate targets may be constrained by health and environmental regulations. Regulations will be influenced by the perceived value of emissions reductions as weighed against the increased risk of Pb contamination.

Perovskite solar cells promise substantial reductions in manufacturing costs over current commercial photovoltaic technologies, due to low energy manufacturing processes and the use of relatively abundant materials in thin films. The further reduction of solar energy pricing is expected to increase the share of renewable energy production, reducing greenhouse gas emissions, and may also lead to improved standards of living for developing countries with limited energy resources. Notably, the expansion of energy supplies in the developing world, driven by low-cost PSC,

may even have the potential to accelerate the demographic transition to a stable population, further advancing long-term sustainability goals. However, this potential will only be fully realized if perovskites can offer a reduced cost of energy relative to commercial technologies and fossil fuels at an acceptable level of environmental and human health risks due to the use of Pb.

1.7 Sustainability Outlook

The state of climate change, biodiversity, and natural resources is difficult to predict in the future due to the number of interacting variables, the inherent unpredictability of future policy decisions and technological innovation, and the need for improved modeling with bi-directional coupling between human and natural systems.[132] In an optimistic scenario for a sustainable future, global population would stabilize, agricultural and dietary choices would permit greater preservation of biodiversity, a move to a circular economy would reduce consumption rates of renewable and non-renewable resources, innovations in energy conversion and storage would make renewable energy ubiquitous and economical, and data-driven policy would create strong incentives to realize all of these changes without widespread dissent. With respect to each of these issues, there is no shortage of strategies to capture substantial improvements over the present state of affairs.

However, there appears to be an equally compelling cause for concern, as Figure 1.1b demonstrates that there are presently no countries with high levels of development that also meet sustainable development goals. China and South Korea provide hope for an escape from poverty for the developing world by achieving remarkable economic gains in a single generation, but their emissions and per capita energy use have increased by a factor of three to ten over recent decades. The clear trend as populations grow and incomes rise is towards reduced biodiversity and increased natural resource consumption, and global CO_2 emissions continue to set a new record with each passing year.[133] While it remains to be seen whether civilization will seize the opportunities

outlined here to ensure a sustainable planet, it is clear that the cost of inaction is too high to simply be a spectator.

1.8 Aims of This Thesis

This central aim of this thesis is to improve the lifetime and efficiency of perovskite solar cells, thereby making this nascent technology more competitive with existing photovoltaic materials. The two approaches used to this end are interface treatments and new materials for charge selective contacts.

Chapter 2 provides a concise overview of physics and materials concepts essential to this thesis. It begins with a review of core semiconductor principles, introduces perovskites, and reviews the operating principles of photovoltaics. This chapter concludes with an overview of perovskite photovoltaics and explores the causes of limited device lifetimes.

Chapter 3 provides an overview of the methods used for the work in this thesis. Sample preparation materials and processes are described in detail. Characterization techniques and parameters are explained, and a brief overview of the principles of less commonly utilized characterization techniques is provided.

Chapter 4 demystifies the function of the mesoporous layer in perovskite solar cells. Early perovskite solar cell architecture borrowed from dye-sensitized solar cells, where limited diffusion lengths required bulk heterojunctions for efficient exciton separation. While later research discovered a bulk perovskite layer could be utilized in a planar architecture, due to long diffusion lengths resulting from low exciton binding energy and high mobility, a thin mesoporous layer continued to be utilized in devices with record power conversion efficiencies. In this chapter, a mesoporous scaffold of Al_2O_3 is applied at p- and n-type contacts, and is shown to provide shallow p or n doping at the perovskite-metal oxide interface. Device data and external quantum efficiency (EQE) measurements demonstrate that the mesoporous layer only improves power conversion efficiency (PCE) in the n-i-p configuration since p-i-n device performance

is limited by the electron diffusion length. Finally, a mesoporous scaffold is utilized for the first time in n-i-p devices on SnO_2, resulting in improvements to open-circuit voltage and steady-state power output.

Chapter 5 explores the instability between ZnO and metal halide perovskites. ZnO offers improved optoelectronic properties relative to the commonly used TiO_2 and SnO_2, such as improved transmittance, increased conductivity, and a shallow conduction band that aligns closely with the perovskite absorber. While these properties should lead to higher current densities, greater fill factors, and improved V_{oc}, the research community has largely neglected ZnO due to poor thermal stability when in contact with $MAPbI_3$. This chapter reports direct evidence for chemical reactions at the ZnO-perovskite interface. It is shown that a perovskite with only formamidinium and cesium cations offers previously unattainable stability on ZnO films. Interface studies and device data demonstrate the benefits of ZnO relative to SnO_2, with ZnO offering reduced non-radiative recombination, increased V_{oc}, and improved fill factor.

Chapter 6 demonstrates chemical and electronic passivation of a perovskite-SnO_2 interface by cesium salt treatment. While SnO_2 has been the most table n-type metal oxide used in perovskite solar cells, this chapter demosntrates a thermal instability that results in the growth of PbI_2 at the perovskite-SnO_2 interface. Pre-treatment of the SnO_2 with a thin layer of Cs salts results in improved thermal stability of the interface, and increased power conversion efficiency in full devices due to the reduced non-radiative recombination and higher V_{oc}.

Chapter 7 employs a novel hole transport material (HTM), EDOT-Amide-TPA, that offers improved stability and power conversion efficiency for devices relative to Spiro-OMeTAD. Due to its high performance and commercial availability, Spiro-OMeTAD has been the most commonly used hole transport material in PSC research since the field's inception. Prior to this work, the only organic hole transport materials to achieve power conversion efficiencies of 20% in perovskite solar cells were Spiro-OMeTAD and PTAA, both of which are an order of magnitude more expensive than EDOT-Amide-TPA.

Chapter 8 reports a UV cross-linkable HTM, CL1-2, that offers similar performance and additional benefits compared to the state-of-the-art PolyTPD. Devices on CL1-2 achieve device efficiencies comparable to those offered by PolyTPD, even when CL1-2 is used without dopants. By utilizing a bi-layer Cr-Au electrode and all organic charge transport layers, devices on both HTM's achieve unprecedented long-term thermal stability. No reduction in power conversion efficiency is observed even after 3,000 hours at 85 °C, and devices are also stable under high-intensity UV irradiation. A solution-processed proof of concept "tandem" also demonstrates the benefit of cross-linkable charge extraction layers.

Finally, Chapter 9 provides a summary of the work described here and offers insights for future research directions.

References

1. S. Pinker, *The Better Angels of Our Nature: The Decline of Violence In History And Its Causes*. Penguin, 2011.
2. "World development indicators," *The World Bank*, 2019 https://datacatalog.worldbank.org/dataset/world-development-indicators.
3. J. Madden, "Slavery in the roman empire numbers and origins," *Classics Ireland*, vol. 3, p. 109–128, 1996.
4. *Historical statistics of the United States - colonial times to 1970. Part 1. Bicentennial edition*. US Census Bureau, Washington, D.C., 1975.
5. D. P. Forsythe, *Encyclopedia of human rights*. Oxford University Press, 2009.
6. S. D. Purlevskii and B. B. Gorshkov, *A life under Russian serfdom memoirs of Savva Dmitrievich Purlevskii, 1800-1868*. Central European University Press, 2005.
7. "The global slavery index, 2018," *Walk Free Foundation*, 2018.
8. *The new plastics economy - rethinking the future of plastics*. Ellen MacArthur Foundation, 2016.
9. T. C. Brown, V. Mahat, and J. A. Ramirez, "Adaptation to future water shortages in the united states caused by population growth and climate change," *Earth's Future*, vol. 7, pp. 219–234, mar 2019.
10. C. N. Waters, J. Zalasiewicz, C. Summerhayes, A. D. Barnosky, C. Poirier, A. G. uszka, A. Cearreta, M. Edgeworth, E. C. Ellis, M. Ellis, C. Jeandel, R. Leinfelder, J. R. McNeill, D. d. Richter, W. Steffen, J. Syvitski, D. Vidas, M. Wagreich, M. Williams, A. Zhisheng, J. Grinevald, E. Odada, N. Oreskes, and A. P. Wolfe, "The anthropocene is functionally and stratigraphically distinct from the holocene," *Science*, vol. 351, pp. aad2622–aad2622, jan 2016.
11. D. Lin, L. Hanscom, A. Murthy, A. Galli, M. Evans, E. Neill, M. Mancini, J. Martindill, F.-Z. Medouar, S. Huang, and M. Wackernagel, "Ecological footprint accounting for countries: Updates and results of the national footprint accounts, 2012–2018," *Resources*, vol. 7, p. 58, sep 2018.
12. G. F. Network, "Working guidebook to the national footprint accounts." `https://www.footprintnetwork.org/content/uploads/2018/05/2018-National-Footprint-Accounts-Guidebook.pdf`. Accessed August, 2019.

13. B. J. Brown, M. E. Hanson, D. M. Liverman, and R. W. Merideth, "Global sustainability: Toward definition," *Environmental Management*, vol. 11, pp. 713–719, nov 1987.

14. D. Cuff and A. Goudie, eds., *The Oxford Companion to Global Change*. Oxford University Press, jan 2008.

15. J. Bolt and J. L. van Zanden, "The maddison project: collaborative research on historical national accounts," *The Economic History Review*, pp. n/a–n/a, mar 2014.

16. S. N. Broadberry, B. M. S. Campbell, A. Klein, M. Overton, and B. v. Leeuwen, *British economic growth, 1270-1870*. Cambridge University Press, 2015.

17. D. de la Croix and O. Licandro, "The longevity of famous people from hammurabi to einstein," *Journal of Economic Growth*, vol. 20, pp. 263–303, jun 2015.

18. N. Koepke and J. Baten, "The biological standard of living in europe during the last two millennia," *European Review of Economic History*, vol. 9, pp. 61–95, apr 2005.

19. B. Sørensen, *Renewable energy: physics, engineering, environmental impacts, economics planning*. Academic Press, 2017.

20. B. Sørensen, "Energy use by eem neanderthals," *Journal of Archaeological Science*, vol. 36, pp. 2201–2205, oct 2009.

21. B. Sorensen, *A History of Energy*. Routledge, feb 2013.

22. B. Petroleum, "Bp statistical review of world energy, 68th edition," *BP Statistical Review.*, 2018.

23. V. Smil, "World history and energy," in *Encyclopedia of Energy*, pp. 549–561, Elsevier, 2004.

24. V. Smil, *Energy and Civilization*. The MIT Press, may 2017.

25. V. Smil, "Detonator of the population explosion," *Nature*, vol. 400, no. 6743, p. 415–415, 1999.

26. P. Turchin, "Does population ecology have general laws?," *Oikos*, vol. 94, no. 1, p. 17–26, 2001.

27. R. Hopfenberg, "Human carrying capacity is determined by food availability," *Population and Environment*, vol. 25, no. 2, p. 109–117, 2003.

28. R. Hopfenberg and D. Pimentel, "Human carrying capacity is determined by food availability," *Environment, Development and Sustainability*, vol. 3, pp. 1–15, 2001.

29. J. Dodson, X. Li, N. Sun, P. Atahan, X. Zhou, H. Liu, K. Zhao, S. Hu, and Z. Yang, "Use of coal in the bronze age in china," *The Holocene*, vol. 24, no. 5, pp. 525–530, 2014.

30. K. K. Goldewijk, A. Beusen, and P. Janssen, "Long-term dynamic modeling of global population and built-up area in a spatially explicit way: HYDE 3.1," *The Holocene*, vol. 20, pp. 565–573, mar 2010.

31. V. Smil, *Energy transitions: global and national perspectives*. Praeger, an imprint of ABC-CLIO, LLC, 2017.

32. C. M. Meure, D. Etheridge, C. Trudinger, P. Steele, R. Langenfelds, T. van Ommen, A. Smith, and J. Elkins, "Law dome CO2, CH4and n2o ice core records extended to 2000 years BP," *Geophysical Research Letters*, vol. 33, no. 14, 2006.

33. C. D. Keeling, S. C. Piper, R. B. Bacastow, M. Wahlen, T. P. Whorf, M. Heimann, and H. A. Meijer, "Atmospheric CO2 and 13co2 exchange with the terrestrial biosphere and oceans from 1978 to 2000: Observations and carbon cycle implications," in *A History of Atmospheric CO2 and Its Effects on Plants, Animals, and Ecosystems*, pp. 83–113, Springer-Verlag.

34. U. N. D. Programme, "United nations human development index," 2018. Data retrieved from http://hdr.undp.org/en/composite/HDI.

35. D. M. Martínez and B. W. Ebenhack, "Understanding the role of energy consumption in human development through the use of saturation phenomena," *Energy Policy*, vol. 36, pp. 1430–1435, apr 2008.

36. "United nations world happiness report," *United Nations Sustainable Development Solutions Network*, 2019 https://datacatalog.worldbank.org/dataset/world-development-indicators.

37. "World energy outlook," *International Energy Agency*, 2018.

38. C. Shearer, N. Mathew-Shah, L. Myllyvirta, A. Yu, and T. Nace, "Boom and bust 2019: Tracking the global coal plant pipeline," 2019.

39. J. P. Holdren, "Energy and sustainability," *Science*, vol. 315, pp. 737–737, feb 2007.

40. T. Schindlmayr, "Explanations of the fertility crisis in modern societies: a search for commonalities," *Demographic Transition Theory*, p. 349–385.

41. P. Gerland, A. E. Raftery, H. Ev Ikova, N. Li, D. Gu, T. Spoorenberg, L. Alkema, B. K. Fosdick, J. Chunn, N. Lalic, and et al., "World population stabilization unlikely this century," *Science*, vol. 346, no. 6206, p. 234–237, 2014.

42. M. Myrskylä, H.-P. Kohler, and F. C. Billari, "Advances in development reverse fertility declines," *Nature*, vol. 460, pp. 741–743, aug 2009.

43. J. G. Canadell, M. R. Raupach, and R. A. Houghton, "Anthropogenic co2 emissions in africa," *Biogeosciences*, vol. 6, no. 3, p. 463–468, 2009.

44. U. N. P. Division, "United nations world population prospects 2019." https://population.un.org/wpp/Download/Standard/Population/, 2019. Accessed August, 2019.

45. S. G. Warren, "Can human populations be stabilized?," *Earths Future*, vol. 3, no. 2, p. 82–94, 2015.

46. J. C. Spicer and S. O. Gustavus, "Mormon fertility through half a century: Another test of the americanization hypothesis," *Social Biology*, vol. 21, pp. 70–76, mar 1974.

47. D. Meurs, P. A. Puhani, and F. von Haaren, "Number of siblings and educational choices of immigrant children: Evidence from first- and second-generation immigrants," *SSRN Electronic Journal*, 2015.

48. T. Forsyth, *Encyclopedia of International Development*. Routledge, 2005.

49. E. O. Wilson, *Half-earth: our planets fight for life*. Liveright Publishing Corporation, a division of W.W. Norton Company, 2017.

50. G. Ceballos, P. R. Ehrlich, A. D. Barnosky, A. García, R. M. Pringle, and T. M. Palmer, "Accelerated modern human–induced species losses: Entering the sixth mass extinction," *Science Advances*, vol. 1, p. e1400253, jun 2015.

51. J. M. D. Vos, L. N. Joppa, J. L. Gittleman, P. R. Stephens, and S. L. Pimm, "Estimating the normal background rate of species extinction," *Conservation Biology*, vol. 29, pp. 452–462, aug 2014.

52. R. Dirzo, H. S. Young, M. Galetti, G. Ceballos, N. J. B. Isaac, and B. Collen, "Defaunation in the anthropocene," *Science*, vol. 345, pp. 401–406, jul 2014.

53. M. Davis, S. Faurby, and J.-C. Svenning, "Mammal diversity will take millions of years to recover from the current biodiversity crisis," *Proceedings of the National Academy of Sciences*, vol. 115, pp. 11262–11267, oct 2018.

54. H. C. Wilting, A. M. Schipper, M. Bakkenes, J. R. Meijer, and M. A. J. Huijbregts, "Quantifying

biodiversity losses due to human consumption: A global-scale footprint analysis," *Environmental Science & Technology*, vol. 51, pp. 3298–3306, jan 2017.

55. E. Crist, C. Mora, and R. Engelman, "The interaction of human population, food production, and biodiversity protection," *Science*, vol. 356, pp. 260–264, apr 2017.
56. A. Shepon, G. Eshel, E. Noor, and R. Milo, "Energy and protein feed-to-food conversion efficiencies in the US and potential food security gains from dietary changes," *Environmental Research Letters*, vol. 11, p. 105002, oct 2016.
57. W. J. Ripple, P. Smith, H. Haberl, S. A. Montzka, C. McAlpine, and D. H. Boucher, "Ruminants, climate change and climate policy," *Nature Climate Change*, vol. 4, pp. 2–5, dec 2013.
58. D. Nijdam, T. Rood, and H. Westhoek, "The price of protein: Review of land use and carbon footprints from life cycle assessments of animal food products and their substitutes," *Food Policy*, vol. 37, pp. 760–770, dec 2012.
59. B. Machovina, K. J. Feeley, and W. J. Ripple, "Biodiversity conservation: The key is reducing meat consumption," *Science of The Total Environment*, vol. 536, pp. 419–431, dec 2015.
60. P. Sans and P. Combris, "World meat consumption patterns: An overview of the last fifty years (1961–2011)," *Meat Science*, vol. 109, pp. 106–111, nov 2015.
61. H. L. Tuomisto and M. J. T. de Mattos, "Environmental impacts of cultured meat production," *Environmental Science & Technology*, vol. 45, pp. 6117–6123, jul 2011.
62. *Carbon Footprint Evaluation of Regenerative Grazing at White Oak Pastures*. Quantis, prepared for General Mills and White Oak Pastures, 2019.
63. D. Merrill and L. Leatherby, "Here's how america uses its land," *Bloomberg*, 2018 https://www.bloomberg.com/graphics/2018-us-land-use/.
64. E. R. Service, D. P. Bigelow, and A. Borchers, *Major uses of land in the United States, 2012*. 2017.
65. K. L. DeLong and D. Hughes, "A land-use map heard all around social media "here's how america uses its land." dave merrill and lauren leatherby, july 31, 2018. accessed august 31, 2018 at https://www.bloomberg.com/graphics/2018-us-land-use/," *American Journal of Agricultural Economics*, vol. 101, pp. 988–990, nov 2018.
66. E. Dinerstein, D. Olson, A. Joshi, C. Vynne, N. D. Burgess, E. Wikramanayake, N. Hahn, S. Palminteri, P. Hedao, R. Noss, and et al., "An ecoregion-based approach to protecting half the terrestrial realm," *BioScience*, vol. 67, p. 534–545, May 2017.
67. *Decoupling natural resource use and environmental impacts from economic growth*. United Nations Environment Programme, 2011.
68. V. Smil, *Making the Modern World - Materials and Dematerialization*. Wiley, 2013.
69. *Resource Efficiency: Potential and Economic Implications Summary for Policy-Makers*. United Nations, 2016.
70. Y. Geng, J. Sarkis, and R. Bleischwitz, "How to globalize the circular economy," *Nature*, vol. 565, pp. 153–155, jan 2019.
71. U. D. I. of Transportation Studies, *Disruptive Transportation: The Adoption, Utilization, and Impacts of Ride-Hailing in the United States*. UC Davis Institute of Transportation Studies, oct 2017.
72. H. Wieser, "Beyond planned obsolescence: Product lifespans and the challenges to a circular economy," *GAIA - Ecological Perspectives for Science and Society*, vol. 25, pp. 156–160, jan 2016.

73. W. R. Stahel, "The circular economy," *Nature*, vol. 531, no. 7595, p. 435–438, 2016.

74. D. Kahneman and A. Deaton, "High income improves evaluation of life but not emotional well-being," *Proceedings of the National Academy of Sciences*, vol. 107, pp. 16489–16493, sep 2010.

75. L. C. Keely, "Why isn't growth making us happier? utility on the hedonic treadmill," *Journal of Economic Behavior & Organization*, vol. 57, pp. 333–355, jul 2005.

76. R. Wang, H. Liu, J. Jiang, and Y. Song, "Will materialism lead to happiness? a longitudinal analysis of the mediating role of psychological needs satisfaction," *Personality and Individual Differences*, vol. 105, pp. 312–317, jan 2017.

77. E. Diener, R. E. Lucas, and C. N. Scollon, "Beyond the hedonic treadmill: Revising the adaptation theory of well-being," in *Social Indicators Research Series*, pp. 103–118, Springer Netherlands, 2009.

78. E. L. Bernays and M. C. Miller, *Propaganda*. IG Publishing, 2005.

79. E. L. Bernays, *Public relations*. Snowball Publishing, 2012.

80. A. A. Berger, *Ads, fads, and consumer culture: advertisings impact on American character and society*. Rowman Littlefield, 2015.

81. "Personal consumption expenditures/gross domestic product," *Economic Research, Federal Reserve Bank of St. Louis*, 2019 https://fred.stlouisfed.org/graph/?g=hh3.

82. S. Carattini, S. Kallbekken, and A. Orlov, "How to win public support for a global carbon tax," *Nature*, vol. 565, pp. 289–291, jan 2019.

83. N. Chalifour, "Jurisdictional wrangling over climate policy in the canadian federation: Key issues in the provincial constitutional challenges to parliament's greenhouse gas pollution pricing act," *Ottawa Law Review*, vol. 50, mar 2019.

84. J. T. Abatzoglou and A. P. Williams, "Impact of anthropogenic climate change on wildfire across western US forests," *Proceedings of the National Academy of Sciences*, vol. 113, pp. 11770–11775, oct 2016.

85. *The rising cost of wildfire operations effects on the Forest Services non-fire work*. USDA Forest Service, 2015.

86. *Climate Stabilization Targets*. National Academies Press, feb 2011.

87. T. R. Knutson, J. L. Mcbride, J. Chan, K. Emanuel, G. Holland, C. Landsea, I. Held, J. P. Kossin, A. K. Srivastava, M. Sugi, and et al., "Tropical cyclones and climate change," *Nature Geoscience*, vol. 3, no. 3, p. 157–163, 2010.

88. "2018's billion dollar disasters in context: Noaa climate.gov," Feb 2019.

89. R. K. Pachauri and L. Meyer, *Climate change 2014: synthesis report*.

90. L. Nazarenko, G. A. Schmidt, R. L. Miller, N. Tausnev, M. Kelley, R. Ruedy, G. L. Russell, I. Aleinov, M. Bauer, S. Bauer, and et al., "Future climate change under rcp emission scenarios with giss modele2," *Journal of Advances in Modeling Earth Systems*, vol. 7, no. 1, p. 244–267, 2015.

91. D. P. V. Vuuren, J. Edmonds, M. Kainuma, K. Riahi, A. Thomson, K. Hibbard, G. C. Hurtt, T. Kram, V. Krey, J.-F. Lamarque, and et al., "The representative concentration pathways: an overview," *Climatic Change*, vol. 109, p. 5–31, May 2011.

92. K. Riahi, S. Rao, V. Krey, C. Cho, V. Chirkov, G. Fischer, G. Kindermann, N. Nakicenovic, and P. Rafaj, "Rcp 8.5—a scenario of comparatively high greenhouse gas emissions," *Climatic Change*, vol. 109, no. 1-2, p. 33–57, 2011.

93. S. Kang and E. A. B. Eltahir, "North china plain threatened by deadly heatwaves due to climate change and irrigation," *Nature Communications*, vol. 9, jul 2018.

94. R. Knutti, J. Rogelj, J. Sedláček, and E. M. Fischer, "A scientific critique of the two-degree climate change target," *Nature Geoscience*, vol. 9, pp. 13–18, dec 2015.

95. V. Masson-Delmotte, P. Zhai, H. O. Portner, D. Roberts, J. Skea, P. R. Shukla, A. Pirani, W. Moufouma-Okia, C. Pean, R. Pidcock, and et al., *Global warming of 1.5°C: an IPCC special report on the impacts of global warming of 1.5°C above pre-industrial levels and related global greenhouse gas emission pathways, in the context of strengthening the global response to the threat of climate change, sustainable development, and efforts to eradicate poverty*. 2018.

96. R. P. Marc Perez, "A fundamental look at supply side energy reserves for the planet," *International Energy Agency, Solar Heating and Cooling Program Update*, vol. November, pp. 4–6, 2015.

97. M. A. Green, "How did solar cells get so cheap?," *Joule*, vol. 3, pp. 631–633, mar 2019.

98. E. I. Massachusetts Institute of Technology, "The future of solar energy," 2015.

99. L. Meng, J. You, and Y. Yang, "Addressing the stability issue of perovskite solar cells for commercial applications," *Nature Communications*, vol. 9, dec 2018.

100. I. R. E. Agency, "Renewable power generation costs in 2018," 2018. Data retrieved from `https://www.irena.org/publications/2019/May/Renewable-power-generation-costs-in-2018`.

101. N. R. E. Laboratory, "Solar maps," 2018. Data retrieved from `https://www.nrel.gov/gis/solar.html`.

102. A. Feltrin and A. Freundlich, "Material considerations for terawatt level deployment of photovoltaics," *Renewable Energy*, vol. 33, pp. 180–185, feb 2008.

103. "International energy outlook: 2009," *Energy Information Administration*, 2009.

104. U. S. G. Survey, "Historical statistics for mineral and material commodities in the united states," 2014. Data retrieved from `https://www.usgs.gov/centers/nmic/historical-statistics-mineral-and-material-commodities-united-states`.

105. "Mineral commodity summaries," *United States Geological Survey*, 2019.

106. J. E. Tilton, *On borrowed time?: assessing the threat of mineral depletion*. Resources for the Future, 2003.

107. M. Henckens, E. V. Ierland, P. Driessen, and E. Worrell, "Mineral resources: Geological scarcity, market price trends, and future generations," *Resources Policy*, vol. 49, p. 102–111, 2016.

108. D. R. Lide, *CRC handbook of chemistry and physics: a ready-reference book of chemical and physical data*. CRC Press, 2009.

109. L. Becker, "Chemical elements by market price," Oct 2018.

110. B. Heard, B. Brook, T. Wigley, and C. Bradshaw, "Burden of proof: A comprehensive review of the feasibility of 100% renewable-electricity systems," *Renewable and Sustainable Energy Reviews*, vol. 76, pp. 1122–1133, sep 2017.

111. M. Z. Jacobson and M. A. Delucchi, "Providing all global energy with wind, water, and solar power, part i: Technologies, energy resources, quantities and areas of infrastructure, and materials," *Energy Policy*, vol. 39, pp. 1154–1169, mar 2011.

112. D. Abbott, "Is nuclear power globally scalable? [point of view]," *Proceedings of the IEEE*, vol. 99, pp. 1611–1617, oct 2011.

113. B. Kroposki, B. Johnson, Y. Zhang, V. Gevorgian, P. Denholm, B.-M. Hodge, and B. Hannegan,

"Achieving a 100% renewable grid: Operating electric power systems with extremely high levels of variable renewable energy," *IEEE Power and Energy Magazine*, vol. 15, pp. 61–73, mar 2017.

114. N. M. Haegel, R. Margolis, T. Buonassisi, D. Feldman, A. Froitzheim, R. Garabedian, M. Green, S. Glunz, H.-M. Henning, B. Holder, and et al., "Terawatt-scale photovoltaics: Trajectories and challenges," *Science*, vol. 356, no. 6334, p. 141–143, 2017.

115. K. Bruening, B. Dou, J. Simonaitis, Y.-Y. Lin, M. F. v. Hest, and C. J. Tassone, "Scalable fabrication of perovskite solar cells to meet climate targets," Oct 2018.

116. J. Qian, M. Ernst, N. Wu, and A. Blakers, "Impact of perovskite solar cell degradation on the lifetime energy yield and economic viability of perovskite/silicon tandem modules," *Sustainable Energy & Fuels*, vol. 3, no. 6, pp. 1439–1447, 2019.

117. J. Gong, S. B. Darling, and F. You, "Perovskite photovoltaics: life-cycle assessment of energy and environmental impacts," *Energy & Environmental Science*, vol. 8, no. 7, pp. 1953–1968, 2015.

118. A. Binek, M. L. Petrus, N. Huber, H. Bristow, Y. Hu, T. Bein, and P. Docampo, "Recycling perovskite solar cells to avoid lead waste," *ACS Applied Materials & Interfaces*, vol. 8, pp. 12881–12886, may 2016.

119. J. M. Kadro, N. Pellet, F. Giordano, A. Ulianov, O. Müntener, J. Maier, M. Grätzel, and A. Hagfeldt, "Proof-of-concept for facile perovskite solar cell recycling," *Energy & Environmental Science*, vol. 9, no. 10, pp. 3172–3179, 2016.

120. Z. Song, C. L. McElvany, A. B. Phillips, I. Celik, P. W. Krantz, S. C. Watthage, G. K. Liyanage, D. Apul, and M. J. Heben, "A technoeconomic analysis of perovskite solar module manufacturing with low-cost materials and techniques," *Energy & Environmental Science*, vol. 10, no. 6, pp. 1297–1305, 2017.

121. H.-J. Song, H. sang Yoon, Y. Ju, S. M. Kim, W. G. Shin, J. Lim, S. Ko, H. mi Hwang, and G. H. Kang, "Conductive paste assisted interconnection for environmentally benign lead-free ribbons in c-si PV modules," *Solar Energy*, vol. 184, pp. 273–280, may 2019.

122. Q. Ma, S. Ma, J. Bai, and H. Wang, "Influence of lead-free glass frit in the front contact paste on the conversion efficiency of polycrystalline silicon solar cells," *RSC Adv.*, vol. 7, no. 75, pp. 47500–47506, 2017.

123. T. Yang, K. Huang, S. Yang, H. Hsieh, and C. Kao, "Growth kinetics of ag3sn in silicon solar cells with a sintered ag metallization layer," *Solar Energy Materials and Solar Cells*, vol. 123, pp. 139–143, apr 2014.

124. Q. Che, H. Yang, L. Lu, and Y. Wang, "Preparation of lead-free nanoglass frit powder for crystalline silicon solar cells," *Applied Energy*, vol. 112, pp. 657–662, dec 2013.

125. N.-G. Park, M. Grätzel, T. Miyasaka, K. Zhu, and K. Emery, "Towards stable and commercially available perovskite solar cells," *Nature Energy*, vol. 1, oct 2016.

126. T. Vorvolakos, , S. Arseniou, and M. Samakouri, "There is no safe threshold for lead exposure: a literature review," *Psychiatriki*, vol. 27, pp. 204–214, jul 2016.

127. B. Hailegnaw, S. Kirmayer, E. Edri, G. Hodes, and D. Cahen, "Rain on methylammonium lead iodide based perovskites: Possible environmental effects of perovskite solar cells," *The Journal of Physical Chemistry Letters*, vol. 6, pp. 1543–1547, apr 2015.

128. J. Li, H.-L. Cao, W.-B. Jiao, Q. Wang, M. Wei, I. Cantone, J. Lü, and A. Abate, "Biological impact of lead from halide perovskites reveals the risk of introducing a safe threshold," *Nature Communications*, vol. 11, jan 2020.

129. Q. Zhang, F. Hao, J. Li, Y. Zhou, Y. Wei, and H. Lin, "Perovskite solar cells: must lead

be replaced – and can it be done?," *Science and Technology of Advanced Materials*, vol. 19, pp. 425–442, may 2018.

130. A. Babayigit, D. D. Thanh, A. Ethirajan, J. Manca, M. Muller, H.-G. Boyen, and B. Conings, "Assessing the toxicity of pb- and sn-based perovskite solar cells in model organism danio rerio," *Scientific Reports*, vol. 6, jan 2016.

131. M. Lyu, J.-H. Yun, P. Chen, M. Hao, and L. Wang, "Addressing toxicity of lead: Progress and applications of low-toxic metal halide perovskites and their derivatives," *Advanced Energy Materials*, vol. 7, p. 1602512, mar 2017.

132. S. Motesharrei, J. Rivas, E. Kalnay, G. R. Asrar, A. J. Busalacchi, R. F. Cahalan, M. A. Cane, R. R. Colwell, K. Feng, R. S. Franklin, K. Hubacek, F. Miralles-Wilhelm, T. Miyoshi, M. Ruth, R. Sagdeev, A. Shirmohammadi, J. Shukla, J. Srebric, V. M. Yakovenko, and N. Zeng, "Modeling sustainability: Population, inequality, consumption, and bidirectional coupling of the earth and human systems," *National Science Review*, p. nww081, dec 2016.

133. "Global energy co2 status report - the latest trends in energy and emissions in 2018," *International Energy Agency*, 2018 https://datacatalog.worldbank.org/dataset/world-development-indicators.

CHAPTER 2

Theory and Background

This chapter provides a concise overview of fundamental concepts that are utilized throughout the work in this thesis. It reviews key semiconductor concepts and operating principles of photovoltaic devices and concludes with an overview of perovskite photovoltaics and degradation mechanisms.

2.1 Semiconductor Theory

When two identical atoms bond, forming a diatomic molecule, their valence electrons are prevented from having identical quantum numbers by the Pauli Exclusion Principle. The atomic orbitals split into distinct energies, allowing the electrons to populate these orbitals without having identical quantum numbers. When atoms bond to form a crystalline solid, many atoms are brought into proximity, resulting in delocalized electrons with overlapping orbitals. Since each orbital can only be occupied by two electrons, one of each spin, this results in energy level splitting such that each electron orbital has a large number of discrete energy states. For instance, in 1 cm^3 of Si there

are about 5 x 10^{22} atoms, giving rise to energy states that are on the order of 10^{-22} eV apart. These closely spaced energy states form a continuum, or an energy band.

The energy levels of electrons, which can be found by solving Schrodinger's equation, require further consideration for crystal lattices. The simplest approach is to treat electrons within a solid as a gas, as in the free electron model, ignoring both the repulsive interaction between electrons and the attraction to positively charged ion cores. The energy-momentum curve for the free electron model is plotted in Figure 2.1a. This simple model fails to account for some properties of solids, such as why some solids are metals while others are insulators, and needs to be improved to address these observations.

A more accurate model incorporates a periodic attractive potential from lattice ion cores as a small perturbation on the free electron potential. A 1-dimensional array of ion cores and their associated potential energy is shown schematically in Figure 2.1b. The electron probability distribution can then be described by a Bloch wave with a periodic component, determined by the crystal structure, and a plane wave component, represented by the wavefunction of the free electron. Electrons with a wavelength commensurate with the periodic lattice, where $k = \pi/a$, form standing wave patterns and diffract from the ion cores comprising the lattice. This results in the energy-momentum dispersion relation shown in Figure 2.1c, where destructive interference of the standing waves results in a forbidden band, also known as a bandgap. The bandgap is a crucial concept for understanding the optoelectronic properties of solids, as will be discussed in further detail.

Due to crystal symmetry, the energy distribution repeats for k $> \pi/a$, and $E(k) = E(-k)$. The region from $-\pi/a$ to $+\pi/a$ forms a region in k-space known as a Brillouin zone, which is the smallest set of k values with a unique Bloch wave solution. Also of note is that in the plotted momentum dispersion relation there is a direct bandgap, as the valence band maximum coincides with the conduction band minimum. Direct bandgap materials allow an electron to transition between bands upon absorption of energy equal to or greater than the bandgap, while for indirect bandgap materials the

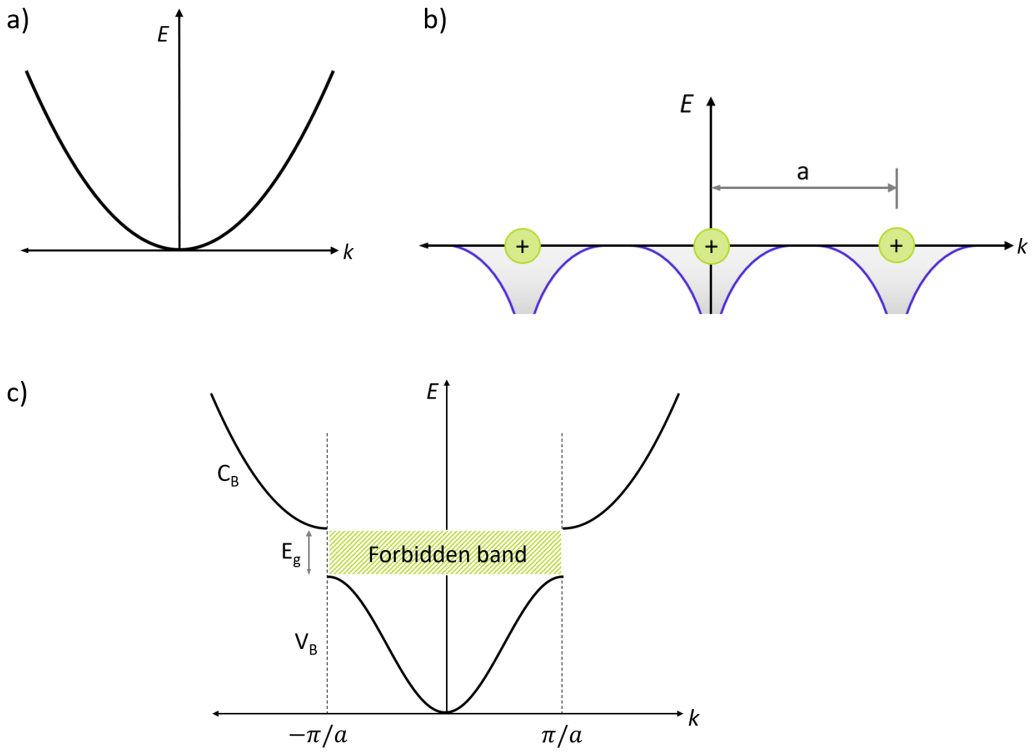

Figure 2.1: a) Electron dispersion for a free electron. b) Periodic potential arising from positive ion cores in a 1-dimensional lattice. c) Band structure for an electron in a 1-dimensional lattice, with the valence band V_B being the first allowed band and the conduction band C_B being the second allowed band. The bands are separated by a bandgap, E_g.

V_B maximum and C_B minimum do not coincide, and electrons absorbing sufficient energy to transition from V_{Bmax} to C_{Bmin} also require a momentum displacement provided by a phonon.

Thus far, the allowed distribution of electron energy has been considered. The probability of finding an electron at a particular energy E is also vital to understanding the properties of materials, and is given by the Fermi-Dirac distribution:

$$n(E) = \frac{1}{exp(\frac{E-E_F}{k_B T}) + 1} \tag{2.1}$$

where n(E) is the number of electrons at a particular energy state E at temperature T, with k being Boltzmann's constant, and E_F the Fermi level. The E_F is the energy level that has a 50% probability of being occupied at any given time for a system in thermodynamic equilibrium. The energy bands adjacent to the E_F are known as the

conduction band (C_B) and the valence band (V_B). The relative energy levels of the C_B, V_B, E_F have central importance in determining the electronic properties of a solid.

Based on their electronic band structure, materials can be classified as metals, semiconductors, or insulators. In isolated atoms, the 2p orbital is at a higher energy level than the 2s orbital, but in a solid where energy levels split some "overlap" can occur. In metals, low energy levels in the 2p orbital can actually be below higher energy levels in the 2s orbital. This "overlap" in metals gives rise to an energy band with nearly continuous states throughout the band. In contrast to metals with a continuous energy band, in a semiconductor distinct energy bands C_B and V_B are separated by an energy gap, known as the bandgap (E_g), of 1 - 4 eV. In insulators, C_B and V_B are separated by a wider gap of $>$ 4 eV. These three classes of materials and a simplified schematic of their characteristic band structures are depicted in Figure 2.2

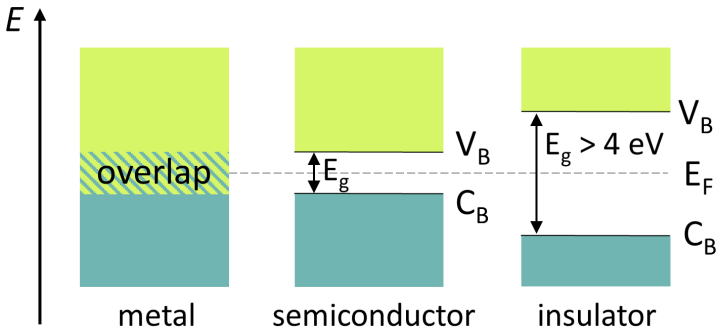

Figure 2.2: Band structure schematic of metals, semiconductors, and insulators. The energy states from atomic orbitals "overlap" in metals, resulting in high conductivity and a single band with nearly continuous states. In semiconductors, distinct energy bands separated by a bandgap result in moderate conductivity. In insulators, it requires $>$ 4 eV to excite the electron across the E_g, resulting in limited conductivity.

In semiconductors and insulators, electrons can be excited from the C_B into the V_B by any energy transfer such that the absorbed energy is greater than E_g. When an electron is excited across the E_g by thermal or electromagnetic energy, it becomes a mobile charge carrier due to a large number of available states in the C_B and contributes to electrical conduction. The resulting vacancy in the V_B has a net positive charge and can be treated as a quasiparticle known as an electron hole (or

simply a hole). The holes are mobilized in the V_B and contribute to hole current. While electrons and holes have equal but opposite charges, they may have different conductivity resulting from their varying effective masses.

As can be seen from Equation 2.1, for a semiconductor at absolute zero all electrons reside in the V_B and there is no electrical conduction. As the temperature increases, electrons are excited across the E_g into the C_B, resulting in increased electrical conductivity. Electrons can also be excited into the C_B through optical absorption when photon energy $E_{Photon} \geq E_g$, and $E_{Photon} = \frac{hc}{\lambda}$, where h is the Planck's constant, c is the speed of light, and λ is the wavelength. The optically excited electrons then contribute to conductivity through a process known as photoconductivity, which is essential to photovoltaic devices.

2.1.1 Doping and Defects

The conductivity of semiconductors can be tuned by adjusting the position of E_F through a process known as doping. Substitutional impurities can be introduced such that atoms with fewer or more valence electrons than those of the host material occupy a small fraction of the lattice sites. Group III elements such as B have one fewer valence electron than Si. Substituting B at Si sites in the lattice creates an acceptor impurity. The excess hole introduces a state near the V_B, which results in p-doping of the crystal and shifts E_F towards the V_B, increasing hole conductivity. Group V elements such as P have one more valence electron than Si. When such an element is used to n-dope a Si crystal, it is referred to as a donor impurity. Since the donor's excess electron is not involved in bonding, it is only weakly attracted to the donor. The donor is easily ionized and the excess electron adds a state near the C_B, resulting in an E_F shift towards the C_B, increasing electron conductivity. These doping techniques and resulting changes to the band structure are depicted in Figure 2.3. Typical doping ranges for crystalline silicon are on the order of one impurity per

10^4-10^9 Si atoms, and conductivity relative to intrinsic silicon can be increased by several orders of magnitude over this doping range.

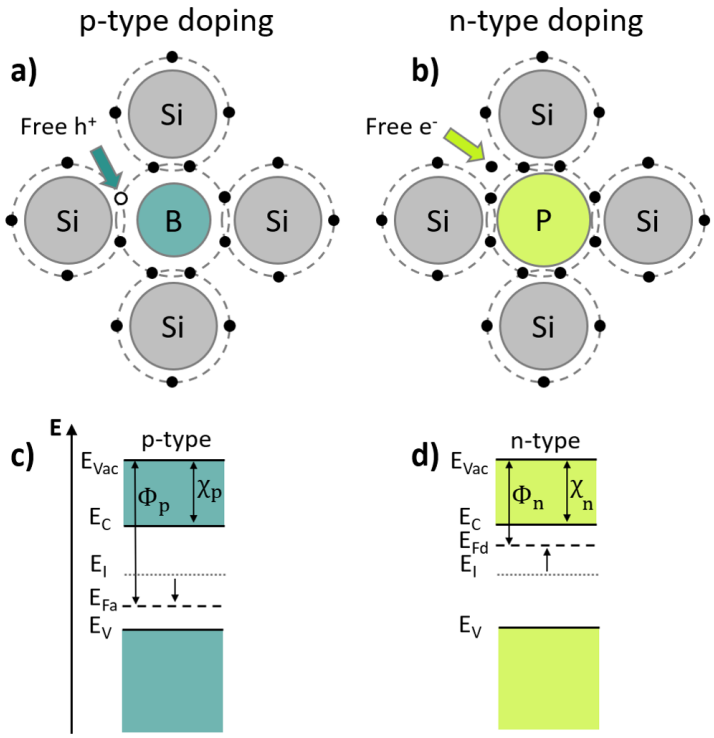

Figure 2.3: p- and n-type Doping of a Semiconductor. a) A substitional phosphorous atom contributes an extra valence electron, n-doping the crystal. b) A substitutional boron atom contributes an excess hole, resulting in p-doping. c) Energy level schematic of n-doping. The intrinsic fermi level, E_I, is shifted towards the conudction band d) Energy level schematic of p-doping.

In contrast to conventional, substitutional doping for semiconductors, organic semiconductors are doped through the addition of molecular dopants which initiate redox reactions with the host material. In the organic semiconductor equivalent of n-type doping, a dopant with a shallower highest occupied molecular orbital (HOMO) energy level than the host's lowest occupied molecular orbital (LUMO) energy level can donate an electron, leaving a hole in the dopant material and an excess electron in the host. Conversely, in the equivalent of p-type doping, a dopant with a deeper LUMO level than the host's HOMO level can withdraw an electron from the host, leaving a hole in the host as shown in Figure 2.4. The materials depicted in Figure 2.4 are discussed in further detail in Chapter 8. Due to the change in carrier concentration

in the host material during doping, organic semiconductor conductivity can often be improved by several orders of magnitude.

In organic semiconductor devices, the concentration of dopants is much higher than the concentration of substitutional impurities for conventional semiconductors, and is often in the range of one dopant molecule per 5-100 host molecules. The need for greatly increased dopant concentration is due to the reduced dielectric constant of organic molecules, which is a factor of 3-4 lower than for Si, and the higher effective carrier masses, which is reflected in the low mobility of organic semiconductors (typically a few cm^2/Vs compared to about 1,000 cm^2/Vs for Si).[1,2] Taken together, the lower dielectric constant and greater effective mass result in a Coloumb binding energy that is two orders of magnitude greater in organic than inorganic semiconductors. As a result, the doping effiency for organic semiconductors, defined as the ratio between free carriers transferred to the host and the dopant molecules added, is typically just a few percent.[1] A high doping concentration is also required in organic semiconductors because at low concentration the introduction of each dopant molecule may create an additional trap state. However, as the doping concentration increases the Coulomb wells from these trap states begin to overlap and allow charge hopping between defect sites.[3,4]

In addition to the intentional point defects introduced through doping, semiconductors have a variety of unintentional defects that alter their optoelectronic properties. Careful defect management is vital ensuring the highest performance for semiconductor devices, and the subject of voluminous research. Therefore, it is essential to understand the types of defects in a crystalline solid, beginning with those that cannot be controlled. A perfect crystal is not thermodynamically stable above 0 K as vacancy formation reduces the free energy of the system. A vacancy occurs when there is no atom occupying a site on the lattice. The concentration of vacancies has an exponential dependence on temperature such that the equilibrium concentration of vacancies is:

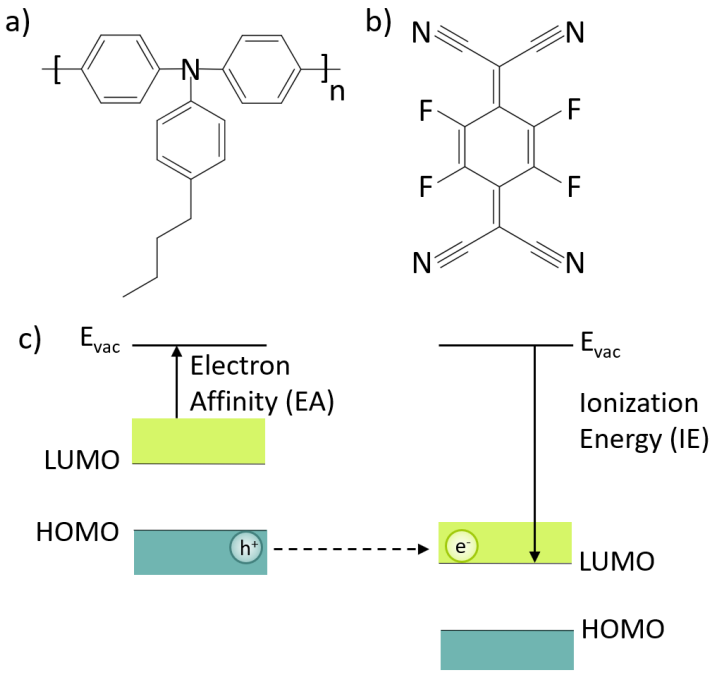

Figure 2.4: p-type doping of an organic semiconductor. a) PolyTPD. b) F4-TCNQ p-type dopant. c) Electron transfer from the conduction band of PolyTPD to the valence band of F4-TCNQ. P-type doping leaving a hole in the host C_B.

$$N_v = Nexp\left(\frac{-Q_v}{k_B T}\right) \tag{2.2}$$

and:

$$N = \rho\frac{N_A}{A} \tag{2.3}$$

where N_v is vacancy concentration, Q_v is the energy required for vacancy formation, and T the absolute temperature. N is the concentration of atomic sites where ρ is density, N_A Avogadro's number, and A the atomic mass. Due to thermodynamic considerations, any crystal above absolute 0 will have a non-zero equilibrium vacancy concentration.

In addition to unavoidable vacancy formation, crystalline materials may have other unintentional defects that can be grouped into broad classifications including point defects, line defects, planar defects, and bulk defects. For the sake of brevity, this review will not exhaustively cover every type of defect.

Point defects include vacancies as previously discussed, interstitial defects, and substitutional defects. Interstitial defects occur when an atom occupies a site in the crystal where there is no corresponding lattice position. Self-interstitials are composed of elements within the ideal crystal, while impurity interstitials occur from elements that do not occur within the ideal crystal and can result from environmental contamination or the limitations of precursor purification. Substitutional defects occur when a lattice site is occupied by an atom of a different type or oxidation state than in the ideal crystal. When introduced intentionally, point defects can have beneficial effects ranging from improved mechanical properties (in the case of solid solution strengthening) to increased conductivity (in the case of doping). However, when uncontrolled point defects can also have undesirable effects, such as reducing the performance of solar cells by creating undesirable states within the bandgap.

Line defects include edge and screw dislocations, both of which result in lattice strain. Planar defects include grain boundaries, twin boundaries, and stacking faults. Grain boundaries occur when two or more crystals nucleate in different orientations and grow outwards until they meet. Grain boundaries are often regions of high strain and can act as a site for impurity segregation, and the concentration of grain boundaries in polycrystalline materials plays a role in determining bulk material properties. Twin boundaries occur when crystals on either side of a plane are mirror images of each other. Stacking faults commonly occur in close-packed structures when one or more atomic layers deviate from the close-packed ordering. An illustration of defects in crystalline materials appears in Figure 2.5.

2.1.2 Semiconductor Junctions

A p-n junction occurs when a p-type semiconductor, having an excess of holes, and an n-type semiconductor, having an excess of electrons, are brought into contact. A variety of techniques such as ion implantation, epitaxial growth, or dopant diffusion are used to minimize or eliminate defects such as grain boundaries at the junction. The

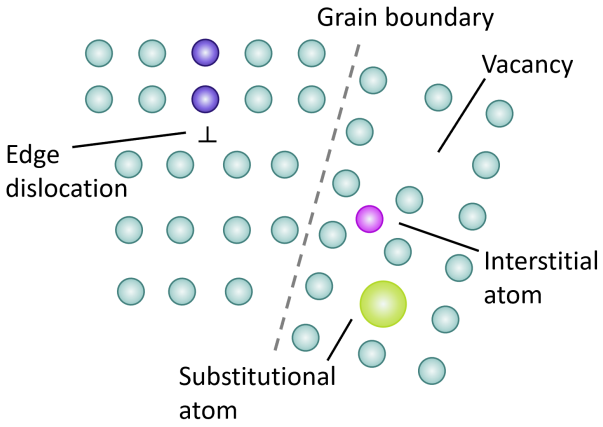

Figure 2.5: A sample of defects in crystalline materials.

p-n junction is key to semiconductor devices including solar cells, diodes, field-effect transistors, and light-emitting diodes.

When the p-n junction is formed, a concentration gradient results from the higher concentration of electrons in the n-type material and the higher concentration of holes in the p-type material. This concentration gradient acts as a driving force, causing free electrons from the n-type material to diffuse to the p-type material and recombine with holes. Likewise, free holes from the p-type material diffuse to the n-type material, recombining with electrons. As holes and electrons diffuse across the junction, negative ions are formed in the p-type region as holes are filled, and positive ions are formed in the n-type region as electrons are removed. The positively charged donors in the n-type region and the negatively charged donors in the p-type region are immobilized by chemical bonds, resulting in a positively charged region near the junction in the n-type semiconductor and a negatively charged region in the p-type semiconductor. As free carriers are removed from the p-n junction, the region near the interface becomes a depletion region (also known as a space charge region). The charge difference between the p- and n-type materials at the depletion region results in an electric field that opposes the diffusion of additional free carriers, and equilibrium is reached when the magnitude of the electric field is sufficient to eliminate further diffusion.

Under forward bias voltage, the p-type material is connected to the positive terminal and the n-type material is connected to a negative terminal. The electric field causes electrons in the bulk of the n-type region and holes in the bulk p-type region to drift towards the junction, reducing the width of the depletion region and increasing conductivity. As the forward-bias increases, the width of the depletion region continues to shrink until its electric field is inadequate to oppose carrier drift. Electrons from the n-type region can then inject into the p-type region, and holes from the p-type region can inject into the n-type region.

Under reverse bias, a negative terminal is connected to the p-type region and a positive terminal is connected to the n-type region. The external bias causes holes to drift towards the cathode and electrons to drift towards the anode, increasing the width of the depletion region and reducing conductivity. Under high bias, the depletion region breaks down and current flows in a process known as avalanche breakdown. In this condition, injected carriers have sufficient kinetic energy to cause impact ionization, liberating additional free carriers during ionized impurity scattering events.[5]

Under forward bias conditions, p-n junctions allow current to increase exponentially as a function of voltage, while under reverse bias no current flows (outside of breakdown conditions). This property allows p-n junctions to act as diodes which rectify current by allowing conduction only in one direction.

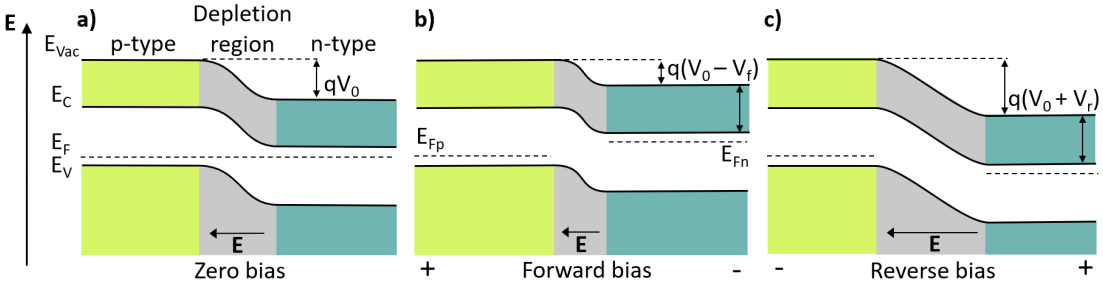

Figure 2.6: a) p-n junction at equilibrium. b) p-n junction under forward bias. c) p-n junction under reverse bias.

2.2 Fundamentals of Photovoltaic Devices

2.2.1 Absorption and Charge Extraction

A solar cell is a device that directly generates both voltage and current when exposed to light, resulting in electrical power. Three principal processes occur to generate power: absorption of light, separation of charge carriers, and extraction of carriers to an external circuit. First, a photon is absorbed by an electron in the solar cell, resulting in an electron and hole pair. Second, the electron and hole are separated. Third, electrons are extracted by electrodes and produce electrical power as they flow through an external circuit. Each process will be examined in greater detail before considering additional factors relevant to solar cell performance.

With respect to absorption, an incident photon can either be reflected at an interface, transmitted through a semiconductor or absorbed. Reflection occurs in many wave phenomena but will be discussed here as an optical process. When light passes between media with different refractive indices, both reflection and refraction occur, with the ratio between the two described by the Fresnel equations. To maximize the optical power transmitted into the solar cell, antireflection layers are utilized in commercial solar cells, such as light trapping inverted pyramidal structures commonly found on silicon solar cells. In tandem solar cells, multiple absorbers are stacked and there may be several times the number of interfaces found in single-junction cells. In such cases, optical modeling is used to maximize transmitted light through index matching and optical spacers that minimize destructive interference between transmitted and reflected waves.

After accounting for optical losses, the photons transmitted into the absorbing semiconductor layer(s) of a solar cell will either be absorbed or transmitted. Photons with energy less than the bandgap of the semiconductor absorber layer will generally be transmitted, as there are no available states to excite an electron into aside from a low concentration of deep trap states. Photons where $E_{Ph} \geq E_g$ will be absorbed by

the semiconductor, exciting an electron from the V_B to the C_B and leaving a positively charged hole in the V_B in the process, as shown in Figure 2.7.

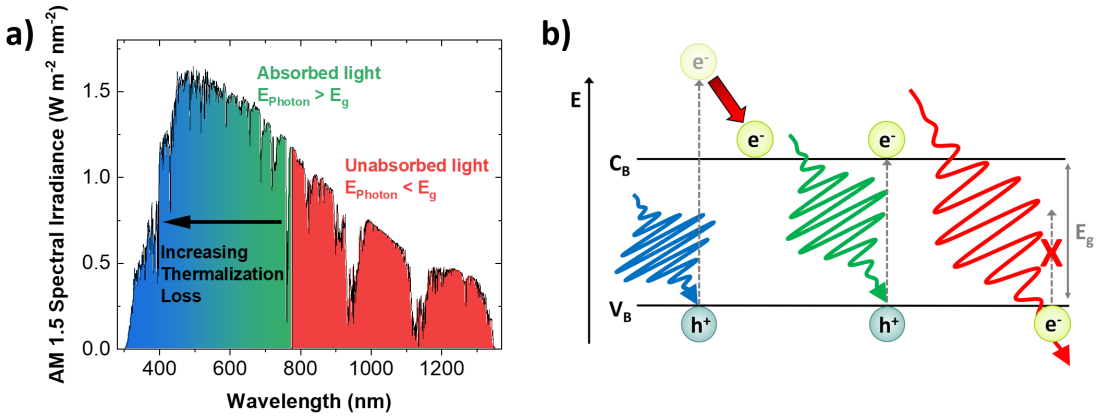

Figure 2.7: a) Absorption of Solar Spectrum. Absorption depicted for a semiconductor with a 1.6 eV bandgap. b) Photon absorption processes. Photons with energy less than E_g are not absorbed, as there are no states available for the electron (left). Photons with $E = E_g$ promote an electron the C_B, leaving a hole in V_B. (center). Photons with $E > E_g$ promote a hole into energy states in C_B above the band edge. The electron rapidly converts the excess energy to heat as it relaxes to the band edge.

Excited free carriers may then recombine through one of three mechanisms, as depicted schematically in Figure 2.8. In the first process, trap-assisted (monomolecular) recombination, an electron in the V_B transitions to an energy level within the bandgap known as a trap state. The trap state is created by a defect in the crystal and the transition into the trap state is accompanied by a phonon, imparting thermal energy to the crystal. If the trap state is shallow, thermal energy $<$ k_BT can promote the electron back to the conduction band edge, and shallow traps, therefore, have a smaller impact on photovoltaic device performance. Alternatively, for deep traps, the energy state is located further into the bandgap, and such deep traps account for detrimental non-radiative recombination. In the second process, band to band recombination (bimolecular), an electron in the V_B recombines with a hole in the C_B, emitting a photon with energy equal to the energy of this transition. The third recombination process is known as Auger recombination (trimolecular), where three carriers are involved. In this process, an electron in the C_B transitions to the V_B but

rather than emitting energy as a photon, the kinetic energy is transferred to a second electron in the C_B.

These three recombination processes occur in different proportions according to the excitation density. At low excitation density, the interaction of photoexcited carriers with defect states dominates. As the excitation density increases, the trap-assisted recombination rate saturates, and bimolecular recombination accounts for an increasing proportion of the recombination. At very high excitation densities trimolecular recombination contributes more significantly to the recombination rate, and these conditions are typically achieved by concentrating sunlight. Solar concentrator photovoltaics use lenses or mirrors to receive power fluxes far in excess of the 1000 W m^{-2} produced by solar irradiation, and the cells used are typically high efficiency multi-junction photovoltaics that are cost-prohibitive to deploy without optical concentration. The three recombination processes can be represented by a rate equation which describes the change in carrier concentration with respect to time as follows:

$$\frac{dn}{dt} = -k_3 n^3 - k_2 n^2 - k_1 n \tag{2.4}$$

where n is the photoexcited carrier density and k_3, k_2, and k_1 are the rate constants for trimolecular, bimolecular, and monomolecular recombination processes. The respective constants can be determined experimentally through time-resolved photoluminescence spectroscopy, as described in the next chapter.

After absorption of a photon, the positively charged hole and negatively charged electron are subject to Coulombic attraction and can be described as an electrically neutral quasiparticle known as an exciton. In conventional semiconductors, a large dielectric constant screens the electric field, reducing the exciton binding energy. In Si, for instance, the exciton binding energy is about 15 meV,[6] and thermal energy at room temperature is sufficient to separate excited carriers. The excitons in conventional

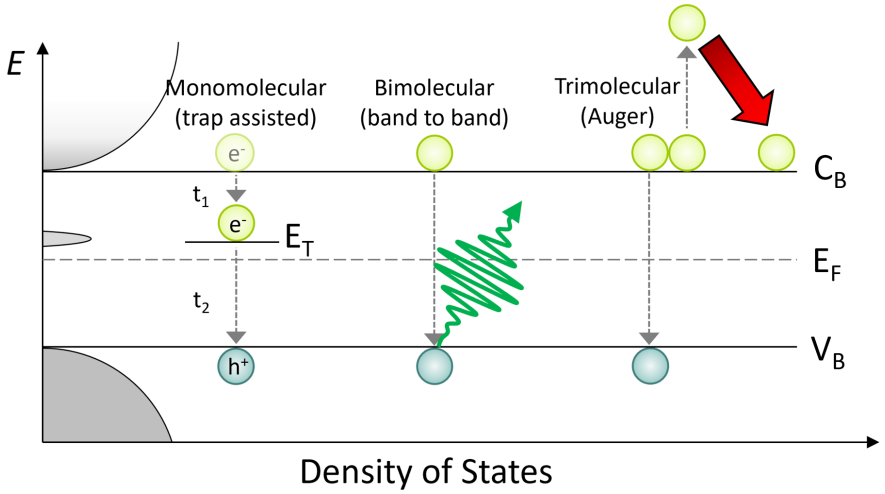

Figure 2.8: Schematic depicting band to band or radiative recombination, trap assisted non-radiative (Shockley-Read-Hall) recombination, and Auger recombiation (from left to right).

semiconductors can be described in terms of their binding energy and radius as follows:

$$E(n) = -\frac{\left(\frac{\mu}{m_e \epsilon_r^2}\right) R_H}{n^2} \tag{2.5}$$

$$r_n = \left(\frac{m_e \epsilon_r a_H}{\mu}\right) n^2 \tag{2.6}$$

where $E(n)$ and r_n are the exciton energy and radius, respectively, ϵ_r the relative permittivity, R_H the Rydberg constant, and a_H the Bohr radius. μ is the reduced mass of the hole and electron and equal to $\frac{m_e^* m_h^*}{m_e^* + m_h^*}$. In comparison to conventional semiconductors, organic semiconductors have a much larger exciton binding energy due to their lower dielectric constant. In these materials, exciton binding energies of 0.3-0.5 eV require a large electric field ($> 10^6$ V cm^{-1}) to effectively separate charges.[7] To bypass the need for such a large field, a bulk heterojunction architecture is employed so that photoexcited charges originate near selective contacts. As discussed later in this chapter, organic solar cell architecture was utilized for early perovskite solar cells, before it was known that the bulk perovskite materials used in solar cells offered large dielectric constants and diffusion lengths that can exceed 1 μm.

Once a photon has been transmitted into the solar cell and absorbed, and the resulting electron-hole pair is separated, the free carriers must finally be collected at electrodes to contribute to current. Charge carrier transport can be described through two processes: drift and diffusion. In the case of drift, an electric field results in the net movement of carriers such that electrons flow in the direction opposite the field. The one-dimensional drift equation is:

$$J_x = q\left(n\mu_n + p\mu_p\right)E_x \tag{2.7}$$

where J_x is the current density in the x-direction, n and p the electron and hole concentrations, μ_n and μ_p the electron and hole mobilities, and E_x the applied electric field.

Diffusion describes the movement of carriers under a concentration gradient as the driving force. Diffusion is described by Fick's Laws, with the one-dimensional case given as:

$$J_n = qD_n\frac{dn(x)}{dx} \tag{2.8}$$

or for holes:

$$J_p = -qD_p\frac{dp(x)}{dx} \tag{2.9}$$

where J_n and J_p are the electron and hole diffusion current densities, respectively, q is the charge of an electron, D_n and D_p the diffusion coefficients for electrons and holes, and n and p the electron and hole concentrations. In diffusion, the random movement of carriers from regions of high to low concentration results in a more uniform distribution of carriers over time.

Absorption, carrier separation, and charge extraction processes are utilized in solar cells to convert sunlight into electrical power. The p-n junction is the basis for conventional solar cells, as shown in figure 2.9. Upon absorption of an incident photon (E $\geq E_g$), an electron is promoted to the conduction band while a hole is generated in the valence band. The dielectric constant of silicon screens the exciton binding energy

for the electron-hole pair and ambient thermal energy is sufficient to separate the free hole and electron. The free carriers undergo drift in opposite directions towards their respective electrodes, which is driven by the built-in potential of the junction, and the built-in potential occurs due to the asymmetry of the doping profile.

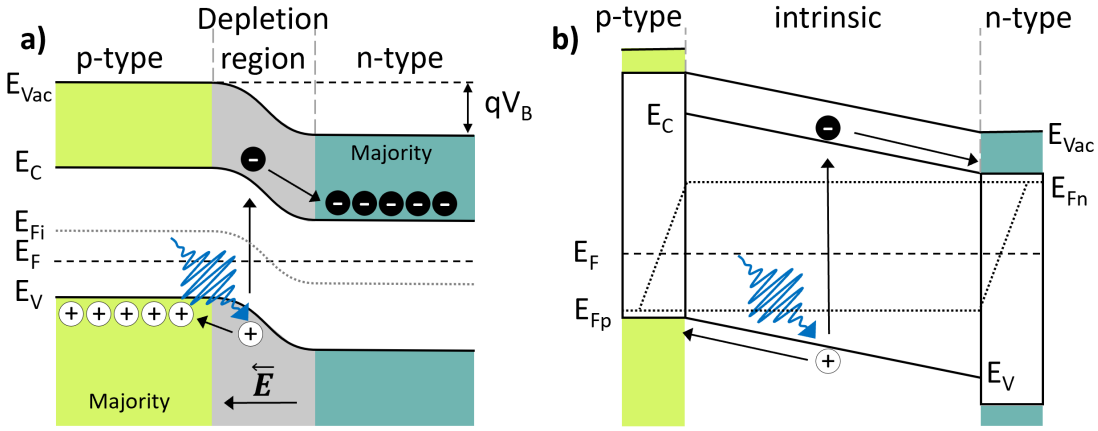

Figure 2.9: a) Conventional p-n junction solar cell. b) p-i-n solar cell used in amorphous silicon and other thin film solar cells. Band bending is neglected for clarity.

In contrast to p-n junction solar cells, p-i-n solar cells utilize an intrinsic absorber layer sandwiched between selective contacts. The selective contacts offer high conductivity for just one type of carrier (electrons, for the n-type contact and holes for the p-type contact). In principle, the p-i-n heterojunction can achieve higher efficiency than the p-n homojunction cell because p-n junctions require heavy doping. Heavy doping improves fill factor by reducing contact resistance to metal electrodes but also results in Auger recombination, decreasing V_{oc} and J_{sc}.[8,9] After forming junctions between the intrinsic layer and selective contacts, the Fermi levels of the materials align and gradients in the conduction band and valence band drive free carriers towards the selective contacts. In the p-i-n architecture, V_{oc} is determined by the quasi-Fermi level splitting as depicted in Figure 2.9b. The large gradient in E_{Fn} within the p-type contact would cause photoexcited electrons generated near this contact to flow in an undesired direction. However, through judicious materials selection, the shallower conduction band of the p-type material relative to the intrinsic layer provides an energetic barrier to electron flow, and the low electron conductivity of the p-type

contact minimizes electron transport. Conversely, the deeper valence band of the n-type layer relative to the intrinsic region and the poor hole conductivity results in hole blocking. Due to the overlapping valence and conduction bands in the electrode metals, the Fermi level splitting collapses at the far left and right sides of the band diagram.

The fundamental processes of absorption, carrier separation and charge extraction are the foundation of all semiconductor solar cells. However, devices with these processes alone do not guarantee the high power conversion efficiency required to make photovoltaics a practical energy source. The next sections discuss solar cell electrical characterization and the theoretical limit to power conversion efficiency.

2.2.2 J-V Characterization of Solar Cells

A solar cell must generate voltage and current to produce power. The magnitude of the current and voltage generated under a given illumination source is essential to determining the device efficiency, and merit further consideration. Solar cells are typically described in terms of current density, rather than absolute current, as the current generated is a function of the device area. First, to model the current, consider the simple case of a solar cell in the dark. The asymmetry of energy levels in the p-n junction causes a solar cell to behave like a rectifying diode, producing a dark current under bias as described by the ideal diode equation:

$$J_{dark}(V) = J_0 \left(exp\left(\frac{qV}{k_B T}\right) - 1 \right) \tag{2.10}$$

where J_{dark} is the dark current, J_0 the dark saturation current (diode leakage in the dark), and V the applied bias. Upon exposure to light, a photocurrent is generated flowing in the opposite direction to the dark current and can be accounted for by adding a J_{sc} term for the maximum current flow for a solar cell (when the terminals

are short-circuited). The ideal diode equation is modified as follows:

$$J(V) = J_{sc} - J_0 \left(exp\left(\frac{qV}{k_B T}\right) - 1 \right) \tag{2.11}$$

The maximum voltage that can be achieved is at the open circuit voltage, V_{oc}, where there is infinite resistance between the terminals and no current flows. Under this condition:

$$V_{oc} = \frac{k_B T}{q} ln\left(\frac{J_{sc}}{J_0} + 1\right) \tag{2.12}$$

In addition to the V_{oc} and J_{sc}, a fill factor determines a solar cell's maximum power point. During J-V characterization of a solar cell, the device is illuminated and current is measured while sweeping the bias voltage. The fill factor is the proportion of the rectangle delimited by V_{oc} and J_{sc} that the J-V curve fills, and is always less than 1:

$$FF = \frac{J_{MPP} V_{MPP}}{J_{sc} V_{oc}} \tag{2.13}$$

The fill factor, in turn, is determined by the combination of series and shunt resistance (R_S and R_{SH}) in the solar cell. R_S arises from resistance to the flow of current in the bulk semiconductor material, at junctions between layers, and within the collection electrodes, and should be minimized. R_{SH} arises from alternate current pathways in the device, which can occur through manufacturing defects such as pinholes within layers, providing direct contact between charge selective contacts or between electrodes and the absorber, or via thermodynamically driven processes such as electrode diffusion through adjacent layers. R_{SH} should be maximized. Modifying the ideal diode equation to account for these losses gives:

$$J(V) = J_{sc} - J_0 \left[exp\left(\frac{q(V + JR_S)}{n k_B T}\right) - 1 \right] - \frac{V + JR_S}{R_{SH}} \tag{2.14}$$

where J is the current density and n is the ideality factor. The ideality factor is typically in the range of 1 to 2 and describes how closely the solar cell follows the

ideal diode equation, which in turn depends on the recombination processes present in the device.

An equivalent circuit model of a solar cell incorporates each of the factors discussed in this section, as shown in Figure 2.10b. The current source (I_L) represents the photocurrent produced when the cell is exposed to light. In parallel with this current source are the dark current, I_D, flowing in the opposing direction, and R_{SH}, the shunt resistance. Also included in the equivalent circuit are the series resistance, R_S, and the voltage across the terminals, V. Figure 2.10a depicts the dark and light J-V curves, the product of current and voltage for the light J-V curve (power density), and the effects of series and shunt resistances. The max power point is also shown, which is the voltage at which the power output is maximized. Figure 2.10b shows the equivalent circuit for a solar cell.

The ideal diode model and J-V characterization allow for a concise representation of solar cell performance but do not set an upper limit for PCE. The limits to efficiency are the subject of the next section.

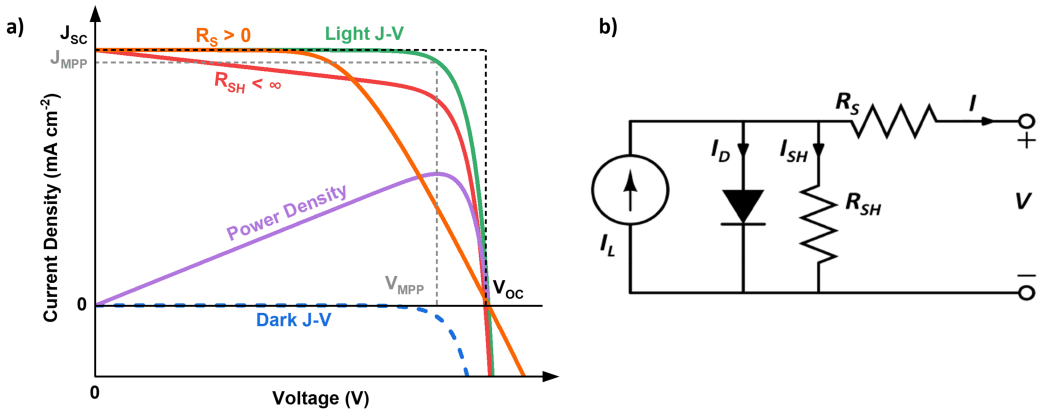

Figure 2.10: Photovoltaic J-V Curves and Equivalent Circuit. a) J-V curves shown for an illuminated solar cell, a solar cell in the dark, a solar cell with high series resistance, and a solar cell with low shunt resistance. The voltage and current at max power point are shown for the light J-V curve, as well as the power density. b) Equivalent circuit model of a solar cell showing dark current, shunt current, series and shunt resistances, and the light current.

2.2.3 Limits to Power Conversion Efficiency

The limits to solar cell efficiency were originally worked out in the detailed balance model of Shockley and Queisser in 1961.[10] This model was further refined by Tiedje et. al. in 1984 to account for free carrier absorption and Auger recombination.[11] Exotic photovoltaic systems can exceed the Shockley-Queisser efficiency limits with a variety of techniques such as multiple exciton generation, thermophotovoltaic downconversion, and photon upconversion. For the sake of brevity, this section will cover the fundamentals of the detailed balance model and the practical implications for conventional, single-junction solar cells; detailed derivations can be found in the references above.

The detailed balance model makes several assumptions, as enumerated below, with considerations for real solar cells shown in bullets:

1. All incident light with $E > E_g$ is absorbed.
    - Absorbing all incident light could in principle be achieved with a sufficient thickness of absorber, but in practice as absorber thickness increases, there may be a trade-off with the reduced current collection due to limited diffusion lengths. In real devices, the parasitic absorption of passivation layers and charge selective contacts and the reflection of light from interfaces prevents some incident light from being absorbed.
2. Each absorbed photon generates one electron-hole pair.
    - This condition is met by conventional photovoltaic technologies. Multiple exciton generation can increase the efficiency limit beyond what is achievable in the detailed balance model, and was first demonstrated in solar cells using PbSe quantum dots in 2011.[12]
3. All excited charges recombine radiatively.

- As discussed previously, all crystals above absolute zero have an equilibrium vacancy concentration resulting in the spontaneous occurrence of defects. While some vacancies may not generate trap states within the bandgap, the presence of other defects is difficult to completely eliminate both in bulk crystalline materials and at their interfaces, resulting in some losses due to non-radiative recombination.

4. All charge is transported to the external circuit without losses.

    - There will be some series resistance from the contacts and non-infinite shunt resistance arising from manufacturing defects and the limited bulk absorber resistivity in real devices.

In the dark, the solar cell can be treated as a blackbody described by Planck's Law, where the emission spectrum is dependent upon its temperature. If the solar cell emits from the top surface and has a mirrored bottom surface the radiative recombination in the dark is then:

$$R_{dark} = \frac{2\pi}{c^2 h^3} \int_{E_g}^{\infty} \frac{E^2 dE}{exp\frac{E}{k_B T} - 1} \tag{2.15}$$

where c is the speed of light and h the plank constant. The minimum recombination rate under illumination, when the quasi-Fermi level is split, is given by:

$$R_{light} = qR_{dark} exp\left(\frac{qV}{k_B T_{cell}}\right) \tag{2.16}$$

where V is the voltage, which is equal to the bandgap in the ideal case.

The ideal current occurs when all photons with $E_{Photon} \geq E_g$ are absorbed and there are no non-radiative recombination losses. In this case, the current is simply the absorbed solar photons less dark recombination rate. The solar flux above the gap can be found by integrating the blackbody spectrum from the sun, with limits from the bandgap of the absorber to infinity, or more accurately for terrestrial solar cells, by utilizing the AM 1.5 data to account for atmospheric absorption, as done here.

For brevity, the limits to fill factor and V_{oc} are computed using simple expressions and the derivation of these can be found elsewhere. The ideal fill factor can be closely approximated by an empirical expression:[13]

$$FF = \frac{v_{oc} - ln(v_{oc} + 0.72)}{v_{oc} + 1} \tag{2.17}$$

where v_{oc} is the normalized voltage:

$$v_{oc} = V_{oc}\frac{q}{nk_BT} \tag{2.18}$$

and n is the ideality factor.

The ideal voltage is as follows:[14]

$$V_{oc} = 0.941E_g - 0.171eV \tag{2.19}$$

Finally, the maximum power conversion efficiency can be found with the product of the ideal J_{sc}, V_{oc}, and FF at each bandgap. The efficiency limits for ideal solar cells are plotted in Figure 2.11. This analysis reveals that the largest remaining improvements for PSC can come from higher fill factors. There is also a notable discrepancy in performance between small area ($<$0.1 cm^2, in red) and large area ($\geq$1 cm^2, in blue) devices that will require improved processing techniques to resolve.

2.3 Perovskites

Perovskites were discovered in 1839 and named after the Russian mineralogist, Lev Perovski.[17] Naturally occuring perovskites are strikingly common, and are found within the Earth's mantle and in meteorites; the perovskite (Mg,Fe)SiO_3 comprises 38 volume % of the Earth's crust, making it the most abundant solid phase on the planet.[18] Perovskites are of interest to both theoretical and experimental research communities and

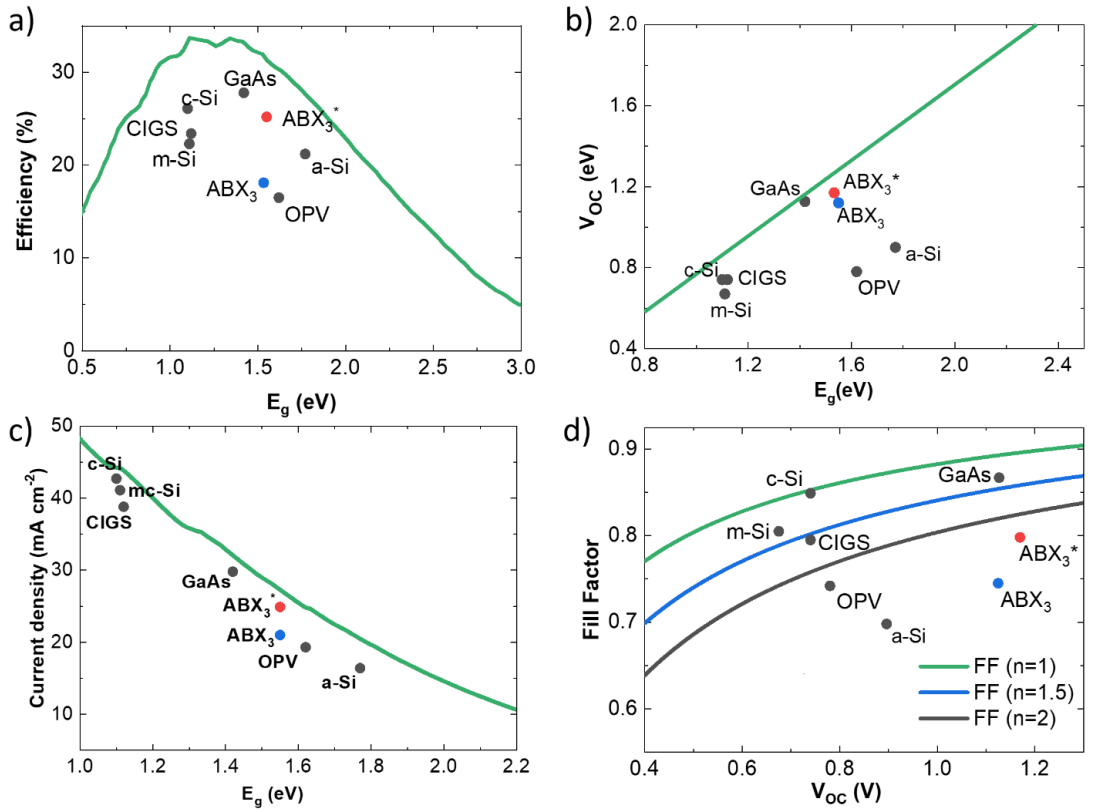

Figure 2.11: Theoretical limits for solar cell parameters under AM 1.5 illumination, and performance of best photovoltaic technologies. Large area perovskite solar cells ($\geq$1 cm^2) are shown in blue while small area (0.1 cm^2) perovskite solar cells are shown in red. a) Shockley-Queisser efficiency limit as a function of E_g. b) V_{oc} limit as a function of E_g. c) Current density limit as a function of V_{oc}. d) Fill factor limit as a function of V_{oc}, with lines showing limits for ideality factors. Data points plotted using perovskite large area cell,[15], NREL efficiency chart,[16] with additional data from review of PV state-of-the-art.[14]

have been studied for decades for exceptional properties that include high-temperature superconductivity, ferroelectricity, and colossal magnetoresistance.[19–21]

Perovskites are a class of materials with an ABX_3 stoichiometry, where A and B are cations such that the ionic radius of A is larger than B, and X is an anion that bonds to both. In the ideal cubic unit cell, the A cations are located at the corners of the cube and the B cation is at the body center, surrounded by an octahedron of X anions located at face center positions, as depicted in Figure 2.12.

Nearly 2,000 perovskites have been discovered, and across this set, the majority of elements have been utilized. An upper bound for charge-neutral unit cells with three cations and one anion places the number of possible perovskite compounds at nearly

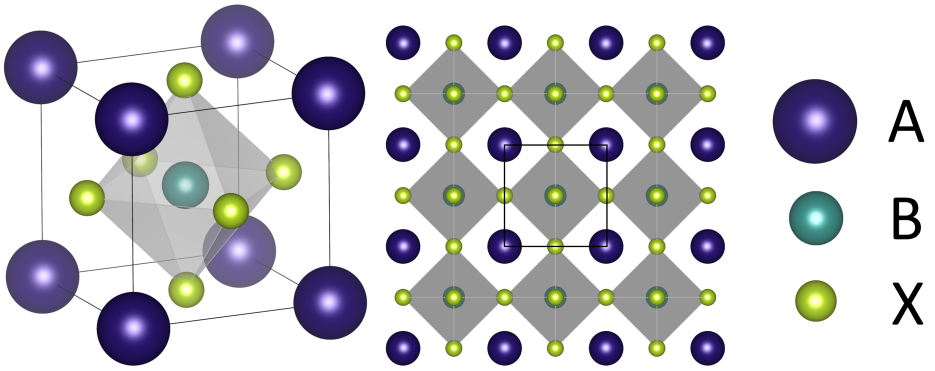

Figure 2.12: Perovskite crystal structure. Ideal high symmetry perovskite unit cell with spacegroup $Pm\bar{3}m$ (left) and supercell (right) with one unit cell outlined in black.

3.7 x 10^6.[22] One method to further constrain the number of possible perovskites is to treat ions as hard spheres and apply a geometric model to determine the packing factor for given ionic radii at each site. The Goldschmidt tolerance factor takes such an approach,[23] expressing the ratio of ionic radii for cations and anions as follows:

$$t = \frac{r_A + r_X}{\sqrt{2}(r_B + r_X)} \tag{2.20}$$

For perfect packing, the tolerance factor $= 1$, yet the perovskite structure can accommodate a much wider range of cation and anion sizes through tilting and distortion of octahedra. Experimentally, perovskite structures are found with tolerance factors $0.8 \leq t \leq 1$. The tolerance factor is a useful first check but has limited predictive accuracy. A review of 576 ABX_3 solids found the tolerance factor is only 33-56% successful at discerning between perovskite and non-perovskite compounds containing iodide and bromide, and a new model utilizing machine learning reports a higher success rate.[24] Interestingly, while about 2,000 perovskites have been experimentally confirmed, considering all permutations of elements with tolerance factors in the empirically verified range gives about 90,000 three dimensional perovskites, providing vast possibilities for future discoveries.[22]

2.3.1 Organic-Inorganic Metal Halide Perovskites for Photovoltaics

Metal halide perovskites (MHP) for photovoltaic applications will be the focus of the remainder of this chapter. In organic-inorganic MHP, the A site is occupied by a monovalent cation, typically methylammonium (MA^+), formamidinium (FA^+), or cesium (Cs^+). The B site is a divalent metal cation, typically Pb^{2+} or Sn^{2+}, and the X site is a monovalent halide anion, typically I^- or Br^-. Cations and anions are often alloyed as in the material $Cs_{0.05}(MA_{0.83}FA_{0.17})_{0.95}PbI_{0.83}Br_{0.17}$. The molecular structure of the organic cations and the tolerance factors for all possible combinations of MA^+, FA^+, and Cs^+ cations are shown in Figure 2.13.

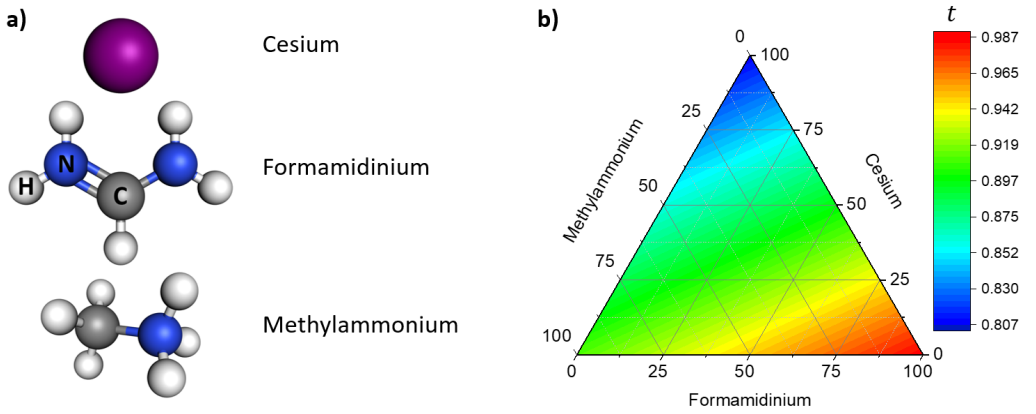

Figure 2.13: a) Molecular diagrams of cations. b) Tolerance factor of cesium, methylammonium, and formamidinium compositions.

While metal halide perovskites were first studied in the late 19th century,[25] the first recognition that these materials were semiconductors came in the late 1950s.[26] Metal halide perovskites were rediscovered for photovoltaic applications in 2009 when $MAPbI_3$ nanocrystals embedded in a liquid electrolyte replaced the light-absorbing dye in dye-sensitized solar cells.[27] These first devices achieved just 3.8% power conversion efficiency, but in 2012 a bulk $MAPbI_3$ film was used to achieve a power conversion efficiency of 10.9%.[28] PSC have become the most rapidly improved photovoltaic device in history, and have recently achieved PCE of 25.2%.[16] This remarkable progress was

due in part to global research interest that generated several thousand publications per year, and also due to several outstanding optoelectronic properties of metal halide perovskites.

$MAPbI_3$ has an optical absorption coefficient of about 10^5 cm^{-1}, about an order of magnitude greater than GaAs, and relatively long diffusion lengths of around 1 μm also permit good carrier extraction from thin-films.[29–31] Surprisingly, MHP films with grains on the order of tens to hundreds of nanometers can also produce PCE over 20% in solar cells. This is explained in part by density functional theory (DFT) studies of point defect formation energies and their energy levels. In general, point defects with low formation energies have higher density than those with large formation energies. When there is a large discrepancy in the formation energy of these two species, point defects with low formation energy tend to have a dominant influence in carrier dynamics. In the archetypal $MAPbI_3$, low formation energy defects produce only shallow traps, while the defects with high formation energy produce deep traps. In Kröger-Vink notation, the point defects with low energies of formation include vacancies of the ABX species (V_{Pb}, V_I, and V_{MA}), the interstitial A and X species (I_i, MA_i), and the substitutional defect MA_{Pb}. Many of these defects have states outside of the bandgap, and those within the bandgap are just 0.05 eV above the V_{Bmax} or below the C_{Bmin}, so they either do not contribute to trapping or only result in shallow traps. The deep trap states are created by the substitutional defects I_{Pb}, I_{MA}, or Pb_I and the interstitial Pb_i. The formation energies of these deep trap states is 3.31 - 4.24 eV, while the formation energy of the shallow trap states is often < 1 eV, with I_i, V_{Pb}, MA_{Pb} all having formation enegies of ~0.25 eV.[32–34]

MHP are also attractive for their compatibility with processing techniques that are unsuitable for conventional, brittle, high melting point semiconductors. MHP achieve efficiency approaching commercial or even state-of-the-art Si solar cells when they are processed with low-temperature solution techniques at 100 °C or even at room temperature, and can also be thermally evaporated, although solution-processed films achieve the highest efficiency in solar cells. Solution processing provides a route to

low-cost processing techniques such as slot-dye coating and roll-to-roll processing that may allow rapid expansion to TW-scale generation capacity, particularly if slow and materially wasteful lab-scale techniques that produce high power conversion efficiencies can be re-engineered for high throughput systems capable of coating substrates at linear rates of meters per minute.

J-V characterization of PSC has been complicated by anomalous hysteresis as shown in Figure 2.14a, with the magnitude of hysteresis varying according to device architecture. Depending on the scan conditions, the PCE determined by the J-V scans in the forward and reverse direction can vary significantly and result in misleading reports of device efficiency. The origin of the hysteresis phenomenon is likely ion migration within the perovskite absorber and charge trapping or surface recombination at the perovskite-charge selective contact interfaces. Halide anion vacancies and interstitials, which will be referred to as mobile ions, are likely the dominant factor in hysteresis since the activation energy required for transport (~0.6 eV) is substantially lower than for other point defects.[35]

A simplified illustration of ion-driven hysteresis is shown in Figure 2.14b-d. In the initial state, the perovskite film contains a uniform distribution of mobile ions. An applied bias produces an electric field across the absorber. Positively charged mobile ions move in the direction of the field, while negatively charged ions move in the opposite direction. As time proceeds, the mobile ions accumulate at the perovskite interfaces and partially screen the applied field.

In a complete device, the difference in work function of the contacts produces a built-in potential across the absorber. Holding the device under forward bias for several seconds reduces the built-in potential and the higher concentration of accumulated mobile ions at the contacts may diffuse back into the bulk. Consequently, after holding the device under forward bias, immediately performing a reverse scan to collect J-V parameters gives an apparently higher performing device, as in Figure 2.14a (blue curve); the greater drift velocity of carriers allows improved charge extraction. A subsequent forward scan of the J-V curve results in a solar cell with lower apparent

performance, as shown in Figure 2.14a (red curve), as mobile ions return to the contacts, screening the potential.[36] The steady-state power output, determined by holding the cell at its maximum power point, is therefore a better indicator of actual performance for PSC than the apparent PCE given by the J-V curves.[37]

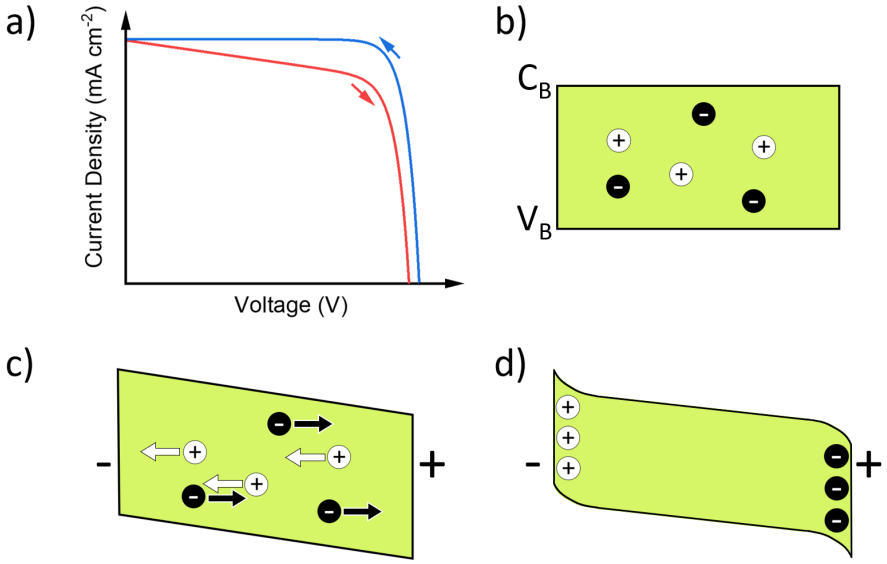

Figure 2.14: a) Hysteretic J-V scans under forward (red) and reverse (blue) scans result in a discrepency between apparent power conversion efficiencies. The reverse scan is collected after pre-biasing the solar cell. b) The initial state of perovskite absorber with uniformly distributed ions. c) Applied bias causes ion motion. d) As applied bias continues, ions accumulate at perovskite interfaces, screening the applied field.

2.4 Perovskite Solar Cell Stability

Now that the power conversion efficiency of PSC is approaching that of conventional photovoltaic technologies, the long-term stability of PSC must be improved to ensure the commercial success that will be vital for reducing greenhouse gas emissions. Initial PSC lost 80% of their efficiency after just 10 minutes of operation due to dissolution in the electrolyte solution adopted from dye sensitized solar cells.[38] In the past decade, the switch to bulk perovskite absorber films with no electrolyte, improved understanding of degradation mechanisms, and the use of more stable contacts and electrode materials have all greatly improved the lifetime of PSC. As Chapter 8 demonstrates, PSC can now retain their initial PCE even after four months

at 85 °C (under N_2 gas). However, the limited stability of PSC remains an issue since commercial Si solar cells can operate for decades before their PCE degrades to 80% of its initial value. Aside from the transparent conducting oxide (TCO), rapid degradation pathways can arise at every layer in the PSC device stack. The perovskite absorber is sensitive to atmospheric effects including light, heat, oxygen, and moisture. Hole transport materials are typically organic molecules that require the use of unstable dopants. Electron transport materials, typically metal oxides, suffer from UV-induced degradation or thermally accelerated chemical reactions at the metal oxide-perovskite interface. Finally, metal electrodes can react with chemical species originating from the perovskite bulk, or diffuse into the device stack, creating short circuit paths. Each of these degradation mechanisms and methods for mitigating them will be discussed in more detail below.

2.4.1 Degradation Mechanisms for Perovskite Absorbers

First, the stability considerations associated with bandgap tuning of metal halide perovskites will be considered. The archetypal perovskite, $MAPbI_3$, has a bandgap of 1.5-1.6 eV[39] and can be tuned to as low as 1.15 eV by alloying Pb^{2+} and Sn^{2+} cations,[40] or increased to about 2.3 eV by substituting I^- with Br^-.[41] The low bandgap mixed Pb-Sn materials are desirable for single-junction solar cells as the ~1.55 eV bandgap of $MAPbI_3$ is larger than ideal for achieving peak theoretical single junction efficiency. However, the Sn^{2+} cation is environmentally unstable and rapidly oxidizes to Sn^{4+} upon exposure to oxygen. The oxidation to Sn^{4+} results in self-doping through an increased hole concentration which degrades photovoltaic performance by reducing the diffusion length of free electrons. While additives such as SnF_2 have been incorporated as reducing agents to mitigate this instability, the Sn-based perovskites are still much less environmentally stable than their Pb counterparts.[42]

Turning to the wider gap perovskites, the bandgap can be continuously increased up to 2.3 eV (for neat Br^-) by increasing the fraction of the Br^- anion,[43] which

is promising for applications including multi-junction solar cells and light-emitting diodes. The challenge with bandgap tuning through anion substitution is reversible, illumination-dependent phase segregation whereby lower gap I^- rich regions form, acting as trapping sites and reducing V_{oc}.[44] A variety of models have been proposed to explain this behavior, including one description of the mixed halide perovskite as a metastable state that phase segregates due to a miscibility gap. An alternative explanation describes an illumination dependent change in the entropy of mixing driven by free carrier coupling to the lattice.[45] In the latter model, replacing the MA cation with Cs/FA blends is expected to reduce carrier coupling to the lattice and make the mixed halide phase more thermodynamically preferable. While this approach has greatly reduced the rate of phase segregation, it has not eliminated it.[46]

With respect to heat induced degradation, $MAPbI_3$ has a low enthalpy of formation, just 0.1 eV per formula unit, which allows a reversible, endothermic transition back to the constituent components MAI and PbI_2.[47] $MAPbI_3$ can also decompose via the following reaction:

$$CH_3NH_3PbI_3(s) \longleftrightarrow CH_3NH_2(g) + HI(g) + PbI_2(s)$$

While this process is reversible, methylamine and hydriodic acid exist as a gas at room temperature and can evaporate before being reincorporated into a perovskite phase. $MAPbI_3$ is stable at room temperature and under N_2 for at least 15 months, but at elevated temperatures and in ambient atmosphere the material substantially degrades on a time scale of a few hours due to instabilities related to oxygen and moisture.[48] In the presence of oxygen, photoexcited electrons can transfer to O_2, forming the superoxide O_2^-. The superoxide may then deprotonate the organic cation, forming H_2O and generating volatile methylamine in the process.[49,50]

H_2O, whether generated after incorporation of oxygen or chemisorbed at a surface through exposure to humidity, plays a catalytic role throughout the degradation process, and numerous intermediate H_2O-driven reaction steps have been proposed.[51] The hydration process is reversible at early stages through exposure to dry air, but irreversible at later stages as increasing quantities of PbI_2 may be phase segregated at

the grain boundaries of hydrate crystals.[52] Moisture induced degradation has severe consequences for device performance, and in one study PSC stored at 90% humidity lost all of their power conversion efficiency within one week.[53]

2.4.2 Degradation Mechanisms for Hole Transport Materials

Organic hole transport materials are commonly used in PSC, but their low conductivity results in poor fill factors until molecular dopants are introduced, often improving their conductivity by orders of magnitude. 2,2,7,7-tetrakis(N,N-di-p-methoxyphenylamine)-9,9-spirobifluorene (spiro-OMeTAD) is the most commonly used hole transport material (HTM) for n-i-p PSC, and is typically doped with lithium bis(trifluoromethanesulfonyl)imide (Li-TFSI) and tert-butylpyridine (tBP) to achieve best performance. For example, doping with 10 mol percent Li-TFSI improves the conductivity of Spiro-OMeTAD by two orders of magnitude, to around 10^{-5} S cm^{-1}, and also improves the fill factor of solar cells from around 0.3 to 0.8.[54] Unfortunately, Li-TFSI is hygroscopic, and moisture adsorption accelerates perovskite decomposition, as discussed previously. Spiro-OMeTAD films are also exposed to dry air for several hours after deposition to allow the metal cation (Li^+) to form O_2 complexes, which are required for doping under this approach, yet O_2 exposure also risks damaging the perovskite absorber.[55] Morphological and electronic benefits are provided by tBP, which inhibits phase segregation of Li-TFSI and Spiro-OMeTAD and may p-dope the perovskite surface, resulting in favorable band bending and improved charge extraction.[37,56] This improved performance from the tBP additive comes at the cost of long-term stability as tBP is volatile; gradual evaporation leaves pinholes in the HTM which, aside from inhibiting charge extraction, allow for the ingress of moisture and oxygen and accelerate the hydration of Li-TFSI.[57]

The limited stability of tBP and Li-TFSI have motivated a search for alternative dopants that ideally provide strong oxidation of the host material, generate inert or beneficial byproducts, allow stable and efficient devices, and can be synthesized

at low cost.[58] Thus far, a variety of alternative dopants have been tested including ionic liquids, lewis-acids, metal-based salts, and tetracyanoquinodimethane derivatives. Many of these approaches have allowed for PSC with longer device lifetimes, but PSC with the highest efficiencies have continued to utilize Spiro-OMeTAD with Li-TFSI and tBP.[59] Aside from the common use of unstable dopants with Spiro-OMeTAD, another difficulty for this material is its high cost due to the extensive purification required, and a low-cost alternative with improved performance and stability is the subject of Chapter 7.

One recent solution to the stability problems posed by Li-TFSI and tBP bypassed dopants altogether by employing a thin interlayer of n-hexyl trimethyl ammonium bromide (HTAB) between the perovskite absorber and a poly(3-hexylthiophene) (P3HT) HTM. While the mobility of amorphous P3HT is low (10^{-5} cm^2 V^{-1} s^{-1}), mobility along aligned chains of P3HT can reach 0.1 cm^2 V^{-1} s^{-1}. In this study, the alkyl chain of the HTAB interlayer promoted P3HT alignment perpendicular to the substrate, and devices reached a PCE of 23.3% with excellent environmental stability.[60] However, stability was only tested at room temperature, and it is not yet known how the elevated temperatures typical of operating conditions will affect device performance.

Relatively thick layers of HTM are required in the n-i-p architecture to prevent shunt pathways that form when evaporated electrodes metals fill pinholes in the HTM. In p-i-n devices the metal contact is adjacent to the n-type layer, allowing for a much thinner HTM. In contrast to the typically 200 nm thick layer of spiro-OMeTAD, in p-i-n devices the HTM can be under 10 nm. This much thinner HTM layer permits reasonable fill factors even for undoped HTMs in p-i-n devices. Chapter 8 utilizes a thin, undoped HTM in a p-i-n architecture to dramatically improve long-term stability relative to n-i-p devices while also achieving a power conversion efficiency of about 19%.

Finally, inorganic HTMs have been less commonly used in organic PSCs but offer low-cost and high conductivity without the need for unstable dopants. CuSCN, NiO_x,

and MoS_2 appear to be the most promising inorganic materials for PSC, and while they have not matched the performance of devices with the best organic HTM, these inorganic materials have all achieved PCE of about 20%.[61] Given this performance and the potential stability benefits of inorganic HTMs, it is somewhat surprising that they have not been more widely adopted within the research community, and a few possible explanations for the limited adoption are discussed here. In the case of CuSCN, despite a reported device stability improvement relative to doped spiro-OMeTAD,[62] there is still an unreported thermal instability as perovskite films in contact with CuSCN will severely discolor after aging at 85 °C. NiO_x is, by multiple anecdotal reports, highly sensitive to ambient humidity and thus device performance suffers from poor reproducibility. MoS_2 has only recently achieved high PCE, and the broader community may not yet be aware of this progress.[63,64] Since the bulk of research efforts with these materials have focused on closing the efficiency gap with organic HTMs, the relative device stability offered by these inorganic materials and any underlying degradation mechanisms have remained largely unexplored.

2.4.3 Degradation Mechanisms for Electron Transport Layers

The most commonly used metal oxide electron transport layers in PSC have been ZnO, TiO_2, and SnO_2, and each of these metal oxides has unique degradation processes in PSC. ZnO-perovskite interfaces suffer acid-base reactions that result in poor thermal stability and will be discussed in much greater detail in Chapter 5. TiO_2 displays accelerated UV-induced degradation in perovskite solar cells. In one study, a loss in photocurrent of more than 50% of the initial value was observed after aging under 1 sun for 5 hours.[65] This phenomenon can be explained through UV-induced defects at the TiO_2 surface. Oxygen vacancies at the TiO_2 surface form deep trap states, with energy around 1 eV below the conduction band minimum. During bandgap excitation of TiO_2 by UV light, a hole in the valence band can recombine with an electron at a defect site, desorbing molecular O_2. This leaves deep electron traps at the surface,

which may be responsible for the photocurrent loss in PSC. Finally, of the commonly used metal oxide n-types in PSC, SnO_2 offers the best operational stability. It does not suffer from the pronounced thermal instability of ZnO, or from the UV instability of TiO_2,[66] as its wider gap (3.8 eV compared to 3.2 eV for TiO_2) is transparent to most of the UV in the AM 1.5 spectrum.[67] The thermal stability of PSC with SnO_2 has been improved by inserting an organic small molecule at the SnO_2-perovskite interface, indicating that there is still a thermal instability although the mechanism is not understood.[68] Chapter 6 proposes degradation mechanisms that may occur at SnO_2-perovskite interfaces and demonstrates that the interface can be passivated with Cs salts.

2.4.4 Degradation Mechanisms for Electrodes

PSC's typically utilize thermally evaporated Au or Ag for electrodes, which offer high fill factors due to their conductivity. However, the diffusivity of Au and the formation of silver halides are important considerations for device stability. A Cr_2O_3 interlayer is one method for protecting metal contacts from these processes.[69] In one study, analysis of samples aged at 70 °C revealed substantial Au migration throughout the device stack, which can result in shunting pathways and reduced fill factor as well as trap states causing voltage losses.[70] A 10 nm layer of Cr thermally evaporated between the hole transport material and Au electrode was found to provide an effective diffusion barrier and greatly improved the stability of the PSCs, at the cost of reduced efficiency (from about 20% for Au to 13% with Cr-Au) due either to work function mismatch between the Cr and Au or the higher resistance of the Cr interlayer.

While Ag offers somewhat higher conductivity than Au and has substantially lower cost, x-ray photoelectron spectroscopy data shows the formation of AgI in PSC after 3 weeks of room temperature aging, both under N_2 and in ambient air.[71] Unlike Au electrodes, Ag was not found to diffuse through the device stack, rather species such as HI and MAI can diffuse from the perovskite absorber through charge selective contacts.

These species then corrode the Ag, forming AgI. There are severe consequences for device performance, and in one study devices with Ag electrodes had just half of their initial efficiency after 24 hours of aging at 85 °C.[72] Thin MoO_3 layers have been used between charge selective contacts and Ag or Al to form AgO_x or AlO_x interfaces that inhibit the diffusion of these reactive species into the metal electrode.[73] The most stable devices with these electrodes still degraded to around half of their initial performance after a few days under operating conditions, but it was unclear to what extent other processes resulted in this decay or whether the electrode degradation had been entirely mitigated.

In contrast to Au and Ag, conductive carbon electrodes are a low-cost alternative with superior stability, but device performance has been limited to about 15% efficiency due in part to limited fill factors.[74,75] Cu offers another lower-cost alternative to noble metal electrodes, and devices with Cu electrodes have achieved power conversion efficiencies slightly above 20%. Although Cu can be oxidized in the presence of moisture and oxygen, and also potentially react with the perovskite absorber, forming Cu halides, it appears to offer greater stability in PSC than Ag, Al, or Au.[76]

References

1. B. Lüssem, M. Riede, and K. Leo, "Doping of organic semiconductors," in *Physics of Organic Semiconductors*, pp. 425–496, Wiley-VCH Verlag GmbH & Co. KGaA, jan 2013.
2. M. Hiramoto, M. Kikuchi, and S. Izawa, "Parts-per-million-level doping effects in organic semiconductor films and organic single crystals," *Advanced Materials*, vol. 31, p. 1801236, aug 2018.
3. H. J. Snaith and M. Grätzel, "Enhanced charge mobility in a molecular hole transporter via addition of redox inactive ionic dopant: Implication to dye-sensitized solar cells," *Applied Physics Letters*, vol. 89, p. 262114, dec 2006.
4. V. I. Arkhipov, P. Heremans, E. V. Emelianova, and H. Bässler, "Effect of doping on the density-of-states distribution and carrier hopping in disordered organic semiconductors," *Physical Review B*, vol. 71, jan 2005.
5. K. Seeger, *Semiconductor Physics*. Springer Berlin Heidelberg, 2002.
6. M. A. Green, "Improved value for the silicon free exciton binding energy," *AIP Advances*, vol. 3, p. 112104, nov 2013.
7. Y. Sudhakar, M. Selvakumar, and D. K. Bhat, "Biopolymer electrolytes for solar cells and electrochemical cells," in *Biopolymer Electrolytes*, pp. 117–149, Elsevier, 2018.
8. P. Würfel, "Thermodynamic limitations to solar energy conversion," *Physica E: Low-dimensional Systems and Nanostructures*, vol. 14, pp. 18–26, apr 2002.
9. C. Battaglia, A. Cuevas, and S. D. Wolf, "High-efficiency crystalline silicon solar cells: status and perspectives," *Energy & Environmental Science*, vol. 9, no. 5, pp. 1552–1576, 2016.
10. W. Shockley and H. J. Queisser, "Detailed balance limit of efficiency of p-n junction solar cells," *Journal of Applied Physics*, vol. 32, pp. 510–519, mar 1961.
11. T. Tiedje, E. Yablonovitch, G. Cody, and B. Brooks, "Limiting efficiency of silicon solar cells," *IEEE Transactions on Electron Devices*, vol. 31, pp. 711–716, may 1984.
12. O. E. Semonin, J. M. Luther, S. Choi, H.-Y. Chen, J. Gao, A. J. Nozik, and M. C. Beard, "Peak external photocurrent quantum efficiency exceeding 100% via MEG in a quantum dot solar cell," *Science*, vol. 334, pp. 1530–1533, dec 2011.
13. M. A. Green, "Solar cell fill factors: General graph and empirical expressions," *Solid-State Electronics*, vol. 24, pp. 788–789, aug 1981.

14. P. K. Nayak, S. Mahesh, H. J. Snaith, and D. Cahen, "Photovoltaic solar cell technologies: analysing the state of the art," *Nature Reviews Materials*, vol. 4, pp. 269–285, mar 2019.

15. S. Hong, J. Lee, H. Kang, G. Kim, S. Kee, J.-H. Lee, S. Jung, B. Park, S. Kim, H. Back, K. Yu, and K. Lee, "High-efficiency large-area perovskite photovoltaic modules achieved via electrochemically assembled metal-filamentary nanoelectrodes," *Science Advances*, vol. 4, p. eaat3604, aug 2018.

16. NREL, "Best research-cell efficiencies." `http://www.nrel.gov/ncpv/images/efficiency_chart.jpg`. Accessed Oct 6, 2019.

17. M. D. Graef and M. E. McHenry, "Symmetry in crystallography," in *Structure of Materials*, pp. 152–192, Cambridge University Press.

18. O. Tschauner, C. Ma, J. R. Beckett, C. Prescher, V. B. Prakapenka, and G. R. Rossman, "Discovery of bridgmanite, the most abundant mineral in earth, in a shocked meteorite," *Science*, vol. 346, pp. 1100–1102, nov 2014.

19. M. Hundley, J. Thompson, and G. Kwei, "Specific heat of the cubic high-tc superconductor ba0·6k0·4bio3," *Solid State Communications*, vol. 70, pp. 1155–1158, jun 1989.

20. S. Mathews, "Ferroelectric field effect transistor based on epitaxial perovskite heterostructures," *Science*, vol. 276, pp. 238–240, apr 1997.

21. Y. Tokura, Y. Tomioka, H. Kuwahara, A. Asamitsu, Y. Moritomo, and M. Kasai, "Origins of colossal magnetoresistance in perovskite-type manganese oxides (invited)," *Journal of Applied Physics*, vol. 79, no. 8, p. 5288, 1996.

22. M. R. Filip and F. Giustino, "The geometric blueprint of perovskites," *Proceedings of the National Academy of Sciences*, vol. 115, pp. 5397–5402, may 2018.

23. T. Sato, S. Takagi, S. Deledda, B. C. Hauback, and S. ichi Orimo, "Extending the applicability of the goldschmidt tolerance factor to arbitrary ionic compounds," *Scientific Reports*, vol. 6, apr 2016.

24. C. J. Bartel, C. Sutton, B. R. Goldsmith, R. Ouyang, C. B. Musgrave, L. M. Ghiringhelli, and M. Scheffler, "New tolerance factor to predict the stability of perovskite oxides and halides," *Science Advances*, vol. 5, p. eaav0693, feb 2019.

25. B. Saparov and D. B. Mitzi, "Organic–inorganic perovskites: Structural versatility for functional materials design," *Chemical Reviews*, vol. 116, pp. 4558–4596, apr 2016.

26. C. C. Stoumpos and M. G. Kanatzidis, "ChemInform abstract: Halide perovskites: Poor man/s high-performance semiconductors," *ChemInform*, vol. 47, aug 2016.

27. A. Kojima, K. Teshima, Y. Shirai, and T. Miyasaka, "Organometal halide perovskites as visible-light sensitizers for photovoltaic cells," *Journal of the American Chemical Society*, vol. 131, p. 6050–6051, Jun 2009.

28. M. M. Lee, J. Teuscher, T. Miyasaka, T. N. Murakami, and H. J. Snaith, "Efficient hybrid solar cells based on meso-superstructured organometal halide perovskites," *Science*, vol. 338, pp. 643–647, oct 2012.

29. Z. Xiao and Y. Yan, "Progress in theoretical study of metal halide perovskite solar cell materials," *Advanced Energy Materials*, vol. 7, p. 1701136, aug 2017.

30. G. Xing, N. Mathews, S. Sun, S. S. Lim, Y. M. Lam, M. Gratzel, S. Mhaisalkar, and T. C. Sum, "Long-range balanced electron- and hole-transport lengths in organic-inorganic CH3nh3pbi3," *Science*, vol. 342, pp. 344–347, oct 2013.

31. S. D. Stranks, G. E. Eperon, G. Grancini, C. Menelaou, M. J. P. Alcocer, T. Leijtens, L. M. Herz, A. Petrozza, and H. J. Snaith, "Electron-hole diffusion lengths exceeding 1 micrometer in an organometal trihalide perovskite absorber," *Science*, vol. 342, pp. 341–344, oct 2013.

32. C. Ran, J. Xu, W. Gao, C. Huang, and S. Dou, "Defects in metal triiodide perovskite materials towards high-performance solar cells: origin, impact, characterization, and engineering," *Chemical Society Reviews*, vol. 47, no. 12, pp. 4581–4610, 2018.

33. D. Han, C. Dai, and S. Chen, "Calculation studies on point defects in perovskite solar cells," *Journal of Semiconductors*, vol. 38, p. 011006, jan 2017.

34. W.-J. Yin, T. Shi, and Y. Yan, "Unusual defect physics in CH3nh3pbi3 perovskite solar cell absorber," *Applied Physics Letters*, vol. 104, p. 063903, feb 2014.

35. J. M. Ball and A. Petrozza, "Defects in perovskite-halides and their effects in solar cells," *Nature Energy*, vol. 1, oct 2016.

36. C. Eames, J. M. Frost, P. R. F. Barnes, B. C. O'Regan, A. Walsh, and M. S. Islam, "Ionic transport in hybrid lead iodide perovskite solar cells," *Nature Communications*, vol. 6, jun 2015.

37. S. N. Habisreutinger, N. K. Noel, H. J. Snaith, and R. J. Nicholas, "Investigating the role of 4-tertbutylpyridine in perovskite solar cells," *Advanced Energy Materials*, vol. 7, p. 1601079, Aug 2016.

38. J.-H. Im, C.-R. Lee, J.-W. Lee, S.-W. Park, and N.-G. Park, "6.5% efficient perovskite quantum-dot-sensitized solar cell," *Nanoscale*, vol. 3, no. 10, p. 4088, 2011.

39. A. M. A. Leguy, P. Azarhoosh, M. I. Alonso, M. Campoy-Quiles, O. J. Weber, J. Yao, D. Bryant, M. T. Weller, J. Nelson, A. Walsh, and et al., "Experimental and theoretical optical properties of methylammonium lead halide perovskites," *Nanoscale*, vol. 8, no. 12, p. 6317–6327, 2016.

40. F. Hao, C. C. Stoumpos, R. P. H. Chang, and M. G. Kanatzidis, "Anomalous band gap behavior in mixed sn and pb perovskites enables broadening of absorption spectrum in solar cells," *Journal of the American Chemical Society*, vol. 136, no. 22, p. 8094–8099, 2014.

41. N. K. Noel, B. Wenger, S. N. Habisreutinger, J. B. Patel, T. Crothers, Z. Wang, R. J. Nicholas, M. B. Johnston, L. M. Herz, H. J. Snaith, and et al., "Highly crystalline methylammonium lead tribromide perovskite films for efficient photovoltaic devices," *ACS Energy Letters*, vol. 3, no. 6, p. 1233–1240, 2018.

42. S. Shao, J. Liu, G. Portale, H.-H. Fang, G. R. Blake, G. H. T. Brink, L. J. A. Koster, and M. A. Loi, "Highly reproducible sn-based hybrid perovskite solar cells with 9p. 1702019, 2017.

43. R. J. Sutton, G. E. Eperon, L. Miranda, E. S. Parrott, B. A. Kamino, J. B. Patel, M. T. Hörantner, M. B. Johnston, A. A. Haghighirad, D. T. Moore, and et al., "Bandgap-tunable cesium lead halide perovskites with high thermal stability for efficient solar cells," *Advanced Energy Materials*, vol. 6, p. 1502458, Feb 2016.

44. M. C. Brennan, S. Draguta, P. V. Kamat, and M. Kuno, "Light-induced anion phase segregation in mixed halide perovskites," *ACS Energy Letters*, vol. 3, no. 1, p. 204–213, 2017.

45. M. C. Brennan, S. Draguta, P. V. Kamat, and M. Kuno, "Light-induced anion phase segregation in mixed halide perovskites," *ACS Energy Letters*, vol. 3, no. 1, p. 204–213, 2017.

46. K. A. Bush, K. Frohna, R. Prasanna, R. E. Beal, T. Leijtens, S. A. Swifter, and M. D. Mcgehee, "Compositional engineering for efficient wide band gap perovskites with improved stability to photoinduced phase segregation," *ACS Energy Letters*, vol. 3, no. 2, p. 428–435, 2018.

47. J. A. Mcleod and L. Liu, "Prospects for mitigating intrinsic organic decomposition in methylammonium lead triiodide perovskite," *The Journal of Physical Chemistry Letters*, vol. 9, no. 9, p. 2411–2417, 2018.

48. I. Deretzis, E. Smecca, G. Mannino, A. L. Magna, T. Miyasaka, and A. Alberti, "Stability and degradation in hybrid perovskites: Is the glass half-empty or half-full?," *The Journal of Physical Chemistry Letters*, vol. 9, no. 11, p. 3000–3007, 2018.

49. A. Senocrate, T. Acartürk, G. Y. Kim, R. Merkle, U. Starke, M. Grätzel, and J. Maier, "Interaction of oxygen with halide perovskites," *Journal of Materials Chemistry A*, vol. 6, no. 23, p. 10847–10855, 2018.

50. N. Aristidou, I. Sanchez-Molina, T. Chotchuangchutchaval, M. Brown, L. Martinez, T. Rath, and S. A. Haque, "The role of oxygen in the degradation of methylammonium lead trihalide perovskite photoactive layers," *Angewandte Chemie International Edition*, vol. 54, no. 28, p. 8208–8212, 2015.

51. J. Huang, S. Tan, P. D. Lund, and H. Zhou, "Impact of h2o on organic–inorganic hybrid perovskite solar cells," *Energy Environmental Science*, vol. 10, no. 11, p. 2284–2311, 2017.

52. A. M. A. Leguy, Y. Hu, M. Campoy-Quiles, M. I. Alonso, O. J. Weber, P. Azarhoosh, M. V. Schilfgaarde, M. T. Weller, T. Bein, J. Nelson, and et al., "Reversible hydration of ch3nh3pbi3in films, single crystals, and solar cells," *Chemistry of Materials*, vol. 27, no. 9, p. 3397–3407, 2015.

53. D. P. Kamat, S. G. Tilve, V. P. Kamat, and J. K. Kirtany, "ChemInform abstract: Syntheses and biological activities of chroman-2-ones. a review," *ChemInform*, vol. 46, pp. no–no, apr 2015.

54. A. Abate, T. Leijtens, S. Pathak, J. Teuscher, R. Avolio, M. E. Errico, J. Kirkpatrik, J. M. Ball, P. Docampo, I. McPherson, and H. J. Snaith, "Lithium salts as "redox active" p-type dopants for organic semiconductors and their impact in solid-state dye-sensitized solar cells," *Physical Chemistry Chemical Physics*, vol. 15, no. 7, p. 2572, 2013.

55. A. Abate, T. Leijtens, S. Pathak, J. Teuscher, R. Avolio, M. E. Errico, J. Kirkpatrik, J. M. Ball, P. Docampo, I. Mcpherson, and et al., "Lithium salts as "redox active" p-type dopants for organic semiconductors and their impact in solid-state dye-sensitized solar cells," *Physical Chemistry Chemical Physics*, vol. 15, no. 7, p. 2572, 2013.

56. E. J. Juarez-Perez, M. R. Leyden, S. Wang, L. K. Ono, Z. Hawash, and Y. Qi, "Role of the dopants on the morphological and transport properties of spiro-MeOTAD hole transport layer," *Chemistry of Materials*, vol. 28, pp. 5702–5709, aug 2016.

57. Z. Wang, Q. Lin, F. P. Chmiel, N. Sakai, L. M. Herz, and H. J. Snaith, "Efficient ambient-air-stable solar cells with 2d–3d heterostructured butylammonium-caesium-formamidinium lead halide perovskites," *Nature Energy*, vol. 2, aug 2017.

58. T. H. Schloemer, J. A. Christians, J. M. Luther, and A. Sellinger, "Doping strategies for small molecule organic hole-transport materials: impacts on perovskite solar cell performance and stability," *Chemical Science*, vol. 10, no. 7, p. 1904–1935, 2019.

59. Q. Jiang, Y. Zhao, X. Zhang, X. Yang, Y. Chen, Z. Chu, Q. Ye, X. Li, Z. Yin, J. You, and et al., "Surface passivation of perovskite film for efficient solar cells," *Nature Photonics*, vol. 13, p. 460–466, Jan 2019.

60. E. H. Jung, N. J. Jeon, E. Y. Park, C. S. Moon, T. J. Shin, T.-Y. Yang, J. H. Noh, and J. Seo, "Efficient, stable and scalable perovskite solar cells using poly(3-hexylthiophene)," *Nature*, vol. 567, no. 7749, p. 511–515, 2019.

61. R. Singh, P. K. Singh, B. Bhattacharya, and H.-W. Rhee, "Review of current progress in inorganic hole-transport materials for perovskite solar cells," *Applied Materials Today*, vol. 14, p. 175–200, 2019.

62. N. Arora, M. I. Dar, A. Hinderhofer, N. Pellet, F. Schreiber, S. M. Zakeeruddin, and M. Grätzel, "Perovskite solar cells with cuscn hole extraction layers yield stabilized efficiencies greater than 20Science
, vol. 358, no. 6364, p. 768–771, 2017.

63. S. Kohnehpoushi, P. Nazari, B. A. Nejand, and M. Eskandari, "Mos2: a two-dimensional hole-transporting material for high-efficiency, low-cost perovskite solar cells," *Nanotechnology*,

vol. 29, no. 20, p. 205201, 2018.

64. L. Najafi, B. Taheri, B. Martín-García, S. Bellani, D. D. Girolamo, A. Agresti, R. Oropesa-Nuñez, S. Pescetelli, L. Vesce, E. Calabrò, and et al., "Mos2 quantum dot/graphene hybrids for advanced interface engineering of a ch3nh3pbi3 perovskite solar cell with an efficiency of over 20

65. T. Leijtens, G. E. Eperon, S. Pathak, A. Abate, M. M. Lee, and H. J. Snaith, "Overcoming ultraviolet light instability of sensitized TiO2 with meso-superstructured organometal tri-halide perovskite solar cells," *Nature Communications*, vol. 4, dec 2013.

66. J. A. Christians, P. Schulz, J. S. Tinkham, T. H. Schloemer, S. P. Harvey, B. J. T. D. Villers, A. Sellinger, J. J. Berry, and J. M. Luther, "Tailored interfaces of unencapsulated perovskite solar cells for >1,000 hour operational stability," *Nature Energy*, vol. 3, no. 1, p. 68–74, 2018.

67. P. Tiwana, P. Docampo, M. B. Johnston, H. J. Snaith, and L. M. Herz, "Electron mobility and injection dynamics in mesoporous zno, sno2, and tio2 films used in dye-sensitized solar cells," *ACS Nano*, vol. 5, no. 6, p. 5158–5166, 2011.

68. K. Choi, J. Lee, H. I. Kim, C. W. Park, G.-W. Kim, H. Choi, S. Park, S. A. Park, and T. Park, "Thermally stable, planar hybrid perovskite solar cells with high efficiency," *Energy Environmental Science*, vol. 11, no. 11, p. 3238–3247, 2018.

69. M. Kaltenbrunner, G. Adam, E. D. Głowacki, M. Drack, R. Schwödiauer, L. Leonat, D. H. Apaydin, H. Groiss, M. C. Scharber, M. S. White, N. S. Sariciftci, and S. Bauer, "Flexible high power-per-weight perovskite solar cells with chromium oxide–metal contacts for improved stability in air," *Nature Materials*, vol. 14, pp. 1032–1039, aug 2015.

70. K. Domanski, J.-P. Correa-Baena, N. Mine, M. K. Nazeeruddin, A. Abate, M. Saliba, W. Tress, A. Hagfeldt, and M. Grätzel, "Not all that glitters is gold: Metal-migration-induced degradation in perovskite solar cells," *ACS Nano*, vol. 10, pp. 6306–6314, may 2016.

71. Y. Kato, L. K. Ono, M. V. Lee, S. Wang, S. R. Raga, and Y. Qi, "Perovskite solar cells: Silver iodide formation in methyl ammonium lead iodide perovskite solar cells with silver top electrodes (adv. mater. interfaces 13/2015)," *Advanced Materials Interfaces*, vol. 2, pp. n/a–n/a, sep 2015.

72. P. Liu, B. Xu, Y. Hua, M. Cheng, K. Aitola, K. Sveinbjörnsson, J. Zhang, G. Boschloo, L. Sun, and L. Kloo, "Design, synthesis and application of a -conjugated, non-spiro molecular alternative as hole-transport material for highly efficient dye-sensitized solar cells and perovskite solar cells," *Journal of Power Sources*, vol. 344, pp. 11–14, mar 2017.

73. E. M. Sanehira, B. J. T. D. Villers, P. Schulz, M. O. Reese, S. Ferrere, K. Zhu, L. Y. Lin, J. J. Berry, and J. M. Luther, "Influence of electrode interfaces on the stability of perovskite solar cells: Reduced degradation using moox/al for hole collection," *ACS Energy Letters*, vol. 1, no. 1, p. 38–45, 2016.

74. Q. Luo, H. Ma, Q. Hou, Y. Li, J. Ren, X. Dai, Z. Yao, Y. Zhou, L. Xiang, H. Du, and et al., "All-carbon-electrode-based endurable flexible perovskite solar cells," *Advanced Functional Materials*, vol. 28, no. 11, p. 1706777, 2018.

75. H. Chen, Z. Wei, H. He, X. Zheng, K. S. Wong, and S. Yang, "Solvent engineering boosts the efficiency of paintable carbon-based perovskite solar cells to beyond 14p. 1502087, 2016.

76. J. Zhao, X. Zheng, Y. Deng, T. Li, Y. Shao, A. Gruverman, J. Shield, and J. Huang, "Is cu a stable electrode material in hybrid perovskite solar cells for a 30-year lifetime?," *Energy Environmental Science*, vol. 9, no. 12, p. 3650–3656, 2016.

CHAPTER 3

Experimental Methods

This chapter describes the materials, device fabrication steps, and characterization methods utilized in this thesis.

3.1 Device Fabrication

3.1.1 n-i-p devices

3.1.1.1 Substrate Cleaning

n-i-p devices were fabricated on top of fluorine-doped tin oxide (FTO) coated glass substrates (Pilkington TEC 7). Substrates were scrubbed with detergent (2% Hellmanex in water) and then sequentially sonicated for 2 min in acetone, isopropyl alcohol, and nanopure deionized water. The FTO was treated in oxygen plasma for 10 minutes.

3.1.1.2 Electron Transport Layers

SnO_2

Tin (IV) chloride pentahydrate was dissolved in isopropanol (17.5 mg ml^{-1}) and stirred for 30 minutes. The solution was spin-coated at 3000 rpm for 30 seconds (200 rpm s^{-1} ramp) onto the plasma cleaned FTO, and then dried at 100 °C for 10 minutes followed by 1 hour of annealing at 180 °C. Substrates were then placed in a chemical bath, consisting of H_2O (200 ml), urea (2.5 g), mercaptoproprionic acid (50 µl), HCl (2.5 ml), and tin (II) chloride dihydrate (540 mg), and left for 3 hours at 70 °C. Substrates were then sonicated for 2 minutes in MilliQ H2O and finally annealed at 180 °C for 1 hour. Finally, substrates were treated with UV ozone for 15 minutes immediately prior to perovskite deposition. A detailed description of the SnO_2 chemical bath route can be found elsewhere.[1]

TiO_2

Titania was prepared with a solution of ethanol (5 ml), DI water (125 µl), and HCl (37%, 30 µl). Titanium ethoxide (375 µl) was added dropwise while stirring. FTO substrates were spin-coated at 1,400 rpm for 30 s, dried at 115 °C for 10 minutes, and then annealed at 450 for 30 minutes.

ZnO

Zinc oxide powder (10 mg ml^{-1}) was dissolved in a solution of 50% ammonia hydroxide and 50% water by stirring for 3 hours. The solution was filtered with a 0.22 um PTFE syringe filter and then sonicated for 15 minutes before use. The zinc oxide solution was spin-coated at 4,000 rpm for 30 s (2,000 rpm s^{-1} ramp) and annealed at 120 °C for 30 minutes. The zinc oxide substrates were treated with UV ozone for 15 minutes prior to depositing the perovskite. A full detailed description of the ZnO processing route can be found elsewhere.[2]

Mesoporous Al_2O_3

The mesoporous Al_2O_3 layers were deposited by spin-coating solutions of commercial alumina nanoparticles dispersion (50 nm, Sigma-Aldrich) diluted at 1:20, 1:5, and 1:3 volume ratio of dispersion:isopropanol to give 50, 100, and 200 nm thicknesses.

3.1.1.3 Perovskite Absorber Layers

A solution of $FA_{0.83}Cs_{0.17}Pb(I_{0.83}Br_{0.17})_3$ precursor was prepared with cesium iodide (64.0 mg), lead bromide (103.8 mg), formamadinium iodide (207.0 mg), and lead iodide (538.2 mg). $Cs_{0.05}(FA_{0.83}Cs_{0.17})_{0.95}Pb(I_{0.83}Br_{0.17})_3$ was prepared by mixing CsI (18.8 mg), MAI (37.2 mg), $PbBr_2$ (116.0 mg), FAI (196.6 mg), and PbI_2 (522.8 mg). Precursors were dissolved in a solution of DMF and DMSO (in a 4 to 1 volume ratio and 1 ml volume) by stirring at 70 °C for 15 minutes. Precursor solution was spread onto substrates and spin coated at 1000 rpm for 10 s (1000 rpm s^{-1} ramp) followed immediately by 6000 rpm for 35 s (2000 rpm s^{-1} ramp). 10 seconds before the end of spin coating, the films were solvent quenched with 100 µl of anhydrous anisole. Substrates were annealed at 100 °C for 15 minutes. All spin coating occurred in a dry box at 10-20% relative humidity.

The $MAPbI_3$ was prepared in acetonitrile by adding PbI_2 (1.466 g) and methylammonium iodide (0.477 g) to acetonitrile (6 ml), and then bubbling the solution with methylamine for about 5 minutes until the solution turned from black and opaque to colorless and transparent. The detailed method can be found elsewhere.[3] The solution was dynamically dispensed onto substrates spinning at 2000 rpm for 35 s. Substrates were then annealed at 100 °C. A full description of the acetonitrile route can be found elsewhere.[3]

3.1.1.4 Hole Transport Layers

Spiro-OMeTAD (85 mg) was dissolved in anhydrous chlorobenzene (1 ml) along with 4-tertbutylpyridine (33 µl) and a solution of 500 mg ml^{-1} bis(trifluoromethane)-sulfonimide lithium salt in acetonitrile (20 µl). The spiro-OMeTAD layer was deposited by spin coating at 2000 rpm for 40 seconds, and devices were then left in a desiccator overnight for the Spiro-OMeTAD to oxidize.

NiO_x HTM was synthesized with a previously reported chemical-precipitation method.[4] The resulting NiO_x powder was dispersed in DI water at a concentration of 23 mg/mL concentration and spin-coated at 3000 rpm for 30 s with a 3 s ramp.

EDOT-Amide-TPA solution was prepared with 10 mg of EDOT in 800 µL anhydrous chlorobenzene and 200 µL chloroform along with 10 µL tBP and 20 µL Li-TFSI salt in acetonitrile (170 mg mL^1). The EDOT-Amide-TPA solution was heated for 5–10 min until the solution went completely transparent (∼85 °C), and then passed through a 0.22 µm polytetrafluoroethylene (PTFE) syringe filter while hot. The filtered solution was left on a hot plate at 75 °C while spin-coating. 50 µL EDOT-Amide-TPA solution was quickly dispensed onto the substrates while they were spinning at 1000 rpm for 40 s.

Electrode Evaporation

An Ag or Au electrode of 50-100 nm thickness was thermally evaporated under a vacuum of $< 9 \times 10^6$ Torr in an Edwards Nano36 evaporator.

3.1.2 p-i-n devices

PolyTPD and CL1-2 were stirred in toluene overnight at 85 °C at a concentration of 1 mg ml^{-1}. Doped PolyTPD was prepared with 20 weight percent F4-TCNQ. HTM's were spin-coated at 2k rpm for 20 seconds and then annealed at 130 °C for 10 minutes. CL1-2 was cross-linked under a UV lamp for 4 minutes.

Perovskite layers were prepared as described for n-i-p devices but at a slightly lower concentration of 1.3-1.4 M.

PCBM was dissolved in a 3:1 volume ratio of chlorobenzene:dichlorobenzene at 20 mg ml^{-1}, stirred overnight and filtered through a 0.22 um PTFE filter before use. PCBM was spin-coated at 2k rpm for 30 seconds, then annealed at 100 C for 5 minutes.

BCP was dissolved in isopropanol at a 0.5 mg ml^{-1} and stirred overnight at room temperature. BCP was spin-coated at 5k rpm for 30 seconds, followed by 1 minute of annealing at 100 °C.

Ag and Au electrodes were deposited as described for n-i-p devices. Cr-Au electrodes were prepared by thermally evaporating 3.5 nm of Cr followed by 100 nm of Au.

3.2 Characterization

3.2.1 Optical and Spectroscopic Characterization

3.2.1.1 Steady State Photoluminescence

Steady-state photoluminescence was measured using a Horiba Fluorolog-3 with an InGaAs detector. Samples were excited with a wavelength of approximately 150 nm less than the PL peak of the perovskite sample. In both steady state and time-resolved photoluminescence measurements, samples were prepared shortly ($<$ 1 hour) before measurement and then measured in ambient conditions.

3.2.1.2 Time-Resolved Photoluminescence Spectroscopy

Time-resolved photoluminescence spectroscopy (TRPL) is used to study carrier dynamics in photoluminescent materials by collecting time-dependent emission data. In this technique, the sample is perturbed from its equilibrium state by a laser pulse emitted at a fixed frequency, and a fast detector is used to record emission as a function of time after excitation. TRPL systems combine several elements, including a pulsed laser source, a triggering system, an optical path, light collecting optics, optical filters, and a detector, as shown schematically in Figure 3.1. Since temporal resolution on the scale of picoseconds is difficult to achieve with a conventional electronics and photodiodes, the sample emission is strongly attenuated before reaching the detector. The probability of collecting a photon at the detector is therefore low in any given collection interval, and a photo-multiplier tube amplifies the signal. The detector

collection frequency is typically 500 kHz to 1 MHz, which overcomes the low probability of single photon collection by building the signal histogram over a sampling period of minutes, a technique known as time-correlated single photon counting (TCSPC).

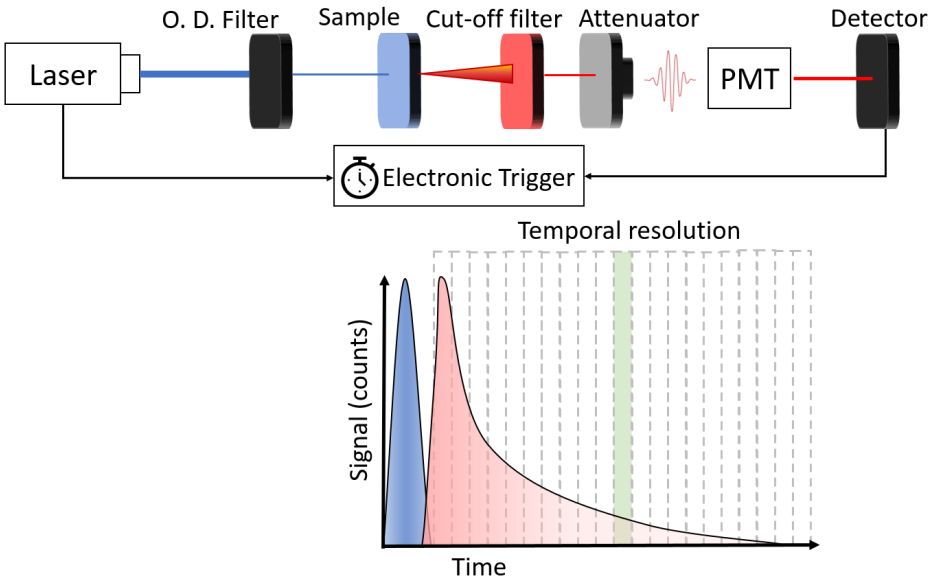

Figure 3.1: Schematic of the time-resolved photoluminescence spectroscopy characterization technique.

TRPL measurements were recorded using a time-correlated single photon counting (TCSPC) setup (FluoTime 300 PicoQuant GmbH). Perovskite film samples on metal oxides and glass were photoexcited with a 507 nm laser head (LDH-P-C-510, PicoQuant GmbH) at frequencies between 0.5 and 2 MHz with a pulse duration of 117 ps, a fluence of 0.3 $\mu J/cm^2$/pulse, and a detection wavelength set to the peak PL emission wavelength from the sample. Due to a small laser spot size and sample inhomogeneity, PL decays from three regions from perovskite films were collected and the most representative decay was presented. Time-dependent effects such as halide segregation and environmental instabilities were accounted for by monitoring the steady-state PL intensity of the perovskite film and waiting until it reached a stable value before collecting TRPL data. Stabilization times were typically from one to a few minutes.

TRPL decays were fitted with a stretched exponential (in Chapter 5) or a bi-exponential model (in Chapter 8). In the stretched exponential:

$$I(t) = exp\left[-\frac{(t-t_0)^\beta}{\tau}\right] \tag{3.1}$$

$I(t)$ is the PL intensity at time t, t_0 is an offset correction (constrained such that $0 \leq t_0 \leq 10$ ns, τ is the characteristic lifetime and β is the stretching exponent. The stretched exponential model is well established in literature, in lieu of a true analytical model.[5–7] The stretching of the exponential has been interpreted as resulting from a distribution of trap-assisted (monomolecular) non-radiative decay states within the material.[8] The mean relaxation time $< \tau >$ is given by:

$$< \tau >= \frac{\tau}{\beta}\Gamma\frac{1}{\beta} \tag{3.2}$$

where $\Gamma(z)$ is the gamma function:

$$\Gamma(z) = \int_0^\infty x^{z-1}e^{-x}dx \tag{3.3}$$

In Chapter 8, a bi-exponential rate law provided an improved fit to the TRPL data. The decay was modeled as:

$$Y = A_1 exp\frac{-t}{\tau_1} + A_2 exp\frac{-t}{\tau_2} + y_0 \tag{3.4}$$

where τ_1 is the lifetime for fast, trap-assisted processes (Shockley-Read-Hall recombination), τ_2 is the lifetime for slower, bi-molecular recombination, and A_1 and A_2 are the relative amplitudes.[9]

3.2.1.3 UV Vis Absorption, Transmittance, and Reflectivity

Absorption spectra were collected with a Varian Cary 1050 UV Vis spectrophotometer.

3.2.1.4 Fourier-Transform Infrared Spectroscopy

ZnO and perovskite films were deposited on single crystal silicon wafers. Spectra were measured with the samples in ambient atmosphere using a Thermo Nicolet iS5 FTIR Spectrometer, with reference to the bare Si background.

3.2.1.5 Time-Resolved Microwave Conductivity

FAMACs films with and without the HTM layer on top were spin-coated on quartz substrates using the same procedure as for the solar cell devices. The thin films on quartz substrates were placed in a sealed microwave cell inside an N_2-filled glovebox. The TRMC technique was used to measure the change in microwave (8.5 GHz) power after pulsed excitation (repetition rate 10 Hz) of the samples at different excitation wavelengths. The bilayers were illuminated from the front side (through the HTM layer) or the backside. For bilayers comprising EDOT-Amide-TPA that were excited through the HTM, the intensity has been corrected for the parasitic absorption of the HTM at 430 nm. TRMC measurments in Chapter 7 were made by Eline Hutter.

3.2.1.6 X-ray Photoelectron Spectroscopy

Photoemission spectroscopy data were collected with a Thermo Scientific K-Alpha+ system. The samples were measured using an Al Kα X-ray source. The measurements were conducted at room temperature and a takeoff angle of 90° with respect to the surface parallel. The core level spectra were recorded using a pass energy of 20 eV (resolution approximately 0.4 eV) from an analysis area of 400 µm $\times$ 400 µm. The spectrometer work function and binding energy scale were calibrated using the Fermi edge and 3d5/2 peak recorded from a polycrystalline Ag sample prior to the commencement of the experiments. Fitting procedures to extract peaks positions from the XPS data were carried out using the Casa XPS software suite. MAI and FAI were dissolved in DMF (5 mg ml^{-1}), spin-coated onto ZnO-glass substrates at 4k rpm for 30 seconds, and annealed at 100 °C for 1, 5, 15, and 30 minutes.

3.2.2 Material Characterization

3.2.2.1 Scanning Electron Microscopy

Cross-sectional images were acquired with an FEI Quanta 600 scanning electron microscope at 10 kV acceleration voltage. Images of film surfaces were acquired with a 5 kV acceleration voltage.

3.2.2.2 X-ray Diffraction

XRD patterns were obtained with a Panalytical X'Pert Pro X-ray diffractometer with a Cu source (λ 1.54 Å).

3.2.2.3 Atomic Force Microscopy

Scanned probe measurements were carried out using an Asylum MFP3D (Asylum Research and Oxford Instruments Co.) in AC (tapping) mode. Olympus AC240-TS silicon tips were used for topography measurements.

3.2.2.4 Kelvin Probe

Kelvin Probe is used to measure the work function of materials. The working principle of the Kelvin Probe is depicted in Figure 3.2.[10] Consider two initially isolated materials, a sample and a probe, with different work functions (Figure 3.2a). When these materials are short circuited (Figure 3.2b), electrons flow from the sample to the probe, since the work function of the probe is larger than that of the sample, thereby equilibrating the Fermi levels. The charge transfer causes the system to function as a parallel plate capacitor, establishing an electric field and a drop in the local vacuum level across the gap. The potential energy drop is simply equal to the difference in work function of the sample and probe, and is commonly referred to as the contact potential difference (CPD). In modern Kelvin Probe systems a vibrating probe creates an AC capacitance between the sample and probe, producing an AC current in the

external circuit. Applying a bias that is equal and opposite to the CPD aligns the probe and sample vacuum levels, discharging the capacitor, as in Figure 3.2c. The CPD is determined when the AC current is zero.

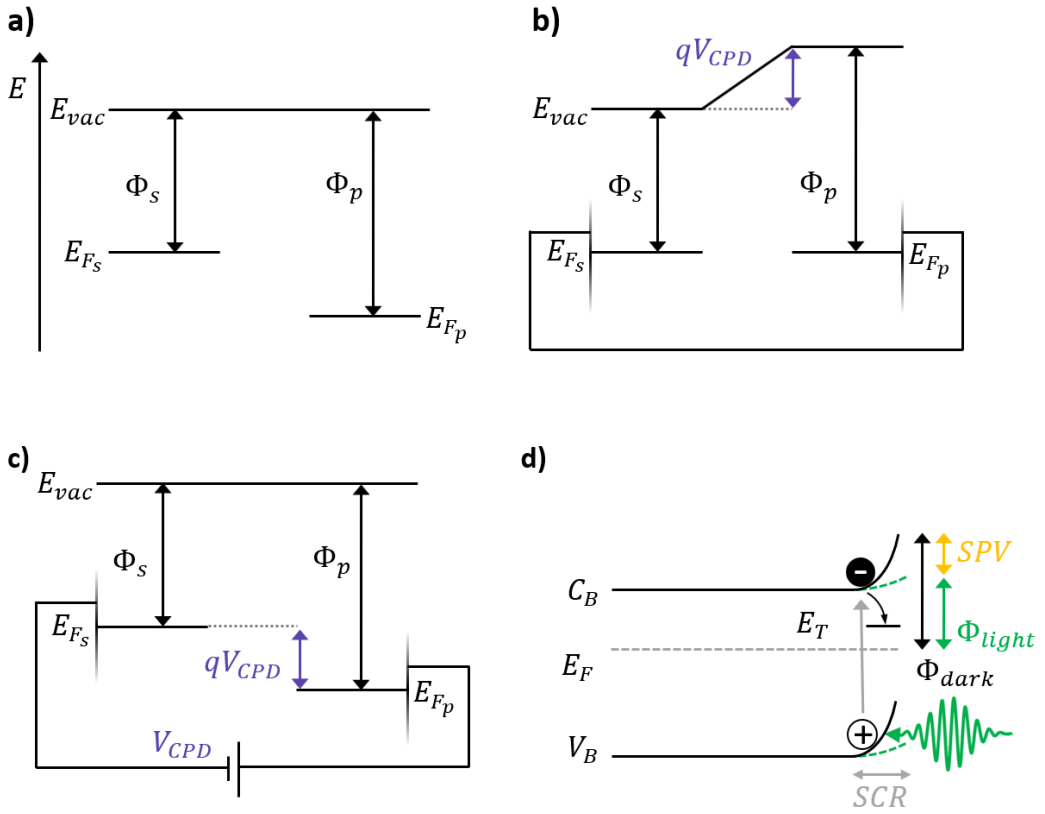

Figure 3.2: a) Isolated sample and probe with varying work functions. b) Short-circuited sample and probe. c) Sample and probe connected with a bias that is equal and opposite to the contact potential difference. d) Surface photovoltage arising from the difference in band bending under dark (black bands) and supra-bandgap illumination (green bands). a-c adapted with permission.[10]

Kelvin Probe can also be used to characterize the surface photovoltage of semiconductors and assess the contribution to V_{oc} from buried interfaces in solar cells. Semiconductor surfaces typically have a higher density of trap states than the bulk; the termination of the periodic structure of the crystal results in dangling bonds, defects, and impurities adsorbed at the surface. The accumulation of either holes or electrons in surface trap states gives rise to a space charge region, where the built-in field depletes mobile carriers near the surface. At a depleted n-type semiconductor surface, the majority carrier is trapped in surface states and the electron density near

the surface is lower than in the bulk, but still greater than the minority carrier density. This results in upward band bending, with electrons being repelled from the surface by trapped charge while holes are attracted to the surface. The surface photovoltage (SPV) manifests as a change in band bending from the dark to illuminated state.[11]

In Figure 3.2d, an n-type semiconductor with electron surface traps is depicted to demonstrate the origin of the surface photovoltage. Under moderate illumination, photogenerated holes drift to the surface and screen trapped electron charge, reducing the magnitude of band bending as shown.[12] Under higher illumination intensity, if the photogenerated hole density at the surface matches the trapped electron density a flat band condition can be achieved. Provided that optical absorption occurs at the interface of interest, SPV measured from the surface can also be used as a probe for buried interfaces.[10] Considering two buried n-type selective contacts, the contact with more efficient carrier separation allows a greater fraction of photogenerated holes to reach the perovskite surface, decreasing the band bending and thus increasing the magnitude of the SPV.

The magnitude of the SPV in "full stack" Si and organic solar cells is linearly correlated to the V_{oc} of the device, allowing quantitative prediction of the V_{oc} from this non-contact method.[13,14]. Additionally, since SPV is sensitive to buried interfaces, it is a useful method to assess the relative quality of interfaces throughout a solar cell fabrication process, and SPV has also been used for assessing the V_{oc} contribution from buried interfaces in Cu(In,Ga)Se_2 (CIGS) and perovskite thin film solar cells.[15,16]

Surface photovoltage measurements in this thesis were collected with the Kelvin Probe system SKP5050. One limitation of this Kelvin Probe system is the lack of a spectrally resolved light source that can unambiguously identify the SPV contribution throughout a complete device stack as a function of photon energy. Therefore, "half-stack" devices consisting of FTO/n-type metal oxide/(optoinal interface treatment)/perovskite were frequently used throughout this thesis. The sample chamber was purged with N_2 gas prior to data collection, since the measurements are very

sensitive to surface conditions. The distance between the probe and sample was typically < 1 mm.

3.2.3 Photovoltaic Device Characterization

3.2.3.1 Current Density-Voltage (JV) Measurements

Devices were characterized under simulated AM 1.5 sunlight at 100 mW cm^{-2} irradiance produced by an Abet Class AAB solar simulator, which was calibrated with an NREL calibrated filtered silicon reference cell (KG5). Current-voltage data were collected with a Keithly Instruments 2400 Series Sourcemeter, with data collected at 30 mV ms^{-1} increments after 5 seconds of initial illumination and forward bias at 1.4 V. Solar cells were masked with a metal aperture giving an active area of 0.0919 cm^{-2}

3.2.3.2 External Quantum Efficiency

External quantum efficiency was acquired with a custom build Fourier transform photocurrent spectrometer utilizing a Bruker Vertex 80v Fourier Transform Interferometer. Devices were calibrated to a Newport-calibrated silicon reference solar cell with known external quantum efficiency, and illuminated with an AM1.5 filtered solar simulator. Device active areas were masked with a metal aperture, having an active area of 0.0919 cm^2.

3.2.3.3 Stability Testing

Chapter 5

In the UV stability test, unencapsulated devices with ZnO and SnO_2 electron transport layers were placed under a high-intensity UV LED lamp (approximately 12 sun intensity with all emission in the UV). The devices were periodically tested, and the stabilized power output was recorded 1 minute after holding the device at its maximum power point. All testing was performed in atmosphere with relative humidity

of about 50%. Thermal stability of devices was tested in atmosphere, with a relative humidity of around 50%, and devices were aged on a hotplate at 85 °C.

Chapter 7

Initial aging was performed in the dark, followed by testing under illumination using an LED array at open-circuit at 40 °C. Devices were aged in a nitrogen-filled glove box without encapsulation and were periodically removed to atmosphere for measurements and to measure the stabilized power output over 50 seconds.

Chapter 8

In the UV aging experiment, unencapsulated devices were aged under a high-intensity UV lamp equivalent to 12 sun UV intensity under a N_2 atmosphere at ∼25 °C. In the thermal stability experiment, unencapsulated devices were aged in an N_2 environment at 85 °C in an oven. In both UV and thermal aging experiments, devices were periodically removed to atmosphere to test photovoltaic performance.

3.3 Hole Transport Material Synthesis

3.3.1 EDOT-Amide-TPA Synthesis

All chemicals were purchased from commercial sources and used as received unless stated otherwise. All synthesis steps were performed by Michiel Petrus and full details are found elsewhere.[17]

3.3.2 CL1-2 Synthesis

All synthesis steps were performed by Yadong Zhang as reported elsewhere.[18]

References

1. E. H. Anaraki, A. Kermanpur, L. Steier, K. Domanski, T. Matsui, W. Tress, M. Saliba, A. Abate, M. Grätzel, A. Hagfeldt, and J.-P. Correa-Baena, "Highly efficient and stable planar perovskite solar cells by solution-processed tin oxide," *Energy & Environmental Science*, vol. 9, no. 10, pp. 3128–3134, 2016.
2. Y.-H. Lin, S. R. Thomas, H. Faber, R. Li, M. A. McLachlan, P. A. Patsalas, and T. D. Anthopoulos, "Al-doped ZnO transistors processed from solution at 120 °c," *Advanced Electronic Materials*, vol. 2, p. 1600070, apr 2016.
3. N. K. Noel, S. N. Habisreutinger, B. Wenger, M. T. Klug, M. T. Hörantner, M. B. Johnston, R. J. Nicholas, D. T. Moore, and H. J. Snaith, "A low viscosity, low boiling point, clean solvent system for the rapid crystallisation of highly specular perovskite films," *Energy & Environmental Science*, vol. 10, no. 1, pp. 145–152, 2017.
4. J. Ciro, D. Ramírez, M. A. M. Escobar, J. F. Montoya, S. Mesa, R. Betancur, and F. Jaramillo, "Self-functionalization behind a solution-processed NiOxFilm used as hole transporting layer for efficient perovskite solar cells," *ACS Applied Materials & Interfaces*, vol. 9, pp. 12348–12354, mar 2017.
5. S. D. Stranks, G. E. Eperon, G. Grancini, C. Menelaou, M. J. P. Alcocer, T. Leijtens, L. M. Herz, A. Petrozza, and H. J. Snaith, "Electron-hole diffusion lengths exceeding 1 micrometer in an organometal trihalide perovskite absorber," *Science*, vol. 342, pp. 341–344, oct 2013.
6. G. E. Eperon, S. D. Stranks, C. Menelaou, M. B. Johnston, L. M. Herz, and H. J. Snaith, "Formamidinium lead trihalide: a broadly tunable perovskite for efficient planar heterojunction solar cells," *Energy & Environmental Science*, vol. 7, no. 3, p. 982, 2014.
7. D. W. de Quilettes, S. M. Vorpahl, S. D. Stranks, H. Nagaoka, G. E. Eperon, M. E. Ziffer, H. J. Snaith, and D. S. Ginger, "Impact of microstructure on local carrier lifetime in perovskite solar cells," *Science*, vol. 348, pp. 683–686, apr 2015.
8. D. W. deQuilettes, S. Koch, S. Burke, R. K. Paranji, A. J. Shropshire, M. E. Ziffer, and D. S. Ginger, "Photoluminescence lifetimes exceeding 8 s and quantum yields exceeding 30% in hybrid perovskite thin films by ligand passivation," *ACS Energy Letters*, vol. 1, pp. 438–444, jul 2016.
9. D. Bi, C. Yi, J. Luo, J.-D. Décoppet, F. Zhang, S. M. Zakeeruddin, X. Li, A. Hagfeldt, and M. Grätzel, "Polymer-templated nucleation and crystal growth of perovskite films for solar cells with efficiency greater than 21%," *Nature Energy*, vol. 1, sep 2016.
10. L. Kronik and Y. Shapira, "Surface photovoltage spectroscopy of semiconductor structures: at

the crossroads of physics, chemistry and electrical engineering," *Surface and Interface Analysis*, vol. 31, no. 10, pp. 954–965, 2001.

11. W. Zhang, S. Pathak, N. Sakai, T. Stergiopoulos, P. K. Nayak, N. K. Noel, A. A. Haghighirad, V. M. Burlakov, D. W. deQuilettes, A. Sadhanala, W. Li, L. Wang, D. S. Ginger, R. H. Friend, and H. J. Snaith, "Enhanced optoelectronic quality of perovskite thin films with hypophosphorous acid for planar heterojunction solar cells," *Nature Communications*, vol. 6, nov 2015.
12. "04/00906 review of surface photovoltage spectra of nanosized semiconductor and its applications in heterogeneous photocatalysis," *Fuel and Energy Abstracts*, vol. 45, p. 117, mar 2004.
13. B. Goldstein, D. Redfield, D. J. Szostak, and L. A. Carr, "Electrical characterization of solar cells by surface photovoltage," *Applied Physics Letters*, vol. 39, pp. 258–260, aug 1981.
14. Y.-J. Lee, J. Wang, and J. W. P. Hsu, "Surface photovoltage characterization of organic photovoltaic devices," *Applied Physics Letters*, vol. 103, p. 173302, oct 2013.
15. L. Kronik, B. Mishori, E. Fefer, Y. Shapira, and W. Riedl, "Quality control and characterization of cu(in,ga)se2-based thin-film solar cells by surface photovoltage spectroscopy," *Solar Energy Materials and Solar Cells*, vol. 51, pp. 21–34, feb 1998.
16. L. Barnea-Nehoshtan, S. Kirmayer, E. Edri, G. Hodes, and D. Cahen, "Surface photovoltage spectroscopy study of organo-lead perovskite solar cells," *The Journal of Physical Chemistry Letters*, vol. 5, pp. 2408–2413, jun 2014.
17. M. L. Petrus, T. Bein, T. J. Dingemans, and P. Docampo, "A low cost azomethine-based hole transporting material for perovskite photovoltaics," *Journal of Materials Chemistry A*, vol. 3, no. 23, pp. 12159–12162, 2015.
18. Y.-D. Zhang, R. D. Hreha, G. E. Jabbour, B. Kippelen, N. Peyghambarian, and S. R. Marder, "Photo-crosslinkable polymers as hole-transport materials for organic light-emitting diodes," *Journal of Materials Chemistry*, vol. 12, pp. 1703–1708, may 2002.

CHAPTER 4

Meso-Superstructured Perovskite Solar Cells: Revealing the Role of the Mesoporous Layer

The research in this chapter is based on the following publication:

Daniel Ramirez; Kelly Schutt; Juan Felipe Montoya; Santiago Mesa; JongChul Lim; Henry J. Snaith; Franklin Jaramillo 'Meso-Superstructured Perovskite Solar Cells: Revealing the Role of the Mesoporous Layer', J. Phys. Chem. C, 122, 37, 21239-21247

DOI: 10.1021/acs.jpcc.8b07124

Direct link: `https://pubs.acs.org/doi/full/10.1021/acs.jpcc.8b07124`

Reproduced with permission. Copyright © 2018 American Chemical Society. License agreement available at `https://pubs.acs.org/page/policy/authorchoice_ccby_termsofuse.html`

D.R. made and characterized p-i-n devices, collected Kelvin Probe work function data and first observed the work function shift with the mesoporous layer, and performed time-resolved photoluminescence measurements. K.S. made n-i-p devices, collected J-V and EQE device data, performed optical characterization and scanning electron microscope cross sectional images, wrote approximately half of the manuscript, and formatted the work for this chapter. J.M. and S.M. assisted with preparation of p-i-n devices and stability testing for an earlier version of the manuscript. J. L. performed surface photovoltage and transient photoconductivity measurements. Professors H.J.S. and F.J. provided laboratory space, additional discussion, and financial support.

4.1 Introduction

Perovskite solar cells (PSCs) have been developed in both planar and mesoporous device architectures. Devices with the mesoporous architectures have achieved record-breaking efficiencies, yet the exact role of the mesoporous layer has not been fully understood. In this chapter, devices with both planar and mesoporous architectures are utilized in p-i-n and n-i-p devices. The mesoporous n-i-p devices provide higher power conversion efficiency than their planar counterparts, due primarily to increased V_{oc} with a smaller contribution from modestly higher J_{sc}. However, the mesoporous p-i-n devices exhibit reduced power conversion efficiency relative to their planar alternatives. The mesoporous p-i-n devices have reduced current density and poor charge extraction especially from shorter wavelength excitation, which is consistent with electron traps dominating in the perovskite bulk. It is further revealed that the electronic nature of the perovskite is modified upon physical confinement in a mesoporous scaffold. The mesoporous layer induces a controllable p- or n-doping effect at the perovskite interface, dependent upon the underlying charge selective contact, resulting in improved band alignment. Therefore, the mesoporous layer provides a method to selectively engineer the p- and n-type nature of the perovskite through interface modification. The

mesoporous layer also appears to have an additional benefit of decreasing the surface trap density of the perovskite layer.

The rapid efficiency gains in perovskite solar cells can be attributed in large part to the desirable optoelectronic properties of these materials. Among these properties, a tunable band gap, large dielectric constant, long carrier diffusion lengths, low nonradiative recombination, and high optical absorption make metal halide perovskites exceptional semiconductors for photovoltaic applications.[1–4] High-quality metal halide perovskite thin films can be achieved with a variety of processing methods including vacuum evaporation and solution processing. Perovskite solar cells also have the potential for commercial viability due to their low cost.[5,6]

While metal halide perovskites offer desirable optoelectronic properties, advancements in device architecture have also played a crucial role in the rapid efficiency improvements in perovskite photovoltaics. Initially, Miyasaka and co-workers utilized metal halide perovskites as light-absorbing nanoparticles.[7] In 2012, mesoporous titania (TiO_2) and alumina (Al_2O_3) scaffolds were developed to achieve power conversion efficiencies of 9.2% and 10.9%, respectively, employing a solid-state hole conductor.[8,9] While mesoporous devices had reduced hysteresis and improved charge extraction, planar devices fabricated with vapor deposition in 2013 boosted power conversion efficiency to 15.4%,[10] raising questions as to whether the mesoporous architecture was necessary. While planar devices have made impressive gains since then,[11–13] the debate over the superior device architecture remains unsettled, with recent state-of-the-art devices still utilizing thin mesoporous TiO_2 interlayers and solid perovskite capping layers,[14] which is an architecture that was first observed to work well with mesoporous alumina scaffolds.[15]

While mesoporous layers have typically been utilized in combination with compact TiO_2,[16] the surface-defect density of TiO_2 and limited stability of perovskites in contact with this semiconductor have created concerns about the viability of this selective contact.[13,17] As alternative materials, other metal oxides have been used, including tin oxide (SnO_2),[18] which provides a higher-performance alternative to TiO_2 with reduced

hysteresis in planar heterojunction cells, and a simple chemical bath processing route that is both more scalable and higher-performance than SnO_2 deposited via atomic layer deposition.[19]

In this work, the function of the mesoporous layer is first investigated with Kelvin Probe measurements. It is shown that a mesoporous interlayer between the perovskite and charge selective contact modifies the work function of the perovskite. When the perovskite is crystallized upon a thin mesoporous layer of Al_2O_3 in contact with a hole selective contact (in this case, NiO_x), the work function (W_F) of the perovskite is deeper than the W_F of the perovskite crystallized directly on the hole selective contact. Similarly, when the perovskite is crystallized on an electron selective contact (in this case, SnO_2) modified with a thin mesoporous layer, the W_F of the perovskite is shallower than the perovskite crystallized directly on the electron selective contact. The shift in work function indicates controllable p- and n-doping of the perovskite at selective contact. Surface photovoltage measurements also reveal an apparent decreased surface trap density in the perovskite layers when a mesoporous interlayer is utilized. With this knowledge, devices with mesoporous layers on NiO_x and SnO_2 selective contacts are fabricated for the first time in a meso-superstructed architecture (MSSC).[20] The interface modification allows improved power conversion efficiency over the planar devices in the n-i-p configuration, with scanned efficiency improving from 20.2% to 21.0% and stabilized power output increasing from 19.0% to 20.3%, respectively. The external quantum efficiency (EQE) of the devices reveals that charge collection is enhanced when thin mesoporous layers are utilized in n-i-p devices, but the charge collection degrades sharply at shorter wavelengths in p-i-n devices as the mesoporous layer thickness increases. This result is consistent with other findings that electron traps dominate and limit performance in metal halide perovskites, as free electrons generated within the perovskite-infiltrated mesoporous layer require longer lifetimes for successful extraction with thicker absorber layers.

4.2 Electronic Effects of Mesoporous Layer

First, in order to better understand the role of the mesoporous layer, "half stack" devices were prepared to isolate the mesoporous-perovskite interface from effects present in full devices. The p-i-n devices were prepared with FTO/NiO_x/Al_2O_3/perovskite and the n-i-p devices were fabricated with FTO/SnO_2/Al_2O_3/perovskite layers. Additional half stack devices were prepared without the mesoporous Al_2O_3 to directly compare the planar architecture. To achieve the much thinner films needed for these interface studies, the perovskite precursor solution was also substantially diluted relative to the solution used for full-stack devices.

Kelvin Probe was used to characterize the half stack devices, as depicted in Figure 4.1a. The perovskite on the NiO_x/ Al_2O_3 has a deeper W_F than the planar counterpart, of 5.21 eV and 5.16 eV, respectively. The W_F indicates p-type behavior for the perovskite with the mesoporous interface modification. Conversely, when the perovskite infiltrates a mesoporous scaffold on SnO_2 the W_F is much shallower, at 4.63 eV, indicating n-type doping. When incorporated into full devices, the mesoporous interface modification could offer increased V_{oc} due to greater quasi-Fermi level splitting.[21]

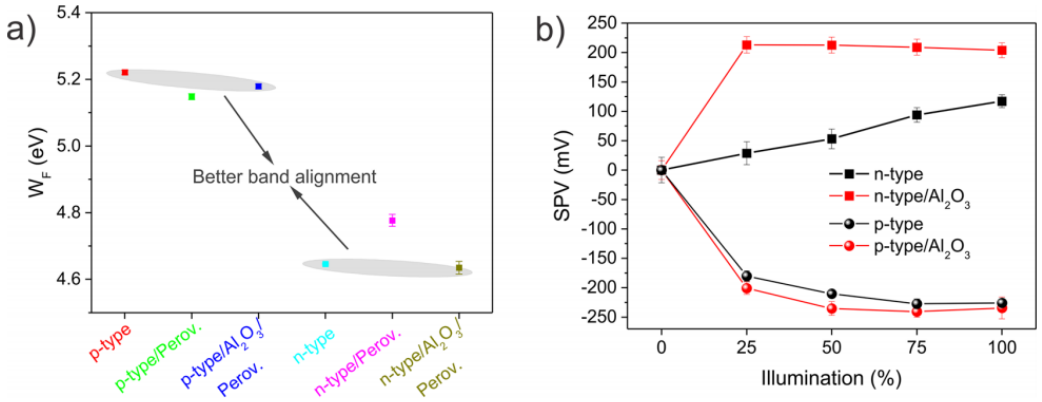

Figure 4.1: Surface electronic properties of the infiltrated perovskite. (a) The work function of a thin layer of perovskite grown on top of p-type or n-type semiconductor demonstrates the band alignment induced by the semiconductor and improved by the mesoporous layer and (b) surface photovoltage (SPV) analysis of the perovskite top surface indicating lower surface trap state density induced by the alumina. Note: 100% illumination corresponds to 3 mW cm^{-2}. Kelvin probe measurements made by Daniel Ramirez, and surface photovoltage measurements made by Jongchul Lim.

While improved band alignment is beneficial for photovoltaic device performance, reducing trap density is also an important factor for minimizing non-radiative recombination pathways. Surface photovoltage (SPV) measurements were utilized to assess band bending in "half stack" devices consisting of FTO/SnO_2/Al_2O_3/Perovskite and FTO/NiO_x/Al_2O_3/Perovskite. SPV has been widely used to characterize surface states and buried semiconductor interfaces, and has also been used to predict the final performance of solar cells at various stages during the manufacturing process.[22] When illuminated by an above bandgap source, n- and p-type behavior of semiconductors can also be observed with SPV. Most semiconductor surfaces are depleted, resulting in downward band bending at the surface for p-type semiconductors and a negative SPV. In contrast, an n-type semiconductor exhibits upward band bending at the surface and a positive SPV.[23] Thus, the sign of the SPV indicates the doping of the semiconductor[24] while the magnitude correlated with the V_{oc} as discussed further in Chapter 4.

In agreement with these principles and the W_F shift observed from Kelvin probe, the perovskite grown on the SnO_2/Al_2O_3 yields a positive SPV signal, as shown in Figure 4.1b. The positive SPV is characteristic of n-type doping and reaches a magnitude of 213 $\pm$ 13.9 mV and 117 $\pm$ 11 mV for the perovskite with and without the mesoporous modification, respectively. In contrast, the perovskite grown on the NiO_x/Al_2O_3/perovskite shows a negative SPV signal, as expected for a p-type semiconductor.

The magnitude of the SPV saturates at 25% of illumination intensity for the perovskite crystallized on SnO_2/Al_2O_3, while the SPV of the perovskite stack without the mesoporous modification shows a slow rise in magnitude through 100% illumination intensity. This discrepancy is in agreement with greater n-type doping accompanying the mesoporous interlayer, which results in greater trap filling relative to the planar alternative. The behavior is similar but less pronounced for the p-type half stack, with the planar device showing a more gradual rise throughout the illumination range. In summary, the Kelvin probe work function measurements and demonstrate that the

p- and n-type character of the perovskite is primarily determined by the underlying selective contact, which is constistent with other findings.[25] The mesoporous layer provides improved band alignment for the heterojunction and the p- or n- doping could result in increased trap occupation.

The physical origin of the doping effect is still unclear. Al_2O_3 has been found to reduce the surface recombination velocity in Si solar cells,[26] and due in part to its wide bandgap (~7 eV) it also provides stable, long-lasting passivation effects under UV irradiation.[27] In perovskite solar cells, the mesoporous layer provides a greater surface area for the perovskite grains infiltrating the mesoporous scaffold, which may allow under-coordinated iodine ions to act as shallow donors at grain boundaries.[21] The Al_2O_3 in contact with the perovskite could possibly passivate or fill surface traps. In hindsight photoluminescence quantum efficiency (PLQE) measurements of perovskite films on glass and glass/Al_2O_3 could have provided additional insight into the trap density at the insulator-metal interface independently from the effects of a charge selective contact.

4.3 Photoluminescence and Photoconductivity

The improved V_{oc} should be reflected in reduced non-radiative recombination. Steady and time-resolved PL were used to corroborate this. As shown in Figure 4.2a, the perovskite deposited on top of glass showed an initial fast electron-trapping process (~40 ns lifetime). After this, the trapped electrons slowly recombine with free holes on tens of μs time scales, deviating significantly from the expected trap-mediated recombination pathway, as also observed by Leijtens et al.[28] The perovskite deposited on top of a mesoporous Al_2O_3 layer showed a slightly longer lifetime up to 1.5 μs, indicating that in this case more surface traps are probably filled at solar fluence,[29] allowing the solar cells to obtain improved photovoltages as previously observed. This is also in agreement with the higher steady-state PL shown in Figure 4.3.

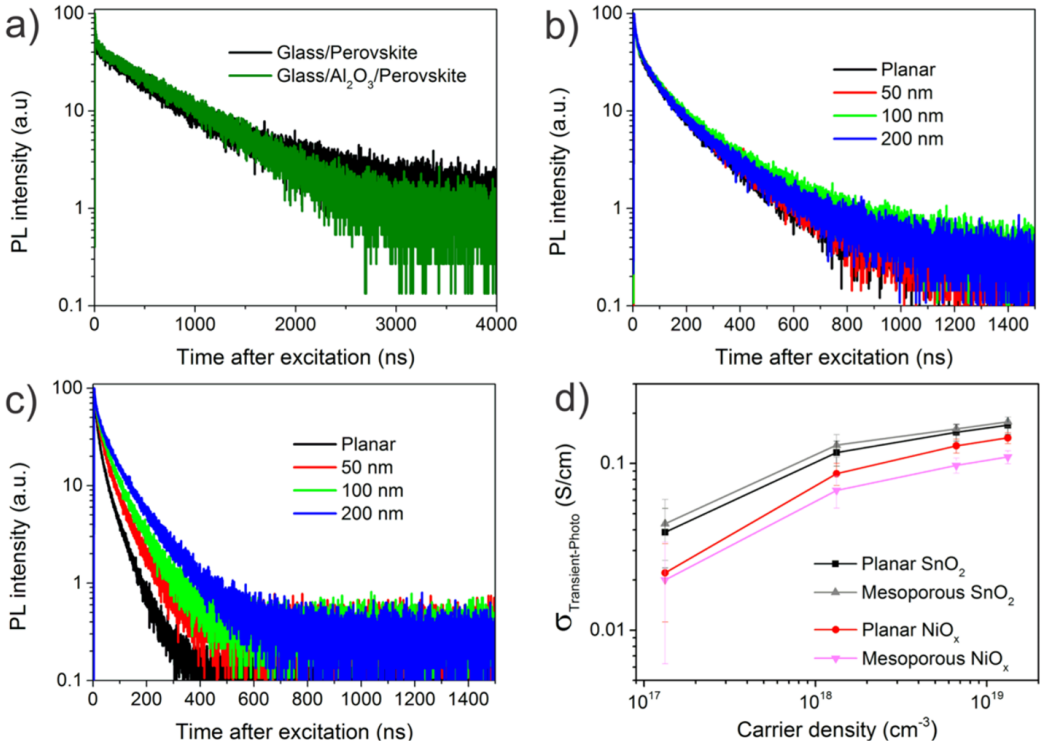

Figure 4.2: Time-resolved PL for (a) planar and mesoporous perovskite deposited on glass, (b) SnO_2, and (c) NiO_x, respectively. (d) Transient photoconductivity perovskite device in the planar and mesoporous n-i-p and p-i-n configuration. Time-resolved PL data were collected by Daniel Ramirez. Transient photoconductivity measurements were made by Jongchul Lim.

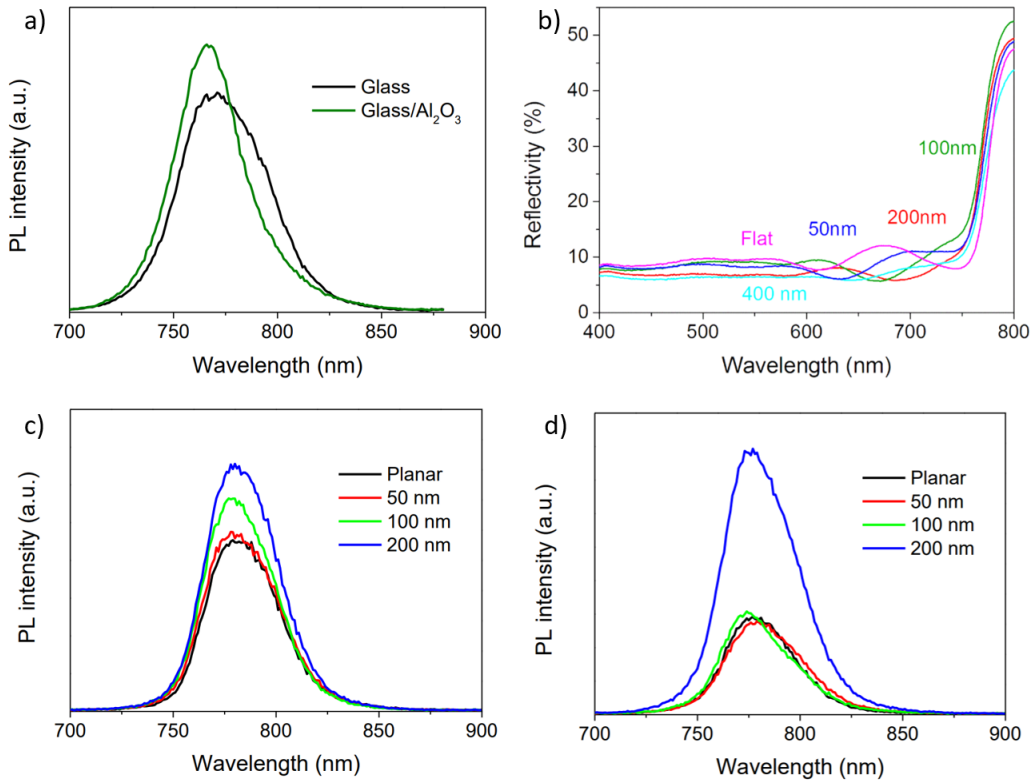

Figure 4.3: Time-resolved PL for (a) Steady-state PL intensity of perovskite on glass and glass with Al_2O_3. (b) Spectral reflectance of planar and mesoporous p-i-n devices. (c) Steady state PL for perovskite films on FTO/SnO_2/mesoporous Al_2O_3. (d) Steady state PL for perovskite films on FTO/NiO_x/mesoporous Al_2O_3.

To have a deeper understanding of the effect of the selective contact in combination with the Al_2O_3 mesoporous layer, PL properties of the meso-superstructured perovskite on top of SnO_2 and NiO_x were measured. Photoluminescence occurs via band-to-band electron-hole recombination while non-radiative trap-assisted recombination, which leads to quenching of the PL. The perovskite PL is not strongly dependent on the Al_2O_3 thickness for the films processed on SnO_2 substrates (Figure 4.3c), indicating that the trap-assisted recombination is not strongly altered by the presence of the Al_2O_3. It is important to note that the long tail in the SnO_2 might indicate that there are shallow electron traps instead of deep electron traps, with a long detrapping time.[30] Steady state PL measurements are similar on p-i-n devices, with the notable exception of the 200 nm mesoporous thickness giving substantially greater emission.

The origin of the enhanced emission for this sample is unclear, and in retrospect remeasuring the 200 nm sample would be desirable.

At the time the measurements were collected, it was also not as apparent that the PL characteristics depended strongly on the sample history, including the illumination time and ambient conditions. In mixed halide perovskites, such as the $FA_{0.83}Cs_{0.17}PbI_{0.83}Br_{0.17}$ used in this chapter, halides segregate into I^- rich regions within the film, resulting in a red shift in the apparent bandgap which can be accompanied by a 7-fold change in PL intensity, although this effect is most noticeable at higher Br^- fractions.[31] Illumination-dependent defect annhiliation has also been observed in metal halide perovskites without mixed halides, and both PL lifetimes and intensity can vary by two orders of magnitude for the same sample depending on illumination intensity and time.[32] Exposure to oxygen can also greatly enhance PL intensity through the formation of superoxide ($O_2{}^-$) that reacts to form a PbO passivated surface.[33] Due to poor film uniformity, carrier lifetimes extracted from time-resolved PL measurements can also vary substantially across a single sample when a small illumination spot size is used. In light of these and other considerations, greater care was taken for PL and TRPL measurements in subsequent chapters; the fabrication conditions, storage, and illumination time before measurements were taken was as consistent as possible from sample to sample and the clear trends between steady-state and time-resolved PL reflect this. In subsequent chapters, TRPL decays were also collected from at least three different locations across the film to ensure a representative decay was chosen.

Returning to Figure 4.2, a large density of subgap states and the degree to which they are filled should influence long-range charge carrier transport. Transient photoconductivity measurements were utilized to probe this possibility, as shown in Figure 4.2d. Excitation densities from 10^{17} cm^{-3} (similar to device operation) to 10^{19} cm^{-3} were used to monitor the photoconductivity. Higher photoconductivity was observed for the perovskite deposited on top SnO_2 compared to the NiO_x, and the difference in photoconductivity between the planar and meso-superstructured

substrates is much larger for the films processed on NiO_x than on SnO_2. These observations are consistent with more trapping and shorter carrier lifetimes for the films processed on NiO_x than on SnO_2, with the presence of the mesoporous Al_2O_3 having a negligible impact on SnO_2 but increasing the trapping rate and reducing the carrier lifetime on NiO_x.

4.4 Comparing Mesoporous and Planar Device Architectures

Schematics of the p-i-n and n-i-p mesoporous device architectures are shown in Figure 1, along with their related performance data. The p-i-n devices were fabricated on nickel oxide (NiO_x), utilizing $PC_{60}BM$ and Rhodamine as electron transport layers, while the n-i-p devices were fabricated on tin oxide (SnO_2), with spiro-OMeTAD as a hole-transport layer. The mesoporous layers were optimized by modifying the spin-coated solution concentration. Notably, for a 50 nm thick mesoporous layer, V_{oc} and fill factor increased in both n-i-p and p-i-n devices while the standard deviation of device parameters decreased relative to planar counterparts. The maximum PCE of the n-i-p/50 nm mesoporous devices was 21.0% while the p-i-n/50 nm mesoporous device reached 16.9% (see Table 4.1 for device parameters). However, as the mesoporous layer thickness increases, both the p-i-n and n-i-p devices exhibit reduced power conversion efficiency in addition to an increased spread of device parameters. As will be discussed in detail, this reduced efficiency can be attributed to the lower current due to insufficient minority carrier diffusion length in the p-i-n devices, as well as increasing series resistance in the normal devices. These results also corroborate findings from Leijtens et al.[21] that subgap, trap-mediated recombination is the dominant recombination mechanism in perovskite solar cells, with electron trapping being the primary decay pathway. Thus, one route to improving V_{oc} is reducing and filling electron traps, promoting bimolecular recombination.

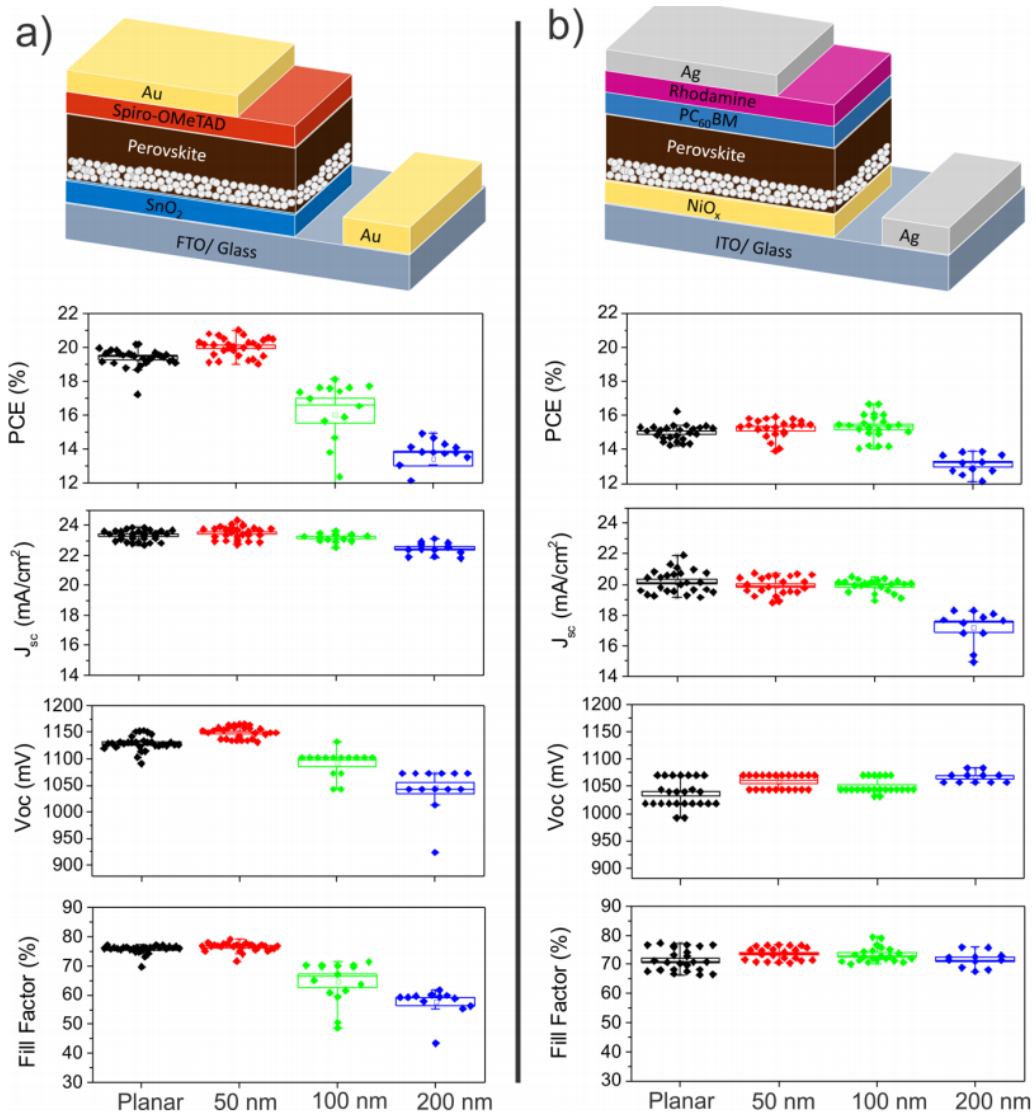

Figure 4.4: Comparative photovoltaic parameters for (a) n-i-p and (b) p-i-n devices with different mesoporous layer thicknesses. p-i-n devices were made and characterized by Daniel Ramirez.

Device	PCE (%)	Jsc (mA/cm2)	Voc (mV)	FF (%)
n-i-p planar				
average	19.4 ± 0.6	23.3 ± 0.3	1128 ± 14	75 ± 2
best	20.2	23.6	1126	76
n-i-p meso 50 nm				
average	20.1 ± 0.6	23.5 ± 0.4	1150 ± 11	76 ± 2
best	21.0	24.3	1140	76
n-i-p meso 100 nm				
average	16.3 ± 2.1	23.2 ± 0.3	1095 ± 24	69 ± 7
best	18.2	23.4	1135	71
n-i-p meso 200 nm				
average	13.8 ± 1.6	22.7 ± 0.43	1048 ± 29	58 ± 6
best	14.7	23.2	1075	61
p-i-n planar				
average	15.0 ± 0.5	20.02 ± 0.7	1026 ± 25	71 ± 4
best	16.2	21.9	1018	73
p-i-n meso 50 nm				
average	15.23 ± 0.6	19.9 ± 0.6	1058 ± 13	74 ± 2
best	16.2	20.7	1044	74
p-i-n meso 100 nm				
average	15.3 ± 0.7	19.9 ± 0.5	1061 ± 12	74 ± 2
best	16.9	20.4	1080	76
p-i-n meso 200 nm				
average	12.5 ± 1.3	16.9 ± 1.3	1066 ± 9	72 ± 4
best	13.9	18.3	1070	71
p-i-n meso 400 nm				
average	7.5 ± 1.2	10.1 ± 0.5	1040 ± 9	72 ± 9
best	9.2	10.9	1044	80

Table 4.1: Solar Cell Performance Parameters Determined from J-V Curves

4.5 Champion Devices and External Quantum Efficiency

In Figure 4.5 the current-voltage characteristics, EQE, and stabilized power output of planar and mesoporous solar cells are examined. As discussed earlier, thin mesoporous layers improve V_{oc} in both the n-i-p and p-i-n devices. In the n-i-p devices, the thin mesoporous layer also improves current density, indicating improved charge extraction,

but also provides a contribution from increased film thickness and light absorption (see Figure 4.6 for a comparative cross-sectional scanning electron microscopy (SEM) image of the planar and mesoporous devices). In p-i-n mesoporous devices, current density decreases as the thickness of the mesoporous alumina layer are increased. To understand this effect more clearly, p-i-n devices with 400 nm mesoporous Al_2O_3 were fabricated (see Table 4.1 for full photovoltaic parameters). These devices had an average J_{sc} of 10.1 mA cm^{-2} , while keeping almost the same V_{oc} and FF as the planar heterojunction and thinner Al_2O_3 cells. Notably, all the mesoporous thicknesses exhibit the same overall specular reflectance (Figure 4.3b), such that the large differences in photocurrent are not expected to come from differences in light absorption. However, because the introduction of the mesoporous layer increased the total thickness of the active layer and decreased the capping layer, these results indicate that charge collection from within the mesoporous scaffold region in the p-i-n architecture is limited.

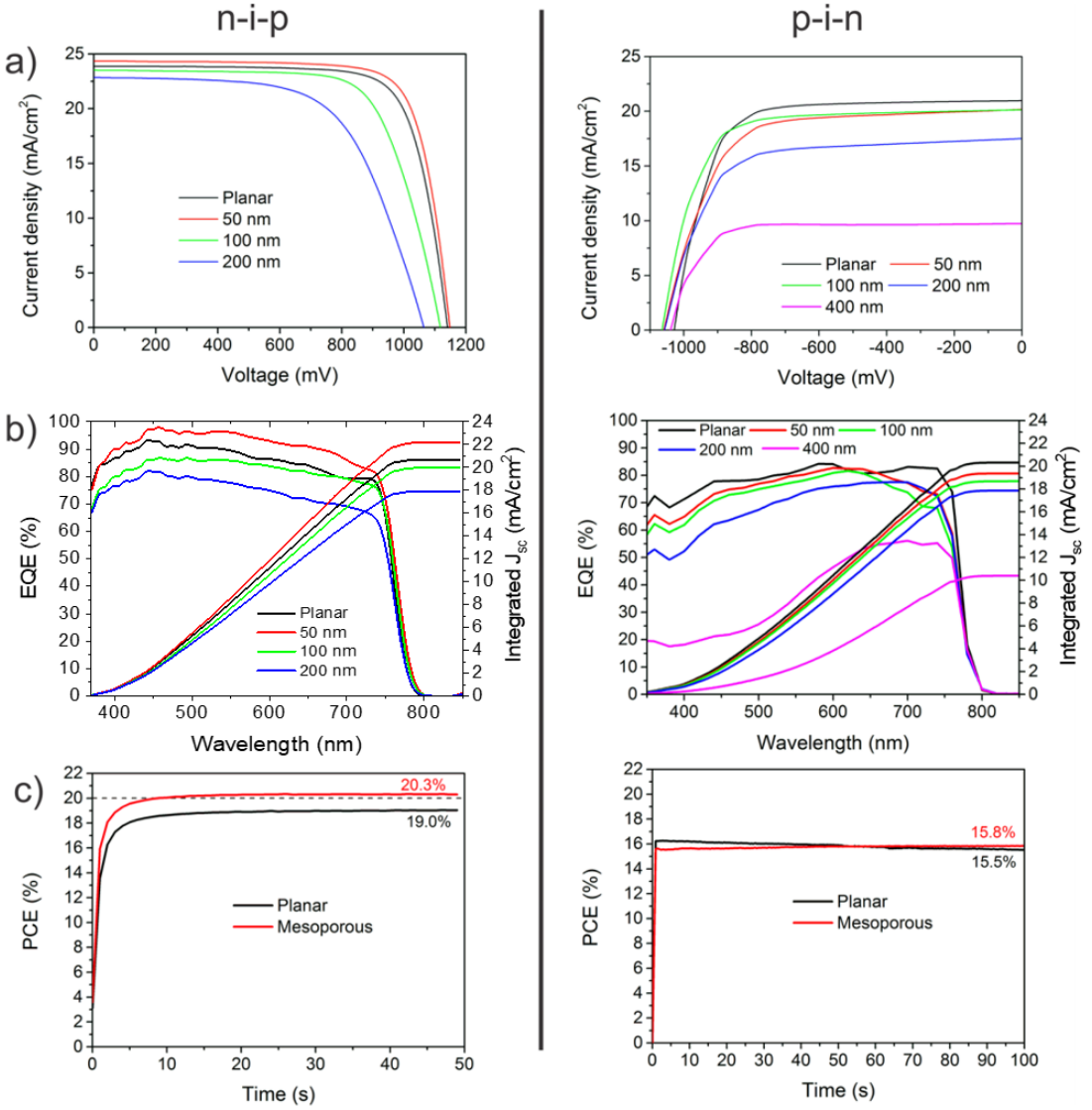

Figure 4.5: Comparative (a) JV curves, (b) EQE, and (c) SPO of n-i-p and p-i-n devices. Note that 400 nm Al_2O_3 p-i-n JV curve and EQE were added to show more clearly the reduction in photocurrent in the blue region. p-i-n devices were made and characterized by Daniel Ramirez.

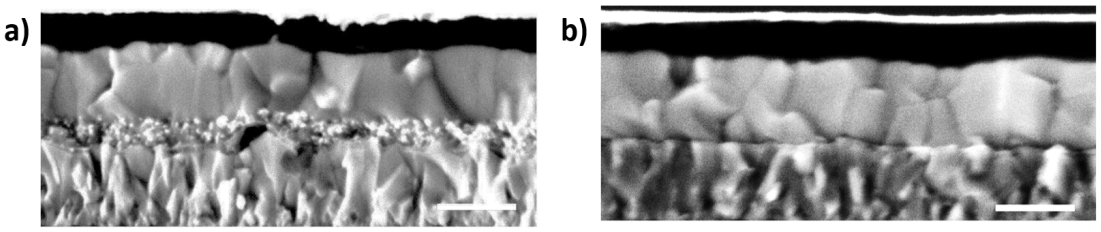

Figure 4.6: (a) Device with mesoporous Al_2O_3-SnO_2 n-type contact. (b) Device with planar SnO_2 n-type contact. Scale bar is 500 nm.

The EQE graphs help to explain this difference in current between the two

architectures by providing insights into the minority carrier diffusion length. In the perovskite film grown onto the p-type selective layer, absorption of shorter wavelengths near and within the mesoporous interface results in current losses with increasing mesoporous thickness. This is consistent with electron traps being the dominant nonradiative recombination pathway,[34] inhibiting the diffusion length of the minority carriers, which in this case are electrons. In the perovskite film grown onto the n-type selective layer, absorption of shorter wavelengths near and within the mesoporous interface results in increased EQE. This indicates that both electrons and holes (the minority carrier in this case) have long diffusion lengths within the n-type perovskite region.

The panchromatic improvement in photocurrent generation for the n-i-p cells suggests that the charge-collection efficiency is improved with the insertion of the mesoporous scaffold interlayer. This is consistent with the more n-type region of perovskite absorber, making improved, lower resistance electronic contact with the SnO_2 charge extraction layer. It is evident that n-i-p devices are more efficient than p-i-n devices, due to the lower V_{oc} obtained in NiO_x-based devices. The steady-state power output (SPO) of the best-performing n-i-p meso-superstructured device with 50 nm Al_2O_3 interlayer was 20.3% compared to 19.0% for the planar counterpart. On the other hand, the SPO for the p-i-n meso-superstructured devices was 15.8% compared to 15.5% for the planar counterpart. Note the fast SPO stabilization of < 2 s for the p-i-n devices; this is related to the absence of hysteresis in this device configuration and the common pronounced hysteresis of the n-i-p devices.[17] In n-i-p devices the mesoporous layer had the additional benefit of slightly reducing the hysteresis.

4.6 Mechanism of Mesoporous Doping Effect

To summarize these findings, Figure 4.7 shows the schematic representation of the proposed recombination mechanisms in which an intrinsic perovskite has subgap, trap-mediated recombination with electron trapping being the primary decay pathway.

For the case of the n-type perovskite infiltrated into the mesoporous layer, the non-radiative recombination is slower due to filled electron traps. The p-type perovskite has more holes in the valence band and fewer filled electron traps, resulting in more rapid non-radiative recombination. Consequently, a reduced EQE at shorter wavelengths was observed for the p-i-n devices, corresponding to the light absorbed near the p-type contact-perovskite interface. These results give new insights into the working mechanisms of different PSC architectures, paving the way for boosting the efficiency of this photovoltaic technology.

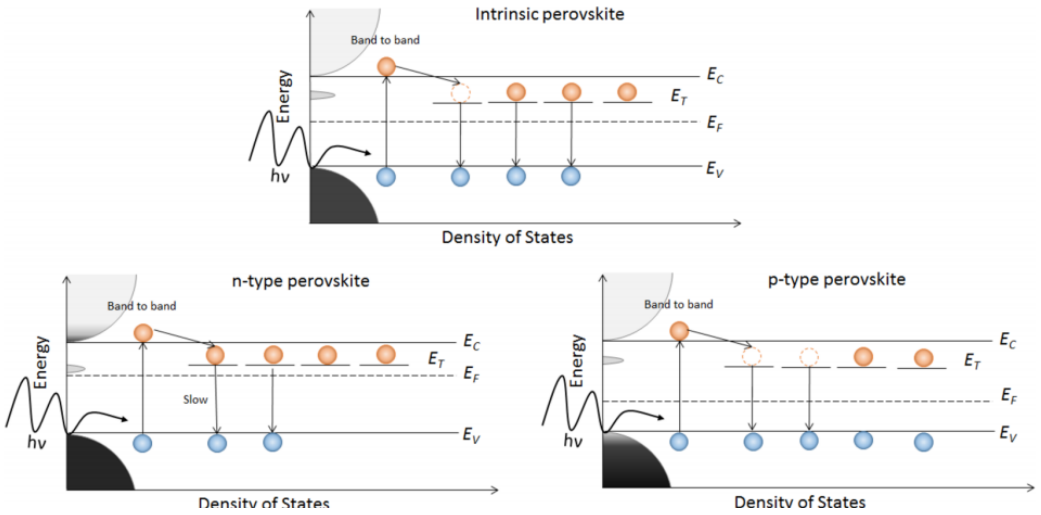

Figure 4.7: Schematic representation of the recombination process of (a) an intrinsic perovskite, (b) n-type perovskite, and (c) p-type perovskite.

4.7 Conclusion

Perovskite solar cells with mesoporous architectures have often outperformed those with planar configurations. The reasons for the performance difference have been attributed to reduced hysteresis and improved charge extraction afforded by conductive, mesoporous TiO_2. In this chapter, an insulating layer of mesoporous Al_2O_3 was shown to provide a method for selectively p- and n-doping the perovskite interface at charge selective contacts. Devices with mesoporous Al_2O_3 on SnO_2 outperformed their planar counterparts, primarily due to enhanced V_{oc}. The V_{oc} improvement can be attributed to a combination of improved band alignment and enhanced quasi-fermi level splitting,

and filling of the surface trap states of the perovskite upon n-doping. In contrast, devices with p-i-n architecture showed inhibited carrier extraction, which became more pronounced with the increasing thickness of the mesoporous layer. This result is consistent with the dominant traps being electron traps. The half stack devices of NiO_x/mesoporous Al_2O_3/perovskite exhibited a moderate p-doping effect relative to their planar counterparts, suggesting that ideal p-i-n perovskite solar cells should have an extremely thin p-type region to minimize current losses from the limiting electron diffusion length. The shorter electron diffusion length is likely to play a significant role in the limited overall performance of p-i-n devices, which has yet to match that of the n-i-p architecture.

References

1. N.-G. Park, "Perovskite solar cells: an emerging photovoltaic technology," *Materials Today*, vol. 18, pp. 65–72, mar 2015.
2. S. S. Mali and C. K. Hong, "p-i-n/n-i-p type planar hybrid structure of highly efficient perovskite solar cells towards improved air stability: synthetic strategies and the role of p-type hole transport layer (HTL) and n-type electron transport layer (ETL) metal oxides," *Nanoscale*, vol. 8, no. 20, pp. 10528–10540, 2016.
3. P.-W. Liang, C.-C. Chueh, S. T. Williams, and A. K.-Y. Jen, "Roles of fullerene-based interlayers in enhancing the performance of organometal perovskite thin-film solar cells," *Advanced Energy Materials*, vol. 5, p. 1402321, feb 2015.
4. W. Chen, Y. Wu, J. Liu, C. Qin, X. Yang, A. Islam, Y.-B. Cheng, and L. Han, "Hybrid interfacial layer leads to solid performance improvement of inverted perovskite solar cells," *Energy & Environmental Science*, vol. 8, no. 2, pp. 629–640, 2015.
5. H. J. Snaith, "Perovskites: The emergence of a new era for low-cost, high-efficiency solar cells," *The Journal of Physical Chemistry Letters*, vol. 4, pp. 3623–3630, oct 2013.
6. J.-P. Correa-Baena, A. Abate, M. Saliba, W. Tress, T. J. Jacobsson, M. Grätzel, and A. Hagfeldt, "The rapid evolution of highly efficient perovskite solar cells," *Energy & Environmental Science*, vol. 10, no. 3, pp. 710–727, 2017.
7. A. Kojima, K. Teshima, Y. Shirai, and T. Miyasaka, "Organometal halide perovskites as visible-light sensitizers for photovoltaic cells," *Journal of the American Chemical Society*, vol. 131, pp. 6050–6051, may 2009.
8. H.-S. Kim, C.-R. Lee, J.-H. Im, K.-B. Lee, T. Moehl, A. Marchioro, S.-J. Moon, R. Humphry-Baker, J.-H. Yum, J. E. Moser, M. Grätzel, and N.-G. Park, "Lead iodide perovskite sensitized all-solid-state submicron thin film mesoscopic solar cell with efficiency exceeding 9%," *Scientific Reports*, vol. 2, aug 2012.
9. M. M. Lee, J. Teuscher, T. Miyasaka, T. N. Murakami, and H. J. Snaith, "Efficient hybrid solar cells based on meso-superstructured organometal halide perovskites," *Science*, vol. 338, pp. 643–647, oct 2012.
10. M. Liu, M. B. Johnston, and H. J. Snaith, "Efficient planar heterojunction perovskite solar cells by vapour deposition," *Nature*, vol. 501, pp. 395–398, sep 2013.
11. J. Ciro, S. Mesa, J. I. Uribe, M. A. Mejía-Escobar, D. Ramirez, J. F. Montoya, R. Betancur, H.-S.

Yoo, N.-G. Park, and F. Jaramillo, "Optimization of the ag/PCBM interface by a rhodamine interlayer to enhance the efficiency and stability of perovskite solar cells," *Nanoscale*, vol. 9, no. 27, pp. 9440–9446, 2017.

12. J. P. C. Baena, L. Steier, W. Tress, M. Saliba, S. Neutzner, T. Matsui, F. Giordano, T. J. Jacobsson, A. R. S. Kandada, S. M. Zakeeruddin, A. Petrozza, A. Abate, M. K. Nazeeruddin, M. Grätzel, and A. Hagfeldt, "Highly efficient planar perovskite solar cells through band alignment engineering," *Energy & Environmental Science*, vol. 8, no. 10, pp. 2928–2934, 2015.

13. H. Tan, A. Jain, O. Voznyy, X. Lan, F. P. G. de Arquer, J. Z. Fan, R. Quintero-Bermudez, M. Yuan, B. Zhang, Y. Zhao, F. Fan, P. Li, L. N. Quan, Y. Zhao, Z.-H. Lu, Z. Yang, S. Hoogland, and E. H. Sargent, "Efficient and stable solution-processed planar perovskite solar cells via contact passivation," *Science*, vol. 355, pp. 722–726, feb 2017.

14. W. S. Yang, B.-W. Park, E. H. Jung, N. J. Jeon, Y. C. Kim, D. U. Lee, S. S. Shin, J. Seo, E. K. Kim, J. H. Noh, and S. I. Seok, "Iodide management in formamidinium-lead-halide–based perovskite layers for efficient solar cells," *Science*, vol. 356, pp. 1376–1379, jun 2017.

15. J. M. Ball, M. M. Lee, A. Hey, and H. J. Snaith, "Low-temperature processed meso-superstructured to thin-film perovskite solar cells," *Energy & Environmental Science*, vol. 6, no. 6, p. 1739, 2013.

16. N. Ahn, D.-Y. Son, I.-H. Jang, S. M. Kang, M. Choi, and N.-G. Park, "Highly reproducible perovskite solar cells with average efficiency of 18.3% and best efficiency of 19.7% fabricated via lewis base adduct of lead(II) iodide," *Journal of the American Chemical Society*, vol. 137, pp. 8696–8699, jul 2015.

17. S.-H. Turren-Cruz, M. Saliba, M. T. Mayer, H. Juárez-Santiesteban, X. Mathew, L. Nienhaus, W. Tress, M. P. Erodici, M.-J. Sher, M. G. Bawendi, M. Grätzel, A. Abate, A. Hagfeldt, and J.-P. Correa-Baena, "Enhanced charge carrier mobility and lifetime suppress hysteresis and improve efficiency in planar perovskite solar cells," *Energy & Environmental Science*, vol. 11, no. 1, pp. 78–86, 2018.

18. W. Ke, G. Fang, Q. Liu, L. Xiong, P. Qin, H. Tao, J. Wang, H. Lei, B. Li, J. Wan, G. Yang, and Y. Yan, "Low-temperature solution-processed tin oxide as an alternative electron transporting layer for efficient perovskite solar cells," *Journal of the American Chemical Society*, vol. 137, pp. 6730–6733, may 2015.

19. E. H. Anaraki, A. Kermanpur, L. Steier, K. Domanski, T. Matsui, W. Tress, M. Saliba, A. Abate, M. Grätzel, A. Hagfeldt, and J.-P. Correa-Baena, "Highly efficient and stable planar perovskite solar cells by solution-processed tin oxide," *Energy & Environmental Science*, vol. 9, no. 10, pp. 3128–3134, 2016.

20. D. Ramirez, M. A. M. Escobar, J. F. Montoya, and F. Jaramillo, "Understanding the role of the mesoporous layer in the thermal crystallization of a meso-superstructured perovskite solar cell," *The Journal of Physical Chemistry C*, vol. 120, pp. 8559–8567, apr 2016.

21. T. Leijtens, S. D. Stranks, G. E. Eperon, R. Lindblad, E. M. J. Johansson, I. J. McPherson, H. Rensmo, J. M. Ball, M. M. Lee, and H. J. Snaith, "Electronic properties of meso-superstructured and planar organometal halide perovskite films: Charge trapping, photodoping, and carrier mobility," *ACS Nano*, vol. 8, pp. 7147–7155, jul 2014.

22. L. Kronik, B. Mishori, E. Fefer, Y. Shapira, and W. Riedl, "Quality control and characterization of cu(in,ga)se2-based thin-film solar cells by surface photovoltage spectroscopy," *Solar Energy Materials and Solar Cells*, vol. 51, pp. 21–34, feb 1998.

23. J. Ciro, S. Mesa, J. F. Montoya, J. I. Uribe, R. Betancur, and F. Jaramillo, "Simultaneous top and bottom perovskite interface engineering by fullerene surface modification of titanium dioxide as electron transport layer," *ACS Applied Materials & Interfaces*, vol. 9, pp. 29654–29659, aug 2017.

24. L. Kronik and Y. Shapira, "Surface photovoltage spectroscopy of semiconductor structures: at the crossroads of physics, chemistry and electrical engineering," *Surface and Interface Analysis*, vol. 31, pp. 954–965, oct 2001.

25. E. M. Miller, Y. Zhao, C. C. Mercado, S. K. Saha, J. M. Luther, K. Zhu, V. Stevanović, C. L. Perkins, and J. V. D. Lagemaat, "Substrate-controlled band positions in ch3nh3pbi3perovskite films," *Phys. Chem. Chem. Phys.*, vol. 16, p. 22122–22130, Apr 2014.

26. A. G. Aberle, "Surface passivation of crystalline silicon solar cells: a review," *Progress in Photovoltaics: Research and Applications*, vol. 8, no. 5, p. 473–487, 2000.

27. R. Hezel, "Low-temperature surface passivation of silicon for solar cells," *Journal of The Electrochemical Society*, vol. 136, no. 2, p. 518, 1989.

28. T. Leijtens, G. E. Eperon, A. J. Barker, G. Grancini, W. Zhang, J. M. Ball, A. R. S. Kandada, H. J. Snaith, and A. Petrozza, "Carrier trapping and recombination: the role of defect physics in enhancing the open circuit voltage of metal halide perovskite solar cells," *Energy & Environmental Science*, vol. 9, no. 11, pp. 3472–3481, 2016.

29. W. Zhang, S. Pathak, N. Sakai, T. Stergiopoulos, P. K. Nayak, N. K. Noel, A. A. Haghighirad, V. M. Burlakov, D. W. deQuilettes, A. Sadhanala, W. Li, L. Wang, D. S. Ginger, R. H. Friend, and H. J. Snaith, "Enhanced optoelectronic quality of perovskite thin films with hypophosphorous acid for planar heterojunction solar cells," *Nature Communications*, vol. 6, nov 2015.

30. R. Brenes, D. Guo, A. Osherov, N. K. Noel, C. Eames, E. M. Hutter, S. K. Pathak, F. Niroui, R. H. Friend, M. S. Islam, H. J. Snaith, V. Bulović, T. J. Savenije, and S. D. Stranks, "Metal halide perovskite polycrystalline films exhibiting properties of single crystals," *Joule*, vol. 1, pp. 155–167, sep 2017.

31. D. J. Slotcavage, H. I. Karunadasa, and M. D. McGehee, "Light-induced phase segregation in halide-perovskite absorbers," *ACS Energy Letters*, vol. 1, pp. 1199–1205, nov 2016.

32. Y. Yamada, M. Endo, A. Wakamiya, and Y. Kanemitsu, "Spontaneous defect annihilation in CH3nh3pbi3 thin films at room temperature revealed by time-resolved photoluminescence spectroscopy," *The Journal of Physical Chemistry Letters*, vol. 6, pp. 482–486, jan 2015.

33. J. S. Godding, A. J. Ramadan, Y.-H. Lin, K. Schutt, H. J. Snaith, and B. Wenger, "Oxidative passivation of metal halide perovskites," *Joule*, vol. 3, no. 11, p. 2716–2731, 2019.

34. S. D. Stranks, V. M. Burlakov, T. Leijtens, J. M. Ball, A. Goriely, and H. J. Snaith, "Recombination kinetics in organic-inorganic perovskites: Excitons, free charge, and subgap states," *Physical Review Applied*, vol. 2, sep 2014.

CHAPTER 5

Overcoming Zinc Oxide Interface Instability with a Methylammonium-free Perovskite for High Performance Solar Cells

The research in this chapter is based on the following publication:

Kelly Schutt; Pabitra K. Nayak; Alexandra J. Ramadan; Bernard Wenger; Yen-Hung Lin; Henry J. Snaith 'Overcoming Zinc Oxide Interface Instability with a Methylammonium-Free Perovskite for High-Performance Solar Cells', Adv. Funct. Mater., 2019, 1900466

DOI: 10.1002/adfm.201900466

Direct link: https://onlinelibrary.wiley.com/doi/10.1002/adfm.201900466

Reproduced with permission. Copyright © 2019 John Wiley and Sons. License agreement available at https://s100.copyright.com/App/PaymentTermsAndConditions.jsp

K.S. made and characterized solar cells, collected data on chemical reactions at the metal oxide-perovskite interface, collected cross sectional images with a scanning electron microscope, performed photoluminescence measurements, and wrote the manuscript and chapter. P.N. provided insights on chemical reactions at the interface and suggested using dinitrotoluene as an amine detector. A.R. performed x-ray photoelectron spectroscopy and provided atomic force microscopy of ZnO films. B.W. provided helpful discussion of photoluminescence characterization and assistance with photoluminescence quantum efficiency measurements. Y.L. provided the solution processed ZnO method. Professor H.J.S. provided laboratory space, additional discussion, and financial support.

5.1 Introduction

Perovskite solar cells have achieved the highest power conversion efficiencies on metal oxide n-type layers, including SnO_2 and TiO_2. Despite ZnO having superior optoelectronic properties to these metal oxides, such as improved transmittance, higher conductivity, and closer conduction band alignment to methylammonium (MA)PbI_3, ZnO has largely been overlooked due to a chemical instability when in contact with metal halide perovskites, which leads to the rapid decomposition of the perovskite. While surface passivation techniques have somewhat mitigated this instability, investigations as to whether all metal halide perovskites exhibit this instability with ZnO are yet to be undertaken. In this chapter, experimental methods are developed to elucidate the degradation mechanisms at ZnO-$MAPbI_3$ interfaces. By substituting MA with formamidinium (FA) and cesium (Cs), the stability of the perovskite-ZnO interface is greatly enhanced and compares more favorably with SnO_2-based devices after high intensity UV irradiation and 85 °C thermal stressing. For devices comprising FA and Cs based metal halide perovskite absorber layers on ZnO, 21.1% scanned power conversion efficiency and 18% steady-state power output is achieved. This work demonstrates that ZnO appears to be as feasible an n-type charge

extraction layer as SnO_2, with many foreseeable advantages, provided that MA cations are avoided.

To date, perovskite solar cells (PSC) with record PCE have been lead by devices with metal oxide n-type layers, with PCE now reaching 23.7%.[1] Despite impressive gains in PCE, often material choices made to deliver the highest efficiencies neglect the essential requirement for simultaneously delivering high stability. Understanding the unique degradation mechanisms present at metal oxide-perovskite interfaces is especially vital, and degradation kinetics between different metal oxides and perovskites vary dramatically. TiO_2-perovskite interfaces are notably unstable under UV light,[2] and a recent test of 1,000 hour operational performance showed devices utilizing SnO_2 achieved longer lifetimes than those with TiO_2.[3] SnO_2-perovskite interfaces, which are shown here to offer greatly improved UV stability relative to TiO_2, also introduce a thermal instability, that is just now being addressed through surface passivation.[4]

While TiO_2 and SnO_2 have been favored candidates for n-type charge extraction layers, ZnO has received comparatively little attention due to a greatly reduced thermal stability and, historically, lower performance.[5,6] However, the optoelectronic properties of ZnO are encouraging: relative to polycrystalline TiO_2 and SnO_2, ZnO offers greater transmittance in the visible to IR regions of the spectrum and lower resistivity,[7] higher mobility than SnO_2 and orders of magnitude higher mobility than TiO_2 due in part to a lower effective electron mass,[8,9] and a shallower conduction band edge that may align more closely with metal halide perovskites.[10] This suggests that if stability issues are overcome, ZnO could deliver improved fill factor from higher conductivity and increased voltages due to improved energetic alignment at the perovskite interface. Additionally, ZnO offers lower energy processing routes than solution-processed TiO_2 or SnO_2, with colloidal nanoparticle synthesis techniques enabling low-temperature annealing or even room temperature deposition, making it suitable for flexible polymer substrates.[11,12]

Furthermore, aluminum-doped ZnO (AZO) is also a very useful transparent conducting oxide (TCO) which avoids the resource scarcity of indium, in indium tin oxide

(ITO), making it more suitable for use as an electrode in PSC at TW scale production. A recent life-cycle assessment of perovskite-on-silicon tandem modules has revealed that indium in the TCO accounts for 29% of the total ecotoxicological environmental impact.[13] In addition, for TCO's on flexible willow glass, it was found that AZO offers improved transmittance and lower sheet resistance in comparison to ITO (85.8% to 81.5% and 17.8 Ω cm^{-2} to 31.3 Ω cm^{-2}, respectively).[14] Therefore, interfacing AZO with ZnO would appear to be a very useful combination of TCO and n-type charge extraction layer.

The ZnO-perovskite interface instability has been widely reported, with a variety of degradation mechanisms proposed. Cheng et. al. experimentally demonstrated that hydroxyl groups present on zinc oxide nanoparticles accelerate $MAPbX_3$ degradation; higher temperature annealing of ZnO decreased the surface density of hydroxyl groups and improved perovskite stability. However, the perovskite films still turned yellow after 30 minutes of annealing at 100 °C.[15] Dkhissi et. al. reported a slightly greater release of physisorbed water from ZnO than from TiO_2 at temperatures above 70 °C, but found this incapable of explaining the stability variation between the two metal oxides. They proposed that as CH_3NH_3I decomposes into CH_3NH_2 + HI, the HI could react with ZnO to form ZnI_2 and H_2O, and yet were unable to detect ZnI_2 with Raman spectroscopy.[6] Yang et al. found nanoparticle ligands and hydroxyl groups accelerated $MAPbX_3$ degradation, but computationally predicted the deprotonation of $CH_3NH_3^+$ by ZnO even in the absence of these surface groups.[16] Collectively, surface chemistry at the ZnO-perovskite interfaces has largely been assessed by monitoring the generation PbI_2.

Recent efforts have increased PCE for ZnO-based PSC to over 20% by addressing these stability concerns by "passivating" the surface with magnesium oxide, ethanolamine, polyethylenimine, and ZnS.[5,15,17–20]. Despite these improvements, however, the reactions of methylammonium cations at ZnO interfaces have remained unresolved, limiting the long-term stability of ZnO-perovskite solar cells. Additionally, these high efficiency devices have required ZnO annealing temperatures in excess of 500

°C, negating many of the potential advantages of ZnO. In this chapter, degradation mechanisms at the perovskite-ZnO interface are probed by utilizing an amine indicator, investigating the generation of hydroxyl groups, and by monitoring the generation of ZnI_2. The root cause of ZnO-perovskite instability is revealed to be the deprotonation of the methylammonium cation, leading to the formation of zinc hydroxide. Based on this finding, the MA cation is replaced with lower acidity formamidinum mixed with cesium cations (FACs) in devices with low temperature (120 °C) processed ZnO. The FACs perovskite offers greatly enhances thermal stability, and in such a configuration it is found that perovskite solar cells on ZnO offer greater UV stability than those on TiO_2.

5.2 Chemical Reactions at the ZnO-Perovskite Interface

Based on the previous studies,[16,17] and the nature of the amphoteric ZnO surface,[21,22] one may hypothesize that the ZnO surface can abstract H^+ from an acid, which may then trigger the degradation process. In organic-inorganic metal halide perovskites, the organic cation (MA in $MAPbI_3$) is the source of the H^+. To elucidate the surface chemistry a series of experiments are designed that probe the ZnO-perovskite interface. First, to determine whether ZnO can deprotonate the MA cation, an indicator molecule is utilized. Aromatic nitro compounds such as dinitrotoluene and dinitrobenzene are sensitive primary amine indicators.[23] 2,4-dinitrotoluene (DNT) rapidly forms a Meisenheimer complex with methylamine, which has a characteristic blue-green color due to an absorption minima between 450 and 500 nm. $MAPbI_3$ powder is added to nitrogen-filled, sealed vials with and without bulk ZnO powder and then heated to 130 °C for 30 minutes. Next, the headspace of these vials is purged into a solution of dimethyl sulfoxide (DMSO) containing DNT. While gases from the vial with only $MAPbI_3$ result in a minimal absorption shift from the baseline solution of DMSO-DNT, gases sampled from the vial of $MAPbI_3$ with ZnO result in a visible blue-green color when introduced to the DMSO-DNT solution, a nearly dynamite

confirmation that CH_3NH_2 is indeed generated due to the deprotonation of MA as depicted in Figure 5.1 (a-c).

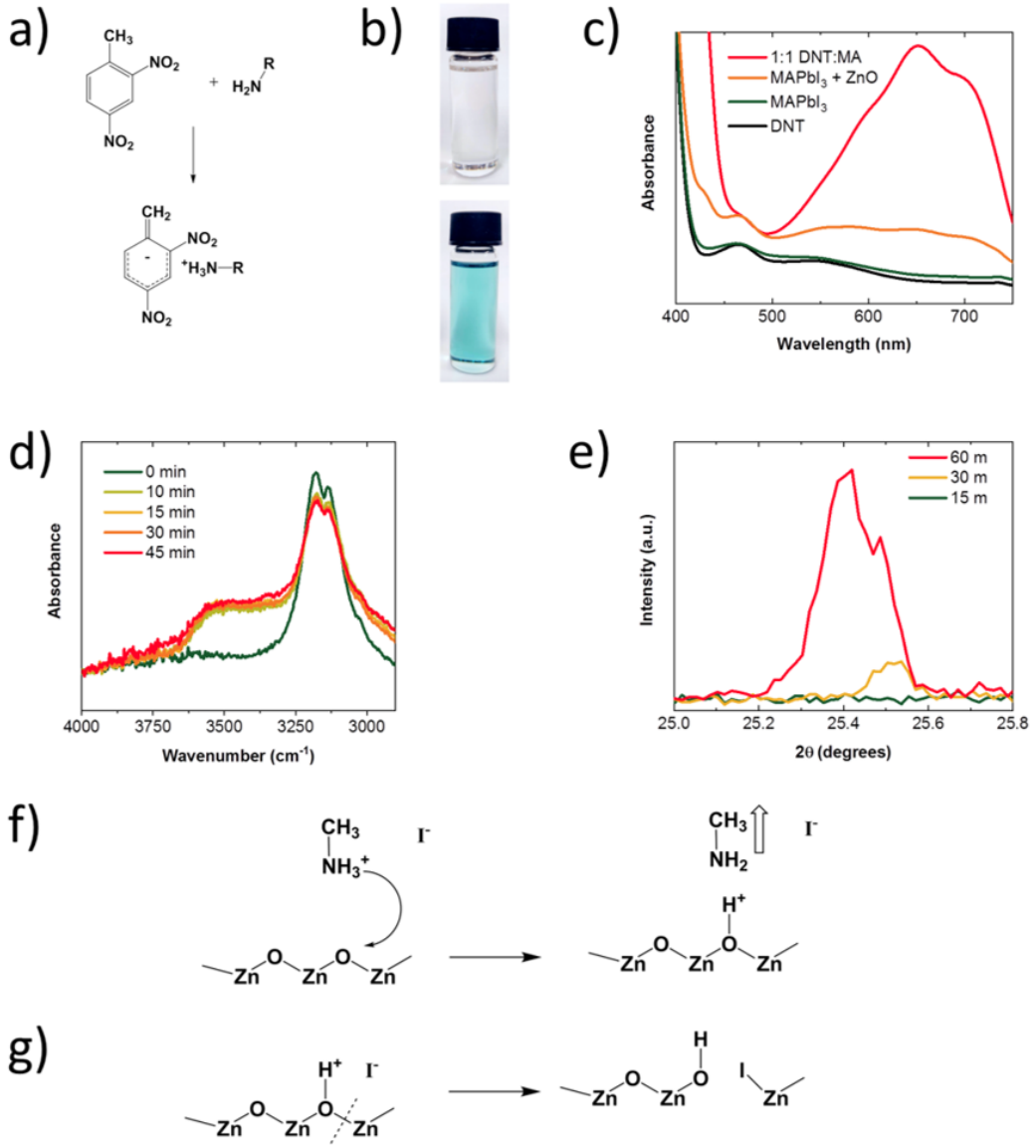

Figure 5.1: a) Schematic of 2,4-dinitrotoluene (DNT) and a primary amine forming a Meisenheimer complex. b) DMSO solution containing 10 mM DNT without methylamine (top) and with 10 mM methylamine (bottom). c) Absorbance of solutions of DNT-DMSO before and after reacting with gases collected from $MAPbI_3$ and ZnO. d) FTIR spectra of $MAPbI_3$ film annealed on ZnO as a function of time. e) XRD of ZnI_2 (111) peak intensity increasing with annealing time for ZnO-$MAPbI_3$ films. f) Schematic for ZnO abstracting H+ from $CH_3NH_3^+$, forming Zn-O-H^+; CH_3NH_2 evaporates. g) Schematic for formation of Zn-I bonds.

The abstraction of H^+ by the ZnO surface will give rise to Zn-O-H^+ which can undergo further changes to produce Zn-O-H. To confirm hydroxide formation is also

part of the degradation mechanism, Fourier transform infrared spectroscopy (FTIR) is employed to inspect ZnO-$MAPbI_3$ films during 100 °C annealing (Figure 5.1d). The acetonitrile solvent system is utilized for $MAPbI_3$, as this provides high crystallinity films, as-cast at room temperature, allowing for initial inspection of the interface with minimal thermally induced effects.[24] The peaks at 3138 and 3179 cm^{-1} are assigned to symmetric and asymmetric stretching of NH_3^+,[25] and the broad band around 3485 cm^{-1} to O-H stretching from hydroxyl groups (or physically adsorbed water).[26–28] Additional annealing results in gradual accumulation of hydroxyl groups and the loss of $CH_3NH_3^+$ to volatile CH_3NH_2. To exclude the possibility of lead hydrates being responsible for this spectral signature, x-ray photoelectron spectroscopy (XPS) is used to examine a ZnO film coated with only a thin layer ($<$ 5 nm, non-continuous) of methylammonium iodide. As annealing progresses, the emergence of Zn hydroxyl groups can be seen as the relative intensity of the O-H bond (532.20 eV) grows in intensity relative to the O-Zn bond (531.09 eV), as shown in Figure 5.2. In addition to MA deprotonation, surface hydroxyl groups are an additional source of instability and have been previously shown to catalyze $MAPbI_3$ decomposition.[6,16] The deprotonation of MA and hydroxylation of ZnO can also result in Zn-I bond formation, as a by-product of the degradation.

X-ray diffraction (XRD) is conducted under an inert atmosphere, since ZnI_2 is hygroscopic in nature. First, HI is added to bulk ZnO powder to produce ZnI_2, and then films are spin-coated and reference pattern are collected, as shown in Figure 5.3. Next, time-dependent XRD of ZnO-$MAPbI_3$ films annealed at 100 °C are collected. An XRD peak emerges at 25.42° 2θ, which closely matches the American Society of Testing and Materials (ASTM) value of 25.45°for the (111) plane of tetragonal ZnI_2,[29] and also matches the dominant peak of the highly oriented ZnI_2 reference spectra.

In the above investigations, a mechanism for the intrinsic instability of ZnO with $MAPbI_3$ was revealed, where the degradation is initiated by the proton abstraction

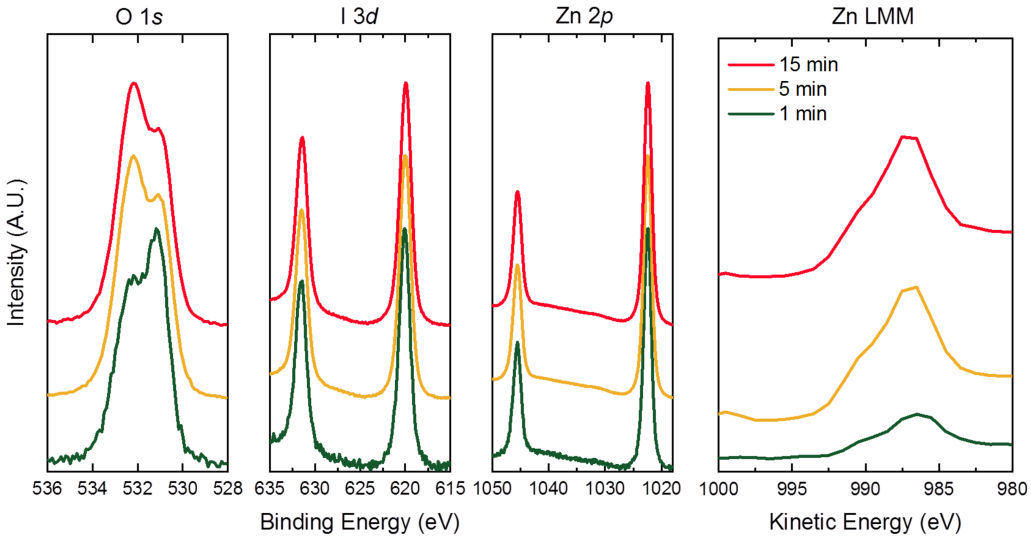

Figure 5.2: XPS Spectra of O, Zn, I, and ZnO for MA cation films annealed on ZnO at 100 °C in a nitrogen filled glove box ($<$ 2 ppm O_2) for 1, 5, and 15 minutes. The O 1s spectra reveal the formation of a metal hydroxide as annealing proceeds. XPS spectra collected by Alexandra Ramadan.

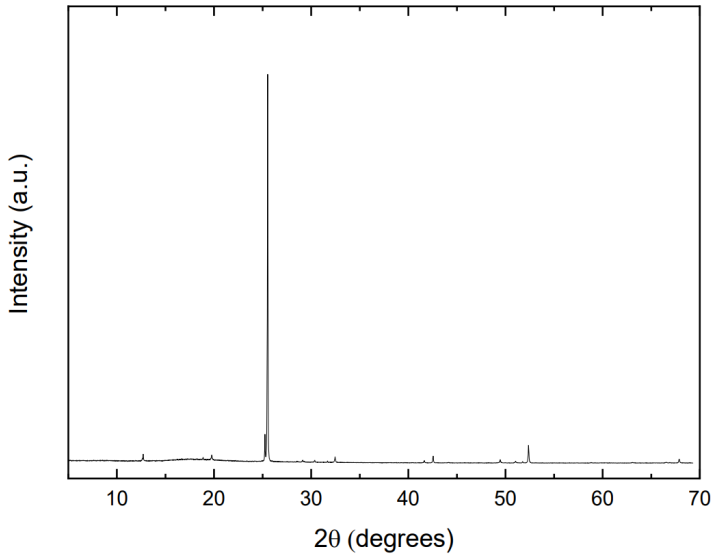

Figure 5.3: The ZnI_2 pattern shows a highly oriented film.

causing the release of MA and formation of Zn-OH bonds (Figure 5.1f) and Zn-I bonds (Figure 5.1g).

5.3 The Effect of Cation Acidity on Interface Degradation

Having confirmed the perovskite-ZnO instability resulting from the MA cation, one approach to improve the thermal stability of the interface is to decrease the acidity of the A site cation (the pKa of MA is ∼10.6). To that end, the less acidic formamidinium (FA) cation, with a pKa of 11.5, is utilized with the mixed FA and Cs cation system as a replacement for MA.[5,30] In the case of the FA cation, the positive charge is resonance stabilized due to the presence of two 'N' centers and thus has lower acidity than the MA cation, which is not resonance stabilized. While ZnO could abstract a proton from the FA cation, the rate of the reaction is expected to be considerably slower compared to the MA cation owing to the lower acidity of FA. This expectation is confirmed by utilizing the amine detector developed previously (Figure 5.1a-c). While the perovskite with MA cations produces sufficient amines for detection after annealing at 130 °C for 30 minutes, the perovskite with FA and Cs cations does not produce an appreciable absorbance change in the indicator solution, even after doubling the annealing time. After increasing the annealing temperature to 200 °C a small change in absorbance of the indicator solution is finally observed, as shown in the inset of Figure 5.4. The absorbance shift for both MA and FACs perovskites demonstrates the versatility of dinitrotoluene in detecting the degradation of these organic cations.

To examine the stability of perovskite thin films $FA_{0.83}Cs_{0.17}Pb(I_{0.83}Br_{0.17})_3$ (from now on termed FACs) is prepared on ZnO coated FTO and annealed at 100 °C from 5 to 60 minutes before collecting X-ray diffraction scans. For completeness, the $Cs_{0.05}(FA_{0.83}MA_{0.17})_{0.95}Pb(I_{0.83}Br_{0.17})_3$ perovskite (from here on termed CsFAMA) is also compared, which is one of the highest performing contemporary perovskite compositions and has also been used frequently in recent ZnO studies.[14,17,20] While there is an initial increase in crystallinity for $MAPbI_3$ from 5 to 15 minutes, continued annealing past this time results in the rapid generation of PbI_2, shown by a dominant XRD peak and a yellowed film (Figure 5.5a). The thermal stability of the CsFAMA perovskite is improved, but the PbI_2 peak intensity is greater than the (110) perovskite

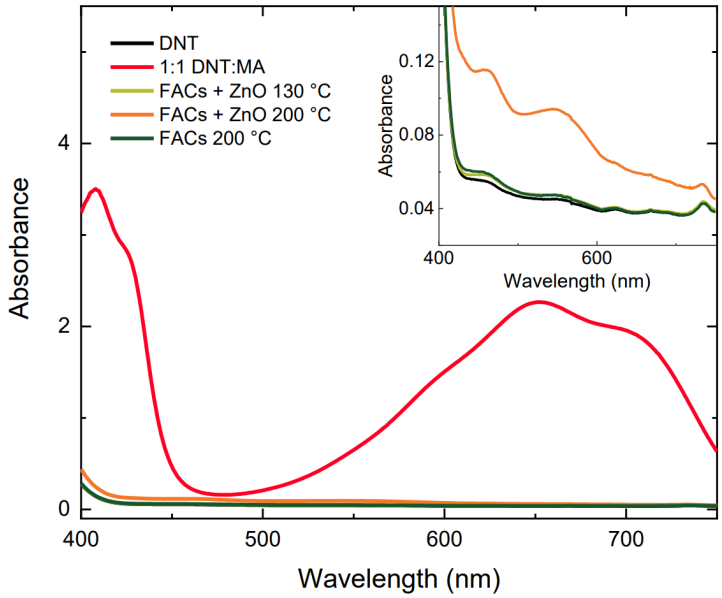

Figure 5.4: The absorbance shift of the indicator requires annealing at 200 °C with the FACs perovskite, as opposed to 130 °C with the MA perovskite.

reflection after an hour of annealing (Figure 5.5b). Close inspection of the CsFAMA film also reveals voids and cracks forming at the ZnO interface. In contrast, after one hour of annealing of the FACs perovskite at 100 °C the film remains dark and uniform, while a small PbI_2 peak is seen in the XRD scan (Figure 5.5c). Remarkably, while the PbI_2 peak intensity increases substantially for the ZnO-$MAPbI_3$ films from 30 to 60 minutes of annealing, the peak intensity remains virtually unchanged over this period for the FACs-ZnO films, indicating greatly reduced thermal degradation. A similar trend is observed on SnO_2, with CsFAMA perovskite being less thermally stable than FACs, which highlights the importance of using methylammonium-free perovskites for long-term stability in devices employing metal-oxide charge transport layers, as depicted in Figure 5.6.

In order to assess stability in operating conditions, devices with MA, CsFAMA, and FACs perovskite layers on ZnO are fabricated and placed under ∼1 sun illumination (76 mW cm^{-2} Xenon lamp solar aging box) at 60 °C for 8 hours. The devices were cross-sectioned to inspect the interface with SEM and dramatic differences were found, depending on the choice of the cation. Devices containing MA have numerous voids

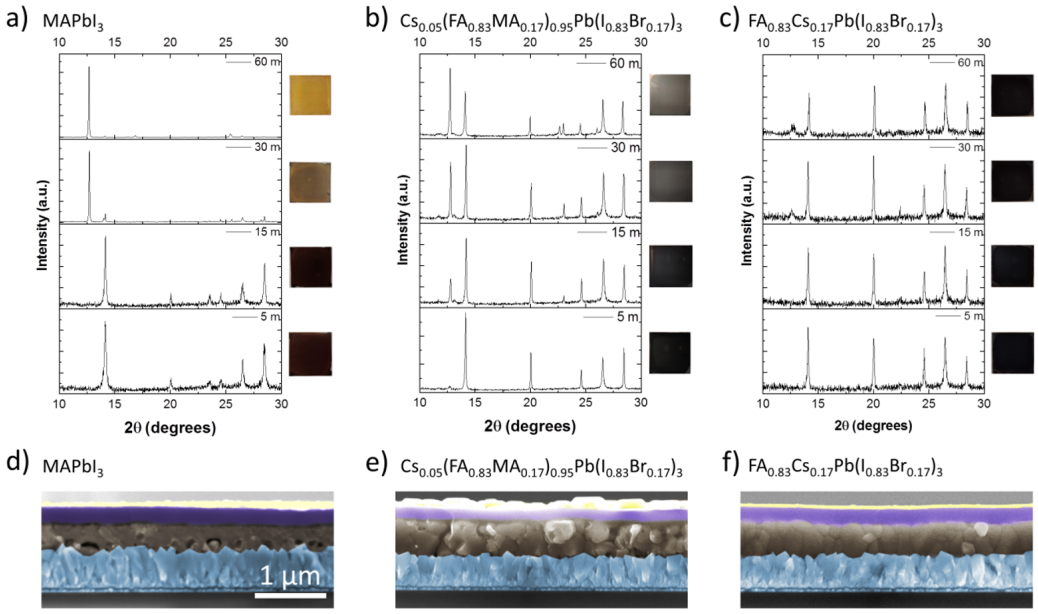

Figure 5.5: a) $MAPbI_3$ rapidly decomposes as 100°C annealing proceeds past 30 minutes, as indicated by a dominant PbI_2 peak and yellow film. The PbI_2 peak intensity increases sharply at 60 minutes of annealing, as the film is converted almost entirely to PbI_2. b) CsFAMA film offers greater stability but still displays clear discoloration after an hour of annealing. c) FACs perovskite shows a small PbI_2 peak after 30 minutes of annealing, and the peak intensity remains unchanged after additional annealing time. d) False-color SEM cross-section of $MAPbI_3$ devices with ZnO after aging 8 hours of unencapsulated aging (1 sun illumination, 60 °C, ∼50% humidity). e) SEM cross-section of aged CsFAMA device. f) SEM cross-section of aged FACs device.

at a visually degraded perovskite-ZnO interface, devices with CsFAMA show the emergence of smaller voids at the interface, and the devices with FACs cations retain conformal contact between the perovskite and ZnO (Figure 5.5d-f). The presence of voids in the perovskite, originating at the ZnO interface, is explainable by the generation of methylamine gas when the MA cation is deprotonated. Methylamine gas has previously been shown to "melt" $MAPbI_3$ upon exposure.[31] A likely explanation for this phenomenon is that the combination of loss of material (methylammonium halide), along with local melting of the perovskite in close proximity to the degradation sites, is responsible for the void growth. Also notable is that no ZnI_2 was detectable with XRD after annealing the FACs films.

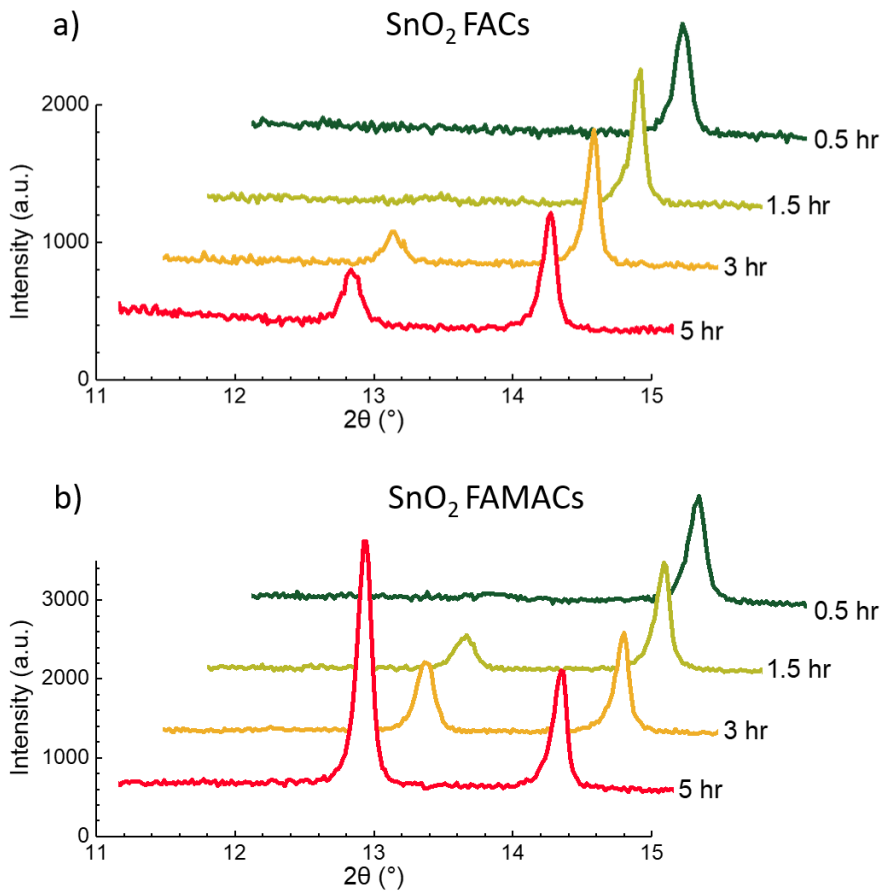

Figure 5.6: The PbI_2 peak evolves much more rapidly in the FAMACs film than in the FACs film when annealing at 100 °C under N_2.

5.4 Device Stability

Next, the stability of FACs PSC under UV irradiation and thermal stressing for devices containing ZnO, TiO_2, and SnO_2 electron transport layers (ETL) are compared. First, device degradation under a high intensity UV lamp is examined. Devices containing TiO_2 rapidly degrade, losing half of their power conversion efficiency in just 10 minutes and all power output within one hour (Figure 5.7a). One explanation for this instability is that upon photo-excitation of TiO_2, holes in the valence band recombine with electrons at oxygen adsorption sites, desorbing oxygen and creating deep trap states.[2] Surprisingly, while SnO_2-based PSC have recently shown improved stability over TiO_2 for long term stability in ambient operating conditions,[3] ZnO exhibits the best UV stability of the three metal oxides. ZnO is known to be UV sensitive as a material,

but these results suggest that unlike TiO_2, deep electron traps are not generated in the ZnO upon UV exposure.

Adding a thin layer of C_{60} to isolate the perovskite from direct ZnO contact further improved UV stability of the ZnO-perovskite interface (Figure 5.7a), similar to previous observations with SnO_2 and TiO_2 charge extraction layers.[31,32] Next, the thermal stability was probed by holding devices at 85 °C in ambient atmosphere and periodically testing their performance (Figure 5.7b). Devices with ZnO and MA cations show markedly reduced stability relative to those with FACs cations. While the C_{60} passivation layer increased ZnO device longevity under UV irradiation, the reduced thermal stability with C_{60} indicates different origins for thermally and UV induced degradation. Early in the thermal stability test, the C_{60} passivated ZnO provides better photovoltaic performance than unpassivated ZnO. However, as aging continues there is reduced Voc and lower fill factor relative to the unpassivated ZnO. The origin of the lower thermal stability with C_{60} is not clear, especially in light of previous observations that the addition of C_{60} to n-i-p cells employing a SnO_2 n-layer has improved the stability under combined light and heat (albeit at lower temperatures to this present study). A possibility is that C_{60} is known to aggregate and crystallize under thermal stress. It may be that the smooth crystalline ZnO surface presents a specifically mobile surface for C_{60} molecules. Previous studies of fullerenes under thermal stress have revealed that aggregations grow to the micron-scale, which would form shunt paths responsible for the observed fill factor and voltage losses.[33]

5.5 Device Performance

Having improved stability of the ZnO-perovskite interface by eliminating the MA cation, the device performance is investigated. Scanned efficiency of devices based on SnO_2 and ZnO achieved efficiencies of 20.3 and 21.1%, with 19.7% and 18.0% steady-state power output (SPO), respectively. Additional photovoltaic parameters are shown in Table 5.1. Scanned efficiency gains for ZnO devices over SnO_2 analogs

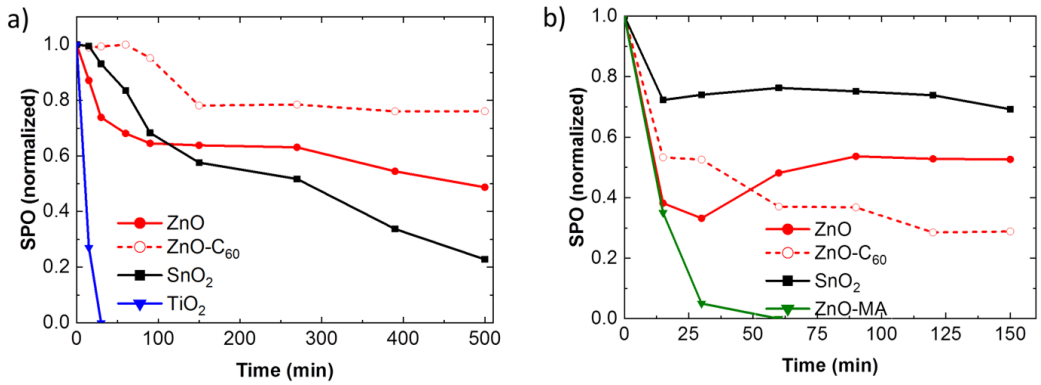

Figure 5.7: a) Under high intensity UV (365nm LED, equivalent to 12 suns UV component of AM 1.5 spectrum). b) Thermal stability of devices aged at 85 °C in air. All devices in UV and thermal stability tests utilized the $FA_{0.83}Cs_{0.17}Pb(I_{0.83}Br_{0.17})_3$ perovskite except for ZnO-MA, which utilized $MAPbI_3$.

are primarily driven by increased open-circuit voltage and a slight increase in fill factor, while the median current density decreased slightly due to reduced transmittance of ZnO in UV region of the spectrum as shown in Figure 5.9. It should be noted that the optical transmittance of ZnO can be increased with a variety of dopants, and B and F doping was recently shown to improve transmittance to 99.8% from 92.8% for undoped ZnO, but only undoped ZnO is evaluated for this study.[7,10] The lower steady-state power output of the ZnO-containing cells can be attributed in part to increased hysteresis relative to SnO_2 based cells. This is likely to originate due to an increased surface recombination velocity.[34] This may be due to either macroscopic defects on one of the charge extraction layers, enabling contact of the electrodes to the perovskite absorber layer, or a higher density of surface traps at the ZnO perovskite interface, responsible for trap assisted recombination. The activity of the surface recombination sites can be modulated by the migration of ions.[34,35] Large aggregates are also observed in the ZnO films, which are shown in the atomic force microscope images in Figure 5.10. It may be that these "spikes" in the ZnO are responsible for shorting paths in the solar cells, or induce pinholes in the perovskite films or subsequent layers, which may also contribute to the lower than anticipated SPO. Recent work has shown a thin passivating layer of MgO and ethanolamine, or ZnS, effectively eliminates hysteresis in ZnO-based PSC.[17,20]

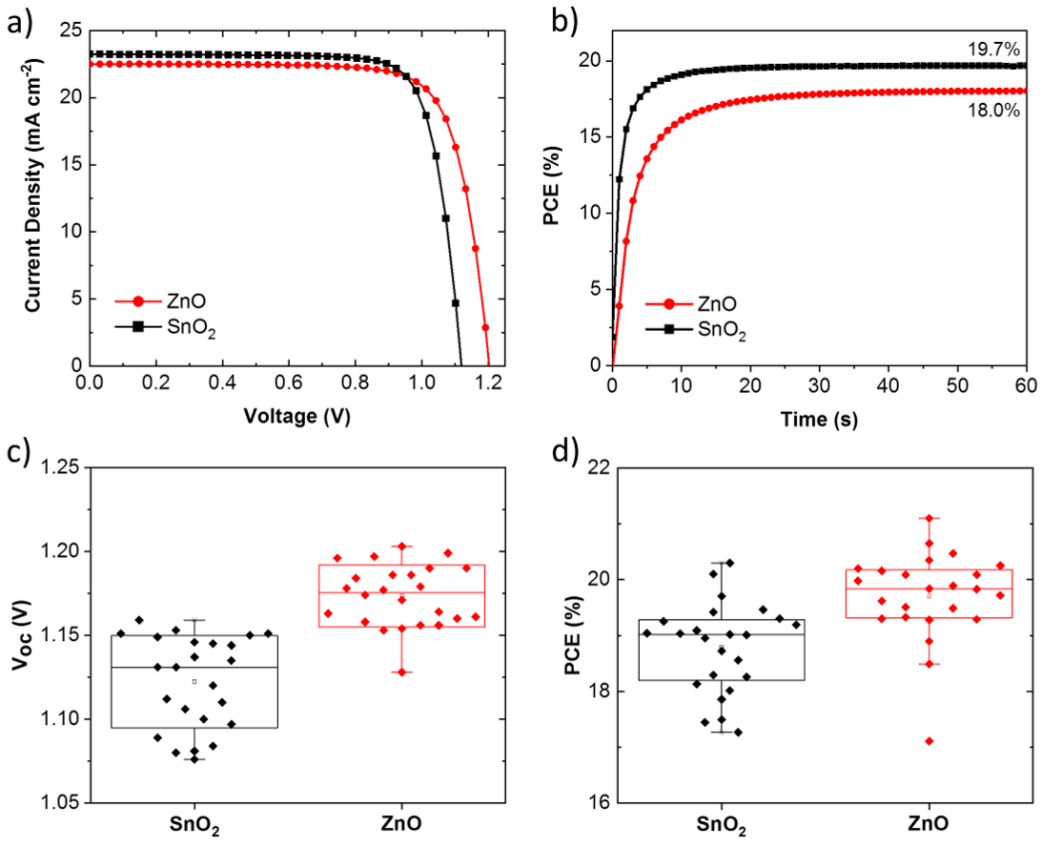

Figure 5.8: a) Champion SnO_2 and ZnO-based devices. b) Steady state power output of devices comprising SnO_2 and ZnO. c) PCE improvements on ZnO devices are driven primarily by improved open circuit voltage. d) PCE for 24 devices.

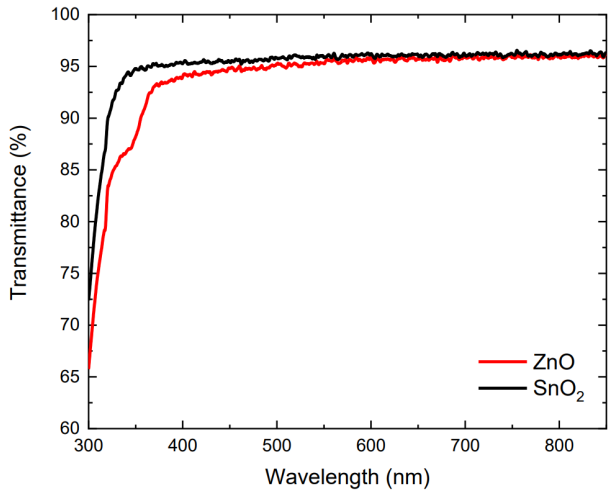

Figure 5.9: ZnO shows lower transmittance in the UV region.

Device	J_{sc} (mA cm^{-2})	V_{oc} (V)	FF	PCE (%)
ZnO				
Average	22.45 ± 1.07	1.17 ± 0.04	0.75 ± 0.03	19.1 ± 1.99
Champion	22.5	1.20	0.78	21.1
Stabilized				16.7 ± 1.74
SnO_2				
Average	22.52 ± 0.76	1.12 ± 0.04	0.75 ± 0.03	18.8 ± 1.52
Champion	23.1	1.13	0.78	20.3
Stabilized				17.9 ± 1.36

Table 5.1: Solar cell performance parameters determined from J-V Curves for 48 Devices

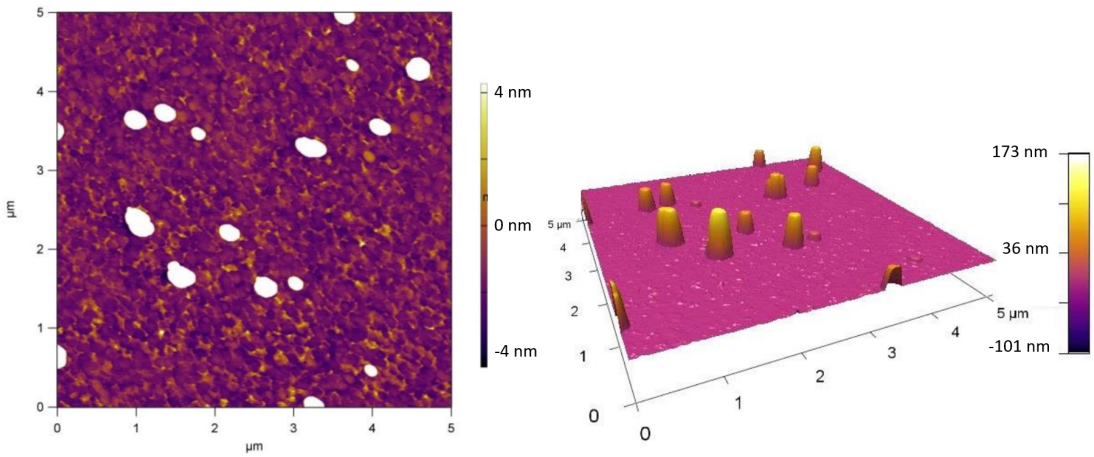

Figure 5.10: Pillars of around 200 nm in height appear, and were not removed after ultrasonication, filtration with 0.22 um PTFE filters, or cenrifugation, suggesting that nanopillars may form during spin coating. Atomic force microscopy performed by Alexandra Ramadan.

5.6 Interface Quality

To better understand the origin of the ZnO-based device performance, Kelvin probe and spectroscopic techniques are utilized to assess the quality of metal oxide-perovskite interfaces. Often, surface photovoltage (SPV) spectroscopy is used to probe the change in surface band bending under illumination. Here, the complete device stack is investigated, which includes the electron extraction layer, perovskite absorber layer, and hole transport layer. The surface photovoltage of the complete device stack is expected to reflect the open-circuit voltage generated within the cell.[36] Because ZnO-

based PSC show greater hysteresis than those with SnO_2, it is necessary to confirm the voltage increases of the ZnO-based PSC were not an artifact of scanning. Kelvin probe-based surface photo-voltage (SPV) measurement is used to asses the interface behavior, and a ∼120 mV higher SPV for the ZnO/perovskite/Spiro-OMeTAD stack is measured compared to their SnO_2 counterpart (Figure 5.11a), confirming a meaningful open-circuit voltage improvement. Similar behavior is observed for the stacks without the Spiro-OMeTAD layer, indicating that the voltage improvement for ZnO-based devices is mostly due to the difference in the metal oxide-perovskite interfaces.

Next, to determine whether the increased voltage results from decreased non-radiative recombination at the ZnO interface photoluminescence spectroscopy is utilized. This reveals more than 7 fold higher steady-state photoluminescence (PL) intensity from perovskite films on ZnO, in comparison to perovskite films on SnO_2. Remarkably, the steady-state PL intensity for FACs on ZnO is also greater than the PL intensity of FACs on glass alone. While a large portion of the PSC research community interprets PL quenching at open circuit to be an indicator of efficient charge transfer to selective contacts, more careful studies have shown that PL quenching is an undesirable result of surface recombination losses. However, some level of PL quenching relative to glass is typically observed when charge selective contacts are applied to the perovskite.[37] It is possible that the improved steady-state PL for ZnO relative to glass resulted from differences in substrate dependent crystallization of the perovskite or stoichiometry differences near the interface. XPS analysis of perovskites crystallized on AZO, for example, shows that the film stoichiometry deviates dramatically from both the precursor solution stoichiometry and from that of films on ITO.[14]

Time-resolved PL (TRPL) reveals average carrier lifetimes also improve from 65.7 ns to 134.4 ns (Figure 5.11b,c). It should be noted that treating ZnO with UV Ozone for 15 minutes substantially enhances the PL intensity, which may be due to removing organic contamination from the surface and/or removing defect sites in the ZnO by filling oxygen vacancies.[38,39] There is also a slight shift in photoluminescence maxima for perovskite films on ZnO and SnO_2 (767 and 765 nm, respectively), which may be

due to slight changes in crystallization or stoichiometry of perovskite films on these metal oxides which has been previously observed with TCO's.[14] The metal oxides also have different refractive indices, and this very small shift in emission wavelength may be due to an optical effect.

Photoluminescence quantum efficiency (PLQE) of perovskite films on SnO_2 and ZnO is also measured to more directly assess the interface defects. When excited with a 405 nm laser absorbed near the metal-oxide interface, PLQE of perovskite on ZnO increases substantially relative to the SnO_2 counterpart (Figure 5.11d), with values of 1.07% and 0.05% respectively, under $\sim$100 mW cm^{-2} irradiance. The increase in steady state PL emission, longer carrier lifetime, and improved PLQE are consistent with ZnO having reduced non-radiative recombination at the metal oxide-perovskite interface relative to SnO_2, which is consistent with the increased Voc.[40,41]

5.7 Conclusion

This chapter utilized thorough experimental evidence to demonstrate the causes of ZnO-perovskite interface instability, which arises primarily due to the deprotonation of the organic cation. While it had previously been hypothesized that the methylammonium cation was thermally unstable and could be degraded into methylamine gas, experimental evidence was lacking. This chapter introduced a novel indicator solution to directly confirm that the deprotonation of the methylammonium cation does, in fact, occur during direct contact with ZnO. FTIR spectra indicate that hydroxyl groups are generated during deprotonation while XRD showed the first evidence for the evolution of Zn halides as a degradation product. It was speculated that the degradation was driven by acid-base reactions between the ZnO and the organic cation, and the mixed formamidinium-cesium perovskite was introduced to mitigate this instability. The FACs perovskite provided greatly improved thermal stability, even when compared to the FAMACs triple cation that is widely used in the research community. It was also found that thermal stability on SnO_2, the most stable n-type metal oxide in

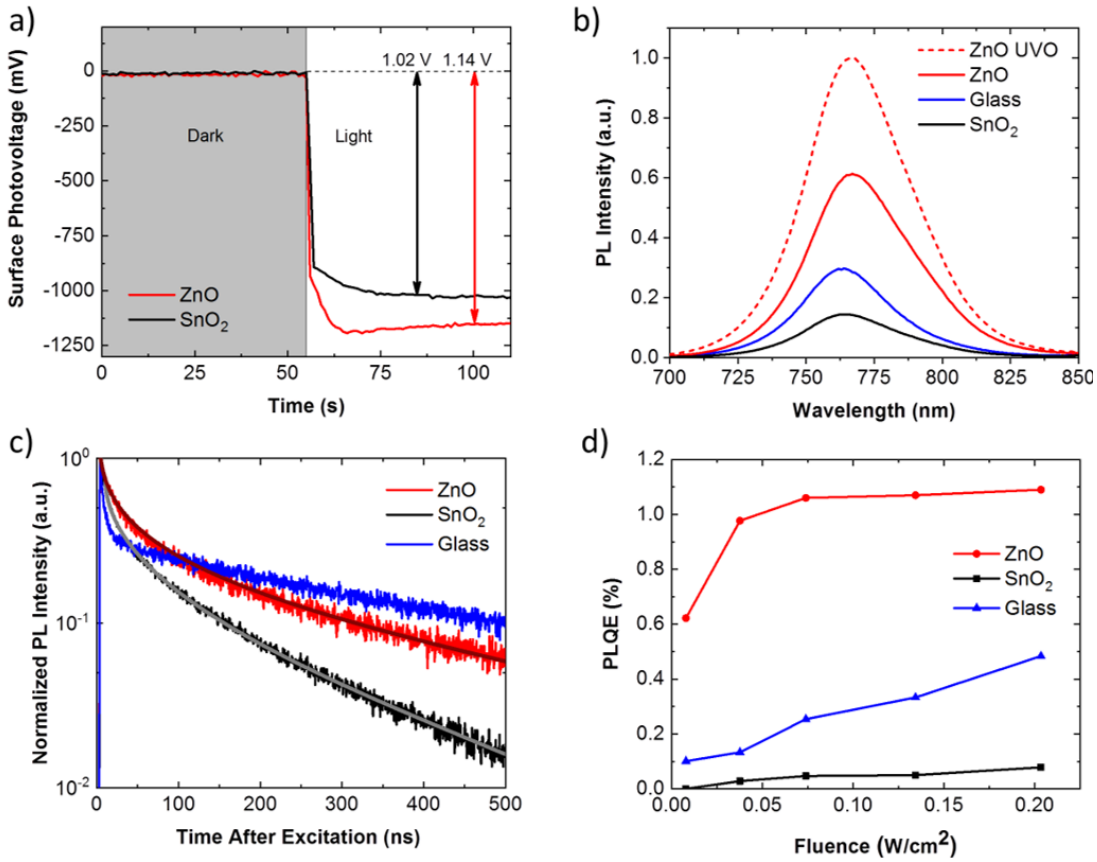

Figure 5.11: a) Kelvin probe measurement of surface photo-voltage of ZnO and SnO_2/perovskite/Spiro-OMeTAD films on FTO substrates. b) Steady state photoluminescence of FACs perovskite on SnO_2 and ZnO coated FTO. c) Time resolved photoluminescence spectroscopy of FACs perovskite on SnO_2 and ZnO substrates on FTO. d) PLQE of perovskite films on ZnO and SnO_2 coated FTO and quartz glass.

PSC, follows a similar trend to ZnO, with the FAMACs perovskite being notably less stable than FACs under thermal stress. Device data demonstrated the potential for ZnO as an n-type layer, with the scanned efficiency of ZnO devices improving over SnO_2 due to higher V_{oc}, but the lower SPO of ZnO devices was attributed to ZnO pillars that penetrate the absorber and/or HTM. Finally, interface studies including SPV and PL were consistent with the observed V_{oc} increase in full devices. The next chapter builds upon the work presented here and shows promising results for work that is currently underway to stabilize the SnO_2 interface and understand its unique degradation mechanisms.

References

1. NREL, "Nrel efficiency chart." `https://www.nrel.gov/pv/assets/pdfs/pv-efficiency-chart.20181221.pdf`. Accessed October, 2018.
2. T. Leijtens, G. E. Eperon, S. Pathak, A. Abate, M. M. Lee, and H. J. Snaith, "Overcoming ultraviolet light instability of sensitized TiO2 with meso-superstructured organometal tri-halide perovskite solar cells," *Nature Communications*, vol. 4, dec 2013.
3. J. A. Christians, P. Schulz, J. S. Tinkham, T. H. Schloemer, S. P. Harvey, B. J. T. de Villers, A. Sellinger, J. J. Berry, and J. M. Luther, "Tailored interfaces of unencapsulated perovskite solar cells for 1,000 hour operational stability," *Nature Energy*, vol. 3, pp. 68–74, jan 2018.
4. K. Choi, J. Lee, H. I. Kim, C. W. Park, G.-W. Kim, H. Choi, S. Park, S. A. Park, and T. Park, "Thermally stable, planar hybrid perovskite solar cells with high efficiency," *Energy & Environmental Science*, vol. 11, no. 11, pp. 3238–3247, 2018.
5. X. Zhao, H. Shen, Y. Zhang, X. Li, X. Zhao, M. Tai, J. Li, J. Li, X. Li, and H. Lin, "Aluminum-doped zinc oxide as highly stable electron collection layer for perovskite solar cells," *ACS Applied Materials & Interfaces*, vol. 8, pp. 7826–7833, mar 2016.
6. Y. Dkhissi, S. Meyer, D. Chen, H. C. Weerasinghe, L. Spiccia, Y.-B. Cheng, and R. A. Caruso, "Stability comparison of perovskite solar cells based on zinc oxide and titania on polymer substrates," *ChemSusChem*, vol. 9, pp. 687–695, feb 2016.
7. S. C. Dixon, D. O. Scanlon, C. J. Carmalt, and I. P. Parkin, "n-type doped transparent conducting binary oxides: an overview," *Journal of Materials Chemistry C*, vol. 4, no. 29, pp. 6946–6961, 2016.
8. Q. Zhang, C. S. Dandeneau, X. Zhou, and G. Cao, "ZnO nanostructures for dye-sensitized solar cells," *Advanced Materials*, vol. 21, pp. 4087–4108, nov 2009.
9. G. Hautier, A. Miglio, D. Waroquiers, G.-M. Rignanese, and X. Gonze, "How does chemistry influence electron effective mass in oxides? a high-throughput computational analysis," *Chemistry of Materials*, vol. 26, pp. 5447–5458, oct 2014.
10. K. Mahmood, S. Sarwar, and M. T. Mehran, "Current status of electron transport layers in perovskite solar cells: materials and properties," *RSC Advances*, vol. 7, no. 28, pp. 17044–17062, 2017.
11. Y.-H. Lin, S. R. Thomas, H. Faber, R. Li, M. A. McLachlan, P. A. Patsalas, and T. D. Anthopoulos, "Al-doped ZnO transistors processed from solution at 120 °c," *Advanced Electronic*

Materials, vol. 2, p. 1600070, apr 2016.

12. S. Bai, Z. Wu, X. Wu, Y. Jin, N. Zhao, Z. Chen, Q. Mei, X. Wang, Z. Ye, T. Song, R. Liu, S. tong Lee, and B. Sun, "High-performance planar heterojunction perovskite solar cells: Preserving long charge carrier diffusion lengths and interfacial engineering," *Nano Research*, vol. 7, pp. 1749–1758, aug 2014.

13. "Life-cycle assessment of silicon-perovskite tandem solar cells." https://www.cheops-project.eu/news-in-brief/first-results-regarding-the-environmental-impact-of-perovskitesilicon-tandem-pv-modules . Accessed October, 2018.

14. B. Dou, E. M. Miller, J. A. Christians, E. M. Sanehira, T. R. Klein, F. S. Barnes, S. E. Shaheen, S. M. Garner, S. Ghosh, A. Mallick, D. Basak, and M. F. A. M. van Hest, "High-performance flexible perovskite solar cells on ultrathin glass: Implications of the TCO," *The Journal of Physical Chemistry Letters*, vol. 8, pp. 4960–4966, sep 2017.

15. Y. Cheng, Q.-D. Yang, J. Xiao, Q. Xue, H.-W. Li, Z. Guan, H.-L. Yip, and S.-W. Tsang, "Decomposition of organometal halide perovskite films on zinc oxide nanoparticles," *ACS Applied Materials & Interfaces*, vol. 7, pp. 19986–19993, aug 2015.

16. J. Yang, B. D. Siempelkamp, E. Mosconi, F. D. Angelis, and T. L. Kelly, "Origin of the thermal instability in CH3nh3pbi3 thin films deposited on ZnO," *Chemistry of Materials*, vol. 27, pp. 4229–4236, jun 2015.

17. J. Cao, B. Wu, R. Chen, Y. Wu, Y. Hui, B.-W. Mao, and N. Zheng, "Efficient, hysteresis-free, and stable perovskite solar cells with ZnO as electron-transport layer: Effect of surface passivation," *Advanced Materials*, vol. 30, p. 1705596, jan 2018.

18. K. Mahmood, M. T. Mehran, F. Rehman, M. S. Zafar, S. W. Ahmad, and R.-H. Song, "Electrosprayed polymer-hybridized multidoped ZnO mesoscopic nanocrystals yield highly efficient and stable perovskite solar cells," *ACS Omega*, vol. 3, pp. 9648–9657, aug 2018.

19. F. Qin, W. Meng, J. Fan, C. Ge, B. Luo, R. Ge, L. Hu, F. Jiang, T. Liu, Y. Jiang, and Y. Zhou, "Enhanced thermochemical stability of CH3nh3pbi3 perovskite films on zinc oxides via new precursors and surface engineering," *ACS Applied Materials & Interfaces*, vol. 9, pp. 26045–26051, jul 2017.

20. R. Chen, J. Cao, Y. Duan, Y. Hui, T. T. Chuong, D. Ou, F. Han, F. Cheng, X. Huang, B. Wu, and N. Zheng, "High-efficiency, hysteresis-less, UV-stable perovskite solar cells with cascade ZnO–ZnS electron transport layer," *Journal of the American Chemical Society*, vol. 141, pp. 541–547, dec 2018.

21. A. Janotti and C. G. V. de Walle, "Fundamentals of zinc oxide as a semiconductor," *Reports on Progress in Physics*, vol. 72, p. 126501, oct 2009.

22. A. Degen and M. Kosec, "Effect of pH and impurities on the surface charge of zinc oxide in aqueous solution," *Journal of the European Ceramic Society*, vol. 20, pp. 667–673, may 2000.

23. A. L. Hunt, S. C. K. Yong, and J. F. Alder, "Towards a colorimetric spot test for the detection of methylamine. part 1. reaction of aliphatic amines with nitro-substituted benzene and toluene compounds to form meisenheimer complexes," *Analytical Communications*, vol. 33, no. 9, p. 323, 1996.

24. N. K. Noel, S. N. Habisreutinger, B. Wenger, M. T. Klug, M. T. Hörantner, M. B. Johnston, R. J. Nicholas, D. T. Moore, and H. J. Snaith, "A low viscosity, low boiling point, clean solvent system for the rapid crystallisation of highly specular perovskite films," *Energy & Environmental Science*, vol. 10, no. 1, pp. 145–152, 2017.

25. T. Glaser, C. Müller, M. Sendner, C. Krekeler, O. E. Semonin, T. D. Hull, O. Yaffe, J. S. Owen, W. Kowalsky, A. Pucci, and R. Lovrinčić, "Infrared spectroscopic study of vibrational modes in

methylammonium lead halide perovskites," *The Journal of Physical Chemistry Letters*, vol. 6, pp. 2913–2918, jul 2015.

26. C. G. V. de Walle, "Hydrogen as a cause of doping in zinc oxide," *Physical Review Letters*, vol. 85, pp. 1012–1015, jul 2000.

27. A. Top and H. Çetinkaya, "Zinc oxide and zinc hydroxide formation via aqueous precipitation: Effect of the preparation route and lysozyme addition," *Materials Chemistry and Physics*, vol. 167, pp. 77–87, nov 2015.

28. M. Y. Ghotbi, "Synthesis and characterization of nano-sized zn(OH)2 and its decomposed product, nano-zinc oxide," *Journal of Alloys and Compounds*, vol. 491, pp. 420–422, feb 2010.

29. İ. Kariper, "Optical and structural properties of zinc iodine thin films," *Optical Materials*, vol. 44, pp. 78–83, jun 2015.

30. T. J. Groshens and R. A. Hollins, "New chemical hydrogen storage materials exploiting the self-sustaining thermal decomposition of guanidinium borohydride," *Chemical Communications*, no. 21, p. 3089, 2009.

31. Z. Wang, D. P. McMeekin, N. Sakai, S. van Reenen, K. Wojciechowski, J. B. Patel, M. B. Johnston, and H. J. Snaith, "Efficient and Air-Stable Mixed-Cation Lead Mixed-Halide Perovskite Solar Cells with n-Doped Organic Electron Extraction Layers," *Advanced Materials*, vol. 29, no. 5, p. 1604186, 2017.

32. K. Wojciechowski, T. Leijtens, S. Siprova, C. Schlueter, M. T. Hörantner, J. T.-W. Wang, C.-Z. Li, A. K.-Y. Jen, T.-L. Lee, and H. J. Snaith, "C60 as an efficient n-type compact layer in perovskite solar cells," *The Journal of Physical Chemistry Letters*, vol. 6, pp. 2399–2405, jun 2015.

33. M. Campoy-Quiles, T. Ferenczi, T. Agostinelli, P. G. Etchegoin, Y. Kim, T. D. Anthopoulos, P. N. Stavrinou, D. D. C. Bradley, and J. Nelson, "Morphology evolution via self-organization and lateral and vertical diffusion in polymer:fullerene solar cell blends," *Nature Materials*, vol. 7, pp. 158–164, jan 2008.

34. S. van Reenen, M. Kemerink, and H. J. Snaith, "Modeling anomalous hysteresis in perovskite solar cells," *The Journal of Physical Chemistry Letters*, vol. 6, pp. 3808–3814, sep 2015.

35. P. Calado, A. M. Telford, D. Bryant, X. Li, J. Nelson, B. C. O'Regan, and P. R. Barnes, "Evidence for ion migration in hybrid perovskite solar cells with minimal hysteresis," *Nature Communications*, vol. 7, dec 2016.

36. F. Lenzmann, J. Krueger, S. Burnside, K. Brooks, M. Grätzel, D. Gal, S. Rühle, and D. Cahen, "Surface photovoltage spectroscopy of dye-sensitized solar cells with TiO2, nb2o5, and SrTiO3nanocrystalline photoanodes: indication for electron injection from higher excited dye states," *The Journal of Physical Chemistry B*, vol. 105, pp. 6347–6352, jul 2001.

37. T. Du, W. Xu, M. Daboczi, J. Kim, S. Xu, C.-T. Lin, H. Kang, K. Lee, M. J. Heeney, J.-S. Kim, J. R. Durrant, and M. A. McLachlan, "p-doping of organic hole transport layers in p–i–n perovskite solar cells: correlating open-circuit voltage and photoluminescence quenching," *Journal of Materials Chemistry A*, vol. 7, no. 32, pp. 18971–18979, 2019.

38. G. Gonçalves, A. Pimentel, E. Fortunato, R. Martins, E. Queiroz, R. Bianchi, and R. Faria, "UV and ozone influence on the conductivity of ZnO thin films," *Journal of Non-Crystalline Solids*, vol. 352, pp. 1444–1447, jun 2006.

39. C. E. Small, S. Chen, J. Subbiah, C. M. Amb, S.-W. Tsang, T.-H. Lai, J. R. Reynolds, and F. So, "High-efficiency inverted dithienogermole–thienopyrrolodione-based polymer solar cells," *Nature Photonics*, vol. 6, pp. 115–120, dec 2011.

40. M. Stolterfoht, C. M. Wolff, J. A. Márquez, S. Zhang, C. J. Hages, D. Rothhardt, S. Albrecht,

P. L. Burn, P. Meredith, T. Unold, and D. Neher, "Visualization and suppression of interfacial recombination for high-efficiency large-area pin perovskite solar cells," *Nature Energy*, vol. 3, pp. 847–854, jul 2018.

41. J.-P. Correa-Baena, W. Tress, K. Domanski, E. H. Anaraki, S.-H. Turren-Cruz, B. Roose, P. P. Boix, M. Grätzel, M. Saliba, A. Abate, and A. Hagfeldt, "Identifying and suppressing interfacial recombination to achieve high open-circuit voltage in perovskite solar cells," *Energy & Environmental Science*, vol. 10, no. 5, pp. 1207–1212, 2017.

CHAPTER 6

Cesium Salt Passivation of SnO_2 for Perovskite Solar Cells with Improved Stability and Performance

The research in this chapter is based on a manuscript in preparation:

Kelly Schutt; Suhas Mahesh; Hendrik Faber; Thomas Anthopoulos; Henry J. Snaith 'Cesium Salt Passivation of SnO_2 for Perovskite Solar Cells with Improved Stability and Performance'

K.S. made and characterized solar cells (J-V, EQE, UV-Vis, PL, and SPV, XRD, and SEM) and wrote the chapter. S.M. is modeling device degradation. H.F. and T.A. fabricated and characterized SnO_2 TFTs. Professor H.J.S. provided laboratory space, additional discussion, and financial support.

6.1 Introduction

SnO_2 has recently been used in recent PSC with a record-breaking power conversion efficiency of 23.3%,[1] where phenethylammonium iodide (PEAI) was used to passivate the perovskite-HTM interface and reduce non-radiative recombination. Despite the performance benefits offered by introducing the thin PEAI layer, devices with and without PEAI degraded at the same rate under thermal aging, and other passivation techniques have similarly failed to offer improved stability.[2] In order to advance PSC closer to their theoretical efficiency limits and improve their commercial viability, there is a clear need for passivation techniques that simultaneously improve device performance and long-term stability.

Metal oxide n-type charge transport layers such as TiO_2, SnO_2, and ZnO are some of the most commonly used selective contacts in PSC,[3–5] and thus passivation to improve the stability and performance at metal-oxide perovskite interfaces is of broad value to the research community. Metal oxide n-types also offer low-cost and improved performance compared to organic n-type materials such as fullerene derivatives. When considered as independent materials, metal oxide n-types should also provide improved thermal stability and be less sensitive to oxidative degradation,[6–9] although when in contact with perovskite absorbers these properties have been less relevant as the improved chemical compatibility of organic interlayers has a greater impact on device stability.

The most promising n-type metal oxide charge selective contact in perovskite solar cells appears to be SnO_2, due to its high performance and stability. Relative to TiO_2, SnO_2 provides greatly improved UV stability[10,11] which may be due to its larger

bandgap, which makes it transparent to most of the UV in the AM 1.5 spectrum.[12] SnO_2 also offers more favorable band alignment with the perovskite than TiO_2 and improved charge extraction due to having bulk mobility that is about 100 times greater than TiO_2.[13] SnO_2 has notable thermal stability for perovskites with organic cations as it is less basic than ZnO, and therefore organic cations in contact with SnO_2 are less susceptible to deprotonation.[14] Despite these benefits, there is a thermal instability that arises due to the direct contact of SnO_2 and perovskite films.[15] While isolating the perovskite absorber from direct contact with SnO_2 has been observed to improve the long-term stability of solar cells, the origin of the instability is not yet understood and potential degradation mechanisms have not been proposed.

Passivating interlayers have been the most widely used approach for mitigating perovskite-metal oxide interface instabilities, and these interlayers have most commonly been fullerene derivatives and carboxylate self-assembled monolayers.[16–24] In this chapter, cesium salts are applied at the SnO_2-perovskite interface as an inorganic passivation layer and found to improve the stability and performance of perovskite solar cells. While a range of alkali metal salts have previously been added to perovskite precursor solutions,[25–30] passivating the metal oxide-perovskite interface with Cs salts provides a thermally stable, inorganic contact to the metal oxide with an option for using salts that are expected to be chemically benign as they are already present in the mixed formamidinium-cesium perovskite absorber layer. While Cs halide salts are insulators with bandgaps of around 6 eV,[31] the remarkable performance of solar cells with a Cs salt interlayer suggests that charge transfer occurs through tunneling or through states at defect sites. In devices with a Cs salt-treated interface, V_{oc} improves by a median value of 50 mV, boosting median device efficiency from 17.7% to up to 19.1%, depending on the type of Cs salt treatment.

With respect to long-term stability, it is shown here that PbI_2 is generated at the SnO_2-perovskite interface during thermal aging. To prevent this degradation, CsBr is deposited on SnO_2 since it has poor solubility in perovskite precursor solutions,[32] making it more likely to remain at the SnO_2 surface during solution-processed perovskite

deposition. Most importantly, during thermal aging at 85 °C the onset of PbI_2 is delayed by a factor of ~6 for CsBr treated films, and in full devices stability is also improved under these conditions. While stability data for PSC are often collected under lower temperatures, 85 °C, is a crucial temperature for stress testing since the International Electrochemical Commission (IEC) damp heat test (85 °C and 85% relative humidity) is an industry-standard used to qualify solar cells for outdoor operation.[33,34] The results presented here demonstrate the potential for interface chemical engineering to achieve both improved performance and long-term stability for perovskite solar cells.

6.2 Device Data

The SnO_2 charge extraction layer was prepared by a low-temperature chemical bath process, as described elsewhere.[35] The SnO_2 layer was cleaned under UV Ozone and then treated with solutions of 2.5 and 10.0 mg/ml of cesium bromide (CsBr), cesium chloride (CsCl), cesium carbonate (Cs_2CO_3), and cesium acetate (CsAc) by spin coating from a 1:1 solution of IPA:H_2O at 4,000 rpm for 30 seconds, followed by annealing in ambient air at 150 °C for 10 minutes. To confirm that cesium salts were deposited on FTO after spin-coating and to evaluate morphology, FTO glass treated with 2.5 mg/ml and 10 mg/ml of CsBr was inspected with SEM, as shown in Figure 6.1. Viewed over small scales, CsBr deposition was non-uniform, with thick, high-contrast regions clearly visible against the underlying FTO. However, energy dispersive x-ray spectroscopy (EDX) confirms that CsBr is present across the regions where the thicker CsBr is not visible. At the higher 10 mg/ml concentration, CsBr grain boundaries are evident with dendritic growth present within grains. CsBr was also thermally evaporated with thicknesses of 5, 10, and 25 nm but film uniformity did not improve and device performance was degraded relative to the spin-coated CsBr treatment. An additional sintering step may improve the uniformity and coverage of

thermally evaporated CsBr films, but this was not attempted here as the spin-coated CsBr already offered notable improvement in device performance.

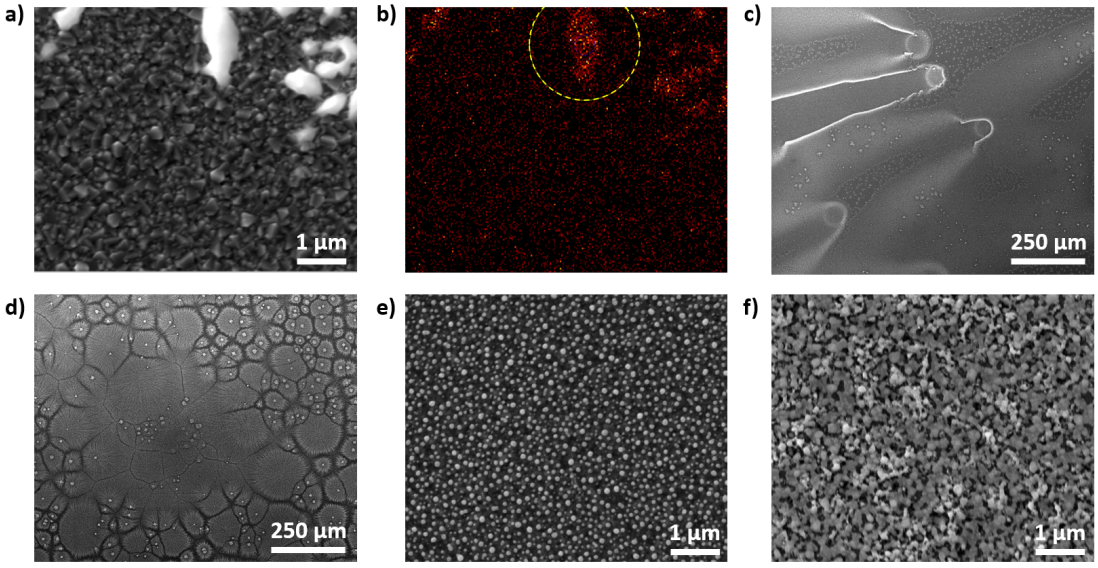

Figure 6.1: a) CsBr spin-coated on FTO at 2.5 mg/ml. b) EDX of the same region shows the bright region, with a higher Cs concentration, but also reveals Cs distributed across the substrate. The beam interaction volume is outlined in yellow. c) Large area view of sample. d) Large area view of sample treated with 10 mg/ml CsBr. e) Thermally evaporated CsBr at 10 nm thickness. f) Thermally evaporated CsBr at 25 nm thickness.

After preparing the Cs salt treated SnO_2, the methylammonium-free perovskite absorber layer $FA_{0.83}Cs_{0.17}Pb(I_{0.90}Br_{0.10})_3$ was deposited since it offers improved stability relative to perovskites with methylammonium cations and reasonably high power conversion efficiencies, exceeding 20%.[2,14,36,37] Improvements in device efficiency were primarily driven by increased V_{oc}, as shown in Figure 6.2, and median device efficiency improved from 17.7% for untreated devices to 19.1% for devices treated with CsCl. The concentration dependence of device performance varied with the type of cesium salt, with most cesium salts showing a negligible effect as concentration increased while Cs_2CO_3 device performance fell due to fill factor loss. The champion device performance improved from 18.4% for the untreated devices to 19.7% for devices treated with CsCl. Stabilized power output rose more dramatically, from 16.4% to 18.7% for the untreated and treated devices, respectively, as shown in Figure 6.3. The

external quantum efficiency also shows a slight improvement for CsBr treated devices, with improved charge collection in the near-infrared.

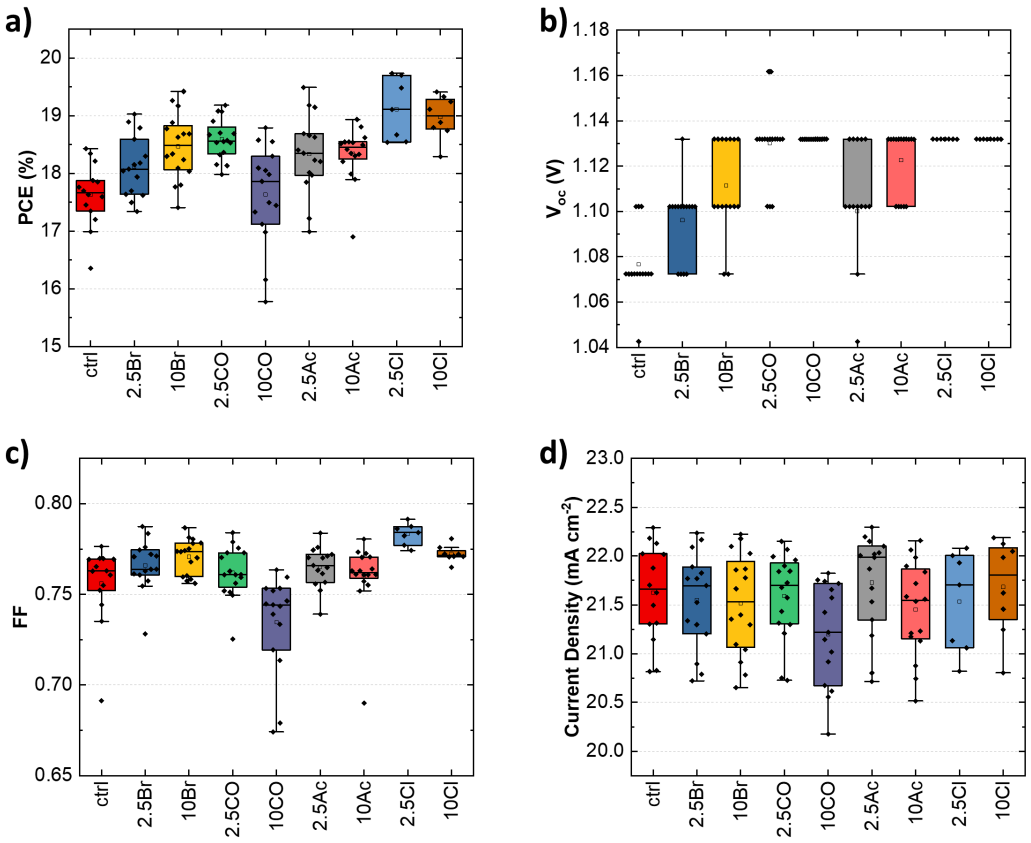

Figure 6.2: Statics for photovoltaic devices with and without cesium salt treatment. Power conversion efficiencies improve mainly due to increased V_{oc}. a) Power conversion efficiencies b) V_{oc} c) Fill factor d) Current density

6.3 Interface Characterization

To better understand the origin of the increased photovoltage, steady-state photoluminescence (PL) spectroscopy and Kelvin probe surface photovoltage (SPV) measurements were employed (Figure 6.4a,b). In the PL and SPV measurements, "half stack" samples were prepared where SnO_2 was grown on FTO and then treated with CsBr, followed by deposition of $FA_{0.83}Cs_{0.17}Pb(I_{0.90}Br_{0.10})_3$, but an HTM was not deposited. Compared to emission from the untreated films, PL intensity increased by a factor of 5 for CsBr treated films, which is consistent with a decreased trap density.

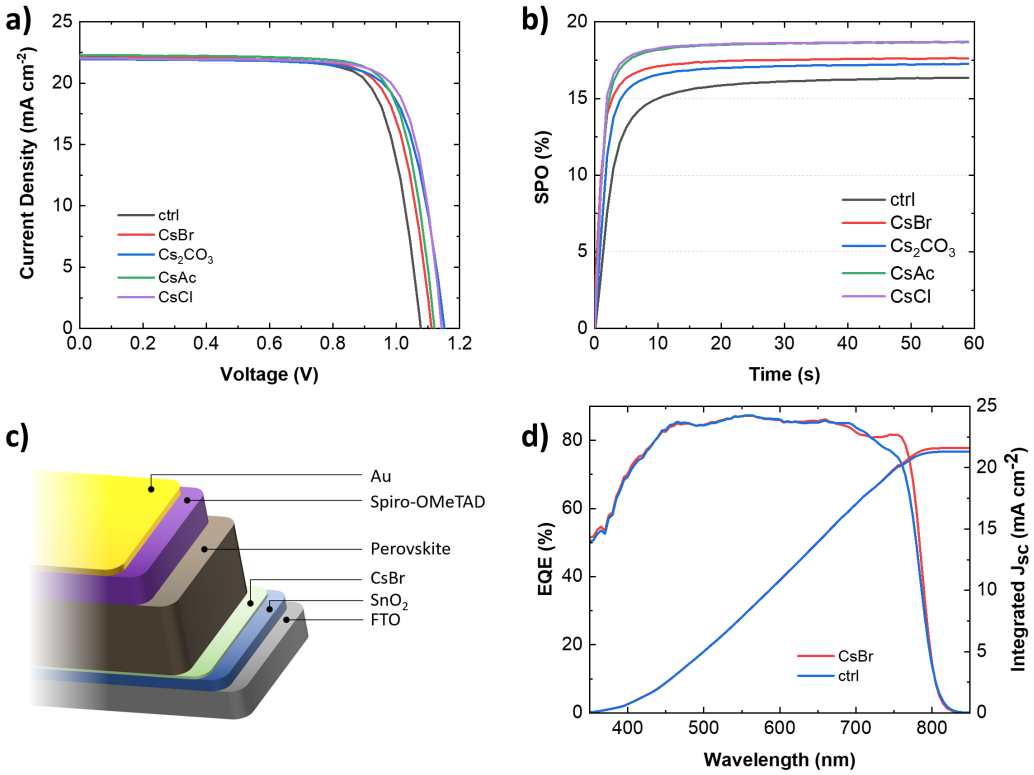

Figure 6.3: Data for champion devices. a) J-V curves b) Steady-state power output c) Device stack for photovoltaic devices is FTO/SnO_2/Cs salt/$FA_{0.83}Cs_{0.17}Pb(I_{0.90}Br_{0.10})_3$ d). External quantum efficiency of champion devices shows a slight improvement in charge collection for CsBr treated devices beyond the 725 nm wavelength.

The films also displayed increasing emission with increased CsBr concentration, which is the same trend observed in the V_{oc} for the devices. There was also a slight shift in the absorption onset to shorter wavelengths for perovskite films deposited on CsBr treated SnO_2, indicating a 10 meV increase in the optical bandgap, but such a small effect fails to account for the observed voltage improvement in devices. The improved open-circuit voltage should also be reflected in the half stack samples during SPV measurements, and indeed this is the case. SPV increased by ~75 mV for the CsBr treated SnO_2/perovskite films relative to the untreated SnO_2.

Thin film transistor (TFT) measurements were made to determine whether the improved voltages were unique to SnO_2-perovskite interfaces or could also be attributed to a change in the surface properties of the SnO_2 itself (Figure 6.4c-f). The optical transparency and reasonable conductivity of SnO_2 give it potential for TFTs used

in next-generation, flexible and transparent displays.[38–40] In the SnO_2 TFTs studied here, a lower concentration of CsBr (0.1 mg/ml) was applied to a ~10 nm thick SnO_2 layer on an Si wafer, since higher concentrations resulted in non-uniform coating and variation between TFT characteristics at the center and outer regions of the wafer. The saturation mobility of the CsBr treated SnO_2 TFTs improved from 0.053 $\pm$ 0.005 to 0.085 $\pm$ 0.012 cm^2 V^{-1} s^{-1}, indicating that CsBr may play a role in passivating surface defects in SnO_2. The field effect mobility increases from 0.040 $\pm$ 0.013 cm^2 V^{-1} s^{-1} for untreated SnO_2 to 0.084 $\pm$ 0.015 cm^2 V^{-1} s^{-1} Saturation mobility μ_{sat} was extracted according to:

$$\mu_{sat} = \frac{L}{WC_i}\frac{\partial^2 I_D}{\partial V_G^2} \tag{6.1}$$

Field effect mobility μ_{fe} was extracted according to:

$$\mu_{fe} = \frac{L}{WC_iV_D}\frac{\partial I_D}{\partial V_G} \tag{6.2}$$

where L was the channel length (40 um), W the channel width (1000 um), I_D the drain current, C_i the dielectric capacitance (69.1 nF cm^{-2}), and V_G the gate voltage. The on/off ratio also improved from 2.9 x 10^4 $\pm$ 1.5 x 10^4 for the untreated SnO_2 to 4.7 x 10^4 $\pm$ 6.7 x 10^3 for the CsBr treated SnO_2 TFTs. The TFT data also exhibit suppression of leakage current for the CsBr-treated devices, as shown by the large shift in threshold voltage (V_{th}), which could be due to passivation of O_2 vacancies. Oxygen vacancies are the main source of free electrons in semiconductor metal oxides,[41–43] and V_{th} can be increased in metal oxide TFTs by reducing the O_2 vacancy concentration.[44]. While a greater concentration of O_2 vacancies results in the high conductivity desirable for maximizing fill factor in solar cells, reducing O_2 vacancies in n-type metal oxides through UV-Ozone treatment has been shown to improve V_{OC} in perovskite solar cells.[14,45] Under these considerations, a CsBr interlayer appears to offer a method for controlling oxygen vacancy-mediated recombination pathways while also improving device stability.

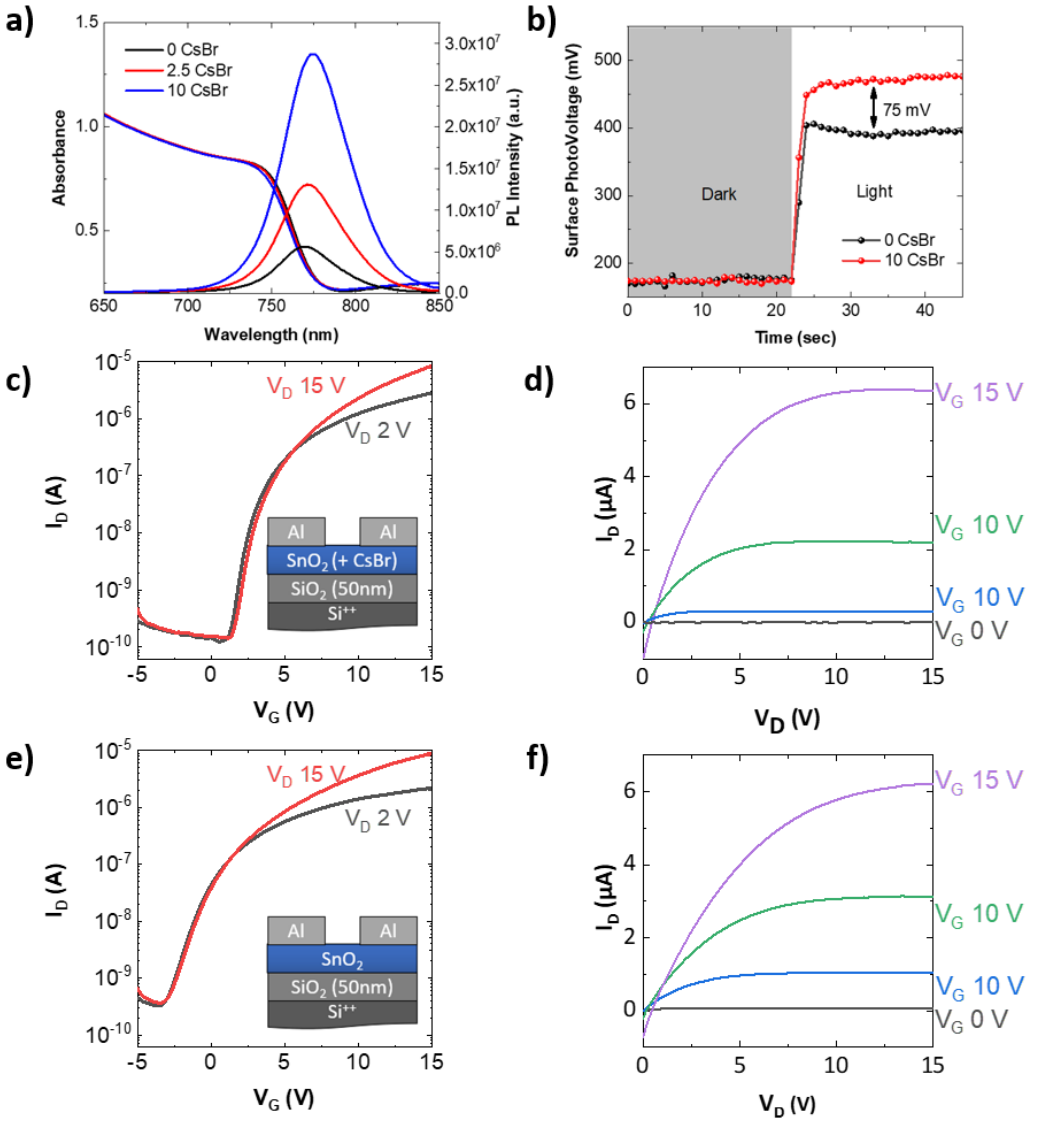

Figure 6.4: Optical and electronic properties of perovskite films on pristine and CsBr treated SnO_2. a) Relative to perovskite films on pristine SnO_2, steady state PL increases roughly ∼5 fold for perovskite films on CsBr treated SnO_2. b) Surface photovoltage increases by ∼75 mV for perovskite films on CsBr treated SnO_2, which matches the trend shown for photovoltaic device. c) Transfer curve for CsBr treated SnO_2 TFT. d) Output curve for CsBr treated SnO_2 TFT. e) Transfer curve for untreated SnO_2 TFT. f) Output curve for untreated SnO_2 TFT. TFT data collected by Hendrik Faber.

6.4 Stability of Cs Salt Passivated Interfaces and Devices

Next, both full devices of FTO/SnO_2/$FA_{0.83}Cs_{0.17}Pb(I_{0.90}Br_{0.10})_3$/Spiro-OMeTAD/Au and "half stacks" of FTO/SnO_2/$FA_{0.83}Cs_{0.17}Pb(I_{0.90}Br_{0.10})_3$ were subjected to thermal aging order to determine the effect of CsBr treatment on stability. The half stack

films were aged under N_2 at 85 °C and periodic x-ray diffraction (XRD) patterns were collected in ambient to determine whether crystalline products indicative of degradation were generated. In untreated devices, a clear peak for PbI_2 emerged after 24 hours of aging, as shown in Figure 6.5. In the half stacks treated with 10 mg ml^{-1} of CsBr at the SnO_2/perovskite interface, the PbI_2 reflection did not appear until after 6 days of aging, indicating greatly improved thermal stability of the interface.

Full devices were also subjected to the same thermal aging conditions and periodically measured, and the J-V scans of the champion SnO_2 devices are shown in Figure 6.5 e-f. While the devices on untreated SnO_2 degraded much more rapidly, both sets of devices exhibited substantial degradation in current, voltage, and fill factor after less than one week of aging, which largely attributable to the use of Li-TFSI and tBP for doping Spiro-OMeTAD. After 100 hours of aging, the device cross-sections were also inspected with SEM, which revealed the presence of brighter regions that appeared to originate at the SnO_2-perovskite interface. The greater contrast of these regions is likely due to the generation of PbI_2 at the interface, consistent with the XRD data.

6.5 Future Work

To better disentangle the contribution of the SnO_2-perovskite interface to device stability, alternative HTM and dopant systems are currently being evaluated including P3HT, PTAA doped with BCF, and CuSCN. Thus far power conversion efficiency has been limited to 15% in the best case with these HTMs. While thermal stability greatly improved, with no degradation observed for devices with a P3HT HTM even after 96 hours of thermal aging at 85 °C, producing simultaneously stable and efficient devices has proved challenging. An organic HTM (designated as CI-B3) and synthesized at Ecole Polytechnique fédérale de Lausanne (EPFL) will be evaluated soon, as it achieves a respectable power conversion efficiency of 18% without the use of dopants.

Additional work is also needed to determine the degradation mechanism(s) for SnO_2-perovskite interfaces, and three pathways are proposed here. First, since SnO_2 is

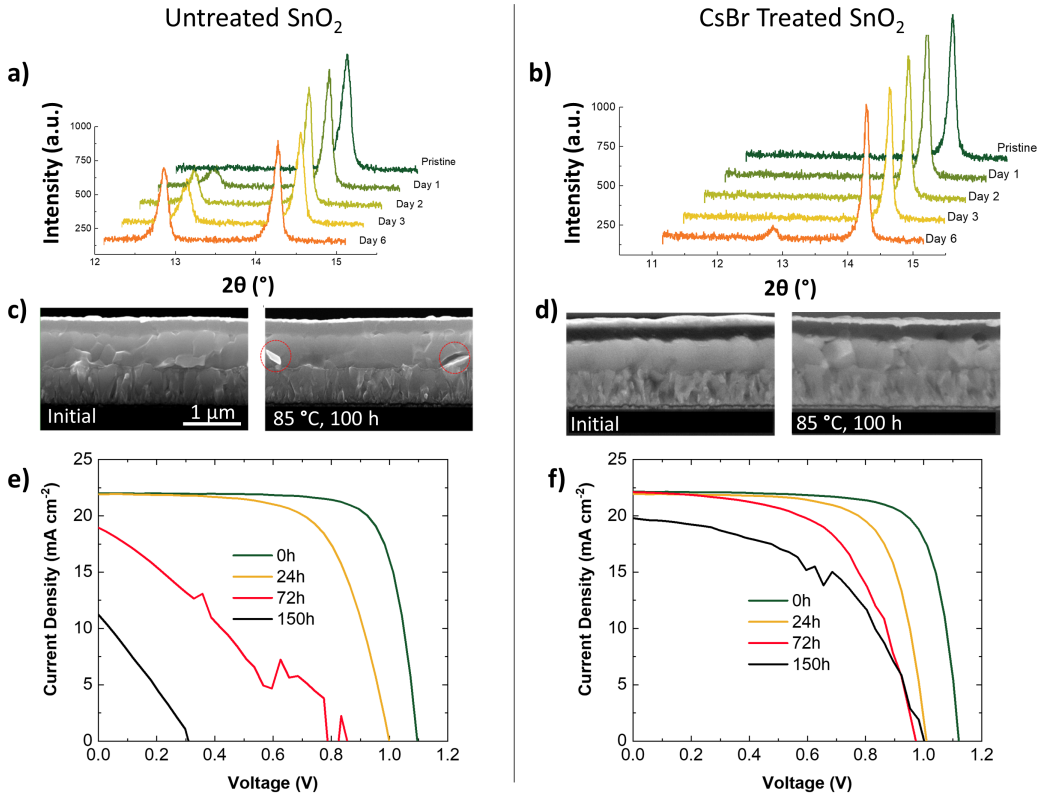

Figure 6.5: XRD shows a delayed onset of PbI_2 generation, while device data shows a slower decay of J-V curves. XRD data for films on SnO_2 and complete devices was collected after aging in an 85 °C oven, under N_2 for the specified time intervals. a) XRD data for bare SnO_2. b) XRD patterns for CsBr treated SnO_2. c) Cross sectional SEM of thermally aged devices on SnO_2 shows bright PbI_2 formation at the SnO_2-perovskite interface. d) Cross sectional SEM of thermally aged devices on CsBr treated SnO_2 shos the interface remains free of observable PbI_2. d) J-V curves for thermally aged devices, without CsBr treatment. e) J-V curves for thermally aged devices with CsBr treatment.

an amphoteric metal oxide, one possibility is that SnO_2 deprotonates the organic cation, forming $Sn(OH)_4$. In this case, the formation of tin hydroxide could be monitored with Fourier-transform infrared spectroscopy (FTIR). A second possibility is that SnO_2 catalyzes the degradation of the organic cation without forming $Sn(OH)_4$, which could be confirmed with the amine detection system presented in Chapter 5. While SnO_2 has generally good chemical resistance, it is susceptible to reactions with HI.[46] The archetypal $MAPbI_3$ has a low enthalpy of formation of just 0.1 eV and can decompose via a reversible reaction as follows:[47]

$$CH_3NH_3PbI_3(s) \longleftrightarrow CH_3NH_2(g) + HI(g) + PbI_2(s)$$

Such a reaction would be consistent with the PbI_2 present at the SnO_2-perovskite

interface shown in Figure 6.5, but additional characterization would be required to confirm that SnO_2 influences this pathway. The third possibility is that HI generated via this degradation pathway could potentially react with the SnO_2:

$$SnO_2(s) + 4\,HI(g) \longleftrightarrow SnI_4(s) + 2\,H_2O(l)$$

The H_2O generated at the interface may then go on to catalyze further perovskite decomposition. In this case, SnI_4 should be evident from the XRD patterns. Additional characterization work is ongoing to elucidate which chemical reactions occur.

6.6 Conclusion

This chapter demonstrates that CsBr passivation of SnO_2-perovskite interfaces simultaneously improves the stability and performance of PSC. The observed improvements in PCE were driven by a 50 mV increase in median V_{oc} for Cs salt-treated devices, which was consistent with the observed ~5-fold increase in PL and the enhanced surface photovoltage. Notably, CsBr treatment delayed the onset of PbI_2 during thermal aging by a factor of ~6. Device stability is inhibited by the Li-TFSI and tBP doped Spiro-OMeTAD, and the search for an HTM and dopant system with high power conversion efficiency and improved thermal stability is ongoing. While no degradation pathways specific to SnO_2-perovskite interfaces have been previously proposed in the literature, future work will evaluate the experimental evidence for the three possible mechanisms presented here.

References

1. Q. Jiang, Y. Zhao, X. Zhang, X. Yang, Y. Chen, Z. Chu, Q. Ye, X. Li, Z. Yin, and J. You, "Surface passivation of perovskite film for efficient solar cells," *Nature Photonics*, vol. 13, pp. 460–466, apr 2019.
2. J. S. Godding, A. J. Ramadan, Y.-H. Lin, K. Schutt, H. J. Snaith, and B. Wenger, "Oxidative passivation of metal halide perovskites," *Joule*, sep 2019.
3. M. Saliba, T. Matsui, K. Domanski, J.-Y. Seo, A. Ummadisingu, S. M. Zakeeruddin, J.-P. Correa-Baena, W. R. Tress, A. Abate, A. Hagfeldt, and M. Gratzel, "Incorporation of rubidium cations into perovskite solar cells improves photovoltaic performance," *Science*, vol. 354, pp. 206–209, sep 2016.
4. H. Tan, A. Jain, O. Voznyy, X. Lan, F. P. G. de Arquer, J. Z. Fan, R. Quintero-Bermudez, M. Yuan, B. Zhang, Y. Zhao, F. Fan, P. Li, L. N. Quan, Y. Zhao, Z.-H. Lu, Z. Yang, S. Hoogland, and E. H. Sargent, "Efficient and stable solution-processed planar perovskite solar cells via contact passivation," *Science*, vol. 355, pp. 722–726, feb 2017.
5. D. P. Mcmeekin, G. Sadoughi, W. Rehman, G. E. Eperon, M. Saliba, M. T. Horantner, A. Haghighirad, N. Sakai, L. Korte, B. Rech, and et al., "A mixed-cation lead mixed-halide perovskite absorber for tandem solar cells," *Science*, vol. 351, p. 151–155, Jul 2016.
6. R. Dattani, K. F. Gibson, S. Few, A. J. Borg, P. A. DiMaggio, J. Nelson, S. G. Kazarian, and J. T. Cabral, "Fullerene oxidation and clustering in solution induced by light," *Journal of Colloid and Interface Science*, vol. 446, pp. 24–30, may 2015.
7. W.-B. Ko and K.-N. Baek, "The oxidation of fullerenes (c60, c70) with various oxidants under ultrasonication," *Physics of the Solid State*, vol. 44, pp. 424–426, mar 2002.
8. K. L. Chen and M. Elimelech, "Aggregation and deposition kinetics of fullerene (c60) nanoparticles," *Langmuir*, vol. 22, pp. 10994–11001, dec 2006.
9. H. Jin, Y. Hou, F. Teng, P. Kopola, M. Tuomikoski, and A. Maaninen, "Effect of molecular aggregation by thermal treatment on photovoltaic properties of MEH-PPV: Fullerene-based solar cells," *Solar Energy Materials and Solar Cells*, vol. 93, pp. 289–294, feb 2009.
10. T. Leijtens, G. E. Eperon, S. Pathak, A. Abate, M. M. Lee, and H. J. Snaith, "Overcoming ultraviolet light instability of sensitized TiO2 with meso-superstructured organometal tri-halide perovskite solar cells," *Nature Communications*, vol. 4, dec 2013.
11. J. A. Christians, P. Schulz, J. S. Tinkham, T. H. Schloemer, S. P. Harvey, B. J. T. de Villers,

A. Sellinger, J. J. Berry, and J. M. Luther, "Tailored interfaces of unencapsulated perovskite solar cells for 1,000 hour operational stability," *Nature Energy*, vol. 3, pp. 68–74, jan 2018.

12. P. Tiwana, P. Docampo, M. B. Johnston, H. J. Snaith, and L. M. Herz, "Electron mobility and injection dynamics in mesoporous ZnO, SnO2, and TiO2 films used in dye-sensitized solar cells," *ACS Nano*, vol. 5, pp. 5158–5166, may 2011.

13. Q. Jiang, L. Zhang, H. Wang, X. Yang, J. Meng, H. Liu, Z. Yin, J. Wu, X. Zhang, and J. You, "Enhanced electron extraction using SnO2 for high-efficiency planar-structure HC(NH2)2pbi3-based perovskite solar cells," *Nature Energy*, vol. 2, nov 2016.

14. K. Schutt, P. K. Nayak, A. J. Ramadan, B. Wenger, Y.-H. Lin, and H. J. Snaith, "Overcoming zinc oxide interface instability with a methylammonium-free perovskite for high-performance solar cells," *Advanced Functional Materials*, p. 1900466, jun 2019.

15. K. Choi, J. Lee, H. I. Kim, C. W. Park, G.-W. Kim, H. Choi, S. Park, S. A. Park, and T. Park, "Thermally stable, planar hybrid perovskite solar cells with high efficiency," *Energy & Environmental Science*, vol. 11, no. 11, pp. 3238–3247, 2018.

16. J. Wang, K. Datta, C. H. L. Weijtens, M. M. Wienk, and R. A. J. Janssen, "Insights into fullerene passivation of SnO 2 electron transport layers in perovskite solar cells," *Advanced Functional Materials*, p. 1905883, sep 2019.

17. A. Pérez-Tomás, A. Mingorance, D. Tanenbaum, and M. Lira-Cantú, "Metal oxides in photovoltaics: All-oxide, ferroic, and perovskite solar cells," in *The Future of Semiconductor Oxides in Next-Generation Solar Cells*, pp. 267–356, Elsevier, 2018.

18. L. Zuo, Q. Chen, N. D. Marco, Y.-T. Hsieh, H. Chen, P. Sun, S.-Y. Chang, H. Zhao, S. Dong, and Y. Yang, "Tailoring the interfacial chemical interaction for high-efficiency perovskite solar cells," *Nano Letters*, vol. 17, pp. 269–275, dec 2016.

19. K. Liu, S. Chen, J. Wu, H. Zhang, M. Qin, X. Lu, Y. Tu, Q. Meng, and X. Zhan, "Fullerene derivative anchored SnO2 for high-performance perovskite solar cells," *Energy & Environmental Science*, vol. 11, no. 12, pp. 3463–3471, 2018.

20. T. Gatti, E. Menna, M. Meneghetti, M. Maggini, A. Petrozza, and F. Lamberti, "The renaissance of fullerenes with perovskite solar cells," *Nano Energy*, vol. 41, pp. 84–100, nov 2017.

21. W. Ke, D. Zhao, C. Xiao, C. Wang, A. J. Cimaroli, C. R. Grice, M. Yang, Z. Li, C.-S. Jiang, M. Al-Jassim, K. Zhu, M. G. Kanatzidis, G. Fang, and Y. Yan, "Cooperative tin oxide fullerene electron selective layers for high-performance planar perovskite solar cells," *Journal of Materials Chemistry A*, vol. 4, no. 37, pp. 14276–14283, 2016.

22. L. Kegelmann, C. M. Wolff, C. Awino, F. Lang, E. L. Unger, L. Korte, T. Dittrich, D. Neher, B. Rech, and S. Albrecht, "It takes two to tango—double-layer selective contacts in perovskite solar cells for improved device performance and reduced hysteresis," *ACS Applied Materials & Interfaces*, vol. 9, pp. 17245–17255, may 2017.

23. D. Yang, R. Yang, K. Wang, C. Wu, X. Zhu, J. Feng, X. Ren, G. Fang, S. Priya, and S. Liu, "High efficiency planar-type perovskite solar cells with negligible hysteresis using EDTA-complexed SnO2," *Nature Communications*, vol. 9, aug 2018.

24. K. Wojciechowski, S. D. Stranks, A. Abate, G. Sadoughi, A. Sadhanala, N. Kopidakis, G. Rumbles, C.-Z. Li, R. H. Friend, A. K.-Y. Jen, and H. J. Snaith, "Heterojunction modification for highly efficient organic–inorganic perovskite solar cells," *ACS Nano*, vol. 8, pp. 12701–12709, dec 2014.

25. W. Zhao, Z. Yao, F. Yu, D. Yang, and S. F. Liu, "Alkali metal doping for improved CH3 NH3 PbI3 perovskite solar cells," *Advanced Science*, vol. 5, p. 1700131, dec 2017.

26. M. Abdi-Jalebi, Z. Andaji-Garmaroudi, S. Cacovich, C. Stavrakas, B. Philippe, J. M. Richter,

M. Alsari, E. P. Booker, E. M. Hutter, A. J. Pearson, S. Lilliu, T. J. Savenije, H. Rensmo, G. Divitini, C. Ducati, R. H. Friend, and S. D. Stranks, "Maximizing and stabilizing luminescence from halide perovskites with potassium passivation," *Nature*, vol. 555, pp. 497–501, mar 2018.

27. R. Zhang, M. Li, Y. Huan, J. Xi, S. Zhang, X. Cheng, H. Wu, W. Peng, Z. Bai, and X. Yan, "A potassium thiocyanate additive for hysteresis elimination in highly efficient perovskite solar cells," *Inorganic Chemistry Frontiers*, vol. 6, no. 2, pp. 434–442, 2019.

28. T. J. Jacobsson, S. Svanström, V. Andrei, J. P. H. Rivett, N. Kornienko, B. Philippe, U. B. Cappel, H. Rensmo, F. Deschler, and G. Boschloo, "Extending the compositional space of mixed lead halide perovskites by cs, rb, k, and na doping," *The Journal of Physical Chemistry C*, vol. 122, pp. 13548–13557, jan 2018.

29. D. J. Kubicki, D. Prochowicz, A. Hofstetter, S. M. Zakeeruddin, M. Grätzel, and L. Emsley, "Phase segregation in potassium-doped lead halide perovskites from 39k solid-state NMR at 21.1 t," *Journal of the American Chemical Society*, vol. 140, pp. 7232–7238, may 2018.

30. J. K. Nam, S. U. Chai, W. Cha, Y. J. Choi, W. Kim, M. S. Jung, J. Kwon, D. Kim, and J. H. Park, "Potassium incorporation for enhanced performance and stability of fully inorganic cesium lead halide perovskite solar cells," *Nano Letters*, vol. 17, pp. 2028–2033, feb 2017.

31. A. Y. Kuznetsov, "First-principles calculations of the electronic structure and plastic properties of CsCl, CsBr, and CsI crystals," *Physics of the Solid State*, vol. 47, no. 11, p. 2030, 2005.

32. D. N. Dirin, I. Cherniukh, S. Yakunin, Y. Shynkarenko, and M. V. Kovalenko, "Solution-grown CsPbBr3 perovskite single crystals for photon detection," *Chemistry of Materials*, vol. 28, pp. 8470–8474, nov 2016.

33. J. H. Wohlgemuth and M. D. Kempe, "Equating damp heat testing with field failures of PV modules," in *2013 IEEE 39th Photovoltaic Specialists Conference (PVSC)*, IEEE, jun 2013.

34. S. Goranti and G. TamizhMani, "Potential induced degradation (PID) study on accelerated stress tested PV modules," in *2012 38th IEEE Photovoltaic Specialists Conference*, IEEE, jun 2012.

35. E. H. Anaraki, A. Kermanpur, L. Steier, K. Domanski, T. Matsui, W. Tress, M. Saliba, A. Abate, M. Grätzel, A. Hagfeldt, and J.-P. Correa-Baena, "Highly efficient and stable planar perovskite solar cells by solution-processed tin oxide," *Energy & Environmental Science*, vol. 9, no. 10, pp. 3128–3134, 2016.

36. D. Ramirez, K. Schutt, J. F. Montoya, S. Mesa, J. Lim, H. J. Snaith, and F. Jaramillo, "Meso-superstructured perovskite solar cells: Revealing the role of the mesoporous layer," *The Journal of Physical Chemistry C*, vol. 122, pp. 21239–21247, aug 2018.

37. M. L. Petrus, K. Schutt, M. T. Sirtl, E. M. Hutter, A. C. Closs, J. M. Ball, J. C. Bijleveld, A. Petrozza, T. Bein, T. J. Dingemans, T. J. Savenije, H. Snaith, and P. Docampo, "New generation hole transporting materials for perovskite solar cells: Amide-based small-molecules with nonconjugated backbones," *Advanced Energy Materials*, vol. 8, p. 1801605, oct 2018.

38. J. H. Na, M. Kitamura, and Y. Arakawa, "High performance n-channel thin-film transistors with an amorphous phase C60 film on plastic substrate," *Applied Physics Letters*, vol. 91, p. 193501, nov 2007.

39. E. N. Dattoli, Q. Wan, W. Guo, Y. Chen, X. Pan, and W. Lu, "Fully transparent thin-film transistor devices based on SnO2 nanowires," *Nano Letters*, vol. 7, pp. 2463–2469, aug 2007.

40. K.-W. Jo, S.-W. Moon, and W.-J. Cho, "Fabrication of high-performance ultra-thin-body SnO2 thin-film transistors using microwave-irradiation post-deposition annealing," *Applied Physics Letters*, vol. 106, p. 043501, jan 2015.

41. S. Hwang, J. H. Lee, C. H. Woo, J. Y. Lee, and H. K. Cho, "Effect of annealing temperature

on the electrical performances of solution-processed InGaZnO thin film transistors," *Thin Solid Films*, vol. 519, pp. 5146–5149, may 2011.

42. S.-Y. Sung, K.-M. Jo, S.-Y. Kim, J.-H. Lee, J.-J. Kim, and Y.-W. Heo, "Effects of post-annealing treatments on the transfer characteristics of amorphous indium-gallium-zinc oxide thin film transistors," *Journal of Nanoelectronics and Optoelectronics*, vol. 6, pp. 310–314, aug 2011.

43. S. Park, S. Bang, S. Lee, J. Park, Y. Ko, and H. Jeon, "The effect of annealing ambient on the characteristics of an indium–gallium–zinc oxide thin film transistor," *Journal of Nanoscience and Nanotechnology*, vol. 11, pp. 6029–6033, jul 2011.

44. P. D.M., R. Mannam, M. R. Rao, and N. DasGupta, "Effect of annealing ambient on SnO2 thin film transistors," *Applied Surface Science*, vol. 418, pp. 414–417, oct 2017.

45. A. Klasen, P. Baumli, Q. Sheng, E. Johannes, S. A. Bretschneider, I. M. Hermes, V. W. Bergmann, C. Gort, A. Axt, S. A. L. Weber, H. Kim, H.-J. Butt, W. Tremel, and R. Berger, "Removal of surface oxygen vacancies increases conductance through TiO2 thin films for perovskite solar cells," *The Journal of Physical Chemistry C*, vol. 123, pp. 13458–13466, may 2019.

46. E. R. Caley, "The action of hydriodic acid on stannic oxide," *Journal of the American Chemical Society*, vol. 54, no. 8, p. 3240–3243, 1932.

47. J. A. Mcleod and L. Liu, "Prospects for mitigating intrinsic organic decomposition in methylammonium lead triiodide perovskite," *The Journal of Physical Chemistry Letters*, vol. 9, no. 9, p. 2411–2417, 2018.

CHAPTER 7

New Generation Hole Transporting Materials for Perovskite Solar Cells: Amide-Based Small-Molecules with Nonconjugated Backbones

The research in this chapter is based on the following publication:

Michiel L. Petrus; Kelly Schutt; Maximilian T. Sirtl; Eline M. Hutter; Anna C. Closs; James M. Ball; Johan C. Bijleveld; Annamaria Petrozza; Thomas Bein; Theo J. Dingemans; Tom J. Savenije; Henry J. Snaith; Pablo Docampo 'New Generation Hole Transporting Materials for Perovskite Solar Cells: Amide-Based Small-Molecules with Nonconjugated Backbones', Adv. Energy Mater., 8, 1801605

DOI: 10.1002/aenm.201801605

Direct link: `https://onlinelibrary.wiley.com/doi/full/10.1002/aenm.201801605`

Reproduced with permission. Copyright © 2019 John Wiley and Sons. License agreement available at https://s100.copyright.com/App/PaymentTermsAndConditions.jsp

M.P. synthesized the EDOT-Amide-TPA HTM and coordinated characterization and device work occurring in other labs. K.S. optimized HTM processing, made and characterized solar cells, provided stability data, provided manuscript edits and formatted the work for this chapter, and provided additional discussion included here. M.S. did additional synthesis and characterization of the HTM. E.M. performed time-resolved microwave conductivity measurements. A.C. characterized hole mobility and conductivity. J.M.B. fabricated and measured organic field effect transistors. J.C.B. provided differential scanning calorimetry and thermogravimetric analysis. Professors A.P., T.B., T.D., T.S., H.J.S., and P.D. provided laboratory space, additional discussion, and financial support.

7.1 Introduction

State-of-the-art perovskite-based solar cells employ expensive, organic hole transporting materials (HTMs) such as Spiro-OMeTAD that, in turn, limit the commercialization of this promising technology. In this chapter, an HTM (EDOT-Amide-TPA) is reported in which a functional amide-based backbone is introduced, which allows this material to be synthesized in a simple condensation reaction with an estimated cost of $<\$5\ g^{-1}$. When employed in perovskite solar cells, EDOT-Amide-TPA demonstrates steady-state power output up to 20.0% and outperforms Spiro-OMeTAD in direct comparisons. Time-resolved microwave conductivity measurements (TMRC) indicate that the observed improvement originates from a faster hole injection rate from the perovskite to EDOT-Amide-TPA. Additionally, the devices exhibit an improved lifetime, which is assigned to the coordination of the amide bond to the Li-additive, offering a novel strategy to hamper the migration of additives. Despite the lack of a conjugated backbone, the amide-based HTM can outperform state-of-the-art HTMs at a fraction

of the cost, thereby providing a novel set of design strategies to develop new, low-cost HTMs.

Although efficient inorganic hole transporting materials (HTMs) have been reported,[1] the most well-known HTMs are the organic materials 2,2,7,7-tetrakis- (N,N-di-4-methoxyphenylamino)-9,9- spirobifluorene (Spiro-OMeTAD) and polytriarylamine (PTAA). Alternatives that compete in performance have been published,[2–4] however, just like Spiro-OMeTAD and PTAA, most of these materials require multi-step synthetic procedures, involving (transition) metal-catalyzed cross-coupling reactions, stringent reaction conditions, and extensive product purification. This results in a relatively high material cost, which contributes significantly to the total device cost.[2,5,6] Additionally, the tedious synthesis hampers large scale production of these materials and thereby could impede the commercial success of perovskite solar cells.

In contrast, condensation chemistry has proven its value as a low-cost and easily scalable chemistry to prepare organic HTMs for perovskite solar cells.[7–9] More importantly, no expensive metal catalysts are required when using this chemistry, the synthesis can be done at ambient conditions and since water is the only side-product, product purification is straightforward.[10] Azomethine-, enamine-, and hydrazone-based organic molecules have been reported as HTMs, although none of these materials have been able to outperform state-of-the-art materials.[7,9,11,12]

Aromatic amides can also be synthesized using simple condensation chemistry and are well-known as building blocks for high-performance polymers with outstanding chemical and thermal stability. Kevlar is perhaps the most well-known example and owes its unique properties to a high backbone rigidity and strong intermolecular hydrogen bonding interactions. Despite the industrial success of these molecules, since the amide-bond is not conjugated it is generally believed to be a poor linker for the preparation of semiconducting materials, as it is postulated to hamper charge transport.[13] However, poor intramolecular charge transport may be overcome via enhanced intermolecular interactions in bulk materials. For instance, favorable hydrogen bonding can promote close molecular packing and good intermolecular orbital overlap, leading to enhanced

charge transport properties.[14] For these reasons, aromatic amide-based HTMs have been overlooked and their great potential remains untapped.

In this chapter a simple HTM (EDOT-AmideTPA) based on well-known building blocks, which are linked together via amide functionalities, demonstrates the first HTM for perovskite solar cells with an amide-based backbone. For a non-conjugated material, this HTM shows outstanding charge carrier properties that can compete with conjugated HTMs used in the current generation of state-of-the-art perovskite solar cells. Based on these results, it is demonstrated that conjugation through the backbone is not essential to obtain materials with good charge transporting properties. The amide bonds in EDOT-Amide-TPA can coordinate with Li-ions, and this may limit the migration of Li-containing additives, resulting in improved device stability.[15] The charge transfer dynamics at the perovskite-HTM interface were studied with TRMC measurements, revealing that EDOT-Amide-TPA extracts holes from the perovskite faster than Spiro-OMeTAD. When used in solar cells, EDOT-Amide-TPA achieves power conversion efficiency (PCEs) of 20.0%. We additionally compare the performance and stability of these devices with those with current state-of-the-art Spiro-OMeTAD. EDOT-Amide-TPA outperforms Spiro-OMeTAD in all categories at a fraction of the cost (5%), which makes this a breakthrough and a key development in the design of future low-cost HTMs.

7.2 Synthesis

The production of amide-based materials has proven its value in industry, as these materials can be made using straightforward chemistry with excellent yields and high purity. Aromatic amides were used as building blocks for the preparation of a semiconducting small-molecule termed "EDOT-Amide-TPA" (Figure 7.1a), which was prepared by condensing 4-amino-4,4,-dimethoxytriphenylamine with 2,3-dihydrothieno[3,4-b][1,4]dioxine-5,7-dihydrochloric acid in the presence of a base in a simple one-pot reaction. During the reaction the product precipitates, making the workup very

straightforward, as only a simple washing step is required for purification. This results in a good isolated yield of 86% and very high purity, while the simplicity of the chemistry reduces batch-to-batch variations. An estimate of the materials cost was performed using previously reported cost-analysis methods based on lab-scale synthesis.[7,16] The estimated materials cost of EDOT-Amide-TPA is only \$5/g, which is more than an order of magnitude lower than the estimated materials cost of Spiro-OMeTAD (\$92/g) and also significantly lower than other high performing organic HTMs.[2,7,17,18] Additionally, EDOT-Amide-TPA can be synthesized without the use of halogenated solvents at only a slightly higher cost, which is essential for industrial production as many halogenated solvents have been banned from industrial processes.[19]

Aromatic amides are well-known for their outstanding thermal and chemical stability.[20] This is relevant for photovoltaic devices as the HTM should not degrade under operational conditions which can reach over 80 °C. Thermogravimetric analysis (TGA) confirms the excellent thermal stability of EDOT-Amide-TPA with a degradation temperature close to 350 °C. In order to estimate the bandgap of EDOT-Amide-TPA, light absorption measurements were performed. The films show an absorption maximum at 395 nm and the absorption onset of the film was determined by a Tauc plot to be 485 nm, corresponding to an optical bandgap of 2.7 eV. A good energy alignment between the perovskite absorber and the HTM is important to minimize losses in photovoltaic devices. The oxidation potential of EDOT-Amide-TPA was determined using cyclic voltammetry, from which the highest occupied molecular orbital (HOMO) energy level was calculated.[7] A reversible oxidation was observed with an onset at 0.53 V versus Ag/Ag+, resulting in a HOMO energy level of -5.23 eV, which is 100 meV deeper than that of Spiro-OMeTAD. The lowest unoccupied molecular orbital (LUMO) energy level was estimated to be -2.5 eV, obtained by adding the optical bandgap to the HOMO energy level. The HOMO energy level matches well with the valance band of the perovskite and is expected to result in minimal losses in the open-circuit voltage (V_{oc}), while the high LUMO energy level

allows EDOT-Amide-TPA to function as an efficient electron blocking layer (Figure 2b).

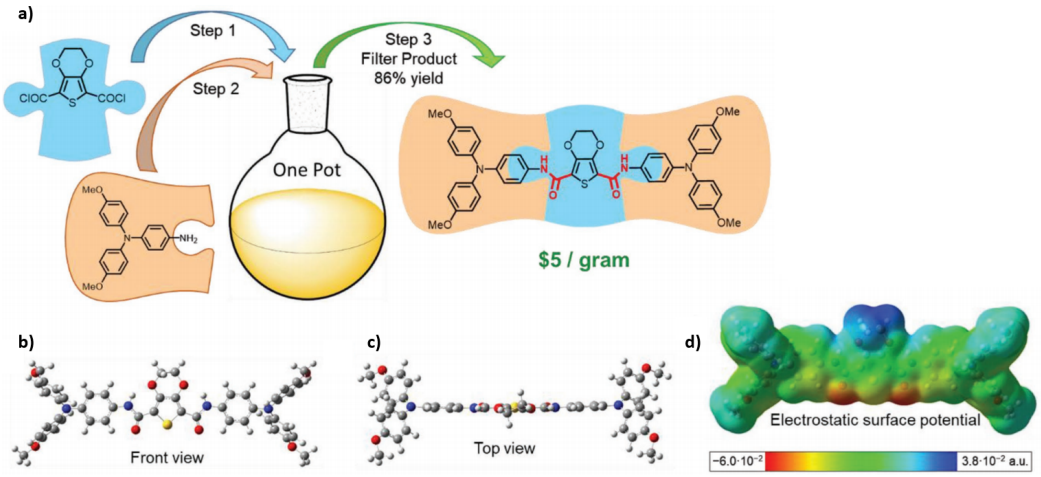

Figure 7.1: a) One-pot reaction scheme and molecular structure of EDOT-Amide-TPA and its starting materials, where the amide bond in the product is highlighted in red. b,c) Optimized geometry obtained from DFT calculation, displaying the planar core. d) Electrostatic surface potential map, revealing the strong dipole in the core. DFT calculations were performed by Michiel Petrus.

7.3 Molecular Geometry Simulations

Computational studies were performed to gain insight into the geometry and electronic structure of EDOT-Amide-TPA. Density functional theory (DFT) geometry optimizations were performed and the optimized geometry shows that the amide bond and the aromatic core of the molecule are all in a single plane, allowing for close molecular packing of the small-molecules (Figure 7.1b,c). The methoxy-containing phenyl rings of the triphenylamines are twisted out-of-plane, promoting the solubility of the small-molecule. The HOMO is concentrated over the triphenylamine side groups, while the LUMO is mostly located on the central thiophene moiety and the amide-bond. The HOMO energy level was theoretically estimated using the empirically obtained procedure published by Chi et al.,[21] and shows a HOMO energy level of -5.30 eV for EDOT-Amide-TPA , which is in excellent agreement with the experimentally obtained value. The electrochemical surface potential (Figure 7.1d) reveals the electronegative character of the oxygens in the amide-bond, while the most electropositive part is

located on the cyclic ether of the EDOT core, resulting in a dipole in the central moiety of the molecule. This dipole, combined with the amide-bond facilitating hydrogen bonding, is anticipated to enable a close molecular packing.[14]

7.4 EDOT-Amide-TPA Characterization

Although charge transport in small molecules relies on intermolecular charge transport, charge delocalization within the small molecules is generally considered important.[22] As the amide bond is not conjugated, materials with amide bonds in the backbone are generally believed to exhibit poor charge transporting properties in the bulk.[13] To study the potential of EDOT-Amide-TPA as an HTM for organic electronics, the charge transporting properties were characterized. For the hole mobility measurements, "hole-only" devices were prepared using the following device architecture: indium-doped tin oxide (ITO)/MoOx/EDOT-Amide-TPA/MoOx/Au.[7] J-V curves were measured, with the current assumed to be space-charge limited at higher voltages. From this, the charge carrier mobility can be estimated using the Mott–Gurney equation.[23] The obtained mobility is 3.9 $\times$ 10^{-5} cm^2 V^{-1} s^{-1} for EDOT-Amide-TPA, which is comparable to that of Spiro-OMeTAD (4.0 $\times$ 10^{-5} cm^2 V^{-1} s^{-1}). Upon addition of Li-TFSI to the HTM, there is a significant increase in the mobility to 2.1 $\times$ 10^{-4} cm^2 V^{-1} s^{-1}, which is attributed to the reduction of the barrier height for charge hopping.[24] The hole mobility is comparable to other non-conjugated HTMs such as N,N-diphenyl-N,N-(3-methylphenyl) -[1,1-biphenyl]-4,4-diamine (TPD),[25] and the low mobility of organic semiconductors relative to crystalline inorganic semiconductors results from a low dielectric constant and energetic disorder.

Organic semiconductors have a high degree of energetic disorder, which is largely due to Van der Waals forces and dipole-dipole interactions that result in the random positionining of molecules in thin films.[26,27] Dopants such as Li-TFSI have two counterbalancing effects.[28,29] First, dopants increase the concentration of holes in the HTM, which improves conductivity and shifts the energy level for transport closer

to the quasi-Fermi-level for holes. Partially negating this effect is the increase in energetic disorder induced by the dopant, which suppresses the mobility.[30] As doping concentration increases, the Coulomb wells associated with dopant anions overlap and Li^+ ions may interact with the deepest wells, partially levelizing the potential surface at these sites. In combination, these effects at higher doping concentrations may allow charge hopping between sites that had previously acted as traps, resulting in increased hole mobility.[24]

In addition to the charge carrier mobility, conductivity is an important measure for the charge transporting properties. In-plane conductivity measurements were collected (Figure 7.2c) with and without Li-TFSI as a p-dopant. Upon increasing the concentration of Li-TFSI in the HTM solution, the conductivity of EDOT-Amide-TPA films increases dramatically as shown in Figure 3a, reaching a value of 1.9 $\times$ 10^{-3} S cm^{-1} when 300 mol% Li-TFSI was added to the solution. In contrast, the conductivity in Spiro-OMeTAD has been reported to reach a maximum of 3 $\times$ 10^{-5} S cm^{-1} upon addition of 20% Li-TFSI, which is significantly lower.[31] These charge transporting properties reveal that despite the anticipated poor intramolecular conjugation, EDOT-Amide-TPA shows excellent charge transporting properties that are at least as good as state-of-the-art reference materials such as Spiro-OMeTAD, as shown in Table 7.1. This also indicates that intramolecular charge delocalization plays a minor role when it comes to facilitating bulk charge transport, which significantly broadens the horizon for the design of new HTMs. Optical absorption measurements upon addition of Li-TFSI reveal the formation of the oxidized species of the HTM (features at 700–800 nm), typical for most oxidized HTMs, and an additional shift of the original absorption peak around 400–440 nm as shown in Figure 7.2d. The shift of the absorption maximum between the pristine film and the films containing Li-TFSI is attributed to the coordination of the Li-ion to the amide-bond. The coordination leads to an increased conjugation through the amide bond, explaining the observed red-shift. It is likely that besides catalyzing the formation of the oxidized species, Li-coordination plays a role in the increased conductivity. Furthermore, this interaction

increases the solubility of EDOT-Amide-TPA, thus enhancing the processability of the material. The improved solubility upon addition of lithium salts is well-known for amide based materials and originates from the coordination of the lithium to the amide-bond which competes with the formation of hydrogen bonds.[32–34]

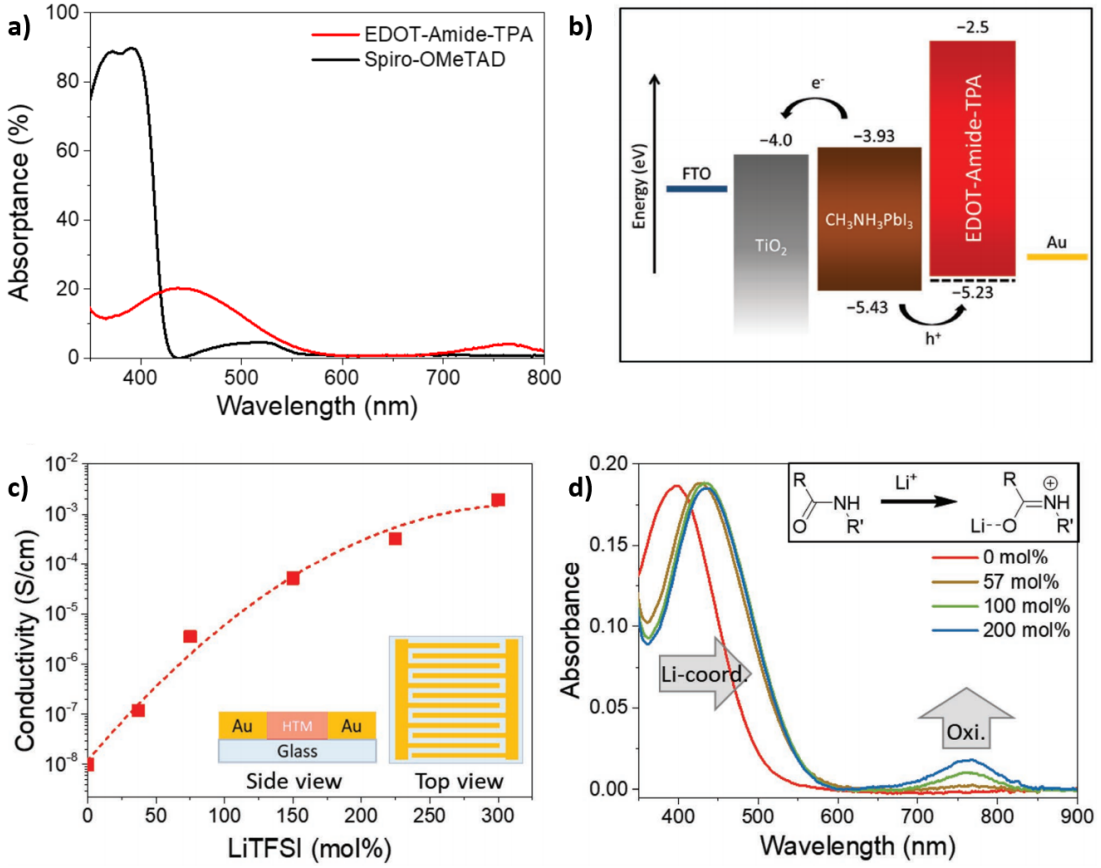

Figure 7.2: a) Absorptance of Spiro-OMeTAD and EDOT-Amide-TPA. b) Energy level diagram showing the energy levels for EDOT-Amide-TPA obtained from cyclic voltammetry and UV–vis measurements. The dotted line shows the HOMO energy level obtained from computational studies. c) The measured electrical conductivity as a function of the amount of Li-TFSI added to the solution used for spin-coating the films. The inset shows a schematic representation of the interdigitated electrode pattern on the device. d) UV–Vis absorption spectra of EDOT-Amide-TPA films as a function of added Li-TFSI. The UV–vis spectra show the formation of the oxidized species in the range of 700–800 nm and a red-shift in the absorption maximum (400–440 nm) of the original species due to the coordination of the lithium-ions with the amide bond, as depicted in the inset. UV-Vis HTM characterization was performed by Michiel Petrus, and additional charge transport measurements were conducted by James Ball and Annamaria Petrozza.

	EDOT-Amide-TPA	Spiro-OMeTAD
$\lambda_{max,abs}$ / nm	395	386
IE / eV	5.23	5.07
EA / eV	2.50	2.17
$E_{g,optical}$ / eV	2.7	3.0
$\mu_{undoped}$ / $cm^2\ V^{-1}\ s^{-1}$	3.9 x 10^{-5}	4.0 x 10^{-5}
μ_{doped} / $cm^2\ V^{-1}\ s^{-1}$	2.1 x 10^{-4}	5.3 x 10^{-4}
σ_{max} / S cm^{-1}	1.9 x 10^{-3}	3.0 x 10^{-5}
T_g / °C	112	121

Table 7.1: Optoelectronic properties of EDOT-Amide-TPA and Spiro-OMeTAD. The values for Spiro-OMeTAD were obtained from literature.[35–37]

7.5 Device Characterization

The photovoltaic performance of EDOT-Amide-TPA as an HTM was studied in mixed cation formamidinium cesium (FACs) perovskite solar cells with the device architecture FTO/SnO_2/$FA_{0.83}Cs_{0.17}Pb(I_{0.83}Br_{0.17})_3$/HTM/Au. A total of 64 individual devices were prepared to compare the photovoltaic performance between EDOT-Amide-TPA and Spiro-OMeTAD, as shown in Figure 7.3. The J_{sc}, fill factor, and power conversion efficiency for the devices with EDOT-Amide-TPA as the HTM all improve relative to devices with Spiro-OMeTAD (Table 7.2). The average J_{sc} increases from 21.7 mA cm^{-2} to 22.5 mA cm^{-2}, which can be attributed to fast carrier extraction as discussed in detail in the section on time-resolved microwave conductivity characterization. Consistent with the greater conductivity of EDOT-Amide-TPA, fill factor also increases, from 0.70 to 0.72. The improved fill factor also results from EDOT-Amide-TPA films in devices being substantially thinner than Spiro-OMeTAD, at ~50 nm compared to ~200 nm. The thinner layer is permitted by the enhanced film formation of EDOT-Amide-TPA which is visibly homogeneous, while spin-coated Spiro-OMeTAD layers inevitably have aggregations that cause "comets", leaving radial inhomogeneities. These inhomogeneities permit evaporated metal electrodes to directly contact the perovskite absorber, resulting in deleterious shunt pathways unless a comparably thick

layer of Spiro-OMeTAD is deposited. Overall, PCE improves from an average of 17.0% for devices with Spiro-OMeTAD to 17.9% for devices with EDOT-Amide-TPA.

The best photovoltaic performance was obtained with EDOT-Amide-TPA in combination with FACs serving as the perovskite absorber, showing a PCE of 20.3% (Voc = 1.16 V; Jsc = 22.7 mA cm^{-2}; FF = 77%), combined with a stunning stabilized power output of 20.0%, as shown in Figure 7.4. In contrast, the champion Spiro-OMeTAD reference device showed a PCE of 19.7% in the JV-scan with a stabilized power of 17.0%. The external quantum efficiency spectrum is shown in Figure 5c and gives an integrated current of 21.4 mA cm^{-2}, which is in close agreement with the JV-scans. The PCE of 20.3%, obtained with EDOT-AmideTPA as the HTM is among the highest reported PCEs for a (planar) perovskite solar cell using an alternative for Spiro-OMeTAD.[2,4,17,38] Furthermore, the stabilized power output of 20.0% is the highest reported efficiency for a device comprising $FA_{0.83}Cs_{0.17}Pb(I_{0.83}Br_{0.17})_3$ as the absorber.[39–41] By exceeding literature values it is clearly demonstrated that EDOT-Amide-TPA truly has the potential to outperform the current state-of-the-art HTMs.

To study the stability of PSC on these two HTMs, an irradiation aging test was performed at open-circuit under an LED array at a temperature of 40 °C in a nitrogen atmosphere. The stabilized power output after 50 s was periodically measured and is displayed in Figure 7.5. Despite the substantially thinner hole transport layer, EDOT-Amide-TPA showed significantly better stability than the devices with Spiro-OMeTAD. While the latter showed a pronounced loss in all photovoltaic parameters, no significant loss in the J_{sc} and FF was observed for devices comprising EDOT-Amide-TPA during the aging experiment. In contrast, Lee et al. showed that in Spiro-OMeTAD layers Li-TFSI accumulates at the perovskite interface, accelerating the degradation.[15] Degradation of the aged devices with Spiro-OMeTAD was obvious after aging, and discoloration could be seen near the electrodes (Figure 7.5). The superior stability of EDOT-Amide-TPA may be related to the presence of the amide bonds, as the interactions between the lithium-ions and the amide bonds facilitate

Device	J_{sc} (mA cm^{-2})	V_{oc} (V)	FF	PCE (%)
Average				
EDOT-Amide-TPA	22.5 ± 0.28	1.11 ± 0.06	0.72 ± 0.07	17.9 ± 2.4
Spiro-OMeTAD	21.7 ± 0.36	1.13 ± 0.03	0.70 ± 0.08	17.0 ± 3.2
Champion				
EDOT-Amide-TPA	22.7	1.16	0.77	20.3
Spiro-OMeTAD	22.5	1.15	0.76	19.7

Table 7.2: Solar Cell Performance Parameters Determined from J-V Curves for 64 Devices.

a homogeneous distribution of the ions throughout the HTM layer and minimize their diffusion. Cross-sections of fresh and aged devices also reveal morphological differences between EDOT-Amide-TPA and Spiro-OMeTAD, with Spiro-OMeTAD developing voids at the perovskite-HTM interface that are detrimental to charge extraction. The morphological degradation is reflected by the J-V curves after aging the devices since Spiro-OMeTAD devices exhibit substantial current and voltage loss loss while there is negligible current loss and only moderate voltage loss in the EDOT-Amide-TPA devices. The voids in Spiro-OMeTAD have previously been attributed to gaseous products that occur under thermal stress when doping with Li-TFSI and tBP simultaneously, but curiously it was shown these voids did not develop when the dopants were used independently.[42] In contrast, no voids or other defects were observed for EDOT-Amide-TPA devices.

7.6 Charge Transfer Characterization

To further investigate the origin of the outstanding performance of EDOT-Amide-TPA time-resolved microwave conductivity was employed, which is a powerful technique to investigate the charge injection and recombination dynamics at the perovskite-charge selective contact interface.[43] Measuring the time-resolved photo-conductance allows insights into the mobility and lifetimes of free charges.[44,45] Figure 7.6 shows the photoconductance as a function of time for a neat triple cation $Cs_{0.05}(FA_{0.83}MA_{0.17})Pb(I_{0.83}Br_{0.17})_3$

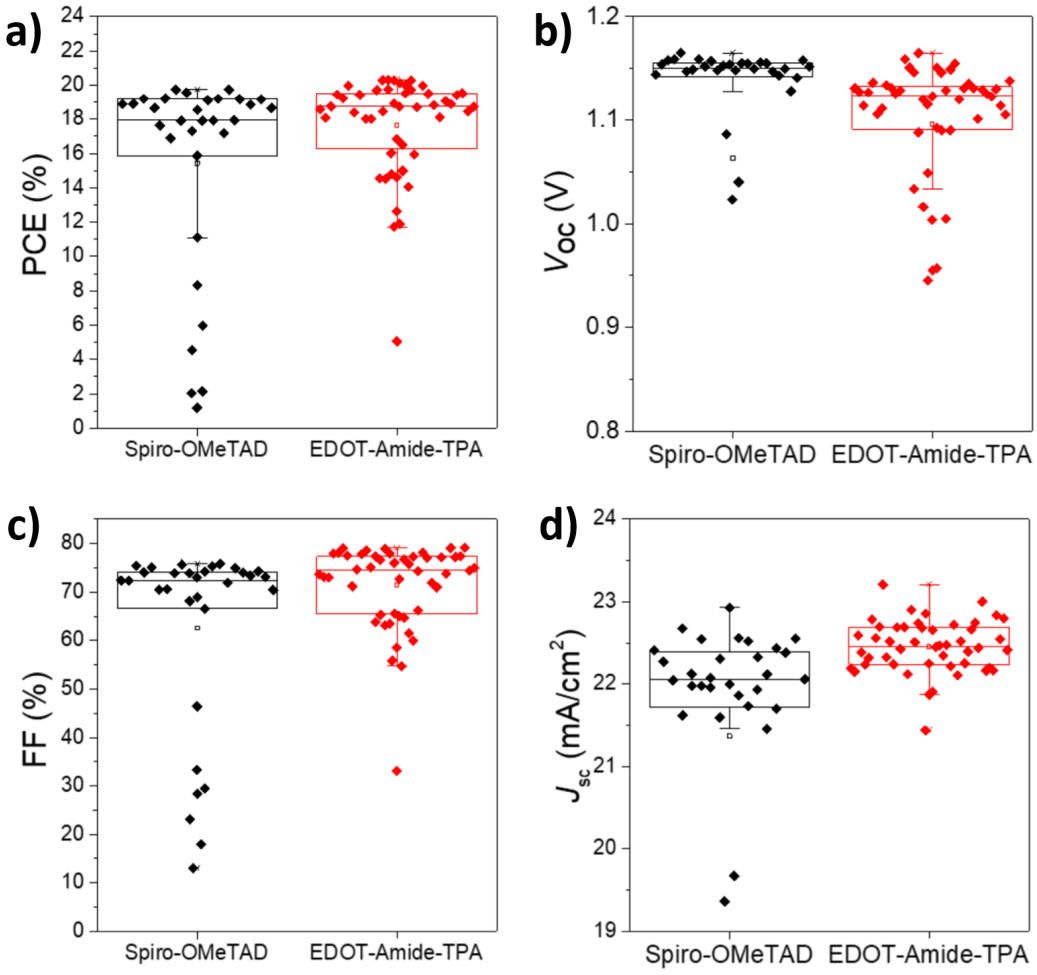

Figure 7.3: Photovoltaic performance of 64 devices comprising EDOT-Amide-TPA and Spiro-OMeTAD. a) Power conversion efficiency. b) Open circuit voltage. c) Fill factor. d) Short circuit current density.

(FAMACs) film (blue) and bilayer films consisting of the triple cation combined with EDOT-Amide-TPA (red) or Spiro-OMeTAD (black). The samples are excited at $\lambda = 430$ nm through the HTM, so that the majority of charge carriers in the perovskite layer are initially generated within 50 nm from the perovskite/HTM interface.[43] For the pure FAMACs film, the maximum signal height is close to 20 cm^2 V^{-1} s^{-1} , representing the sum of electron and hole mobilities in the perovskite layer. For the bilayer samples, if holes are extracted by the HTM, these no longer significantly contribute to the signal as their mobility is only $\sim 10^{-4}$ cm^2 V^{-1} s^{-1}.[46] Therefore, the substantially reduced maximum signal height of 10 cm^2 V^{-1} s^{-1} in the FAMACs/EDOT-Amide-TPA bilayer shows that holes are extracted by the EDOT-Amide-TPA on a sub-ns timescale (i.e.,

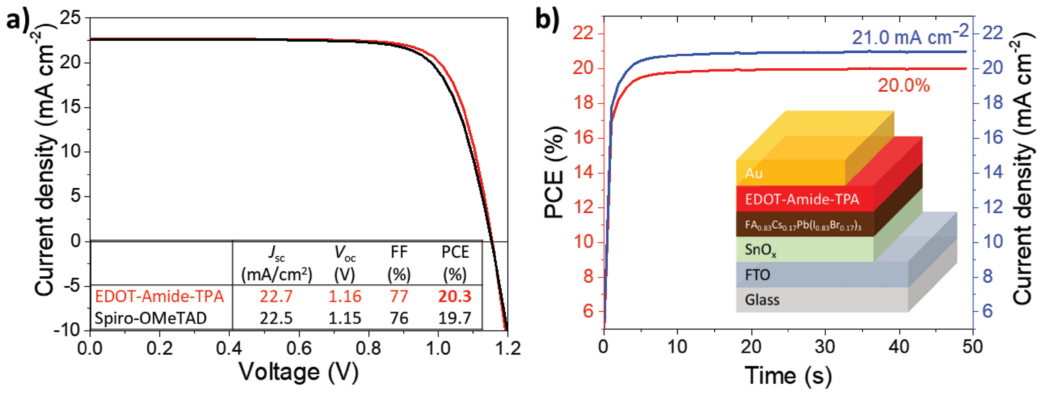

Figure 7.4: a) JV-curves collected under AM 1.5 simulated sunlight of the champion devices comprising EDOT-Amide-TPA and Spiro-OMeTAD in the following device architecture: FTO/SnO_2/$FA_{0.83}Cs_{0.17}Pb(I_{0.83}Br_{0.17})_3$/HTM/Au. The photovoltaic parameters are extracted from the J-V curves. b) Stabilized power output for the champion device comprising EDOT-Amide-TPA. c) External quantum efficiency with the integrated current. d) Stabilized power output after aging the devices. Initial aging is performed in the dark, followed by testing under illumination at open-circuit at 40 °C. Cells were aged under nitrogen without encapsulation and periodically brought into atmosphere for measurements.

faster than the instrumental response time).[46] Additionally, it suggests that both the electron and hole mobilities in these FAMACs perovskites are about 10 cm^2 V^{-1} s^{-1} and hence, highly balanced.[45] This is further confirmed by TRMC experiments in which the sample was illuminated from the other side (at $\lambda = 430$ nm), thereby generating the charges several hundred nanometers away from the interface. As shown in Figure 7.6b, in the case of backside illumination, the sum of electron and hole mobilities is identical to the FAMACs layer, indicating that no charge extraction has occurred on a sub-ns timescale. This can be understood by considering that the holes first need to diffuse to the perovskite-EDOT-Amide-TPA interface before they can be extracted. Therefore, the above results show that EDOT-Amide-TPA extracts holes on a sub-ns timescale provided that the holes are close to the interface. In contrast to the EDOT-Amide-TPA, the maximum signal height in the FAMACs-Spiro-OMeTAD bilayer is the same as for the pure FAMACs, even if charges are excited close to the interface. In light of this data, the extraction of holes from FAMACs by Spiro-OMeTAD is slower than by EDOT-Amide-TPA. Fast injection into charge transport layers has been linked to a high Jsc in photovoltaic devices,[47,48] which also helps to explain the increase in the photocurrent observed for EDOT-Amide-TPA.

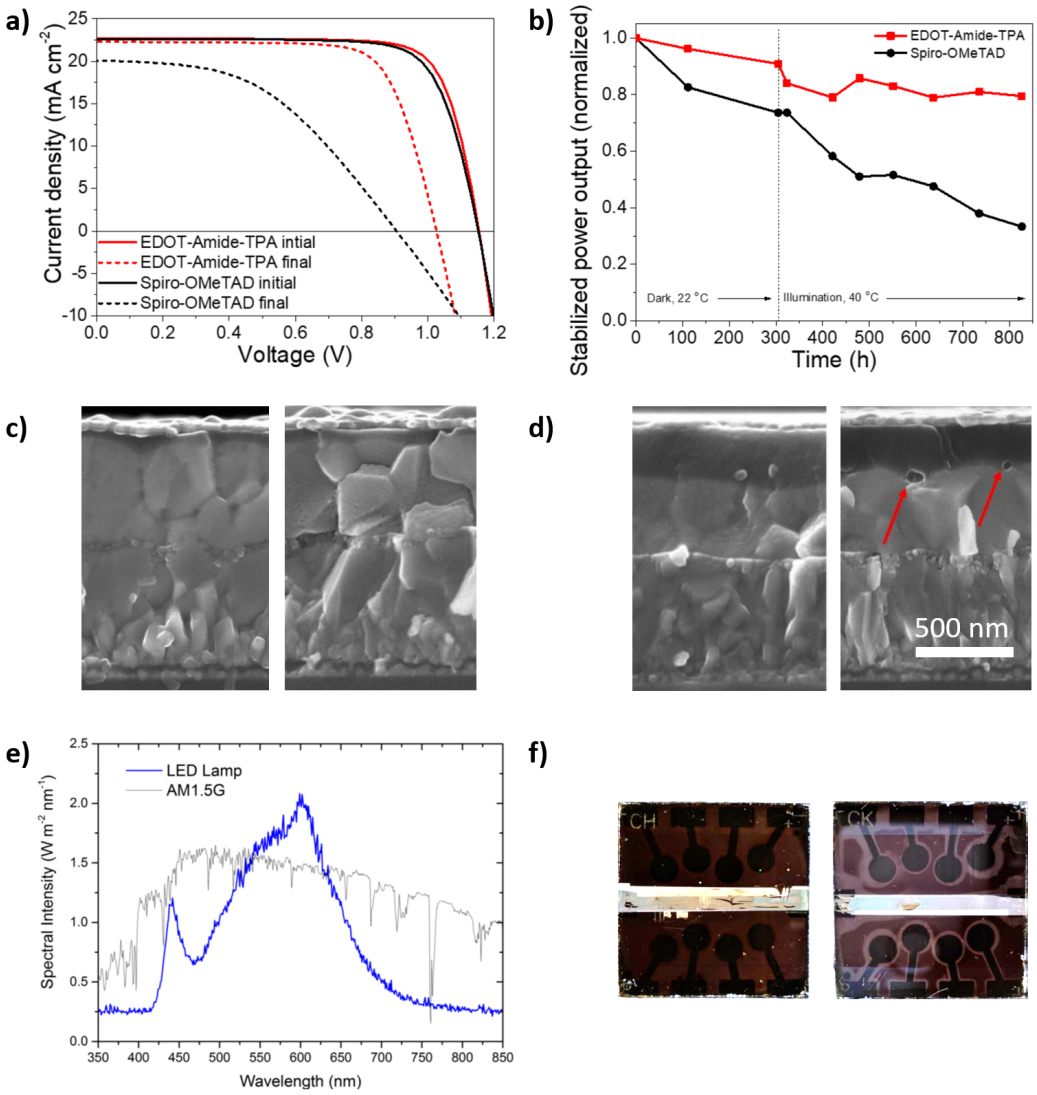

Figure 7.5: a) J-V curves of initial and aged devices. b) Stabilized power output during ~300 hours in the dark under N_2 atmosphere, followed by over 500 hours under illumination. c) Pristine and aged cross-section of the device with EDOT-Amide-TPA. d) Pristine and aged device with Spiro-OMeTAD, revealing void formation at the perovskite-HTM interface. e) Spectra of the LED aging lamp. f) Photographs of aged EDOT-Amide-TPA (left) and Spiro-OMeTAD (right) devices.

7.7 Conclusion

In summary, this Chapter introduced a small-molecule hole conductor, EDOT-Amide-TPA, which outperforms the state-of-the-art hole-transport material Spiro-OMeTAD when employed as an HTM in perovskite solar cells. PCEs of up to 20.3% were obtained with a stabilized power output of 20.0%. This stabilized power output was one of the highest reported stabilized efficiencies for HTMs in perovskite solar

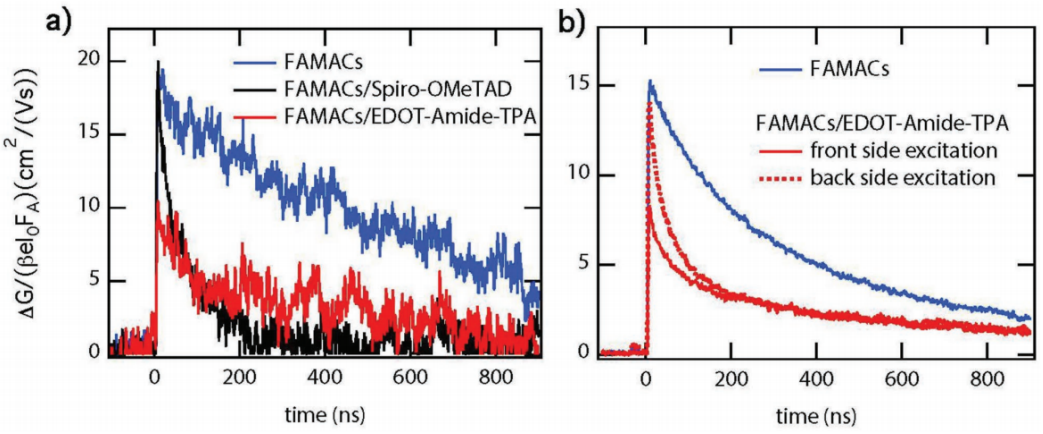

Figure 7.6: a) for FAMACs (blue) and the bilayers FAMACs/EDOT-Amide-TPA (red) and FAMACs/SpiroOMeTAD (black), recorded at 2×10^{10} absorbed photons cm^{-2} ($\lambda = 430$ nm). b) for FAMACs (blue) and FAMACs/EDOT-Amide-TPA (red) illuminated through the HTM (front side, solid line) and through the perovskite (back side, dotted line), at 2×10^{11} absorbed photons cm^{-2} ($\lambda = 430$ nm). TRMC measurements were performed by Eline Hutter.

cells, and at the time of this research in August 2017 EDOT-Amide-TPA became third organic small molecule HTM to have achieved a stabilized power output of 20.0% (in addition to Spiro-OMeTAD and PTAA).[49–52] The improved performance is the result of fast charge injection at the perovskite-EDOT-Amide-TPA interface, as was demonstrated by TRMC measurements. Photovoltaic devices comprising EDOT-Amide-TPA show superior stability, which was attributed to the unique ability of the amide bond to coordinate with Li-TFSI, providing a novel strategy to overcome degradation caused by migration of additives. These results also demonstrate that nonconjugated small-molecules can feature charge transporting properties comparable to conjugated materials, indicating that intermolecular charge delocalization can play a dominant role when it comes to facilitating bulk charge transport behavior. By introducing amide bonds, this HTM can be synthesized in a simple condensation reaction that is amenable to scale-up, leading to an estimated material cost of only \$5 g^{-1} , while this chemistry can also be easily combined with a wide variety of other building blocks. This is the first demonstration of an HTM with a cost that is at least 10 times lower than Spiro-OMeTAD and that outperforms state-of-the-art HTMs.

References

1. N. Arora, M. I. Dar, A. Hinderhofer, N. Pellet, F. Schreiber, S. M. Zakeeruddin, and M. Grätzel, "Perovskite solar cells with CuSCN hole extraction layers yield stabilized efficiencies greater than 20%," *Science*, vol. 358, pp. 768–771, sep 2017.
2. M. Saliba, S. Orlandi, T. Matsui, S. Aghazada, M. Cavazzini, J.-P. Correa-Baena, P. Gao, R. Scopelliti, E. Mosconi, K.-H. Dahmen, F. D. Angelis, A. Abate, A. Hagfeldt, G. Pozzi, M. Graetzel, and M. K. Nazeeruddin, "A molecularly engineered hole-transporting material for efficient perovskite solar cells," *Nature Energy*, vol. 1, jan 2016.
3. K. Rakstys, S. Paek, P. Gao, P. Gratia, T. Marszalek, G. Grancini, K. T. Cho, K. Genevicius, V. Jankauskas, W. Pisula, and M. K. Nazeeruddin, "Molecular engineering of face-on oriented dopant-free hole transporting material for perovskite solar cells with 19% PCE," *Journal of Materials Chemistry A*, vol. 5, no. 17, pp. 7811–7815, 2017.
4. D. Bi, B. Xu, P. Gao, L. Sun, M. Grätzel, and A. Hagfeldt, "Facile synthesized organic hole transporting material for perovskite solar cell with efficiency of 19.8%," *Nano Energy*, vol. 23, pp. 138–144, may 2016.
5. A. Binek, M. L. Petrus, N. Huber, H. Bristow, Y. Hu, T. Bein, and P. Docampo, "Recycling perovskite solar cells to avoid lead waste," *ACS Applied Materials & Interfaces*, vol. 8, pp. 12881–12886, may 2016.
6. L. K. Ono, S. R. Raga, M. Remeika, A. J. Winchester, A. Gabe, and Y. Qi, "Pinhole-free hole transport layers significantly improve the stability of MAPbI3-based perovskite solar cells under operating conditions," *Journal of Materials Chemistry A*, vol. 3, no. 30, pp. 15451–15456, 2015.
7. M. L. Petrus, T. Bein, T. J. Dingemans, and P. Docampo, "A low cost azomethine-based hole transporting material for perovskite photovoltaics," *Journal of Materials Chemistry A*, vol. 3, no. 23, pp. 12159–12162, 2015.
8. J. C. Hindson, B. Ulgut, R. H. Friend, N. C. Greenham, B. Norder, A. Kotlewski, and T. J. Dingemans, "All-aromatic liquid crystal triphenylamine-based poly(azomethine)s as hole transport materials for opto-electronic applications," *J. Mater. Chem.*, vol. 20, no. 5, pp. 937–944, 2010.
9. M. L. Petrus, M. T. Sirtl, A. C. Closs, T. Bein, and P. Docampo, "Hydrazone-based hole transporting material prepared via condensation chemistry as alternative for cross-coupling chemistry for perovskite solar cells," *Molecular Systems Design & Engineering*, vol. 3, no. 5, pp. 734–740, 2018.
10. M. L. Petrus, R. K. M. Bouwer, U. Lafont, S. Athanasopoulos, N. C. Greenham, and T. J.

Dingemans, "Small-molecule azomethines: organic photovoltaics via schiff base condensation chemistry," *J. Mater. Chem. A*, vol. 2, no. 25, pp. 9474–9477, 2014.

11. M. Daskeviciene, S. Paek, Z. Wang, T. Malinauskas, G. Jokubauskaite, K. Rakstys, K. T. Cho, A. Magomedov, V. Jankauskas, S. Ahmad, H. J. Snaith, V. Getautis, and M. K. Nazeeruddin, "Carbazole-based enamine: Low-cost and efficient hole transporting material for perovskite solar cells," *Nano Energy*, vol. 32, pp. 551–557, feb 2017.

12. M. L. Petrus, A. Music, A. C. Closs, J. C. Bijleveld, M. T. Sirtl, Y. Hu, T. J. Dingemans, T. Bein, and P. Docampo, "Design rules for the preparation of low-cost hole transporting materials for perovskite solar cells with moisture barrier properties," *Journal of Materials Chemistry A*, vol. 5, no. 48, pp. 25200–25210, 2017.

13. C. R. Kemnitz and M. J. Loewen, "Amide resonance correlates with a breadth of c-n rotation barriers," *Journal of the American Chemical Society*, vol. 129, pp. 2521–2528, mar 2007.

14. I. Paraschiv, K. de Lange, M. Giesbers, B. van Lagen, F. C. Grozema, R. D. Abellon, L. D. A. Siebbeles, E. J. R. Sudhölter, H. Zuilhof, and A. T. M. Marcelis, "Hydrogen-bond stabilized columnar discotic benzenetrisamides with pendant triphenylene groups," *Journal of Materials Chemistry*, vol. 18, no. 45, p. 5475, 2008.

15. I. Lee, J. H. Yun, H. J. Son, and T.-S. Kim, "Accelerated degradation due to weakened adhesion from li-TFSI additives in perovskite solar cells," *ACS Applied Materials & Interfaces*, vol. 9, pp. 7029–7035, feb 2017.

16. T. P. Osedach, T. L. Andrew, and V. Bulović, "Effect of synthetic accessibility on the commercial viability of organic photovoltaics," *Energy & Environmental Science*, vol. 6, no. 3, p. 711, 2013.

17. T. Malinauskas, M. Saliba, T. Matsui, M. Daskeviciene, S. Urnikaite, P. Gratia, R. Send, H. Wonneberger, I. Bruder, M. Graetzel, V. Getautis, and M. K. Nazeeruddin, "Branched methoxydiphenylamine-substituted fluorene derivatives as hole transporting materials for high-performance perovskite solar cells," *Energy & Environmental Science*, vol. 9, no. 5, pp. 1681–1686, 2016.

18. F. Zhang, Z. Wang, H. Zhu, N. Pellet, J. Luo, C. Yi, X. Liu, H. Liu, S. Wang, X. Li, Y. Xiao, S. M. Zakeeruddin, D. Bi, and M. Grätzel, "Over 20% PCE perovskite solar cells with superior stability achieved by novel and low-cost hole-transporting materials," *Nano Energy*, vol. 41, pp. 469–475, nov 2017.

19. D. Prat, O. Pardigon, H.-W. Flemming, S. Letestu, V. Ducandas, P. Isnard, E. Guntrum, T. Senac, S. Ruisseau, P. Cruciani, and P. Hosek, "Sanofi's solvent selection guide: A step toward more sustainable processes," *Organic Process Research & Development*, vol. 17, pp. 1517–1525, nov 2013.

20. N. García, J. Guzman, E. Riande, F. García, J. L. D. L. Pena, P. Calle, and M. L. Jimeno, "Influence of the stereochemical configuration on the radical polymerization of methacrylic monomers:cis- andtrans-(2-cyclohexyl-1,3-dioxan-5-yl) methacrylate," *Journal of Polymer Science Part A: Polymer Chemistry*, vol. 38, no. 21, pp. 3883–3891, 2000.

21. W.-J. Chi, Q.-S. Li, and Z.-S. Li, "Exploring the electrochemical properties of hole transport materials with spiro-cores for efficient perovskite solar cells from first-principles," *Nanoscale*, vol. 8, no. 11, pp. 6146–6154, 2016.

22. P. Liu, B. Xu, Y. Hua, M. Cheng, K. Aitola, K. Sveinbjörnsson, J. Zhang, G. Boschloo, L. Sun, and L. Kloo, "Design, synthesis and application of a -conjugated, non-spiro molecular alternative as hole-transport material for highly efficient dye-sensitized solar cells and perovskite solar cells," *Journal of Power Sources*, vol. 344, pp. 11–14, mar 2017.

23. M. L. Petrus, F. S. F. Morgenstern, A. Sadhanala, R. H. Friend, N. C. Greenham, and T. J. Dingemans, "Device performance of small-molecule azomethine-based bulk heterojunction solar

cells," *Chemistry of Materials*, vol. 27, pp. 2990–2997, apr 2015.

24. H. J. Snaith and M. Grätzel, "Enhanced charge mobility in a molecular hole transporter via addition of redox inactive ionic dopant: Implication to dye-sensitized solar cells," *Applied Physics Letters*, vol. 89, p. 262114, dec 2006.

25. S. Naka, H. Okada, H. Onnagawa, Y. Yamaguchi, and T. Tsutsui, "Carrier transport properties of organic materials for EL device operation," *Synthetic Metals*, vol. 111-112, pp. 331–333, jun 2000.

26. A. Dieckmann, H. Bässler, and P. M. Borsenberger, "An assessment of the role of dipoles on the density-of-states function of disordered molecular solids," *The Journal of Chemical Physics*, vol. 99, pp. 8136–8141, nov 1993.

27. S. V. Novikov and A. V. Vannikov, "Cluster structure in the distribution of the electrostatic potential in a lattice of randomly oriented dipoles," *The Journal of Physical Chemistry*, vol. 99, pp. 14573–14576, oct 1995.

28. V. I. Arkhipov, P. Heremans, E. V. Emelianova, G. J. Adriaenssens, and H. Bässler, "Charge carrier mobility in doped semiconducting polymers," *Applied Physics Letters*, vol. 82, pp. 3245–3247, may 2003.

29. C. Tanase, P. W. M. Blom, D. M. de Leeuw, and E. J. Meijer, "Charge carrier density dependence of the hole mobility in poly(p-phenylene vinylene)," in *Physics of Organic Semiconductors*, pp. 305–318, Wiley-VCH Verlag GmbH & Co. KGaA, feb 2006.

30. V. I. Arkhipov, P. Heremans, E. V. Emelianova, and H. Bässler, "Effect of doping on the density-of-states distribution and carrier hopping in disordered organic semiconductors," *Physical Review B*, vol. 71, jan 2005.

31. A. Abate, T. Leijtens, S. Pathak, J. Teuscher, R. Avolio, M. E. Errico, J. Kirkpatrik, J. M. Ball, P. Docampo, I. McPherson, and H. J. Snaith, "Lithium salts as "redox active" p-type dopants for organic semiconductors and their impact in solid-state dye-sensitized solar cells," *Physical Chemistry Chemical Physics*, vol. 15, no. 7, p. 2572, 2013.

32. F. C. Grozema, A. S. Best, L. van Eijck, J. Stride, G. J. Kearley, S. W. de Leeuw, and S. J. Picken, "Dynamics and lithium binding energies of polyelectrolytes based on functionalized poly(para-phenylene terephthalamide)," *The Journal of Physical Chemistry B*, vol. 109, pp. 7705–7712, apr 2005.

33. D. Balasubramanian and R. Shaikh, "On the interaction of lithium salts with model amides," *Biopolymers*, vol. 12, pp. 1639–1650, jul 1973.

34. H. Sigel and R. B. Martin, "Coordinating properties of the amide bond. stability and structure of metal ion complexes of peptides and related ligands," *Chemical Reviews*, vol. 82, pp. 385–426, aug 1982.

35. M. L. Petrus, A. Music, A. C. Closs, J. C. Bijleveld, M. T. Sirtl, Y. Hu, T. J. Dingemans, T. Bein, and P. Docampo, "Design rules for the preparation of low-cost hole transporting materials for perovskite solar cells with moisture barrier properties," *Journal of Materials Chemistry A*, vol. 5, no. 48, pp. 25200–25210, 2017.

36. X. Liu, X. Ding, Y. Ren, Y. Yang, Y. Ding, X. Liu, A. Alsaedi, T. Hayat, J. Yao, and S. Dai, "A star-shaped carbazole-based hole-transporting material with triphenylamine side arms for perovskite solar cells," *Journal of Materials Chemistry C*, vol. 6, no. 47, pp. 12912–12918, 2018.

37. K. Rakstys, M. Saliba, P. Gao, P. Gratia, E. Kamarauskas, S. Paek, V. Jankauskas, and M. K. Nazeeruddin, "Highly efficient perovskite solar cells employing an easily attainable bifluorenylidene-based hole-transporting material," *Angewandte Chemie*, vol. 128, pp. 7590–7594, may 2016.

38. B. Xu, J. Zhang, Y. Hua, P. Liu, L. Wang, C. Ruan, Y. Li, G. Boschloo, E. M. Johansson, L. Kloo, A. Hagfeldt, A. K.-Y. Jen, and L. Sun, "Tailor-making low-cost spiro[fluorene-9,9′-xanthene]-based 3d oligomers for perovskite solar cells," *Chem*, vol. 2, pp. 676–687, may 2017.

39. M. Saliba, T. Matsui, J.-Y. Seo, K. Domanski, J.-P. Correa-Baena, M. K. Nazeeruddin, S. M. Zakeeruddin, W. Tress, A. Abate, A. Hagfeldt, and M. Grätzel, "Cesium-containing triple cation perovskite solar cells: improved stability, reproducibility and high efficiency," *Energy & Environmental Science*, vol. 9, no. 6, pp. 1989–1997, 2016.

40. Z. Wang, Q. Lin, F. P. Chmiel, N. Sakai, L. M. Herz, and H. J. Snaith, "Efficient ambient-air-stable solar cells with 2d–3d heterostructured butylammonium-caesium-formamidinium lead halide perovskites," *Nature Energy*, vol. 2, aug 2017.

41. D. P. McMeekin, G. Sadoughi, W. Rehman, G. E. Eperon, M. Saliba, M. T. Hörantner, A. Haghighirad, N. Sakai, L. Korte, B. Rech, M. B. Johnston, L. M. Herz, and H. J. Snaith, "A mixed-cation lead mixed-halide perovskite absorber for tandem solar cells," *Science*, vol. 351, no. 6269, pp. 151–155, 2016.

42. A. K. Jena, M. Ikegami, and T. Miyasaka, "Severe morphological deformation of spiro-OMeTAD in (CH3nh3)PbI3 solar cells at high temperature," *ACS Energy Letters*, vol. 2, pp. 1760–1761, jul 2017.

43. E. M. Hutter, J.-J. Hofman, M. L. Petrus, M. Moes, R. D. Abellón, P. Docampo, and T. J. Savenije, "Charge transfer from methylammonium lead iodide perovskite to organic transport materials: Efficiencies, transfer rates, and interfacial recombination," *Advanced Energy Materials*, vol. 7, p. 1602349, feb 2017.

44. T. J. Savenije, A. J. Ferguson, N. Kopidakis, and G. Rumbles, "Revealing the dynamics of charge carriers in polymer:fullerene blends using photoinduced time-resolved microwave conductivity," *The Journal of Physical Chemistry C*, vol. 117, pp. 24085–24103, oct 2013.

45. Y. Hu, E. M. Hutter, P. Rieder, I. Grill, J. Hanisch, M. F. Aygüler, A. G. Hufnagel, M. Handloser, T. Bein, A. Hartschuh, K. Tvingstedt, V. Dyakonov, A. Baumann, T. J. Savenije, M. L. Petrus, and P. Docampo, "Perovskite solar cells: Understanding the role of cesium and rubidium additives in perovskite solar cells: Trap states, charge transport, and recombination (adv. energy mater. 16/2018)," *Advanced Energy Materials*, vol. 8, p. 1870073, jun 2018.

46. C. S. Ponseca, T. J. Savenije, M. Abdellah, K. Zheng, A. Yartsev, T. Pascher, T. Harlang, P. Chabera, T. Pullerits, A. Stepanov, J.-P. Wolf, and V. Sundström, "Organometal halide perovskite solar cell materials rationalized: Ultrafast charge generation, high and microsecond-long balanced mobilities, and slow recombination," *Journal of the American Chemical Society*, vol. 136, pp. 5189–5192, mar 2014.

47. J. Jiménez-López, W. Cambarau, L. Cabau, and E. Palomares, "Charge injection, carriers recombination and HOMO energy level relationship in perovskite solar cells," *Scientific Reports*, vol. 7, jul 2017.

48. J. Zhang, Y. Hua, B. Xu, L. Yang, P. Liu, M. B. Johansson, N. Vlachopoulos, L. Kloo, G. Boschloo, E. M. J. Johansson, L. Sun, and A. Hagfeldt, "The role of 3d molecular structural control in new hole transport materials OutperformingSpiro-OMeTAD in perovskite solar cells," *Advanced Energy Materials*, vol. 6, p. 1601062, jul 2016.

49. J. Urieta-Mora, I. García-Benito, A. Molina-Ontoria, and N. Martín, "Hole transporting materials for perovskite solar cells: a chemical approach," *Chemical Society Reviews*, vol. 47, no. 23, pp. 8541–8571, 2018.

50. K. Rakstys, C. Igci, and M. K. Nazeeruddin, "Efficiency vs. stability: dopant-free hole transporting materials towards stabilized perovskite solar cells," *Chemical Science*, vol. 10, no. 28, pp. 6748–6769, 2019.

51. P. Agarwala and D. Kabra, "A review on triphenylamine (TPA) based organic hole transport materials (HTMs) for dye sensitized solar cells (DSSCs) and perovskite solar cells (PSCs): evolution and molecular engineering," *Journal of Materials Chemistry A*, vol. 5, no. 4, pp. 1348–1373, 2017.

52. Z. H. Bakr, Q. Wali, A. Fakharuddin, L. Schmidt-Mende, T. M. Brown, and R. Jose, "Advances in hole transport materials engineering for stable and efficient perovskite solar cells," *Nano Energy*, vol. 34, pp. 271–305, apr 2017.

CHAPTER 8

A Photo-Crosslinkable Bis-Triarylamine Side-Chain Polymer as a Hole-Transport Material for Stable Perovskite Solar Cells

The research in this chapter is based on the following publication:

Marie-Hélène Tremblay; Kelly Schutt; Yadong Zhang; Jongchul Lim; Yen-Hung Lin; Jonathan Warby; Stephen Barlow; Henry J. Snaith; Seth R. Marder 'A Photo-Crosslinkable Bis-Triarylamine Side-Chain Polymer as a Hole-Transport Material for Stable Perovskite Solar Cells'

DOI: 10.1039/C9SE00513G

Direct link: `https://pubs.rsc.org/en/content/articlelanding/2019/se/c9se00513g`

Reproduced with permission from The Royal Society of Chemistry.

M.T. performed HTM characterization, HTM processing optimization, and fabricated solar cells for the long-term stability measurements. K.S. made and characterized solar cells and provided PL, TRPL, XRD, AFM, SEM, and conductivity measurements, wrote some of the manuscript and formatted the chapter. Y.Z. synthesized the HTM. Y.L. provided methods and guidance on p-i-n solar cell fabrication. J.W. provided the 85 °C oven under N_2 for stability measurements. S.B. provided manuscript editing and feedback. Professors H.J.S. and S.M. provided laboratory space, additional discussion, and financial support.

8.1 Introduction

The stability of perovskite solar cells must be improved in order for commercial applications to succeed,[1,2] and often the most efficient cells are not the most stable.[3] Among the methods used to achieve improved stability are mixed-cation perovskites[4,5] or a quasi two-dimensional perovskite,[6–11] and modification of the chemical structure of the hole-[12–15] and electron-transport materials[16–18] (HTMs and ETMs, respectively) and of the dopants used to enhance their conductivity.

HTMs play a crucial role in PSCs by reducing the recombination that occurs at perovskite-HTM interface, and HTMs and p-dopants can strongly influence the overall device stability.[19,20] Organic molecules and polymers, as well as various inorganic materials, can be used as HTMs in PSCs.[21] The development of cross-linkable HTMs and ETMs for multilayer organic electronic devices, such as light-emitting diodes (OLEDs), was motivated by the need to avoid possible dissolution of the first layer during solution deposition of subsequent layers. Once cross-linked (thermally or photochemically), the material becomes insoluble, allowing the subsequent layer to be easily processed on top of it and protecting the layer(s) underneath. Cross-linking could offer similar advantages for the HTMs of p-i-n PSC, potentially allowing the lead-halide perovskite to be solution-processed without damaging underlying layers.

Easily processed and insolubilized HTMs are ideal candidates for solution-processed tandem solar cells, where multiple perovskite absorber layers are sequentially processed. A few cross-linkable HTMs and ETMs have been reported in PSC literature. Thermal crosslinking has been achieved using HTMs with two or more styrene[19,22,23] or other vinyl moieties,[24] or by reacting styrene-functionalized HTMs with oligo(thiol) derivatives.[20] While respectable photo and thermal stability, and performance have been achieved with those materials, the high temperature and cross-linking time needed is not optimal for multilayer printable electronics. Furthermore, none of the cross-linkable HTMs used in PSC devices thus far has demonstrated the capability for multiple layers of perovskite absorber, deposited from solution. The polar, aprotic solvents typically used for PSC, dimethylformamide and dimethylsulfoxide, can induce swelling and chain scission in polymers[25,26] that can lead to the dissolution of layers beneath the HTM, making printable tandem perovskite solar cells particularly challenging.

A dopant-free HTM or one in which dopant diffusion is minimized is also clearly desirable for long-term stability, and cross-linking could help achieve these objectives. Most HTMs in perovskite solar cells utilize lithium bis(trifluoromethanesulfonyl)imide (Li-TFSI), in combination with oxygen exposure and 4-tert-butylpyridine (tBP), which helps prevent phase segregation of the HTM and Li-TFSI.[27] Unfortunately, the use of both Li-TFSI and tBP have been shown to degrade performance in long term stability tests, since Li-TFSI is hygroscopic and tBP is volatile.[2,27,28] While alternative dopants have not been as heavily investigated, F4-TCNQ is commonly utilized in p-i-n PSCs, but has been found to migrate into adjacent layers in device stacks due to its relatively high diffusivity, and is also highly volatile.[29,30]

In this chapter, a cross-linkable acrylate random copolymer with both hole transporting bis(triarylamine) and photo-cross-linkable cinnamate side chains[31] is compared to the widely used poly(4-butyl-triphenylamine-4',4''-diyl) (poly(4-butyl-triphenylamine-4',4''-diyl) (PolyTPD) as a hole transport material in p-i-n perovskite solar cells (PSC). The crosslinked films of this HTM exhibit improved wettability by precursor solutions of the perovskite relative to PolyTPD; this facilitates high-quality full film coverage

by the subsequently deposited perovskite layer on smooth substrates, which is difficult to achieve with PolyTPD without the use of additional interlayers. PSCs fabricated using undoped and cross-linked copolymer achieve steady-state power outputs (SPOs) that are comparable to those of cells incorporating p-doped PolyTPD as the HTM. The devices made with this material also exhibited improved initial stability under high-intensity ultraviolet LED irradiation, in comparison to those with the PolyTPD analogue.

Remarkably, after 3,000 h of aging in an oven at 85 °C in a nitrogen-filled glovebox, device efficiency showed no degradation with steady-state power output comparable to the initial performance. In previous chapters, n-i-p devices on metal oxide n-types and with Spiro-OMeTAD exhibited comparatively rapid degradation under typically milder aging conditions. Even the devices utilizing the most stable metal oxide n-type, SnO_2, and a methylammonium-free perovskite, $FA_{0.83}Cs_{0.17}Pb(I_{0.90}Br_{0.10})_3$, completely failed within 100 hours under the same aging conditions of 85 °C under N_2. These results highlight the importance of interface management by demonstrating that organic contacts, used in conjunction with more stable p-type dopants and a Cr-Au bi-layer electrode, can improve device lifetimes by more than 30-fold over the conventional n-i-p device stack.

8.2 Characterization of the HTM

HTMs for PSCs often contain the bis(diarylamino)biphenyl moiety. For example, the widely used spiro-OMeTAD consists of two such moieties linked by a bridging carbon atom. More recently, polymeric materials containing the same moiety, such as PolyTPD and PTAA (poly(2,4,6-trimethyltriphenylamine-4',4''-diyl)), have shown great potential as HTMs in inverted, p-i-n PSCs,[32–34] where the HTM is the first layer deposited. Cells using PolyTPD have achieved a record of 19.1% PCE.[35] The same bis(diarylamino)biphenyl motif has also been widely used in OLEDs and random copolymers of monomers with bis(diarylamino)biphenyl functionalization and monomers

with cinnamate side chains have been used as solution-processable materials that can subsequently be insolubilized through brief UV irradiation to induce cross-linking of the cinnamate groups.[31,36–39] This approach is modular in that the properties of the polymer can be adjusted through varying the HTM:crosslinker ratio, the ionization energy (IE) of the polymer can be varied through the substitution pattern of the HTM monomer, and other polymer properties can be varied through the choice of the polymer backbone. Previously reported polymers P1-2, the copolymer of a bis(diarylamino)biphenyl-acrylate monomer (1), and a cinnamate-acrylate monomer (2)[31] were selected as a candidate HTM for investigation in PSC here. The molecular structure and the absorbance and emission spectra of these HTMs are shown in Figure 8.1a.

Monomers 1 and 2 and copolymer P1-2 were synthesized as previously described.[31] Films of the polymer were insolubilized using a short illumination time at 356 nm, which does not significantly degrade the HTM unit of the polymer. This facile photo-cross-linking is potentially advantageous over alternative thermal crosslinker approaches that require high temperatures > 150 °C since the process can be done at ambient temperature on plastic substrates. Moreover, for n-i-p structures, the low power UV-lamp used would not degrade the underlying perovskite layer, whereas the temperatures required for many thermal cross-linking reactions could degrade volatile organic cations.

P1-2 has a slightly higher energy onset of optical absorption than PolyTPD (Figure 8.1c and Table 8.1), which is potentially advantageous in allowing more of the solar spectrum to reach the active layer, potentially reducing parasitic absorption and maximizing current density. The addition of F4-TCNQ to solutions of either PolyTPD or P1-2 leads to only moderate changes in the optical spectra, suggesting inefficient doping with this oxidant. This is further illustrated by Figure 8.1d, where the effects of successive dopant addition are shown for the case of P1-2.

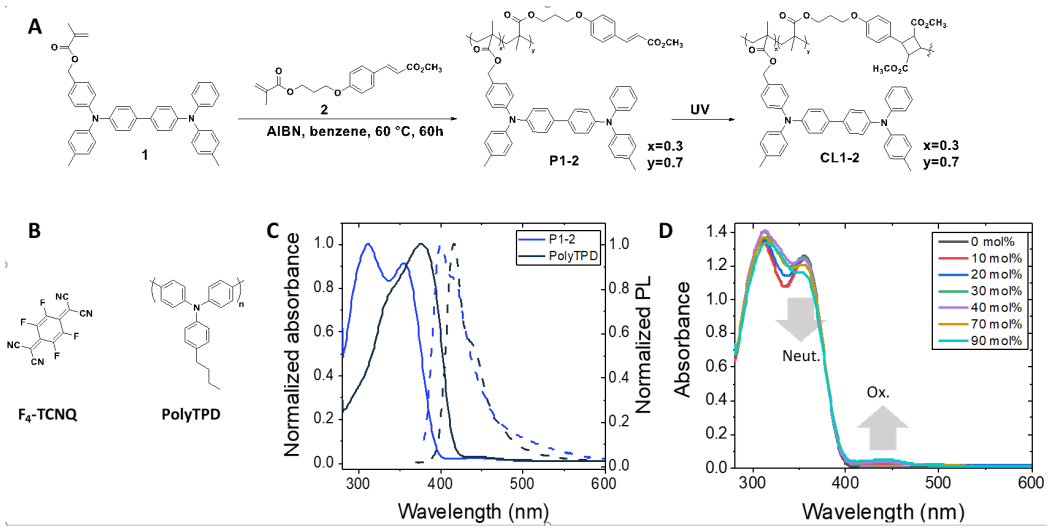

Figure 8.1: Synthesis, Doping, and Absorption of P1-2 and PolyTPD. (A) Synthesis of copolymer P1-2 from the bis(triarylamine) 1 and the cinnamate 2. The crosslinked material CL1-2 can be obtained after illumination with UV light. (B) Chemical structure of PolyTPD and F4-TCNQ, the dopant usually used to dope triarylamine-based HTMs. (C) Comparison of the absorbance (solid line) and photoluminescence (dashed line) spectra of P1-2 and PolyTPD in toluene (with 20 mol% F4-TCNQ per triarylamine unit). (D) UV-vis spectrum showing the doping in toluene solution of P1-2 with F4-TCNQ (where Neut. and Ox. indicate signals attributable to the neutral and oxidized bis(diarylamino)biphenyl units, respectively, and x mol% is relative to the number of triarylamine units, i.e. corresponds 2x molar equivalents per 100 moles of monomer) These data were collected by Marie-Hélène Tremblay.

8.3 Characterization of HTM Films and Perovskite Growth

Atomic force microscopy of thin films of CL1-2 and PolyTPD on glass substrates showed similar homogeneity and smoothness (Figure 8.2a,b). Perovskite films crystallized on top of the two HTM films on FTO substrates also appeared similar by scanning electron microscopy (SEM), although a larger distribution of bright color grains is observed on the CL1-2 film than on PolyTPD, which are typically composed of PbI_2 (Figure 8.2c-e). It is unclear whether this has any device consequences, but excess PbI_2 has been found to be beneficial in previous PSC studies.[41,42] The X-ray diffraction (XRD) patterns of the perovskite films on top of the two different HTMs are also similar, indicating comparable perovskite growth on both materials when FTO is used as the substrate (see Figure 8.3).

The conductivity of the HTMs was characterized using four-point probe measure-

	PolyTPD	P1-2
$\lambda_{max,abs}$ / nm	377 (338)	313 (356)
$\lambda_{max,PL}$ / nm	417 (441)	400 (416)
IE / eV	5.2	5.1
EA / eV	2.1	1.8
$E_{g,optical}$ / eV	3.06	3.23
σ / S m^{-1}	0.0100	0.0141
T_g / °C	230	137

Table 8.1: Key properties of PolyTPD and P1-2. The spectra were measured in toluene. IE and EA stand for ionization energy and electron energy, respectively. IE estimated by cyclic voltammetry. The electron affinity was estimated using EA = IE - $E_{g,optical}$. Optical gap was calculated using the normalized absorbance and fluorescence spectra. The conductivity was measured by 4-point probe measurements of undoped films. T_g values are from literature.[31,40]

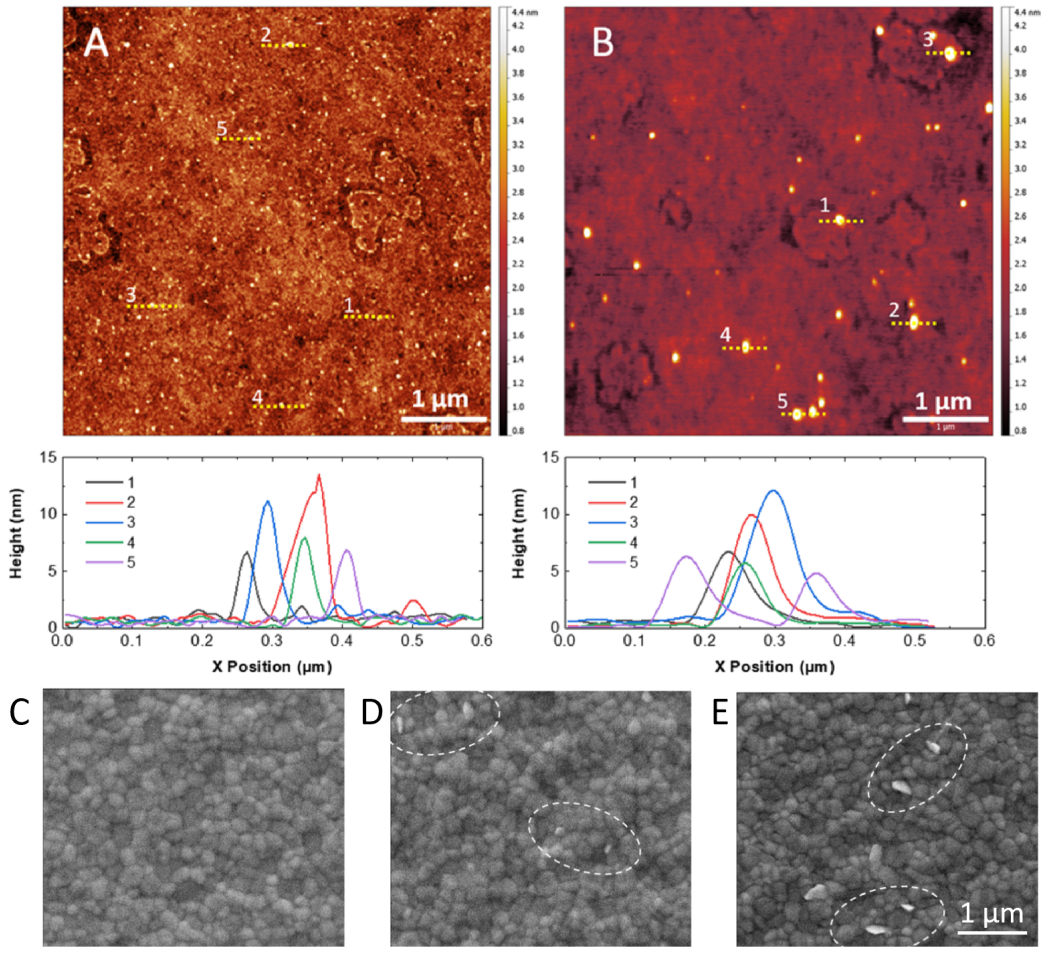

Figure 8.2: A) AFM topography of doped PolyTPD on quartz glass. B) AFM topography of Doped CL1-2 on quartz glass. C) SEM images of perovskite grown on doped PolyTPD, D) undoped CL1-2, and E) doped CL1-2.

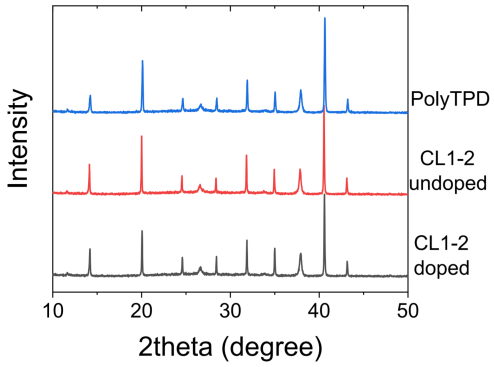

Figure 8.3: XRD patterns reveal no substantial differences in perovskite film crystallization.

ments with and without F4-TCNQ doping. Slightly lower conductivity was measured for CL1-2 compared to PolyTPD (see Figure 8.4) after annealing at 130 °C, which was the same annealing temperature used during device fabrication. In both cases, doping the HTM with F4-TCNQ p-dopant increased the conductivity of the HTM by similar amounts. However, PSC device performance was comparable for undoped and doped CL1-2, while the performance increased upon doping of PolyTPD, as shown in the device data further on. Although the active layers of the PSCs fabricated in this work are annealed at only 100 °C, some perovskite materials necessitate high annealing temperature (e.g., often >200 °C for inorganic $CsPbX_3$ perovskites).[43,44] Therefore, the effect of higher annealing temperatures was investigated on both doped CL1-2 and doped uncross-linked P1-2. After annealing at 180 °C, the doped CL1-2 conductivity was found to be higher than that of doped uncross-linked P1-2, which is consistent with cross-linking perhaps helping to retain the volatile F4-TCNQ within the film. When films were further annealed at 250 °C, the conductivity of CL1-2 increased, while the electronic integrity of the PolyTPD film was damaged, and conductivity decreased dramatically, perhaps due to film damage occurring above the T_g of the latter polymer. This enhanced dopant retention of doped CL1-2 may make it a suitable HTM for perovskite layers that require a high annealing temperature, such as the inorganic $CsPbX_3$ materials.

To investigate the charge transfer at the perovskite and the HTM interface, steady-state and time-resolved photoluminescence (PL) measurements were performed (see

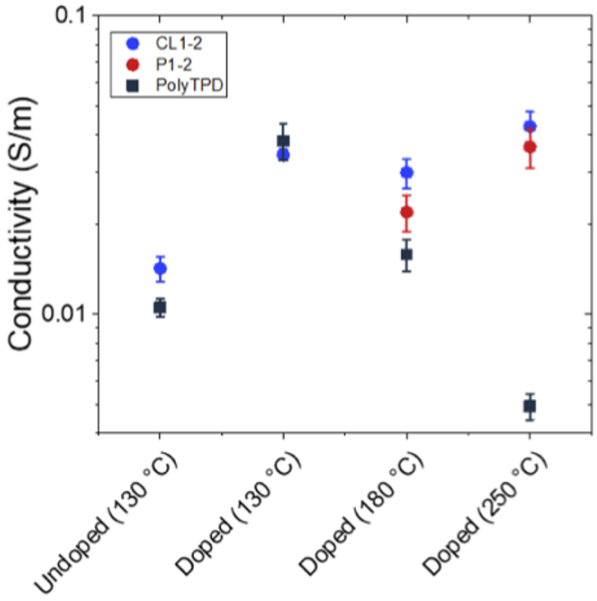

Figure 8.4: 4-point probe conductivity measurement of PolyTPD and P1-2/CL1-2. Films are 10 nm thick. The samples are first annealed 130 °C, which correspond to the processing temperature in the solar cells, and further annealed at the indicated temperature for 10 min. The HTMs are both doped with 20 mol% F4-TCNQ in solution prior to film deposition.

Figure 8.5). The doped CL1-2 showed similar PL quenching compared to that of PolyTPD, indicating comparable hole-extraction capability for both HTMs at the perovskite-HTM interface, but exhibited different PL lifetimes. The PL maximum for the PolyTPD sample is slightly redshifted (770 nm) relative to the CL1-2 and the perovskite-on-glass samples (both 768 nm), which may indicate more band-bending due to shallow-trap formation in the case of PolyTPD.[45,46] Carrier lifetimes were extracted by fitting a bi-exponential decay model to the time-resolved PL data:

$$Y = A_1 exp\left(\frac{-t}{\tau_1}\right) + A_2 exp\left(\frac{-t}{\tau_2}\right) + y_0 \tag{8.1}$$

where τ_1 is the lifetime for fast, trap-assisted processes (Shockley-Read-Hall recombination), and τ_2 is the lifetime for slower bimolecular recombination, and A_1 and A_2 are the relative amplitudes.[14] The fitting gave lifetimes of $\tau_1 = 16.1$ ns and $\tau_2 = 127.5$ ns for the CL1-2 sample, while the perovskite film on PolyTPD exhibited lifetimes of $\tau_1 = 15.7$ ns and $\tau_2 = 74.5$ ns. In contrast, bulk recombination processes dominate for the perovskite film on glass, giving a much longer τ_2 lifetime of 342.2 ns.

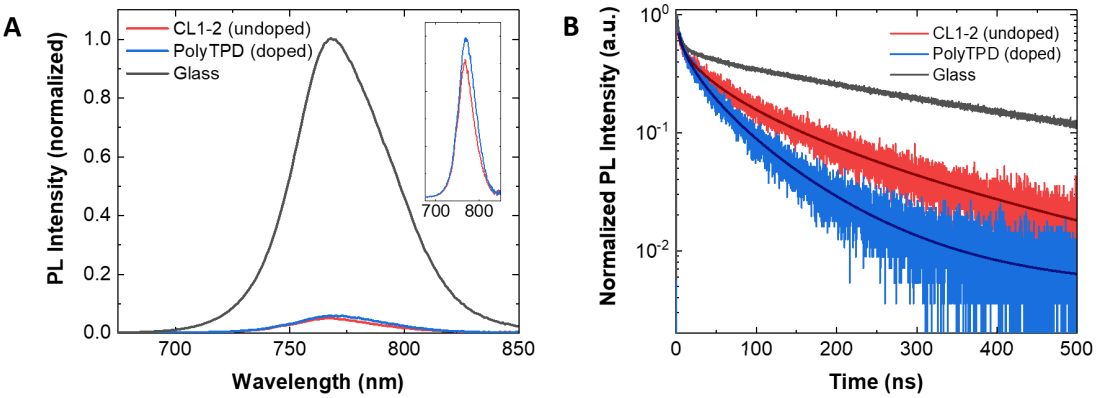

Figure 8.5: A) Steady State PL spectra of FACs films grown on CL1-2, PolyTPD, and quartz glass. B) Time-Resolved PL decays of FACs films grown on CL1-2, PolyTPD, and quartz glass, with model fit displayed as the darker line within the TRPL traces.

8.4 Device Fabrication and Characterization

The photovoltaic performance of CL1-2 and PolyTPD as HTMs in PSCs was compared using the architecture: FTO/HTM/$Cs_{0.05}(FA_{0.85}MA_{0.15})_{0.95}Pb(I_{0.9}Br_{0.1})_3$/PCBM /BCP/Ag (or Cr/Au for thermal stability tests), where FTO = fluorine-doped tin oxide, MA = methylammonium, FA = formamidinium, PCBM = phenyl-C_{61}-butyric acid methyl ester, and BCP = bathocuproine. The two HTM layers had approximately the same thickness of 6-8 nm as determined by surface profilometry. Both pristine and doped CL1-2 showed similar performance to PolyTPD. The current-density–voltage (J–V) characteristics were measured under a simulated AM 1.5G (100 mW cm-2) sunlight (see Figure 8.6, Table 8.2).

Only a slight improvement was noticed when CL1-2 was doped using F4-TCNQ, while a significant improvement was obtained for PolyTPD devices. The devices using undoped CL1-2 show a PCE of (16±2)%, which is similar to the control device with doped PolyTPD ((16±2)%; Table S1). The SPO provides a more complete view of solar cell performance under operating conditions and avoids the ambiguities associated with J-V hysteresis. CL1-2 achieves 18.7% SPO, matching its scanned efficiency, while PolyTPD achieves 17.7%, and exhibits a transient decay. Typically, when SPO is lower than scanned efficiency it is related to hysteresis induced by ion

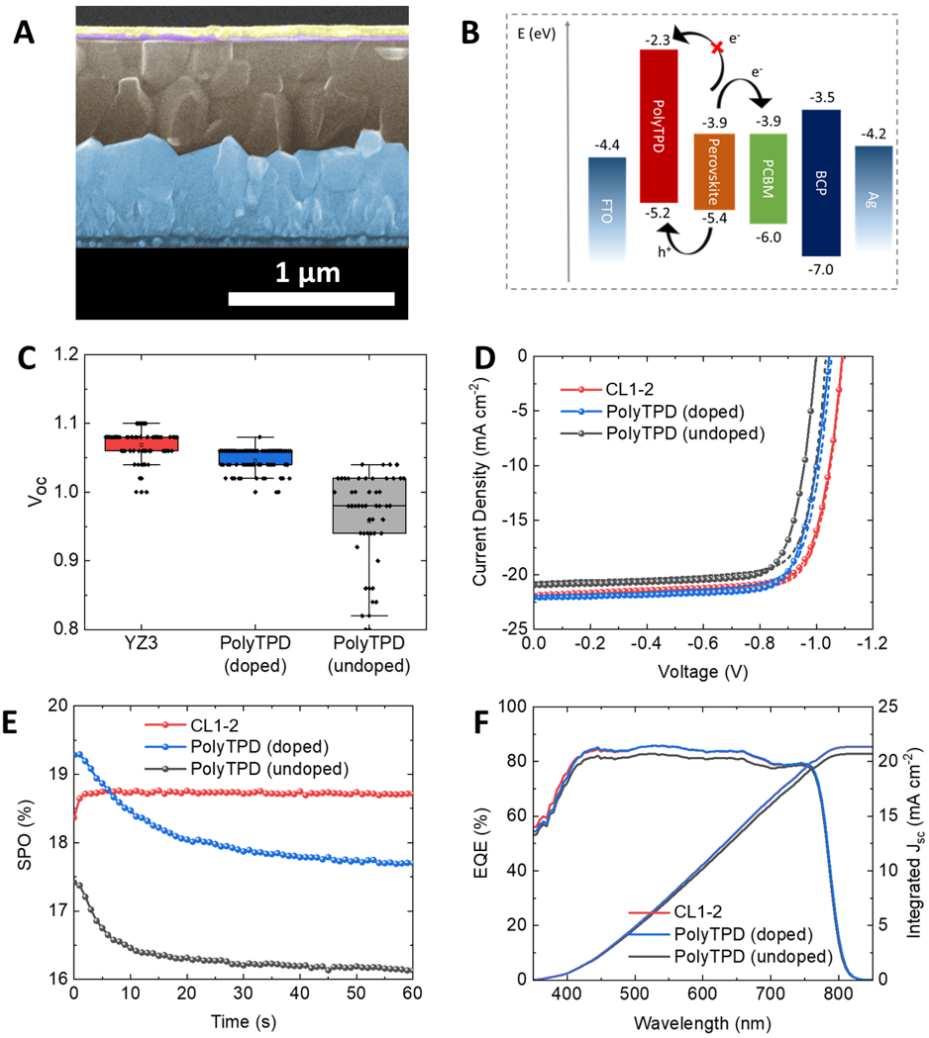

Figure 8.6: Device Data for CL1-2 and PolyTPD. (A) SEM device cross section with FTO (blue), CL1-2, $Cs_{0.05}(FA_{0.85}MA_{0.15})_{0.95}Pb(I_{0.9}Br_{0.1})_3$ (gray), PCBM and BCP (purple), and Ag electrode (yellow). (B) Schematic representation of the inverted "p-i-n" PSCs. (C) Comparison of Voc for undoped CL1-2, doped PolyTPD, and undoped PolyTPD. (D) J-V characteristics for champion devices employing undoped CL1-2, doped PolyTPD, and undoped PolyTPD collected under AM 1.5G simulated sunlight. (E) Steady-state power output. (F) External quantum efficiency (EQE).

migration and unbalanced charge extraction rates at selective contacts,[47,48] yet with doped PolyTPD SPO decay is observed without accompanying J-V hysteresis. This behavior may be related to a photo-instability, such as the evolution of photo-induced trap states, rather than to mobile ions and unbalanced charge extraction. In such a case, a J-V scan collected over a few seconds may not reflect the longer-term SPO. This possibility is consistent with photoluminescence quantum efficiency for half devices (FTO/PolyTPD/perovskite), collected at comparable time scales to the

Device	J_{sc} (mA cm^{-2})	V_{oc} (V)	FF	PCE (%)
Undoped CL1-2				
Average	20.6 ± 0.9	1.07 ± 0.02	0.72 ± 0.05	16 ± 2
Champion	22.6	1.10	0.80	18.7
Undoped PolyTPD				
Average	18.0 ± 1.4	0.96 ± 0.08	0.72 ± 0.07	13 ± 2
Champion	21.0	1.04	0.79	16.4
Doped PolyTPD				
Average	21.0 ± 1.1	1.05 ± 0.02	0.74 ± 0.04	16 ± 2
Champion	23.1	1.08	0.79	18.1

Table 8.2: Solar Cell Performance Parameters Determined from J-V Curves for 144 Devices Prepared in 2 Batches

SPO, and the intermediate-term UV stability of full devices. Both measurements reflect an illumination- and time-dependent decay similar to that observed in the SPO, as discussed further in the device stability section. The performance of the cells over time is consistent with the trend seen on the J-V curves. Despite the longer wavelength onset of absorption seen for PolyTPD, all devices gave similar external quantum efficiency (EQE) spectra, which is consistent with the similar Jsc measured in the J-V scans.

One way that the solar-cell performance of cells with PolyTPD and CL1-2 HTMs differ is that the latter exhibit somewhat larger V_{oc} values (Figure 8.6C). It has previously been shown that Lewis base-containing HTMs or small molecules can passivate the surface traps and electronic disorder at the surface of the perovskite layer;[4,49–51] in this case coordination of the ester moieties present in CL1-2 to the perovskite surface might act similarly, thus reducing recombination and increasing V_{oc} (Figure 8.6c). PL lifetime experiments on films of perovskite in contact with undoped CL1-2 or doped PolyTPD are consistent, the former exhibiting longer lifetimes associated with bimolecular recombination. Correlations between PL decay and V_{oc} have also been reported in the literature.[46,52,53] In addition, esters can play a useful role in perovskite growth and/or passivation. Poly(methyl methacrylate) has been

deposited on perovskite films as an addition to the "solvent quenching" solution[54] and also used an interlayer between perovskite and HTM in both n-i-p[55] and p-i-n[56] cells.

8.5 HTM Wettability and Tandem Proof of Concept

While the crystallization and morphology of perovskite films on PolyTPD and CL1-2 were similar when FTO substrates were used, there was a dramatic difference in the surface coverage of perovskite films processed on these two HTMs in conjunction with smoother substrates such as glass or tin-doped indium oxide (ITO). ITO may offer slightly improved performance for solar cells, as reported transmittance in the visible spectrum and conductivity are higher than FTO.[57,58] The CL1-2 film displays a more hydrophilic surface, with a water contact angle, θ, of (82$\pm$3)°, than the PolyTPD film (θ = 93$\pm$6)°, which could explain why it is easier to spin-coat perovskite on smooth CL1-2 films on glass or ITO, while it is not possible or difficult for PolyTPD films on glass and ITO. Stronger perovskite-HTM interactions could also be the cause for the improved wettability of CL1-2 relative to PolyTPD. Indeed, the esters and ether on CL1-2 could hydrogen bond with the cations of the perovskite to facilitate its deposition, or the carbonyl group could form an intermediate adduct with PbI_2.[52] While PolyTPD can be treated with UV-Ozone to improve its wettability, sufficient treatment time to ensure full perovskite film coverage of the substrate substantially degrades photovoltaic device performance.[59] To make PSCs on ITO using PolyTPD, a polyelectrolyte was tested that has previously been used to improve the wettability and performance of PTAA in p-i-n PSCs, as shown in Figure 8.7.[53,60] Consistent with other reports, the (9,9-bis(3-(N,N-dimethylamino)propyl)fluorene-2,7-diyl)-alt-(9,9-dioctylfluoren-2,7-diyl) (PFN) treatment on PolyTPD improves the V_{oc} of the solar cells, but the relatively larger loss in fill factor results in degraded performance. While the fill factor loss was reduced with lower thicknesses of PFN, concentrations that were just adequate to ensure uniform perovskite surface coverage (0.1 mg ml^{-1}) still resulted in a loss to the device efficiency.

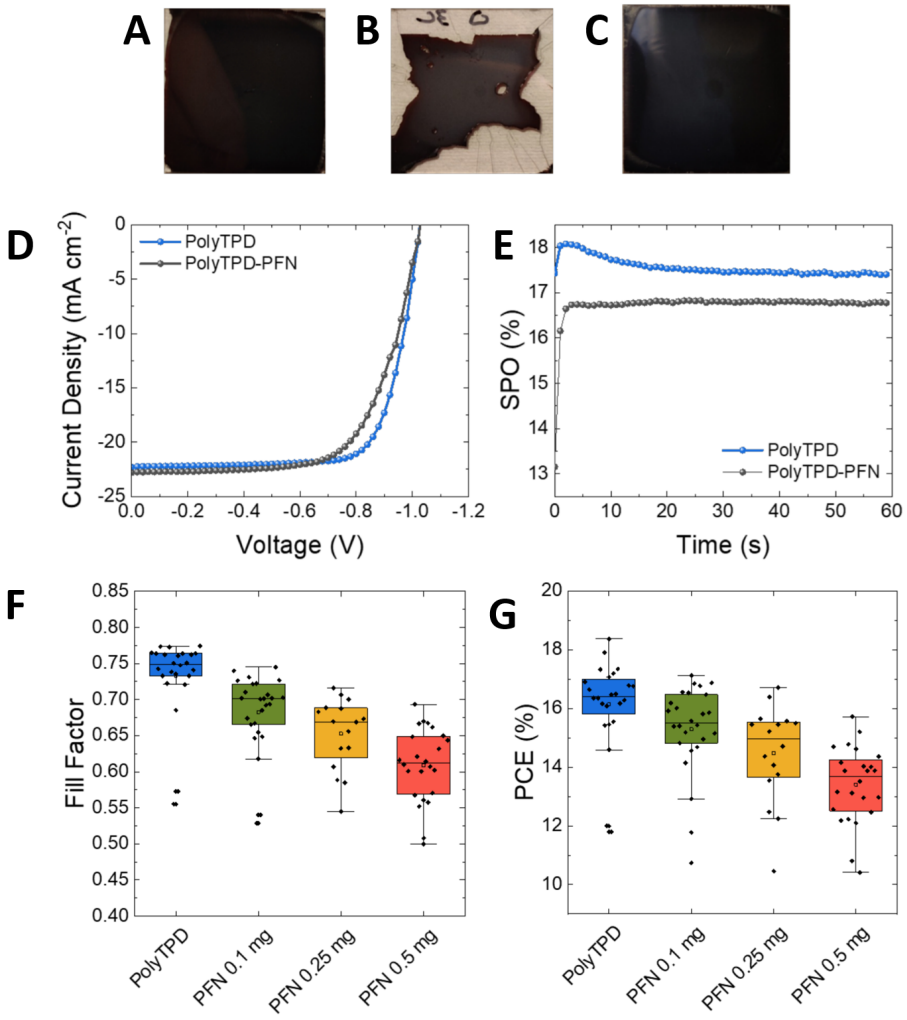

Figure 8.7: a) Perovskite film on CL1-2. b) Perovskite film on PolyTPD. c) Perovskite film on PFN treated PolyTPD (PFN concentration 0.1 mg ml^{-1}). Note that all photographs are of films on ITO, while device data is for films on FTO. d) J-V scans of champion devices. e) SPO of champion devices. f) Fill factor of devices with and without PFN. g) Power conversion efficiency of devices with and without PFN.

In the first proof of concept for cross-linkable HTMs, CL1-2 also demonstrated the potential for solution-processed tandem PSC as shown in Figure 8.8. A layer of $MAPbI_3$ can be successively coated onto CL1-2, which was deposited on top of $FA_{0.83}Cs_{0.17}Pb(I_{0.90}Br_{0.10})_3$ (itself grown on FTO). When a PolyTPD HTM interlayer was used instead of CL1-2, the $MAPbI_3$ precursor appeared to permeate the HTM and partially dissolve the underlying perovskite. In the case of the PolyTPD interlayer, two absorption onsets were observed for $FA_{0.83}Cs_{0.17}Pb(I_{0.90}Br_{0.10})_3$ and $MAPbI_3$,

indicating the presence of both perovskites, but the low absorbance of the films indicates there was no improvement in light harvesting.

This suggests cross-linked organic semiconductors may facilitate solution processing of tandem solar cells, where the cross-linking approach could potentially be extended to allow for a recombination layer that is itself a multilayer composed of sequentially deposited and crosslinked materials with separate hole- and electron-transport functions and potentially with and without dopants. Although multilayer recombination layers of this kind have been fabricated using organic semiconductors,[61] they generally require vacuum evaporation to avoid the deposition of one layer leading to the dissolution of another. An alternative solution-processed approach to tandem fabrication uses bi-layers of PEDOT:PSS and ITO nanoparticles,[62] but the former may lead to the incorporation of traces of water in the device, and both of these materials impair transmission in the visible.

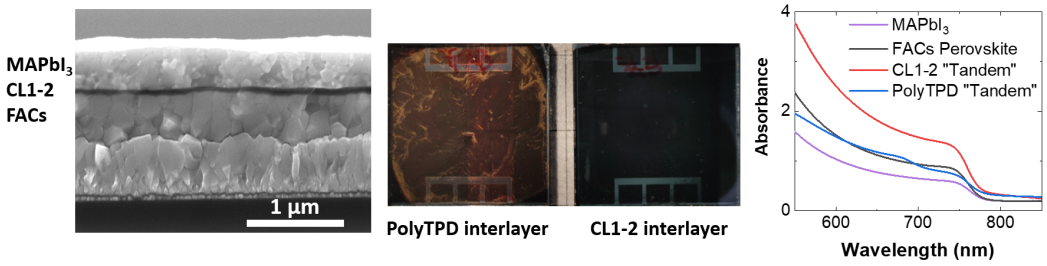

Figure 8.8: Solution Processed Tandem Proof of Concept. Left: SEM cross section showing a "tandem" structure FTO/FACs/CL1-2/MAPbI3 (FACs = $FA_{0.83}Cs_{0.17}Pb(I_{0.90}Br_{0.10})_3$). Note: The $MAPbI_3$ precursor was prepared in acetonitrile rather than dimethylformamide. Center: photographs from the top of structures with PolyTPD and CL1-2 interlayers. When $MAPbI_3$ was deposited on top of PolyTPD, the underlying FACs film dissolved. Right: absorption spectra of the films shown in the center, compared to those of films of the two perovskite materials deposited separately. These data show use of CL1-2 leads to a structure that is much more strongly absorbing than FACs alone due to successful deposition of $MAPbI_3$.

8.6 Device Stability Studies

The photo- and thermal-stability of the $Cs_{0.05}(FA_{0.85}MA_{0.15})_{0.95}Pb(I_{0.9}Br_{0.1})_3$ PSCs incorporating CL1-2 and PolyTPD were studied without encapsulation in an N_2-filled glovebox. The devices were periodically removed to ambient atmosphere for

measurements under an AM 1.5G solar simulator, where the stabilized power output was measured after 50 s. Figure 8.9 shows the stability in an oven at 85 °C; CL1-2 showed similar stability to PolyTPD devices. Remarkably, the devices show an improvement in performance over the first 1,000 hours of aging, and retain greater than their initial efficiency until after 3,000 h, which appears to be the longest 85 °C thermal stability timescale reported in the literature.[27,63–65]

Photostability was studied under a high intensity LED array (365 nm LED, equivalent to 12 suns UV component of the AM 1.5G spectrum). Initially, a drop in SPO is seen for the PolyTPD devices, while the CL1-2 devices stayed approximately at the same initial SPO (Figure 8.9b). The current density decreased at a greater extent for PolyTPD devices (Figure 8.9c). To study this instability, the photoluminescence quantum efficiency (PLQE) of the perovskite film crystallized on top of the HTM layer on FTO was measured over time. A 70% drop in PolyTPD PLQE was observed after stabilization (2 min), while the CL1-2 doped and pristine PLQE retained 81% and 87% of their initial values, as displayed in (Figure 8.9d).

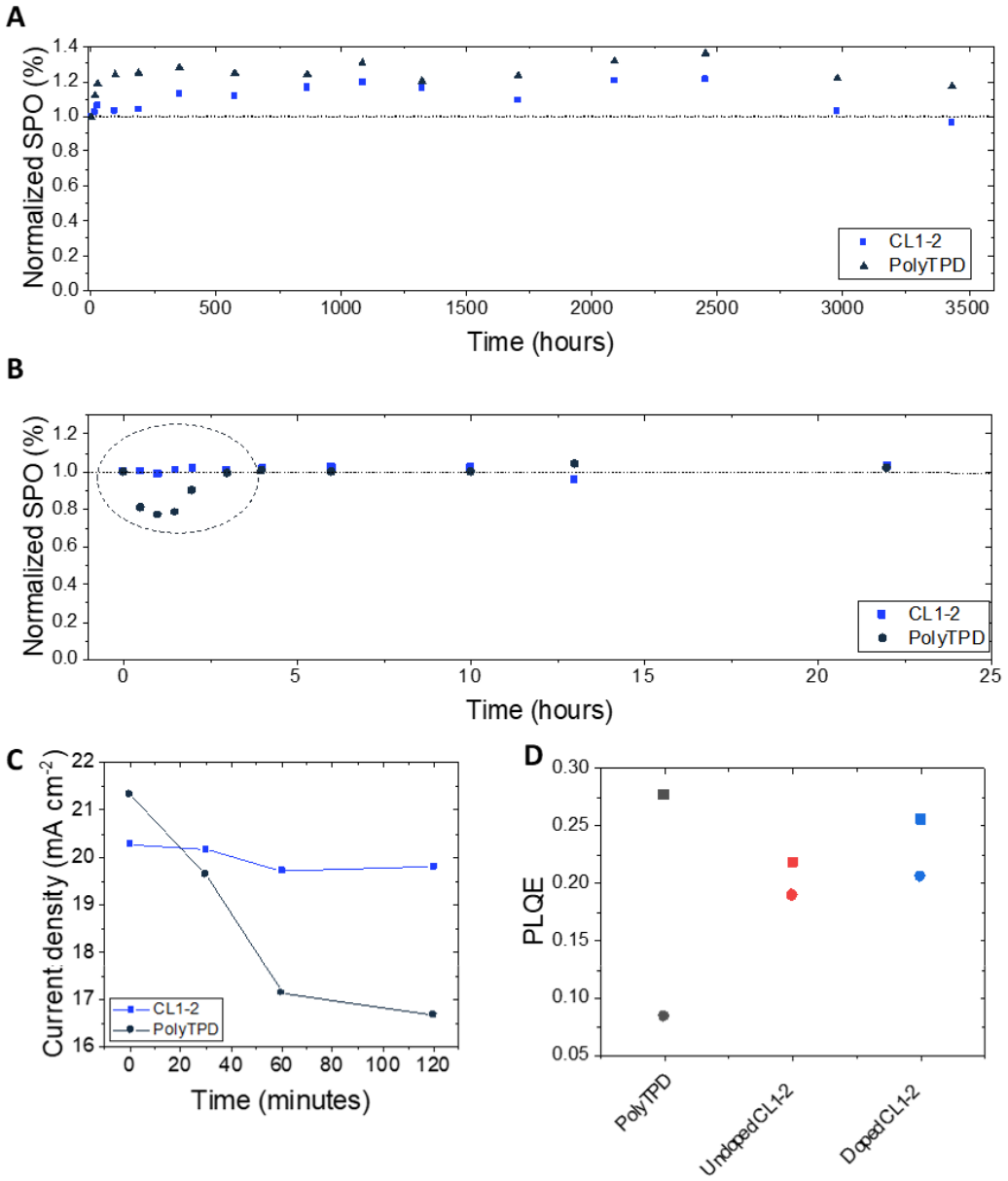

Figure 8.9: Device Stability Data for CL1-2 and PolyTPD. Normalized stabilized power output (SPO) over 50 s after (A) aging the devices at 85 °C in an oven inside an N_2-filled glovebox without encapsulation, (B) aging the devices with a UV LED light inside an N_2-filled glovebox without encapsulation. The devices were periodically removed to atmosphere for measurements. Both HTMs are doped with F4-TCNQ. (C) Evolution of the current density of CL1-2 and PolyTPD devices when aged under UV LED light (same experiments as B). (D) Initial (square) and stabilized (circle) PLQE of the half devices (FTO/HTM/perovskite). Devices for stability measurements were made by Marie-Hélène Tremblay. Data for UV stability and first ~500 hours of thermal stability were collected by Marie-Hélène Tremblay.

8.7 Conclusion

In summary, this work presents the first use of a photo-crosslinked HTM in PSCs, an acrylate copolymer with bis(triarylamine) and cinnamate side chains. While solar cells using CL1-2 match the state-of-the-art HTM PolyTPD in terms of photovoltaic performance, comparative stability between CL1-2 and PolyTPD provides a more ambiguous picture. CL1-2 clearly offers improved short-term photostability, which may be relevant in real-world conditions if a dark reset at night results in the initial illumination dependent degradation observed for PolyTPD with each new day cycle. However, PolyTPD provides improved long-term thermal stability at 85 °C and devices with PolyTPD also exhibit a greater improvement over initial performance as aging continues. Thermal stability tests were started with F4-TCNQ doped CL1-2, before it was realized that the dopant was not necessary to achieve high performance. It may be the case that undoped CL1-2 provides improved thermal stability, since F4-TCNQ is volatile and has previously been observed to diffuse into adjacent layers of organic solar cells,[29,30] but the undoped thermal stability of devices with CL1-2 was not evaluated here. Nevertheless, multiple advantages of CL1-2 over PolyTPD were demonstrated: CL1-2 does not need to be doped to achieve comparatively high PCE while PolyTPD does, the HTM is transparent in the visible region while PolyTPD is not, the perovskite is easier to process on top of the CL1-2 HTM due to its improved wettability, and CL1-2 is a less permeable interlayer for stacking multiple perovskite absorbers. Collectively, these findings suggest that the cross-linkable CL1-2 is a promising candidate for single-junction and tandem solar cells.

References

1. N.-G. Park, M. Grätzel, T. Miyasaka, K. Zhu, and K. Emery, "Towards stable and commercially available perovskite solar cells," *Nature Energy*, vol. 1, oct 2016.
2. G. Niu, X. Guo, and L. Wang, "Review of recent progress in chemical stability of perovskite solar cells," *Journal of Materials Chemistry A*, vol. 3, no. 17, pp. 8970–8980, 2015.
3. Q. Jiang, Y. Zhao, X. Zhang, X. Yang, Y. Chen, Z. Chu, Q. Ye, X. Li, Z. Yin, and J. You, "Surface passivation of perovskite film for efficient solar cells," *Nature Photonics*, vol. 13, pp. 460–466, apr 2019.
4. M. Saliba, T. Matsui, J.-Y. Seo, K. Domanski, J.-P. Correa-Baena, M. K. Nazeeruddin, S. M. Zakeeruddin, W. Tress, A. Abate, A. Hagfeldt, and M. Grätzel, "Cesium-containing triple cation perovskite solar cells: improved stability, reproducibility and high efficiency," *Energy & Environmental Science*, vol. 9, no. 6, pp. 1989–1997, 2016.
5. D. P. McMeekin, G. Sadoughi, W. Rehman, G. E. Eperon, M. Saliba, M. T. Horantner, A. Haghighirad, N. Sakai, L. Korte, B. Rech, M. B. Johnston, L. M. Herz, and H. J. Snaith, "A mixed-cation lead mixed-halide perovskite absorber for tandem solar cells," *Science*, vol. 351, pp. 151–155, jan 2016.
6. I. C. Smith, E. T. Hoke, D. Solis-Ibarra, M. D. McGehee, and H. I. Karunadasa, "A layered hybrid perovskite solar-cell absorber with enhanced moisture stability," *Angewandte Chemie International Edition*, vol. 53, pp. 11232–11235, sep 2014.
7. D. H. Cao, C. C. Stoumpos, O. K. Farha, J. T. Hupp, and M. G. Kanatzidis, "2d homologous perovskites as light-absorbing materials for solar cell applications," *Journal of the American Chemical Society*, vol. 137, pp. 7843–7850, jun 2015.
8. Y. Chen, Y. Sun, J. Peng, W. Zhang, X. Su, K. Zheng, T. Pullerits, and Z. Liang, "Tailoring organic cation of 2d air-stable organometal halide perovskites for highly efficient planar solar cells," *Advanced Energy Materials*, vol. 7, p. 1700162, may 2017.
9. C. Ma, D. Shen, T.-W. Ng, M.-F. Lo, and C.-S. Lee, "2d perovskites with short interlayer distance for high-performance solar cell application," *Advanced Materials*, vol. 30, p. 1800710, apr 2018.
10. L. Mao, W. Ke, L. Pedesseau, Y. Wu, C. Katan, J. Even, M. R. Wasielewski, C. C. Stoumpos, and M. G. Kanatzidis, "Hybrid dion–jacobson 2d lead iodide perovskites," *Journal of the American Chemical Society*, vol. 140, pp. 3775–3783, feb 2018.

11. H. Tsai, W. Nie, J.-C. Blancon, C. C. Stoumpos, R. Asadpour, B. Harutyunyan, A. J. Neukirch, R. Verduzco, J. J. Crochet, S. Tretiak, L. Pedesseau, J. Even, M. A. Alam, G. Gupta, J. Lou, P. M. Ajayan, M. J. Bedzyk, M. G. Kanatzidis, and A. D. Mohite, "High-efficiency two-dimensional ruddlesden–popper perovskite solar cells," *Nature*, vol. 536, pp. 312–316, jul 2016.

12. S. N. Habisreutinger, T. Leijtens, G. E. Eperon, S. D. Stranks, R. J. Nicholas, and H. J. Snaith, "Carbon nanotube/polymer composites as a highly stable hole collection layer in perovskite solar cells," *Nano Letters*, vol. 14, pp. 5561–5568, sep 2014.

13. K. Rakstys, S. Paek, P. Gao, P. Gratia, T. Marszalek, G. Grancini, K. T. Cho, K. Genevicius, V. Jankauskas, W. Pisula, and M. K. Nazeeruddin, "Molecular engineering of face-on oriented dopant-free hole transporting material for perovskite solar cells with 19% PCE," *Journal of Materials Chemistry A*, vol. 5, no. 17, pp. 7811–7815, 2017.

14. D. Bi, C. Yi, J. Luo, J.-D. Décoppet, F. Zhang, S. M. Zakeeruddin, X. Li, A. Hagfeldt, and M. Grätzel, "Polymer-templated nucleation and crystal growth of perovskite films for solar cells with efficiency greater than 21%," *Nature Energy*, vol. 1, sep 2016.

15. M. Saliba, S. Orlandi, T. Matsui, S. Aghazada, M. Cavazzini, J.-P. Correa-Baena, P. Gao, R. Scopelliti, E. Mosconi, K.-H. Dahmen, F. D. Angelis, A. Abate, A. Hagfeldt, G. Pozzi, M. Graetzel, and M. K. Nazeeruddin, "A molecularly engineered hole-transporting material for efficient perovskite solar cells," *Nature Energy*, vol. 1, jan 2016.

16. J. Cao, B. Wu, R. Chen, Y. Wu, Y. Hui, B.-W. Mao, and N. Zheng, "Efficient, hysteresis-free, and stable perovskite solar cells with ZnO as electron-transport layer: Effect of surface passivation," *Advanced Materials*, vol. 30, p. 1705596, jan 2018.

17. C. Liu, K. Wang, P. Du, T. Meng, X. Yu, S. Z. D. Cheng, and X. Gong, "High performance planar heterojunction perovskite solar cells with fullerene derivatives as the electron transport layer," *ACS Applied Materials & Interfaces*, vol. 7, pp. 1153–1159, jan 2015.

18. Z. Zhu, Y. Bai, X. Liu, C.-C. Chueh, S. Yang, and A. K.-Y. Jen, "Enhanced efficiency and stability of inverted perovskite solar cells using highly crystalline SnO2nanocrystals as the robust electron-transporting layer," *Advanced Materials*, vol. 28, pp. 6478–6484, may 2016.

19. C.-C. Chang, J.-H. Tao, C.-E. Tsai, Y.-J. Cheng, and C.-S. Hsu, "Cross-linked triarylamine-based hole-transporting layer for solution-processed PEDOT:PSS-free inverted perovskite solar cells," *ACS Applied Materials & Interfaces*, vol. 10, pp. 21466–21471, jun 2018.

20. Z. Li, Z. Zhu, C.-C. Chueh, J. Luo, and A. K.-Y. Jen, "Facile thiol-ene thermal crosslinking reaction facilitated hole-transporting layer for highly efficient and stable perovskite solar cells," *Advanced Energy Materials*, vol. 6, p. 1601165, aug 2016.

21. Z. Yu and L. Sun, "Recent progress on hole-transporting materials for emerging organometal halide perovskite solar cells," *Advanced Energy Materials*, vol. 5, p. 1500213, apr 2015.

22. T.-Y. Chiang, G.-L. Fan, J.-Y. Jeng, K.-C. Chen, P. Chen, T.-C. Wen, T.-F. Guo, and K.-T. Wong, "Functional p-type, polymerized organic electrode interlayer in CH3nh3pbi3 perovskite/fullerene planar heterojunction hybrid solar cells," *ACS Applied Materials & Interfaces*, vol. 7, pp. 24973–24981, oct 2015.

23. J. Xu, O. Voznyy, R. Comin, X. Gong, G. Walters, M. Liu, P. Kanjanaboos, X. Lan, and E. H. Sargent, "Crosslinked remote-doped hole-extracting contacts enhance stability under accelerated lifetime testing in perovskite solar cells," *Advanced Materials*, vol. 28, pp. 2807–2815, jan 2016.

24. Y. Zhang, C. Kou, J. Zhang, Y. Liu, W. Li, Z. Bo, and M. Shao, "Crosslinked and dopant free hole transport materials for efficient and stable planar perovskite solar cells," *Journal of Materials Chemistry A*, vol. 7, no. 10, pp. 5522–5529, 2019.

25. D. Messmer, O. Bertran, R. Kissner, C. Alemán, and A. D. Schlüter, "Main-chain scission of individual macromolecules induced by solvent swelling," *Chemical Science*, vol. 10, no. 24,

pp. 6125–6139, 2019.

26. J.-Y. Lai, S.-J. Huang, and S.-H. Chen, "Poly(methyl methacrylate)/(DMF/metal salt) complex membrane for gas separation," *Journal of Membrane Science*, vol. 74, pp. 71–82, oct 1992.

27. T. H. Schloemer, J. A. Christians, J. M. Luther, and A. Sellinger, "Doping strategies for small molecule organic hole-transport materials: impacts on perovskite solar cell performance and stability," *Chemical Science*, vol. 10, no. 7, pp. 1904–1935, 2019.

28. W. Li, H. Dong, L. Wang, N. Li, X. Guo, J. Li, and Y. Qiu, "Montmorillonite as bifunctional buffer layer material for hybrid perovskite solar cells with protection from corrosion and retarding recombination," *J. Mater. Chem. A*, vol. 2, no. 33, pp. 13587–13592, 2014.

29. J. Li, C. W. Rochester, I. E. Jacobs, S. Friedrich, P. Stroeve, M. Riede, and A. J. Moulé, "Measurement of small molecular dopant f4tcnq and c60f36 diffusion in organic bilayer architectures," *ACS Applied Materials & Interfaces*, vol. 7, pp. 28420–28428, dec 2015.

30. Z. Q. Gao, B. X. Mi, G. Z. Xu, Y. Q. Wan, M. L. Gong, K. W. Cheah, and C. H. Chen, "An organic p-type dopant with high thermal stability for an organic semiconductor," *Chem. Commun.*, no. 1, pp. 117–119, 2008.

31. Y.-D. Zhang, R. D. Hreha, G. E. Jabbour, B. Kippelen, N. Peyghambarian, and S. R. Marder, "Photo-crosslinkable polymers as hole-transport materials for organic light-emitting diodes," *Journal of Materials Chemistry*, vol. 12, pp. 1703–1708, may 2002.

32. N. J. Jeon, J. H. Noh, Y. C. Kim, W. S. Yang, S. Ryu, and S. I. Seok, "Solvent engineering for high-performance inorganic–organic hybrid perovskite solar cells," *Nature Materials*, vol. 13, pp. 897–903, jul 2014.

33. S. Ryu, J. H. Noh, N. J. Jeon, Y. C. Kim, W. S. Yang, J. Seo, and S. I. Seok, "Voltage output of efficient perovskite solar cells with high open-circuit voltage and fill factor," *Energy Environ. Sci.*, vol. 7, no. 8, pp. 2614–2618, 2014.

34. D. Zhao, M. Sexton, H.-Y. Park, G. Baure, J. C. Nino, and F. So, "High-efficiency solution-processed planar perovskite solar cells with a polymer hole transport layer," *Advanced Energy Materials*, vol. 5, p. 1401855, dec 2014.

35. J. T.-W. Wang, Z. Wang, S. Pathak, W. Zhang, D. W. deQuilettes, F. Wisnivesky-Rocca-Rivarola, J. Huang, P. K. Nayak, J. B. Patel, H. A. M. Yusof, Y. Vaynzof, R. Zhu, I. Ramirez, J. Zhang, C. Ducati, C. Grovenor, M. B. Johnston, D. S. Ginger, R. J. Nicholas, and H. J. Snaith, "Efficient perovskite solar cells by metal ion doping," *Energy & Environmental Science*, vol. 9, no. 9, pp. 2892–2901, 2016.

36. B. Domercq, R. D. Hreha, Y.-D. Zhang, A. Haldi, S. Barlow, S. R. Marder, and B. Kippelen, "Organic light-emitting diodes with multiple photocrosslinkable hole-transport layers," *Journal of Polymer Science Part B: Polymer Physics*, vol. 41, pp. 2726–2732, oct 2003.

37. R. D. Hreha, A. Haldi, B. Domercq, S. Barlow, B. Kippelen, and S. R. Marder, "Synthesis of acrylate and norbornene polymers with pendant 2,7-bis(diarylamino)fluorene hole-transport groups," *Tetrahedron*, vol. 60, pp. 7169–7176, aug 2004.

38. B. Domercq, R. D. Hreha, Y.-D. Zhang, N. Larribeau, J. N. Haddock, C. Schultz, S. R. Marder, and B. Kippelen, "Photo-patternable hole-transport polymers for organic light-emitting diodes," *Chemistry of Materials*, vol. 15, pp. 1491–1496, apr 2003.

39. A. Kimyonok, B. Domercq, A. Haldi, J.-Y. Cho, J. R. Carlise, X.-Y. Wang, L. E. Hayden, S. C. Jones, S. Barlow, S. R. Marder, B. Kippelen, and M. Weck, "Norbornene-based copolymers with iridium complexes and bis(carbazolyl)fluorene groups in their side-chains and their use in light-emitting diodes," *Chemistry of Materials*, vol. 19, pp. 5602–5608, nov 2007.

40. Q. Sun, G. Subramanyam, L. Dai, M. Check, A. Campbell, R. Naik, J. Grote, and Y. Wang,

"Highly efficient quantum-dot light-emitting diodes with DNA-CTMA as a combined hole-transporting and electron-blocking layer," *ACS Nano*, vol. 3, pp. 737–743, feb 2009.

41. D. H. Cao, C. C. Stoumpos, C. D. Malliakas, M. J. Katz, O. K. Farha, J. T. Hupp, and M. G. Kanatzidis, "Remnant PbI2, an unforeseen necessity in high-efficiency hybrid perovskite-based solar cells?," *APL Materials*, vol. 2, p. 091101, sep 2014.

42. B. wook Park, N. Kedem, M. Kulbak, D. Y. Lee, W. S. Yang, N. J. Jeon, J. Seo, G. Kim, K. J. Kim, T. J. Shin, G. Hodes, D. Cahen, and S. I. Seok, "Understanding how excess lead iodide precursor improves halide perovskite solar cell performance," *Nature Communications*, vol. 9, aug 2018.

43. B. Yu, H. Zhang, J. Wu, Y. Li, H. Li, Y. Li, J. Shi, H. Wu, D. Li, Y. Luo, and Q. Meng, "Solvent-engineering toward CsPb(IxBr1-x)3 films for high-performance inorganic perovskite solar cells," *Journal of Materials Chemistry A*, vol. 6, no. 40, pp. 19810–19816, 2018.

44. A. Ho-Baillie, M. Zhang, C. F. J. Lau, F.-J. Ma, and S. Huang, "Untapped potentials of inorganic metal halide perovskite solar cells," *Joule*, vol. 3, pp. 938–955, apr 2019.

45. Y. Shao, Z. Xiao, C. Bi, Y. Yuan, and J. Huang, "Origin and elimination of photocurrent hysteresis by fullerene passivation in CH3nh3pbi3 planar heterojunction solar cells," *Nature Communications*, vol. 5, dec 2014.

46. H. Li, L. Tao, F. Huang, Q. Sun, X. Zhao, J. Han, Y. Shen, and M. Wang, "Enhancing efficiency of perovskite solar cells via surface passivation with graphene oxide interlayer," *ACS Applied Materials & Interfaces*, vol. 9, pp. 38967–38976, oct 2017.

47. Y. Zhang, M. Liu, G. E. Eperon, T. C. Leijtens, D. McMeekin, M. Saliba, W. Zhang, M. de Bastiani, A. Petrozza, L. M. Herz, M. B. Johnston, H. Lin, and H. J. Snaith, "Charge selective contacts, mobile ions and anomalous hysteresis in organic–inorganic perovskite solar cells," *Materials Horizons*, vol. 2, no. 3, pp. 315–322, 2015.

48. V. W. Bergmann, S. A. L. Weber, F. J. Ramos, M. K. Nazeeruddin, M. Grätzel, D. Li, A. L. Domanski, I. Lieberwirth, S. Ahmad, and R. Berger, "Real-space observation of unbalanced charge distribution inside a perovskite-sensitized solar cell," *Nature Communications*, vol. 5, sep 2014.

49. H. Zhang, L. Xue, J. Han, Y. Q. Fu, Y. Shen, Z. Zhang, Y. Li, and M. Wang, "New generation perovskite solar cells with solution-processed amino-substituted perylene diimide derivative as electron-transport layer," *Journal of Materials Chemistry A*, vol. 4, no. 22, pp. 8724–8733, 2016.

50. B. Chaudhary, A. Kulkarni, A. K. Jena, M. Ikegami, Y. Udagawa, H. Kunugita, K. Ema, and T. Miyasaka, "Poly(4-vinylpyridine)-based interfacial passivation to enhance voltage and moisture stability of lead halide perovskite solar cells," *ChemSusChem*, vol. 10, pp. 2473–2479, may 2017.

51. M. L. Petrus, K. Schutt, M. T. Sirtl, E. M. Hutter, A. C. Closs, J. M. Ball, J. C. Bijleveld, A. Petrozza, T. Bein, T. J. Dingemans, T. J. Savenije, H. Snaith, and P. Docampo, "New generation hole transporting materials for perovskite solar cells: Amide-based small-molecules with nonconjugated backbones," *Advanced Energy Materials*, vol. 8, p. 1801605, oct 2018.

52. J. Peng, Y. Wu, W. Ye, D. A. Jacobs, H. Shen, X. Fu, Y. Wan, T. Duong, N. Wu, C. Barugkin, H. T. Nguyen, D. Zhong, J. Li, T. Lu, Y. Liu, M. N. Lockrey, K. J. Weber, K. R. Catchpole, and T. P. White, "Interface passivation using ultrathin polymer–fullerene films for high-efficiency perovskite solar cells with negligible hysteresis," *Energy & Environmental Science*, vol. 10, no. 8, pp. 1792–1800, 2017.

53. M. Stolterfoht, C. M. Wolff, J. A. Márquez, S. Zhang, C. J. Hages, D. Rothhardt, S. Albrecht, P. L. Burn, P. Meredith, T. Unold, and D. Neher, "Visualization and suppression of interfacial recombination for high-efficiency large-area pin perovskite solar cells," *Nature Energy*, vol. 3,

pp. 847–854, jul 2018.

54. D. Bi, C. Yi, J. Luo, J.-D. Décoppet, F. Zhang, S. M. Zakeeruddin, X. Li, A. Hagfeldt, and M. Grätzel, "Polymer-templated nucleation and crystal growth of perovskite films for solar cells with efficiency greater than 21%," *Nature Energy*, vol. 1, sep 2016.

55. F. Wang, A. Shimazaki, F. Yang, K. Kanahashi, K. Matsuki, Y. Miyauchi, T. Takenobu, A. Wakamiya, Y. Murata, and K. Matsuda, "Highly efficient and stable perovskite solar cells by interfacial engineering using solution-processed polymer layer," *The Journal of Physical Chemistry C*, vol. 121, pp. 1562–1568, jan 2017.

56. X. Liu, Y. Cheng, C. Liu, T. Zhang, N. Zhang, S. Zhang, J. Chen, Q. Xu, J. Ouyang, and H. Gong, "20.7% highly reproducible inverted planar perovskite solar cells with enhanced fill factor and eliminated hysteresis," *Energy & Environmental Science*, vol. 12, no. 5, pp. 1622–1633, 2019.

57. W.-J. Choi, D.-J. Kwak, C.-S. Park, and Y.-M. Sung, "Characterization of transparent conductive ITO, ITiO, and FTO films for application in photoelectrochemical cells," *Journal of Nanoscience and Nanotechnology*, vol. 12, pp. 3394–3397, apr 2012.

58. M. A. Aouaj, R. Diaz, A. Belayachi, F. Rueda, and M. Abd-Lefdil, "Comparative study of ITO and FTO thin films grown by spray pyrolysis," *Materials Research Bulletin*, vol. 44, pp. 1458–1461, jul 2009.

59. X. Xu, C. Ma, Y. Cheng, Y.-M. Xie, X. Yi, B. Gautam, S. Chen, H.-W. Li, C.-S. Lee, F. So, and S.-W. Tsang, "Ultraviolet-ozone surface modification for non-wetting hole transport materials based inverted planar perovskite solar cells with efficiency exceeding 18%," *Journal of Power Sources*, vol. 360, pp. 157–165, aug 2017.

60. S. Hong, J. Lee, H. Kang, G. Kim, S. Kee, J.-H. Lee, S. Jung, B. Park, S. Kim, H. Back, K. Yu, and K. Lee, "High-efficiency large-area perovskite photovoltaic modules achieved via electrochemically assembled metal-filamentary nanoelectrodes," *Science Advances*, vol. 4, p. eaat3604, aug 2018.

61. D. Forgács, L. Gil-Escrig, D. Pérez-Del-Rey, C. Momblona, J. Werner, B. Niesen, C. Ballif, M. Sessolo, and H. J. Bolink, "Efficient monolithic perovskite/perovskite tandem solar cells," *Advanced Energy Materials*, vol. 7, p. 1602121, dec 2016.

62. D. P. McMeekin, S. Mahesh, N. K. Noel, M. T. Klug, J. Lim, J. H. Warby, J. M. Ball, L. M. Herz, M. B. Johnston, and H. J. Snaith, "Solution-processed all-perovskite multi-junction solar cells," *Joule*, vol. 3, pp. 387–401, feb 2019.

63. J. A. Christians, S. N. Habisreutinger, J. J. Berry, and J. M. Luther, "Stability in perovskite photovoltaics: A paradigm for newfangled technologies," *ACS Energy Letters*, vol. 3, pp. 2136–2143, aug 2018.

64. F. A. Roghabadi, M. Alidaei, S. M. Mousavi, T. Ashjari, A. S. Tehrani, V. Ahmadi, and S. M. Sadrameli, "Stability progress of perovskite solar cells dependent on the crystalline structure: From 3d ABX3 to 2d ruddlesden–popper perovskite absorbers," *Journal of Materials Chemistry A*, vol. 7, no. 11, pp. 5898–5933, 2019.

65. E. Raza, F. Aziz, and Z. Ahmad, "Stability of organometal halide perovskite solar cells and role of HTMs: recent developments and future directions," *RSC Advances*, vol. 8, no. 37, pp. 20952–20967, 2018.

CHAPTER 9

Conclusion

9.1 Summary

The research presented in this thesis demonstrates progress towards stable and efficient single-junction perovskite solar cells through the use of interface modifications and new materials for charge selective contacts.

Chapter 4 focused on understanding the function of the mesoporous layer, which was originally borrowed from dye sensitized solar cells where short diffusion lengths required a bulk heterojunction architecture. A thin mesoporous layer capped by a bulk perovskite remained a common feature of PSCs with record-breaking efficiency but the function of the mesoporous layer was not fully understood. Chapter 4 demonstrated that the mesoporous layer provides p- or n-doping near the p- and n-type contacts, shifting the work function of the perovskite near the interface. This understanding was then applied to improve the efficiency of SnO_2, the most stable metal oxide-perovskite interface, by applying a thin layer of mesoporous Al_2O_3, resulting in improved V_{oc} and power conversion efficiency.

Chapter 6 demonstrated that both photovoltaic performance and thermal stability could be improved by treating the SnO_2 interface with cesium salts. While device stability was greatly limited by the use of Spiro-OMeTAD, tBP, and Li-TFSI and the search for a thermally stable, dopant free HTM to complete this work is ongoing. Thus far, CuSCN was found to be much less thermally stable than reported in literature, PTAA with BCF dopant was stable over hundreds of hours at 85 °C but failed to achieve efficiencies higher than 15%, and work on a stable HTM-dopant system is ongoing.

Chapter 5 continued with the exploration of metal oxide-perovskite interfaces. While ZnO had been largely neglected as an n-type within the PSC research community, it was shown through a literature review that the band alignment, transmittance, and conductivity compared favorably with the more commonly used TiO_2 and SnO_2. The hypothesized acid-base reaction between methylammonium cations and ZnO was confirmed with strong experimental evidence, indicating the release of methylamine gas from the deprotonated organic cation, the formation of hydroxyl groups at the ZnO-perovskite interface, and the development of zinc halides. The pKa of the organic cation was shown to play a decisive role in device stability, and substituting formamidinium and cesium for methylammonium greatly improved the thermal stability of the interface.

The focus of the thesis then shifted from metal oxides to novel hole transport materials. Chapter 7 demonstrated that a low-cost, organic small molecule hole transport material based on an ethylenedioxythiophone core provided slightly improved efficiency to the commonly used Spiro-OMeTAD. It was shown that EDOT-Amide-TPA also provided device stability improvements, possibly due to achieving the same performance as Spiro with a lower concentration of hygroscopic and volatile dopants, or potentially due to Li cation coordination with the HTM. While this chapter presented an economical and high-performance alternative to Spiro-OMeTAD, the elimination of tBP and Li-TFSI would be preferable for long-term stability. In addition, the HTM required heating during deposition from solution due to low solubility (70-90 °C), which

also resulted in a maximum HTM layer thickness of just 50 nm. While a thinner HTM is desirable for an improved fill factor, it appeared there were pinholes in the HTM since evaporation of Ag electrodes resulted in poor device performance ($<$ 7% PCE). In addition, obvious film discoloration occurred within a few hours under ambient conditions which may have been due to the formation of silver halides.

Chapter 8 reports the first use of a UV crosslinkable HTM which performs comparably to state-of-the-art PolyTPD even when undoped. By utilizing all organic charge transport layers, limiting the use of the methylammonium cation, and evaporating a Cr-Au bi-layer electrode, the devices showed outstanding thermal stability, achieving 3,000 hours at 85 °C with no loss from the initial power conversion efficiency. A tandem proof of concept was also demonstrated, with the UV-crosslinkable HTM withstanding the deposition of a sequential, solution-processed perovskite layer while the PolyTPD failed to do so.

9.2 Future Work

There are multiple estimates on the manufacturing costs of perovskite solar cells at commercial scale.[1–3] Despite the low costs of metal halide perovskite absorbers, the aggregate cost of other materials in the solar cell is often the single largest cost component (greater than labor, capital expenses, or overhead). The largest components of material costs, in turn, are precious metal electrodes, organic charge transport materials, and FTO glass. To achieve the lowest possible production costs, further research may be needed to evaluate and improve the long-term stability of PSC with alternative electrodes metals, such as Cu and Al. Metal oxide selective contacts also provide much lower cost and improved performance relative to organic counterparts, but the degradation mechanisms in SnO_2 and NiO_x are still largely unknown and thus their suitability for commercial deployment remains questionable. If the greater interfacial stability of organic contacts makes them a necessity for commercial photovoltaics, perhaps the high cost of fullerene derivatives such as PCBM

could be avoided with novel synthesis routes for non-fullerene acceptors, but these materials have only achieved power conversion efficiencies of about 10% in perovskite solar cells.[4–6]

The stability of the perovskite absorbers might also be improved, but progress is constrained by a small choice of suitable cations. Guanidinium is about two orders of magnitude less acidic than formamidinium and should provide greatly improved thermal stability when in contact with amphoteric metal oxides. Despite the large ionic radius over perovskite films have incorporated over 10% of guanidinium cations on the A site, and the reduced acidity make this cation for an organic passivation layer at perovskite-charge transport interfaces. However, initial studies not reported elsewhere in this thesis appear to indicate that even 1% guanidinium incorporation substantially compromises the long-term stability of formamidinium-cesium absorbers in ambient. Bulky organic cations have also been used to form 2D Ruddlesden–Popper layered perovskites at grain boundariers and interfaces,[7,8] but the relative stability of these mixed phases needs better evaluation under a variety of aging conditions such as moisture, heat, bias, and irradiation. While there is progress in stabilizing the thermally stable $CsPbI_3$,[9,10] whether this material can achieve the scale required to substantially reduce emissions is called into question as global cesium production may be quite low and is not even tracked by the United States Geological Survey. In general, it would be beneficial for the community to understand more of the root causes of degradation, but perhaps due to time constraints and pressure to publish these deeper levels of understanding are often substituted for simple time-dependent comparisons between competing materials or processing techniques.

In conclusion, perovskite solar cells are promising candidates for next-generation photovoltaics. This thesis has shown several routes to further improving device performance and stability. While the research community has largely focused on improvements to power conversion efficiency, long-term device stability is arguably a larger concern now that (small area) perovskite solar cells are approaching parity with the best silicon cells. Ensuring operational lifetimes of decades remains a formidable

challenge, but Oxford Photovoltaics has recently reported that perovskite solar cells passed damp heat tests (IEC 61215) over 2000 hours. The progress made with organic LED lifetimes over the past two decades also provides some hope, since it demonstrates that organic thin film device lifetimes can be improved by three orders of magnitude on relatively short time scales.

References

1. M. Cai, Y. Wu, H. Chen, X. Yang, Y. Qiang, and L. Han, "Cost-performance analysis of perovskite solar modules," *Advanced Science*, vol. 4, p. 1600269, sep 2016.
2. Z. Song, C. L. McElvany, A. B. Phillips, I. Celik, P. W. Krantz, S. C. Watthage, G. K. Liyanage, D. Apul, and M. J. Heben, "A technoeconomic analysis of perovskite solar module manufacturing with low-cost materials and techniques," *Energy & Environmental Science*, vol. 10, no. 6, pp. 1297–1305, 2017.
3. N. L. Chang, A. W. Y. Ho-Baillie, P. A. Basore, T. L. Young, R. Evans, and R. J. Egan, "A manufacturing cost estimation method with uncertainty analysis and its application to perovskite on glass photovoltaic modules," *Progress in Photovoltaics: Research and Applications*, vol. 25, pp. 390–405, feb 2017.
4. G. Liu, X. Xie, X. Xu, Y. Wei, F. Zeng, and Z. Liu, "High-performance inverted two-dimensional perovskite solar cells using non-fullerene acceptor as electron transport layer," *Organic Electronics*, vol. 62, pp. 189–194, nov 2018.
5. P. Karuppuswamy, H.-C. Chen, P.-C. Wang, C.-P. Hsu, K.-T. Wong, and C.-W. Chu, "The 3 d structure of twisted benzo[ghi]perylene-triimide dimer as a non-fullerene acceptor for inverted perovskite solar cells," *ChemSusChem*, vol. 11, pp. 415–423, dec 2017.
6. S. S. Kim, S. Bae, and W. H. Jo, "A perylene diimide-based non-fullerene acceptor as an electron transporting material for inverted perovskite solar cells," *RSC Advances*, vol. 6, no. 24, pp. 19923–19927, 2016.
7. Z. Wang, Q. Lin, F. P. Chmiel, N. Sakai, L. M. Herz, and H. J. Snaith, "Efficient ambient-air-stable solar cells with 2d–3d heterostructured butylammonium-caesium-formamidinium lead halide perovskites," *Nature Energy*, vol. 2, aug 2017.
8. D. Ramirez, K. Schutt, Z. Wang, A. J. Pearson, E. Ruggeri, H. J. Snaith, S. D. Stranks, and F. Jaramillo, "Layered mixed tin–lead hybrid perovskite solar cells with high stability," *ACS Energy Letters*, vol. 3, pp. 2246–2251, aug 2018.
9. C. Wang, A. S. R. Chesman, and J. J. Jasieniak, "Stabilizing the cubic perovskite phase of CsPbI3 nanocrystals by using an alkyl phosphinic acid," *Chemical Communications*, vol. 53, no. 1, pp. 232–235, 2017.
10. Y. Wang, M. I. Dar, L. K. Ono, T. Zhang, M. Kan, Y. Li, L. Zhang, X. Wang, Y. Yang, X. Gao, Y. Qi, M. Grätzel, and Y. Zhao, "Thermodynamically stabilized -CsPbI3–based perovskite solar cells with efficiencies 18%," *Science*, vol. 365, pp. 591–595, aug 2019.